Yanzhu Liu
Liqun Chen

Chaos in Attitude Dynamics of Spacecraft

TSINGHUA UNIVERSITY PRESS

Springer

Yanzhu Liu
Liqun Chen

Chaos in Attitude Dynamics of Spacecraft

Yanzhu Liu
Liqun Chen

Chaos in Attitude Dynamics of Spacecraft

With 86 figures

TSINGHUA UNIVERSITY PRESS

Springer

Authors:

Yanzhu Liu
Department of Engineering Mechanics
Shanghai Jiao Tong University
Shanghai, China
E-mail: liuyzhc@online.sh.cn

Liqun Chen
Department of Mechanics
Shanghai University
Shanghai, China
E-mail: lqchen@staff.shu.edu.cn

ISBN 978-7-302-28298-3
Tsinghua University Press, Beijing

ISBN 978-3-642-30079-0 ISBN 978-3-642-30080-6 (eBook)
Springer Heidelberg New York Dordrecht London

Library of Congress Control Number: 2012937465

© Tsinghua University Press, Beijing and Springer-Verlag Berlin Heidelberg 2013
This work is subject to copyright. All rights are reserved by the Publishers, whether the whole or part of the material is concerned, specifically the rights of translation, reprinting, reuse of illustrations, recitation, broadcasting, reproduction on microfilms or in any other physical way, and transmission or information storage and retrieval, electronic adaptation, computer software, or by similar or dissimilar methodology now known or hereafter developed. Exempted from this legal reservation are brief excerpts in connection with reviews or scholarly analysis or material supplied specifically for the purpose of being entered and executed on a computer system, for exclusive use by the purchaser of the work. Duplication of this publication or parts thereof is permitted only under the provisions of the Copyright Law of the Publishers' locations, in its current version, and permission for use must always be obtained from Springer. Permissions for use may be obtained through RightsLink at the Copyright Clearance Center. Violations are liable to prosecution under the respective Copyright Law.
The use of general descriptive names, registered names, trademarks, service marks, etc. in this publication does not imply, even in the absence of a specific statement, that such names are exempt from the relevant protective laws and regulations and therefore free for general use.
While the advice and information in this book are believed to be true and accurate at the date of publication, neither the authors nor the editors nor the publishers can accept any legal responsibility for any errors or omissions that may be made. The publishers make no warranty, express or implied, with respect to the material contained herein.

Printed on acid-free paper

Springer is part of Springer Science+Business Media (www.springer.com)

Yanzhu Liu
Liqun Chen

航天器姿态动力学中的混沌

Chaos in Attitude Dynamics of Spacecraft

Yanzhu Liu
Liqun Chen

航天器姿态动力学中的混沌

Chaos in Attitude Dynamics of Spacecraft

With 86 figures

TSINGHUA UNIVERSITY PRESS

Springer

内 容 简 介

航天器混沌姿态运动的识别和控制问题在航天科学中具有重要实际意义。本书致力于总结该领域的近期发展，提供研究航天器姿态运动的新方法和观点，也为该领域进一步的深入分析研究提供有明确工程背景的新的数学模型。读者可从本书获得混沌和混沌控制理论及其在航天器姿态运动中应用的知识，包括基本概念，主要方法以及最新进展。

图书在版编目(CIP)数据

航天器姿态动力学中的混沌 = Chaos in Attitude Dynamics of Spacecraft: 英文/刘延柱，陈立群著. --北京：清华大学出版社，2012.10

ISBN 978-7-302-28298-3

Ⅰ.①航…　Ⅱ.①刘…　②陈…　Ⅲ.①航天器–姿态运动–动力学–混沌理论–英文　Ⅳ.①V412.4

中国版本图书馆 CIP 数据核字(2012)第 043270 号

责任编辑：陈朝晖
责任校对：王淑云
责任印制：

出版发行：清华大学出版社
网　　址：http://www.tup.com.cn, http://www.wqbook.com
地　　址：北京清华大学学研大厦 A 座　　　**邮　　编：**100084
社 总 机：010-62770175　　　**邮　　购：**010-62786544
投稿与读者服务：010-62776969, c-service@tup.tsinghua.edu.cn
质量反馈：010-62772015, zhiliang@tup.tsinghua.edu.cn
印 刷 者：
装 订 者：
经　　销：全国新华书店
开　　本：153mm×235mm　　**印　　张：**11　　**字　　数：**243 千字
版　　次：2012 年 10 月第 1 版　　**印　　次：**2012 年 10 月第 1 次印刷
印　　数：1～0000
定　　价：00.00 元

产品编号：

Preface

The development of spacecraft has drawn considerable attentions in the field of dynamics since the 1950s. The spacecraft can be regarded as a particle or as a body, depending on whether one focuses on the spacecraft's orbital motion or on its rotational motion about the center of mass. Spacecraft attitude dynamics deals with the rotational motion of spacecraft. In the discussion of attitude dynamics, the rotation of spacecraft is usually assumed not to alter the orbit, while the orbit sometimes influences the rotational motion. Almost all spacecraft have some attitude requirements, either explicit pointing requirements for antennas or cameras, requirements for solar panel orientation, or simply a requirement for a given spin-axis direction. All the requirements are implemented by the design of attitude controls. The strategies chosen in the control process may limit the useful lifetime of the spacecraft, since an all-thruster control system depletes its propellant supply. Attitude dynamics forms a theoretical basis of the design and control of spacecraft. The present monograph is concerned with spacecraft attitude motion, although essential elements of orbital dynamics will be introduced and the effects of orbital motion will be included in a few cases.

With the development of nonlinear dynamics, chaos in spacecraft attitude dynamics has stirred renewed interests since the 1990s. In fact, for astronautical investigations, the predictability of spacecraft rotations is critical, and thus chaotic motions must be avoided. On the other hand, there are scientific experiments that require the whole celestial sphere to be scanned, and in those cases the chaotic rotation may be desirable. Therefore chaos theory offers a new method and viewpoint for designing spacecraft. In addition, spacecraft attitude dynamics also provides new mathematical models for engineering application of chaos analysis. Although there are some excellent monographs and textbooks on spacecraft attitude dynamics, there are few treatises on chaotic attitude motion. The present monograph focuses on chaos in spacecraft attitude dynamics.

The monograph begins with the necessary fundamentals. Chapter 1 provides a primer on spacecraft dynamics, and Chapter 2 presents a survey of chaos theory. Different chaotic attitude motions are treated in Chapters 3 and 4. Chapter 3 considers only the planar motion of spacecraft, while Chapter 4 covers the spatial motion. The monograph ends with Chapter 5, dealing with controlling chaotic attitude motion.

The main goal of the monograph is to provide readers with the knowledge of theory and application of chaos and its control in spacecraft attitude dynamics, including the basic concepts, main approaches and the latest research progress. The material is appropriate for university teachers, scientists, engineers, and graduate students in the fields of mechanics, applied mathematics, and aerospace science.

Except for some background presented in Chapters 1 and 2, as well as Sections 4.1 and 5.1, all other materials contained in the monograph are adopted from research papers of the authors and their co-workers. The research work was financially supported by the National Natural Science Foundation of China (Project Nos. 19782003 and 10082003), the National Outstanding Young Scientists Foundation of China (Project No. 10725209), Shanghai Municipal Development Foundation of Science and Technology (Project Nos. 98JC14032 and 98SHB1417), Shanghai Municipal Education Commission Scientific Research Project (No. 2000A12), and Shanghai Leading Academic Discipline Project (No. Y0103). The first author thanks his former PhD students Professor Peng Jianhua, Professor Chen Liqun, Dr. Cheng Gong, and his postdoctoral fellow Professor Yu Hongjie for their collaborations on related research. The second author thanks Professor Liu Yanzhu, who, serving as his PhD supervisor, introduced him to this field. He also thanks his hosts, Professor Jean W. Zu (University of Toronto) and Professor C. W. Lim (City University of Hong Kong) for their assistance during his visit to their institutes so that he could complete his portions of the book.

The authors thank Tsinghua University Press and Springer for the publication of this book. They also thank Shanghai Jiao Tong University for partial financial support of the publication.

Yanzhu Liu (Shanghai Jiao Tong University)
Liqun Chen (Shanghai University)

Contents

Chapter 1 Primer on Spacecraft Dynamics

Abstract This chapter provides a fundamental theory of spacecraft dynamics. After a brief survey of gravitational field, the two-body problem is summarized as a simplified model of orbit motion of a spacecraft around the Earth. The main environmental torques acting on spacecraft, the gravitational torque and magnetic torque are introduced. The dynamical equations of attitude motion of a spacecraft are established, where the Euler's equations and Poisson's equations are applied for a rigid spacecraft in gravitational field. The stability problems of the relative equilibrium of a rigid spacecraft in circular orbit under gravitational torque are analyzed by using the first approximation method and the Lyapunov's direct method. The attitude motions of a gyrostat are analyzed as a model of spacecraft with axisymmetric rotors. The permanent rotations and its stability of a spinning spacecraft are discussed under torque-free assumption.

Keywords orbit dynamics, two-body problem, gravitational torque, magnetic torque, Euler's equations, Poisson's equations, torque-free rigid bodies, gyrostats

This chapter presents fundamental theory of spacecraft dynamics that will be needed in chapters 3 and 4. The chapter begins with elementary orbit dynamics, which provides necessary background for attitude dynamics in addition to its own merits. After a brief survey of gravitational field of a particle and a rigid body, a satellite around the Earth is modeled as the two-body problem, and the first integrals are derived from the dynamical equations as the energy integral, the momentum integral, the Laplace integral and the time integral. The Keplerian orbit is discussed with the emphasis on the elliptic motion. Then the chapter turns to attitude dynamics by introducing main environmental torques acting on spacecraft, the gravitational torque and the magnetic torque. Euler's equations and Poisson's equations are applied to the attitude motion of spacecraft in the gravitational field. As two significant special solutions to Euler's equations and Poisson's equations, planar libration and spatial relative equilibrium are analyzed. The dynamical equations of a gyrostat are also developed. The chapter ends with attitude motion of torque-free rigid bodies and gyrostats. The influence of energy dissipation to spinning spacecraft is investigated. The complete treatments of spacecraft dynamics can be found in [1–10].

1.1 Orbital Motion of Spacecraft

1.1.1 Gravitational Field of a Particle

According to Newton's law of universal gravitation, a particle m is attracted by another particle m_{e} by a force

$$\boldsymbol{F} = -G\frac{mm_{\mathrm{e}}}{r^2}\left(\frac{\boldsymbol{r}}{r}\right) \tag{1.1.1}$$

where $\boldsymbol{r}$ denotes the position vector of point m with respect to point m_{e}, m and m_{e} stand for the masses of corresponding points, and $G = 6.67\times10^{-11}\ \mathrm{m}^3/\mathrm{kg}\cdot\mathrm{s}^2$ is the universal gravitational constant (Fig. 1.1).

Define the potential function U of the gravitational field produced by the point m_{e} as

$$U = \frac{Gm_{\mathrm{e}}}{r} = \frac{\mu}{r} \tag{1.1.2}$$

where $\mu = Gm_{\mathrm{e}}$ is a constant depending only on point m_{e}. The gravitational force $\boldsymbol{F}$ acting on point m can be written as

$$\boldsymbol{F} = m\nabla U \tag{1.1.3}$$

where $\nabla = (\partial/\partial x)\boldsymbol{i} + (\partial/\partial y)\boldsymbol{j} + (\partial/\partial z)\boldsymbol{k}$, and $\boldsymbol{i}, \boldsymbol{j}, \boldsymbol{k}$ represent basis-vectors of a reference coordinate frame $(O\text{-}xyz)$ with point m_{e} as the origin O. Define $V = -mU$ as the potential energy of point m in the gravitational field of particle m_{e}.

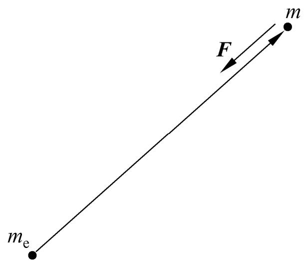

Figure 1.1 Gravitational force of a particle

1.1.2 Gravitational Field of a Rigid Body

To discuss the gravitational field of a rigid body, the central principal axes of a body are established as the reference coordinate frame $(O_{\mathrm{e}}\text{-}xyz)$, where O_{e} is the mass center of a body. The position vectors of a particle m with respect to the point O_e and an arbitrary point P of the body are denoted as $\boldsymbol{r}$ and $\boldsymbol{r}'$, respectively. It follows that $\boldsymbol{r}' = \boldsymbol{r} - \boldsymbol{\rho}$, where $\boldsymbol{\rho}$ is the position vector of point P with respect to point O_e (Fig. 1.2). Let α_i $(i = 1,2,3)$ be the direct cosines of the vector $\boldsymbol{r}$ relative to axes of $(O_\mathrm{e}\text{-}xyz)$, and x, y, z be the coordinates of point P in $(O_\mathrm{e}\text{-}xyz)$. Then the vector $\boldsymbol{r}'$ can be written as

$$\boldsymbol{r}' = (r\alpha_1 - x)\boldsymbol{i} + (r\alpha_2 - y)\boldsymbol{j} + (r\alpha_3 - z)\boldsymbol{k} \tag{1.1.4}$$

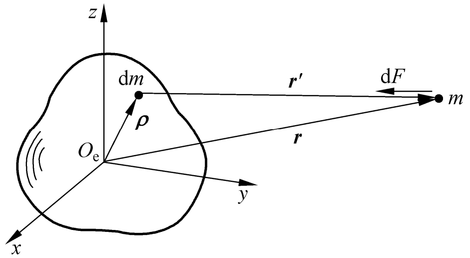

Figure 1.2 Gravitational force of a rigid body

The potential function U of a body is defined as

$$U = G \iiint_S \frac{\mathrm{d}m}{r'} \tag{1.1.5}$$

where the domain of integration S is the whole body. When $\rho \ll r$, substituting Eq. (1.1.4) into Eq. (1.1.5) and considering only the second terms of ρ/r, one obtains

$$U = \frac{Gm_\mathrm{e}}{r}\left[1 + \frac{1}{2m_\mathrm{e}r^2}(A + B + C - 3I)\right] \tag{1.1.6}$$

where m_e is the mass, and A, B, C are the principal moments of inertia of a body in $(O_\mathrm{e}\text{-}xyz)$, respectively,

$$A = \iiint_S (y^2 + z^2)\mathrm{d}m,\ B = \iiint_S (z^2 + x^2)\mathrm{d}m,\ C = \iiint_S (x^2 + y^2)\mathrm{d}m \tag{1.1.7}$$

and I is defined as

$$I = A\alpha_1^2 + B\alpha_2^2 + C\alpha_3^2 \tag{1.1.8}$$

In the case when a body is axisymmetric with respect to z-axis, let $A = B$ and introduce $\mu = Gm_\mathrm{e}$ as the gravitational parameter. Equation (1.1.6) can be simplified as

$$U = \frac{\mu}{r}\left[1 - \frac{C - A}{2m_\mathrm{e}r^2}(3\alpha_3^2 - 1)\right] \tag{1.1.9}$$

For a sphere-symmetric body, $A = C$. Thus

$$U = \frac{\mu}{r} \tag{1.1.10}$$

which is the same as Eq. (1.1.2). It means that the gravitational field of a spherical body is equivalent to that of a particle, in which the whole body mass is located in its mass center. Equation (1.1.9) or (1.1.10) can be used to express the gravitational field of the Earth, which has the gravitational parameter $\mu = 398\,601.19\,\text{km}^3/\text{s}^2$.

1.1.3 Dynamical Equations of Two-body System

Assume that the Earth may be simplified as a rigid sphere. The orbital motion of a satellite around the Earth can be treated as the two-body problem $(m_{\rm e}, m)$ with particle m as a satellite attracted by particle $m_{\rm e}$ as the Earth. Let $O_{\rm e}$ denote the mass center of this system, $\boldsymbol{r}_1$ and $\boldsymbol{r}_2$ denote the position vectors of m and $m_{\rm e}$ with respect to $O_{\rm e}$. Then three points m, $m_{\rm e}$ and $O_{\rm e}$ are collinear with the following relationship (Fig. 1.3):

$$m\boldsymbol{r}_1 + m_{\rm e}\boldsymbol{r}_2 = 0 \tag{1.1.11}$$

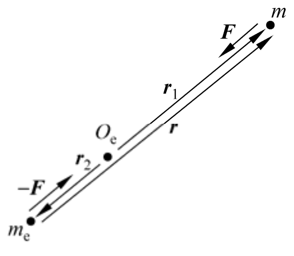

Figure 1.3 Two-body system

The dynamical equations of points m and $m_{\rm e}$ can be derived from Newton's second law as

$$m\ddot{\boldsymbol{r}}_1 = \boldsymbol{F}, \quad m\ddot{\boldsymbol{r}}_{\rm e} = -\boldsymbol{F} \tag{1.1.12}$$

where $\boldsymbol{F}$ is the gravitational force acting on point m,

$$\boldsymbol{F} = -G\frac{mm_{\rm e}}{r^2}\left(\frac{\boldsymbol{r}}{r}\right) \tag{1.1.13}$$

Substitution of $\boldsymbol{r} = \boldsymbol{r}_1 - \boldsymbol{r}_2$ into Eq. (1.1.12) leads to

$$\boldsymbol{r} = \left(1 + \frac{m}{m_\mathrm{e}}\right)\boldsymbol{r}_1 = -\left(1 + \frac{m_\mathrm{e}}{m}\right)\boldsymbol{r}_2 \tag{1.1.14}$$

Thus the following equation can be derived from Eq. (1.1.12)

$$\ddot{\boldsymbol{r}} + \frac{\mu}{r^3}\boldsymbol{r} = 0 \tag{1.1.15}$$

where $\mu = G(m_\mathrm{e} + m)$, which is approximately equal to the gravitational parameter of the Earth $\mu = Gm_\mathrm{e}$, and the mass center O_e coincides with m_e with sufficient accuracy since $m \ll m_\mathrm{e}$. Introduce the velocity $\boldsymbol{v}$ of point m and then rewrite the dynamical Eq. (1.1.15) as

$$\dot{\boldsymbol{v}} + \frac{\mu}{r^3}\boldsymbol{r} = 0 \tag{1.1.16a}$$

$$\dot{\boldsymbol{r}} = \boldsymbol{v} \tag{1.1.16b}$$

1.1.4 First Integrals

(1) Energy Integral

Dot-multiplying each term of Eq. (1.1.16a) by $\boldsymbol{v} = \dot{\boldsymbol{r}}$, and observing that $\boldsymbol{v} \cdot \dot{\boldsymbol{v}} = v\dot{v}$, $\boldsymbol{r} \cdot \dot{\boldsymbol{r}} = r\dot{r}$, one obtains

$$\frac{\mathrm{d}}{\mathrm{d}t}\left(\frac{v^2}{2} - \frac{\mu}{r}\right) = 0 \tag{1.1.17}$$

Thus the integral of energy can be derived as

$$\frac{v^2}{2} - \frac{\mu}{r} = E \tag{1.1.18}$$

where $v^2/2$ and μ/r are, respectively, the kinetic energy and the potential energy of a satellite with unit mass, and the constant E is the conserved total specific energy.

(2) Integral of Angular Momentum

Cross-multiplying each term of Eq. (1.1.16a) with $\boldsymbol{r}$ leads to

$$\frac{\mathrm{d}}{\mathrm{d}t}(\boldsymbol{r} \times \boldsymbol{v}) = 0 \tag{1.1.19}$$

from which the integral of angular momentum is derived as

$$\boldsymbol{r} \times \boldsymbol{v} = \boldsymbol{h} \tag{1.1.20}$$

where $\boldsymbol{h}$ is the conserved specific angular momentum of a satellite with respect to the Earth center O_e. Since the constant vector $\boldsymbol{h}$ is orthogonal to vectors $\boldsymbol{r}$ and $\boldsymbol{v}$, the orbital plane composed of vectors $\boldsymbol{r}$ and $\boldsymbol{v}$ has a fixed orientation in space. In order to determine the spatial position of the orbital plane, define an inertial reference frame (O_e - $X_0Y_0Z_0$) with the mass center of the Earth O_e as the origin, where Z_0-axis is parallel to the polar axis of the Earth, the plane (X_0, Y_0) is parallel to the equatorial plane of the Earth, and X_0-axis is along the node of the ecliptic plane and the equatorial plane with direction to the first point of Aries. A celestial sphere is fixed on (O_e - $X_0Y_0Z_0$) with center O_e and arbitrary radius. Within two intersection points of the node line of plane (X_0, Y_0) and the orbital plane with the celestial sphere, select point N corresponding to the ascension of a satellite as the ascending point. The angle $\boldsymbol{\Omega}$ between $O_\mathrm{e}N$ and $O_\mathrm{e}X_0$ is defined as the right ascension of the ascending node. The incline angle i of the orbital plane with respect to the plane (X_0, Y_0) is defined as the inclination angle of the orbital plane. Therefore, the orientation of the orbital plane can be determined by two angles $\boldsymbol{\Omega}$ and i (Fig. 1.4). Denote the angle between the velocity $\boldsymbol{v}$ and the local horizontal plane by θ. Then the area $\mathrm{d}S$ swept by the position vector $\boldsymbol{r}$ in time interval $\mathrm{d}t$ can be calculated as (Fig. 1.5)

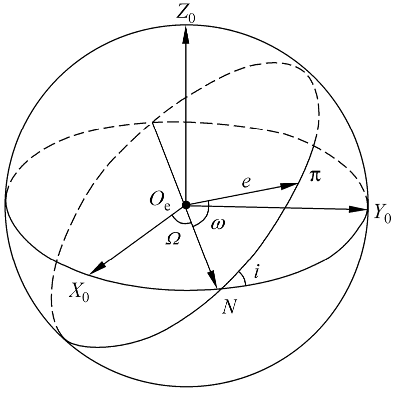

Figure 1.4 Celestial sphere and orbital plane

$$\mathrm{d}S = \frac{1}{2} r (v\mathrm{d}t) \cos\theta = \frac{1}{2} |\boldsymbol{r} \times \boldsymbol{v}| \mathrm{d}t = \frac{1}{2} h \mathrm{d}t \tag{1.1.21}$$

Then the magnitude of vector $\boldsymbol{h}$ is equal to two times the area velocity swept by position vector $\boldsymbol{r}$.

$$h = 2\frac{\mathrm{d}S}{\mathrm{d}t} \tag{1.1.22}$$

It means that the satellite moves in the orbit with a constant area velocity.

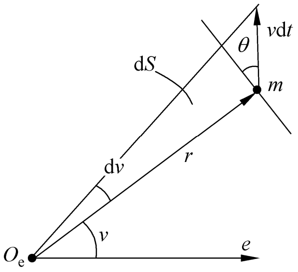

Figure 1.5 Area swept by vector $\boldsymbol{r}$

(3) Laplace's Integral

Cross-multiplying each term of Eq. (1.1.16a) by $\boldsymbol{h}$, one obtains

$$\dot{\boldsymbol{v}}\times\boldsymbol{h}+\frac{\mu}{r^3}\boldsymbol{r}\times\boldsymbol{h}=\frac{\mathrm{d}}{\mathrm{d}t}\left(\boldsymbol{v}\times\boldsymbol{h}-\frac{\mu\boldsymbol{r}}{r}\right)=0 \tag{1.1.23}$$

from which the Laplace's integral is derived as follows

$$\boldsymbol{v}\times\boldsymbol{h}-\frac{\mu\boldsymbol{r}}{r}=e \tag{1.1.24}$$

Since both vectors $\boldsymbol{v}\times\boldsymbol{h}$ and $\boldsymbol{r}$ lie in the orbital plane, the constant vector $\boldsymbol{e}$ should be also restricted to the same plane (Fig. 1.4). The magnitude of vector $\boldsymbol{e}$ can be determined by constants E and h as

$$e^2=\frac{1}{\mu^2}\left(\boldsymbol{v}\times\boldsymbol{h}-\frac{\mu\boldsymbol{r}}{r}\right)^2=1+\frac{2Eh^2}{\mu^2} \tag{1.1.25}$$

Consequently, the Laplace's integral provides only one scalar relationship to specify the location of vector $\boldsymbol{e}$ in the orbital plane. The angle ω between $\boldsymbol{e}$ and $O_\mathrm{e}N$ is selected as an independent constant, which is called the orbit angle of perigee. Dot-multiplying $\boldsymbol{r}$ by $\boldsymbol{e}$ leads to

$$\boldsymbol{r}\cdot\boldsymbol{e}=\boldsymbol{r}\cdot\left(\frac{1}{\mu}\boldsymbol{v}\times\boldsymbol{h}-\frac{\boldsymbol{r}}{r}\right)=p-r \tag{1.1.26}$$

where p is called the semi-parameter expressed as

$$p=\frac{h^2}{\mu} \tag{1.1.27}$$

Let the angle ν between the position vector $\boldsymbol{r}$ and vector $\boldsymbol{e}$ be the angular coordinate of point m in the orbital plane. ν is called the true anomaly of a satellite. Since $\boldsymbol{r}\cdot\boldsymbol{e}=re\cos\nu$, comparing it with Eq. (1.1.26) yields

$$r=\frac{p}{1+e\cos\nu} \tag{1.1.28}$$

Equation (1.1.28) determining the position of point m in the orbital plane is a conic section with eccentricity e. Therefore, vector $\boldsymbol{e}$ is called the eccentricity vector. The angle u between vector $\boldsymbol{r}$ and O_eN is used as another angular coordinate to specify the location of point m in the orbital plane.

$$u=\nu+\omega \tag{1.1.29}$$

(4) Time Integral

In order to determine the relationship between the position and the time, Eq. (1.1.22) is rewritten as

$$r^2\frac{\mathrm{d}\nu}{\mathrm{d}t}=h \tag{1.1.30}$$

Thus the angular velocity of radius-vector $\boldsymbol{r}$ in the orbital plane can be expressed as

$$\frac{\mathrm{d}\nu}{\mathrm{d}t}=\frac{\sqrt{\mu p}}{r^2} \tag{1.1.31}$$

Substitution of Eq. (1.1.28) into Eq. (1.1.31) leads to the time integral as

$$t=t_0+\sqrt{\frac{p^3}{\mu}}\int_0^\nu\frac{\mathrm{d}\nu}{(1+e\cos\nu)} \tag{1.1.32}$$

where t_0 is the time at $\nu=0$, i.e. the time of passing the perigee.

Aforementioned first integrals contain 8 integration constants: E, h, Ω, I, ω, p, e, and t_0, in which only 6 constants are needed in order to determine the motion of point m. When 6 constants are chosen, the other 2 can be calculated by Eqs. (1.1.25) and (1.1.27). The 6 independent integration constants are called orbital elements.

1.1.5 Characteristics of Keplerian Orbit

Establish a reference frame (O_e -$\xi\eta\zeta$) in the orbital plane with O_e as the origin, $O_e\xi$ along the eccentricity vector $\boldsymbol{e}$, and $O_e\zeta$ normal to the plane. Since $r(\nu)=r(-\nu)$, the orbit curve is symmetrical with respect to $O_e\xi$. The intersection point of the orbit and the vector $\boldsymbol{e}$ is called the perigee, and denoted by π, which has a minimum distance to point O_e. The distance between m and O_e is equal to the semi-parameter p when the orbit intersects $O_e\eta$ (Fig. 1.6).

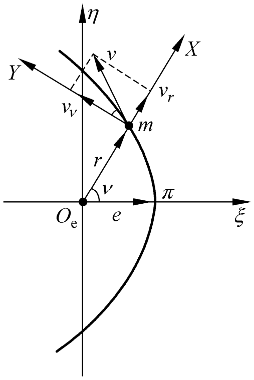

Figure 1.6 Keplerian orbit

According to the character of conic section, the orbit curve belongs to different types determined by the eccentricity e: ellipse $(e<1)$, parabola $(e=1)$, or hyperbola $(e>1)$. As the hyperbolic curve is unrestricted in space, in order to ensure the positiveness of v^2, the constant of the energy integral (1.1.18) should be $E>0$. On the contrary, when $E<0$, the range of point m is restricted by $r \leqslant \mu/|E|$ and corresponds to an ellipse. The parabola is a critical case when $E=0$. The velocity v_p of a parabolic orbit can be obtained from Eq. (1.1.18) as

$$v_p = \sqrt{\frac{2\mu}{r}} \tag{1.1.33}$$

which is called the parabolic velocity or the escape velocity. Thus the following criteria can be derived:

$E<0$, $v<v_p$: ellipse

$E=0$, $v=v_p$: parabola

$E>0$, $v>v_p$: hyperbola

Establish a cylindrical coordinates frame $(O_e\text{-}XYZ)$ with radial axis O_eX along the vector $\boldsymbol{r}$, transverse axis O_eY towards the advanced direction of motion, and the normal axis O_eZ parallel to $O_e\zeta$. The true anomaly ν is the angle between two coordinate planes (X,Y) and (ξ,η). $(O_e\text{-}XYZ)$, rotating around O_e with angular velocity $\mathrm{d}\nu/\mathrm{d}t$, is called the orbital reference frame. Equations (1.1.31) and (1.1.28) yield, respectively, the radial velocity v_X and transverse velocity v_Y of point m

$$v_X = \frac{\mathrm{d}r}{\mathrm{d}t} = \frac{\mathrm{d}r}{\mathrm{d}\nu}\frac{\mathrm{d}\nu}{\mathrm{d}t} = \sqrt{\frac{\mu}{p}}\, e\sin\nu \tag{1.1.34a}$$

$$v_Y = r\frac{\mathrm{d}\nu}{\mathrm{d}t} = \sqrt{\frac{\mu}{p}}(1 + e\cos\nu) \tag{1.1.34b}$$

Transforming it to $(O_{\mathrm{e}}\text{-}\xi\eta\zeta)$ leads to

$$v_\xi = -\sqrt{\frac{\mu}{p}}\, e\sin\nu, \quad v_\eta = \sqrt{\frac{\mu}{p}}(e + \cos\nu) \tag{1.1.35}$$

1.1.6 Elliptic Orbit

The elliptic orbit with O_{e} as one of focuses is a special case of Keplerian motion when $e < 1$. Assume that the orbit intersects $O_{\mathrm{e}}\xi$ at two points: perigee π and apogee α, the distances from which to point O_{e} are minimum and maximum, respectively (Fig. 1.7).

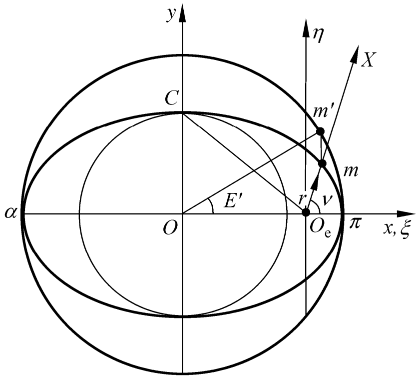

Figure 1.7 Elliptic orbit

From Eq. (1.1.28),

$$\begin{aligned} r_\pi &= r(0) = r_{\min} = \frac{p}{1+e} \\ r_\alpha &= r(\pi) = r_{\max} = \frac{p}{1-e} \end{aligned} \tag{1.1.36}$$

Thus the semi-major axis a of ellipse can be obtained

$$a = \frac{1}{2}(r_\pi + r_\alpha) = \frac{p}{1-e^2} \tag{1.1.37}$$

Equation (1.1.36) can be rewritten as

$$r_\pi = a(1-e),\ r_\alpha = a(1+e) \tag{1.1.38}$$

The distance of the center O of ellipse to O_{e} is

$$OO_{\text{e}} = a - r_\pi = ae \tag{1.1.39}$$

The distance of the top C of ellipse to O_{e} is equal to the semi-major axis a, then the semi-minor axis b can be obtained with the help of the triangle $OO_{\text{e}}C$ as

$$b = a\sqrt{1-e^2} \tag{1.1.40}$$

The formula of eccentricity e is derived as

$$e = \frac{\sqrt{a^2-b^2}}{a} = \frac{r_\pi - r_\alpha}{r_\pi + r_\alpha} \tag{1.1.41}$$

Eliminating h from Eqs. (1.1.25) and (1.1.27) and using Eq. (1.1.37), one obtains

$$E = -\frac{\mu}{2a} < 0 \tag{1.1.42}$$

Substitution of Eq. (1.1.42) into the energy integral (1.1.18) results in the velocity v as the function of r

$$v = \sqrt{\mu\left(\frac{2}{r} - \frac{1}{a}\right)} \tag{1.1.43}$$

Thus the velocities at π and α can be determined as

$$\left.\begin{aligned} v_\pi &= v_{\max} = v_c\sqrt{\frac{1+e}{1-e}} \\ v_\alpha &= v_{\min} = v_c\sqrt{\frac{1-e}{1+e}} \end{aligned}\right. \tag{1.1.44}$$

where v_c is the velocity of a circular orbit with radius a

$$v_c = \sqrt{\frac{\mu}{a}} \tag{1.1.45}$$

The circular velocity v_c is equal to the velocity at the top point C.

In order to calculate the time integral (1.1.32), one sets Cartesian coordinates $(O\text{-}xy)$ on the ellipse with center O as the origin and Ox along $O_{\text{e}}\xi$. Assume that point m' lies on the auxiliary circles with center O and radius b and has the same abscissa as point m. Define the angle of $\angle O_{\text{e}}Om'$ as the eccentric anomaly and denote it by *E*. The coordinates of point *m* in $(O\text{-}xy)$ can be expressed by *E* as

$$x = a\cos E, \quad y = b\sin E \tag{1.1.46}$$

The projections of point m on $O_\mathrm{e}\xi$ and $O_\mathrm{e}\eta$ are

$$\begin{aligned} \xi &= r\cos\nu = x - ae = a(\cos E - e) \\ \eta &= r\sin\nu = y = a\sqrt{1-e^2}\sin E \end{aligned} \tag{1.1.47}$$

from which the orbit equation with variable E is obtained as

$$r = a(1 - e\cos E) \tag{1.1.48}$$

Substitution of Eq. (1.1.48) into Eq. (1.1.47) gives

$$\cos\nu = \frac{\cos E - e}{1 - e\cos E}, \quad \sin\nu = \frac{\sqrt{1-e^2}\sin E}{1 - e\cos E} \tag{1.1.49}$$

Differentiation of Eq. (1.1.49) with respect ν and E leads to

$$\mathrm{d}\nu = \frac{\sqrt{1-e^2}}{1 - e\cos E}\mathrm{d}E \tag{1.1.50}$$

Substituting Eqs. (1.1.49) and (1.1.50) into Eq. (1.1.32), and expressing *p* by *a*, one obtains

$$t = \tau + \sqrt{\frac{a^3}{\mu}}(E - e\sin E) \tag{1.1.51}$$

Inserting $E = 2\pi$, one can derive the period of the elliptic motion

$$T = 2\pi\sqrt{\frac{a^3}{\mu}} \tag{1.1.52}$$

1.2 Environmental Torques Acting on Spacecraft

1.2.1 Gravitational Torque

The gravitational torque is fundamental to the attitude motion of a spacecraft. Consider an arbitrary rigid body attracted by the Earth, which is simplified by a central gravitational field with center O_e and gravitational parameter μ. Denote the position vectors of the mass center O and an arbitrary point P of the body with respect to the attracted center O_e by $\boldsymbol{r}$ and $\boldsymbol{r}'$, respectively. Let $\boldsymbol{r}' = \boldsymbol{r} + \boldsymbol{\rho}$, where $\boldsymbol{\rho}$ is the position vector of point P with respect to point O (Fig. 1.8).

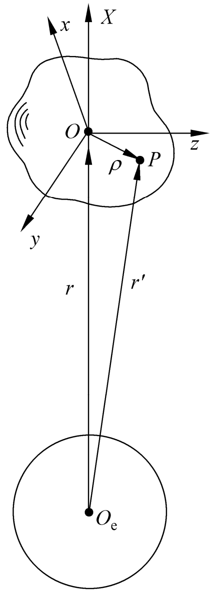

Figure 1.8 Gravitational torque on a rigid body

Establish a principal coordinate frames $(O\text{-}xyz)$ fixed on the body, and $(O\text{-}XYZ)$ with the axes parallel to $(O_e\text{-}XYZ)$. The direct cosines between $(O\text{-}xyz)$ and $(O\text{-}XYZ)$ are listed in Table 1.1.

Table 1.1 Direct cosines

	X	Y	Z
x	α_1	β_1	γ_1
y	α_2	β_2	γ_2
z	α_3	β_3	γ_3

Let $\boldsymbol{i},\boldsymbol{j},\boldsymbol{k}$ be the basis-vectors of $(O\text{-}xyz)$ and x,y,z be the coordinates of point P in $(O\text{-}xyz)$. Then the vectors $\boldsymbol{r}$ and $\boldsymbol{\rho}$ can be written as

$$\boldsymbol{r}=r(\alpha_1\boldsymbol{i}+\alpha_2\boldsymbol{j}+\alpha_3\boldsymbol{k}), \quad \boldsymbol{\rho}=x\boldsymbol{i}+y\boldsymbol{j}+z\boldsymbol{k} \tag{1.2.1}$$

Substitution of Eq. (1.2.1) into $\boldsymbol{r}'=\boldsymbol{r}+\boldsymbol{\rho}$ leads to

$$\boldsymbol{r}'=r\left[\left(\alpha_1+\frac{x}{r}\right)\boldsymbol{i}+\left(\alpha_2+\frac{y}{r}\right)\boldsymbol{j}+\left(\alpha_3+\frac{z}{r}\right)\boldsymbol{k}\right] \tag{1.2.2}$$

The gravitational force $\mathrm{d}\boldsymbol{F}$ acting on an infinitesimal mass element $\mathrm{d}m$ at point P is

$$\mathrm{d}\boldsymbol{F} = -\frac{\mu \mathrm{d}m}{r'^2}\left(\frac{\boldsymbol{r}'}{r'}\right) \tag{1.2.3}$$

The gravitational torque $\boldsymbol{M}_g$ acting on the whole body with respect to point O is

$$\boldsymbol{M}_g = \iiint_S \boldsymbol{\rho} \times \mathrm{d}\boldsymbol{F} = -\mu \iiint_S \frac{\boldsymbol{\rho} \times \boldsymbol{r}'}{r'^3}\mathrm{d}m \tag{1.2.4}$$

Substituting Eqs. (1.2.1) and (1.2.2) into Eq. (1.2.4), and considering only the second terms of $x/r, y/r, z/r$, one obtains the components M_{gi} $(i=1,2,3)$ of $\boldsymbol{M}_g$ in $(O\text{-}xyz)$

$$\begin{aligned} M_{g1} &= \frac{3\mu}{r^3}(C-B)\alpha_2\alpha_3 \\ M_{g2} &= \frac{3\mu}{r^3}(A-C)\alpha_3\alpha_1 \\ M_{g3} &= \frac{3\mu}{r^3}(B-A)\alpha_1\alpha_2 \end{aligned} \tag{1.2.5}$$

The gravitational torque depends on the principal moments of inertia, the attitude of the body in the orbit, and the distance of the body to the Earth.

The potential energy V of the body can be calculated as

$$V = -\mu \iiint_S \frac{\mathrm{d}m}{r'} \tag{1.2.6}$$

Substitution of Eq. (1.2.2) into Eq. (1.2.6) yields

$$V = -\frac{\mu}{r}\left[m + \frac{1}{2r^2}(A+B+C-3I)\right] \tag{1.2.7}$$

where I is defined by Eq. (1.1.8). The components M_{gi} $(i=1,2,3)$ of the gravitational torque can be expressed by the derivatives of potential energy V as

$$\begin{aligned} M_{g1} &= \alpha_2\frac{\partial V}{\partial \alpha_3} - \alpha_3\frac{\partial V}{\partial \alpha_2} \\ M_{g2} &= \alpha_3\frac{\partial V}{\partial \alpha_1} - \alpha_1\frac{\partial V}{\partial \alpha_3} \\ M_{g3} &= \alpha_1\frac{\partial V}{\partial \alpha_2} - \alpha_2\frac{\partial V}{\partial \alpha_1} \end{aligned} \tag{1.2.8}$$

1.2.2 Magnetic Torque

In addition to the gravitational torque, the magnetic torque has a significant influence on a magnetized vehicle moving in the geomagnetic field. The polar axis of the geomagnetic field is inclined by about 11.5° against the geographic dipole O_eZ_e. When the difference between geomagnetic dipole and the geographic dipole is neglected, the vector $\boldsymbol{H}_m$ of the magnetic flux density of the Earth can be described by a simple model as

$$\boldsymbol{H}_m = H_{m0}\left[\boldsymbol{Z}_0^0 - 3(\boldsymbol{Z}_0^0 \cdot \boldsymbol{X}^0)\boldsymbol{X}^0\right] \tag{1.2.9}$$

where $H_{m0} = \mu_m/r^3$, $\mu_m = 1\times10^{17}\ \text{wb}\cdot\text{m}$ is the Earth magnetic dipole strength, and $\boldsymbol{Z}_0^0$ and $\boldsymbol{X}^0$ are basis-vectors of geographic axis O_eZ_0 and the Earth-pointing axis O_eX at the location of spacecraft, respectively (Fig. 1.9). Define the inertial reference frame $(O_e\text{-}X_0Y_0Z_0)$ with geographic axis O_eZ_0 and O_eX_0 along the ascending node O_eY of the orbital plane (Fig. 1.10). The direct cosines between

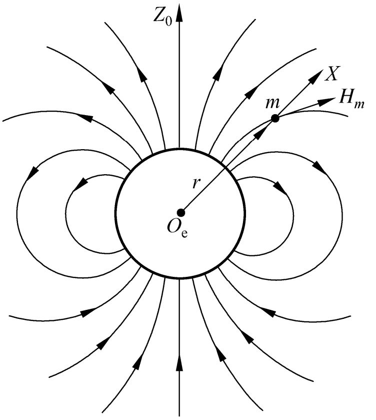

Figure 1.9 The geomagnetic field

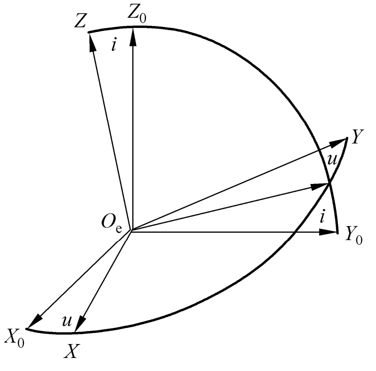

Figure 1.10 The relationship between the orbital frame and inertial frame

$(O_e\text{-}XYZ)$ and $(O_e\text{-}X_0Y_0Z_0)$ are listed in Table 1.2, where i is the inclination angle of the orbital plane and the orbital angle $u = \nu + \omega$ is defined by Eq. (1.1.29).

Table 1.2 Direct cosines

	X	Y	Z
X_0	$\cos u$	$-\sin u$	0
Y_0	$\cos i \sin u$	$\cos i \cos u$	$-\sin i$
Z_0	$\sin i \sin u$	$\sin i \cos u$	$\cos i$

Projecting the vector $\boldsymbol{H}_{\mathrm{m}}$ into the orbital frame $(O_e\text{-}XYZ)$, we obtain

$$\boldsymbol{H}_{\mathrm{m}} = H_{\mathrm{m}X}\boldsymbol{X}^0 + H_{\mathrm{m}Y}\boldsymbol{Y}^0 + H_{\mathrm{m}Z}\boldsymbol{Z}^0 \tag{1.2.10}$$

where

$$\begin{aligned} H_{\mathrm{m}X} &= -2H_{\mathrm{m}0}\sin i \sin u \\ H_{\mathrm{m}Y} &= H_{\mathrm{m}0}\sin i \cos u \\ H_{\mathrm{m}Z} &= H_{\mathrm{m}0}\cos i \end{aligned} \tag{1.2.11}$$

Assume that the spacecraft is magnetized with a magnetic moment $\boldsymbol{I}_{\mathrm{m}}$, the direct cosines of which with respect to $(O_e\text{-}XYZ)$ are denoted by α, β, γ. It follows that

$$\boldsymbol{I}_{\mathrm{m}} = I_{\mathrm{m}}(\alpha\boldsymbol{X}^0 + \beta\boldsymbol{Y}^0 + \gamma\boldsymbol{Z}^0) \tag{1.2.12}$$

The magnetic torque $\boldsymbol{M}_{\mathrm{m}}$ induced by the geomagnetic field is

$$\boldsymbol{M}_{\mathrm{m}} = \boldsymbol{I}_{\mathrm{m}} \times \boldsymbol{H}_{\mathrm{m}} \tag{1.2.13}$$

Substitution of Eqs. (1.2.11) and (1.2.12) into Eq. (1.2.13) leads to

$$\begin{aligned} M_{\mathrm{m}X} &= I_{\mathrm{m}}(H_{\mathrm{m}Z}\beta - H_{\mathrm{m}Y}\gamma) \\ M_{\mathrm{m}Y} &= I_{\mathrm{m}}(H_{\mathrm{m}X}\gamma - H_{\mathrm{m}Z}\alpha) \\ M_{\mathrm{m}Z} &= I_{\mathrm{m}}(H_{\mathrm{m}Y}\alpha - H_{\mathrm{m}X}\beta) \end{aligned} \tag{1.2.14}$$

The magnetic torque (1.2.14) can be expressed by the derivatives of the magnetic potential energy V_{m} as

$$\begin{aligned} M_{\mathrm{m}X} &= \gamma\frac{\partial V_{\mathrm{m}}}{\partial \beta} - \beta\frac{\partial V_{\mathrm{m}}}{\partial \gamma} \\ M_{\mathrm{m}Y} &= \alpha\frac{\partial V_{\mathrm{m}}}{\partial \gamma} - \gamma\frac{\partial V_{\mathrm{m}}}{\partial \alpha} \\ M_{\mathrm{m}Z} &= \beta\frac{\partial V_{\mathrm{m}}}{\partial \alpha} - \alpha\frac{\partial V_{\mathrm{m}}}{\partial \beta} \end{aligned} \tag{1.2.15}$$

where the potential energy of magnetic field V_{m} is defined as

$$V_{\mathrm{m}} = -I_{\mathrm{m}}(H_{\mathrm{m}X}\alpha + H_{\mathrm{m}Y}\beta + H_{\mathrm{m}Z}\gamma) \tag{1.2.16}$$

Besides the aforementioned gravitational and magnetic torques, there exist other environmental torques, for example, the aerodynamic torque and electromagnetic radiation torque [9,10].

1.3 Attitude Motion of Spacecraft in the Gravitational Field

1.3.1 Euler's Equations and Poisson's Equations

The theorem of angular momentum requires that the absolute time derivative of the angular momentum $\boldsymbol{G}$ of a rigid body respect to its mass center O equals to the resultant external torque $\boldsymbol{M}$ on the body with respect to the same point, namely

$$\dot{\boldsymbol{G}} = \boldsymbol{M} \tag{1.3.1}$$

When the differentiation of $\boldsymbol{G}$ is performed in the body-fixed reference frame, it yields

$$\overset{\circ}{\boldsymbol{G}} + \boldsymbol{\omega}\times\boldsymbol{G} = \boldsymbol{M} \tag{1.3.2}$$

where the hollow point symbol denotes the local derivation in the body-fixed frame, and $\boldsymbol{\omega}$ is the angular velocity of the body. Let $\boldsymbol{J}$ be the inertia tensor of the body. The angular momentum $\boldsymbol{G}$ is expressed as

$$\boldsymbol{G} = \boldsymbol{J}\cdot\boldsymbol{\omega} \tag{1.3.3}$$

Then Eq. (1.3.2) becomes

$$\boldsymbol{J}\cdot\dot{\boldsymbol{\omega}} + \boldsymbol{\omega}\times\left(\boldsymbol{J}\cdot\boldsymbol{\omega}\right) = \boldsymbol{M} \tag{1.3.4}$$

Let A, B, C be the central principal inertia moments of the body relative to $(O\text{-}xyz)$, ω_i and G_i $(i = 1,2,3)$ be components of $\boldsymbol{\omega}$ and $\boldsymbol{G}$ in $(O\text{-}xyz)$, then Eq. (1.3.3) gives

$$G_1 = A\omega_1,\ G_2 = B\omega_2,\ G_3 = C\omega_3 \tag{1.3.5}$$

Projecting Eq. (1.3.2) into $(O\text{-}xyz)$, one obtains the Euler's equations as follows

$$A\dot{\omega}_1 + \left(C - B\right)\omega_2\omega_3 = M_1 \tag{1.3.6a}$$

$$B\dot{\omega}_2 + \left(A - C\right)\omega_3\omega_1 = M_2 \tag{1.3.6b}$$

$$C\dot{\omega}_3 + \left(B - A\right)\omega_1\omega_2 = M_3 \tag{1.3.6c}$$

The Euler's equations can also be expressed by the components of $\boldsymbol{G}$ as

$$\dot{G}_1 + \left(\frac{C - B}{BC}\right)G_2G_3 = M_1 \tag{1.3.7a}$$

$$\dot{G}_2 + \left(\frac{A - C}{CA}\right)G_3G_1 = M_2 \tag{1.3.7b}$$

$$\dot{G}_3 + \left(\frac{B - A}{AB}\right)G_1G_2 = M_3 \tag{1.3.7c}$$

If the spacecraft is only subjected to the gravitational torque, let $M_i = M_{gi}$ ($i = 1, 2, 3$), then the substitution of Eq. (1.2.5) into Eq. (1.3.6) yields

$$A\dot{\omega}_1 + (C - B)\omega_2\omega_3 = \frac{3\mu}{r^3}(C - B)\alpha_2\alpha_3 \tag{1.3.8a}$$

$$B\dot{\omega}_2 + (A - C)\omega_3\omega_1 = \frac{3\mu}{r^3}(A - C)\alpha_3\alpha_1 \tag{1.3.8b}$$

$$C\dot{\omega}_3 + (B - A)\omega_1\omega_2 = \frac{3\mu}{r^3}(B - A)\alpha_1\alpha_2 \tag{1.3.8c}$$

Moving in the orbit, the orbital reference frame $(O\text{-}XYZ)$ rotates around the point O_{e} with the angular velocity $\omega_\nu = \mathrm{d}\nu/\mathrm{d}t$ determined by Eq. (1.1.31). Then the following equations can be derived from derivatives of the basis vectors $\boldsymbol{X}^0, \boldsymbol{Y}^0, \boldsymbol{Z}^0$ of $(O\text{-}XYZ)$ with respect to time t

$$\overset{\circ}{\boldsymbol{X}}{}^0 + \boldsymbol{\omega}\times\boldsymbol{X}^0 = \omega_\nu\boldsymbol{Z}^0\times\boldsymbol{X}^0 \tag{1.3.9a}$$

$$\overset{\circ}{\boldsymbol{Y}}{}^0 + \boldsymbol{\omega}\times\boldsymbol{Y}^0 = \omega_\nu\boldsymbol{Z}^0\times\boldsymbol{Y}^0 \tag{1.3.9b}$$

$$\overset{\circ}{\boldsymbol{Z}}{}^0 + \boldsymbol{\omega}\times\boldsymbol{Z}^0 = \boldsymbol{0} \tag{1.3.9c}$$

Projection of Eqs. (1.3.9) into $(O\text{-}xyz)$ leads to the Poisson's equations as

$$\dot{\alpha}_1 = \omega_3\alpha_2 - \omega_2\alpha_3 + \omega_\nu\beta_1 \tag{1.3.10a}$$

$$\dot{\alpha}_2 = \omega_1\alpha_3 - \omega_3\alpha_1 + \omega_\nu\beta_2 \tag{1.3.10b}$$

$$\dot{\alpha}_3 = \omega_2\alpha_1 - \omega_1\alpha_2 + \omega_\nu\beta_3 \tag{1.3.10c}$$

$$\dot{\beta}_1 = \omega_3\beta_2 - \omega_2\beta_3 - \omega_\nu\alpha_1 \tag{1.3.10d}$$

$$\dot{\beta}_2 = \omega_1\beta_3 - \omega_3\beta_1 - \omega_v\alpha_2 \tag{1.3.10e}$$

$$\dot{\beta}_3 = \omega_2\beta_1 - \omega_1\beta_2 - \omega_v\alpha_3 \tag{1.3.10f}$$

$$\dot{\gamma}_1 = \omega_3\gamma_2 - \omega_2\gamma_3 \tag{1.3.10g}$$

$$\dot{\gamma}_2 = \omega_1\gamma_3 - \omega_3\gamma_1 \tag{1.3.10h}$$

$$\dot{\gamma}_3 = \omega_2\gamma_1 - \omega_1\gamma_2 \tag{1.3.10i}$$

If the influence of attitude variation on the orbit motion can be neglected, the variables r and ω_v are known in the analysis of the Keplerian orbit. Then the attitude motion of the body is determined by a set of closed Eqs. (1.3.8) and (1.3.10).

1.3.2 Planar Libration

Euler's and Poisson's Eqs. (1.3.8) and (1.3.10) admit the following special solution

$$\begin{array}{lll} \alpha_1 = \cos\varphi, & \beta_1 = \sin\varphi, & \gamma_1 = 0 \\ \alpha_2 = -\sin\varphi, & \beta_2 = \cos\varphi, & \gamma_2 = 0 \\ \alpha_3 = 0, & \beta_3 = 0, & \gamma_3 = 1 \\ \omega_1 = 0, & \omega_2 = 0, & \omega_3 = \dot{\varphi} + \omega_v \end{array} \tag{1.3.11}$$

As a special type of attitude motion, the solution (1.3.11) corresponds to an oscillation in the orbital plane, so-called the planar libration (Fig. 1.11). The gravitational torque $\boldsymbol{M}_{\mathrm{g}}$ of planar libration is along the normal axis of the orbital plane and depends on the swing angle φ only. From Eq. (1.2.5) one obtains

$$M_{g3} = -\frac{3\mu}{2r^3}(B - A)\sin 2\varphi \tag{1.3.12}$$

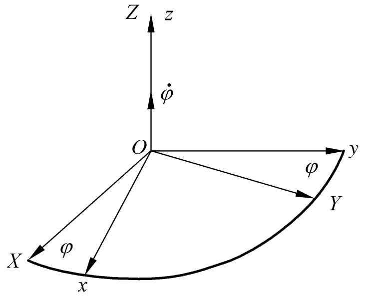

Figure 1.11 Planar libration

The Euler's Eq. (1.3.8c) becomes

$$C\ddot{\varphi}+\frac{3\mu}{2r^3}(B-A)\sin 2\varphi=-\dot{\omega}_v \tag{1.3.13}$$

In the case of circular orbit, the parameters r and ω_v are constants

$$r=a,\quad \omega_v=\omega_c=\sqrt{\frac{\mu}{a^3}} \tag{1.3.14}$$

Thus Eq. (1.3.13) becomes

$$C\ddot{\varphi}+\frac{3}{2}(B-A)\omega_c^2\sin 2\varphi=0 \tag{1.3.15}$$

Equation (1.3.15) has an energy integral as

$$C\dot{\varphi}^2+3(B-A)\omega_c^2\sin^2\varphi=2E \tag{1.3.16}$$

where the constant E is the total energy of the system. Eq. (1.3.16) describes phase trajectories in phase plane $(\varphi,\dot{\varphi})$ as shown in Fig. 1.12. The phase trajectories have singularities at $\varphi=n\pi/2$ $(n=0,1,2,\cdots)$. The types of the singularities depend on the sign of $B-A$. In the case of $B>A$, the singularity is a center when n is even, or a saddle when n is odd. The result is opposite when $B<A$. Thus the stability condition for the relative equilibrium $\varphi=0$ is

$$\begin{aligned} B>A&: \quad \text{stable}\\ B<A&: \quad \text{unstable}\end{aligned} \tag{1.3.17}$$

The condition (1.3.17) requires that the principal axis directed to the Earth should correspond to the minimal inertia moment of the satellite.

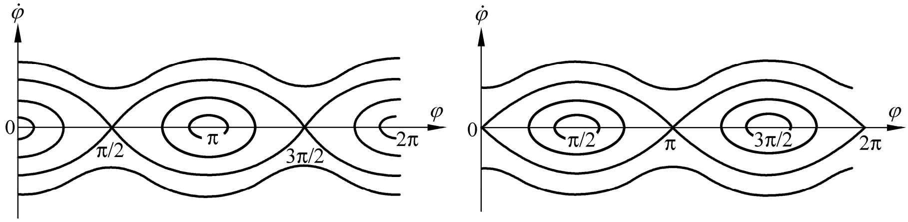

(a) $B>A$ (b) $B<A$

Figure 1.12 Phase trajectories in phase plane $(\varphi,\dot{\varphi})$

When the stability condition (1.3.17) is satisfied, for given initial conditions

$$\varphi(0)=0,\quad \dot{\varphi}(0)=\dot{\varphi}_0 \tag{1.3.18}$$

an analytical solution of Eq. (1.3.16) can be expressed in the form of elliptic function

$$\varphi = \arcsin[k \operatorname{sn}(nt, k)] \tag{1.3.19}$$

where

$$n = \omega_c \sqrt{\frac{3(B-A)}{C}}, \quad k = \frac{|\dot{\varphi}_0|}{n} \tag{1.3.20}$$

The amplitude of libration φ_m can be obtained from the parameter k as

$$\varphi_m = \arcsin\left[\frac{|\dot{\varphi}_0|}{\omega_c}\sqrt{\frac{C}{3(B-A)}}\right] \tag{1.3.21}$$

The period of libration T is

$$T = \frac{2T_c K(k)}{\pi}\sqrt{\frac{C}{3(B-A)}} \tag{1.3.22}$$

where $T_c = 2\pi\sqrt{a^3/\mu}$ is the period of circular orbit and $K(k)$ is the first complete elliptic integral. If the amplitude of libration is small enough, $k \ll 1$, $K \approx \pi/2$, the period is simplified as

$$T = T_c\sqrt{\frac{C}{3(B-A)}} \tag{1.3.23}$$

In more general case of an elliptic orbit, the parameters r and ω_ν in Eq. (1.3.13) are functions of the true anomaly ν as shown in Eqs. (1.1.28) and (1.1.31)

$$r = \frac{p}{1+e\cos\nu}, \quad \omega_\nu = \frac{\sqrt{\mu p}}{r^2} = \sqrt{\frac{\mu}{p^3}}(1+e\cos\nu)^2 \tag{1.3.24}$$

To replace the argument t by ν in Eq. (1.3.13), let

$$\frac{\mathrm{d}}{\mathrm{d}t} = \frac{\sqrt{\mu p}}{r^2}\frac{\mathrm{d}}{\mathrm{d}\nu}, \quad \frac{\mathrm{d}^2}{\mathrm{d}t^2} = \frac{\mu p}{r^4}\left(\frac{\mathrm{d}^2}{\mathrm{d}\nu^2} - \frac{2e\sin\nu}{1+e\cos\nu}\frac{\mathrm{d}}{\mathrm{d}\nu}\right) \tag{1.3.25}$$

Substitution of Eqs. (1.3.24) and (1.3.25) into Eqs. (1.3.13) leads to

$$\frac{\mathrm{d}^2\varphi}{\mathrm{d}\nu^2} - \frac{2e\sin\nu}{1+e\cos\nu}\frac{\mathrm{d}\varphi}{\mathrm{d}\nu} + \frac{\kappa}{2(1+e\cos\nu)}\sin 2\varphi = \frac{2e\sin\nu}{1+e\cos\nu} \tag{1.3.26}$$

where $\kappa = 3(B-A)/C$.

Zlatoustov *et al.* (1964) analyzed the oscillation determined by nonlinear Eq. (1.3.26) with periodic coefficients and provided a stability diagram in the parameter plane (e, κ) (Fig. 1.13) [12]. It was shown that when $e = 0$ the entire domain of $\kappa > 0$ is stable, and afterwards the stable area is reduced with increasing eccentricity. When $e > 0.682$ the stable area appears in another half-plane $\kappa < 0$. It means that an unstable satellite in a circular orbit can be stable in an elliptic orbit with large eccentricity.

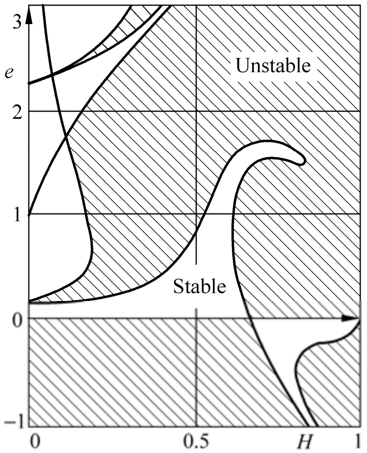

Figure 1.13 Stability diagram (e, κ) of planar libration in an elliptic orbit

1.3.3 Stability of Relative Equilibrium

A satellite in relative equilibrium state is a special case of solution (1.3.11) when $\varphi \equiv 0$. Then the body-fixed frame $(O\text{-}xyz)$ coincides with the orbital frame $(O\text{-}XYZ)$. Normally the relative equilibrium is a working state of satellites, and the Ox-axis of which points to the center of the Earth.

To analyze the stability of relative equilibrium, let us introduce angular coordinates as follows: a rotation θ of $(O\text{-}XYZ)$ about OX as $(O\text{-}x_0y_0z_0)$, a rotation ψ of $(O\text{-}x_0y_0z_0)$ about Oy_0 as $(O\text{-}x_1y_1z_1)$, and a rotation φ of $(O\text{-}x_1y_1z_1)$ about Oz_1-axis as a body-fixed frame $(O\text{-}xyz)$. Then θ, ψ, φ are small angles of a satellite deviating from the orbital frame $(O\text{-}XYZ)$ after disturbances (Fig. 1.14). Assume that the orbit is circular and the terms of θ, ψ, φ higher than the second order are negligible. Then

$$\begin{aligned}
&\alpha_1 = 1, && \beta_1 = \varphi, && \gamma_1 = -\psi \\
&\alpha_2 = -\varphi, && \beta_2 = 1, && \gamma_2 = \theta \\
&\alpha_3 = \psi, && \beta_3 = -\theta, && \gamma_3 = 1 \\
&\omega_1 = \dot{\theta} - \omega_c\psi, && \omega_2 = \dot{\psi} + \omega_c\theta, && \omega_3 = \dot{\varphi} + \omega_c
\end{aligned} \tag{1.3.27}$$

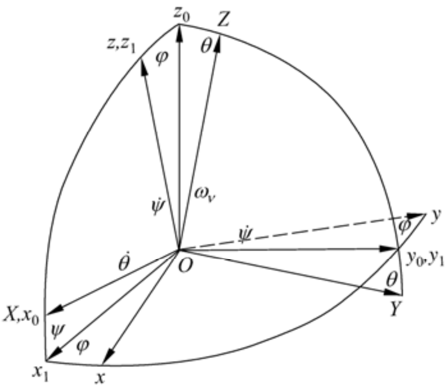

Figure 1.14 Attitude expression of spacecraft in the orbital frame

Substitution of Eq. (1.3.27) into Eq. (1.3.8c) leads to

$$A\ddot{\theta} - (A+B-C)\omega_c\dot{\psi} + (C-B)\omega_c^2\theta = 0 \tag{1.3.28a}$$

$$B\ddot{\psi} + (A+B-C)\omega_c\dot{\theta} + 4(C-A)\omega_c^2\psi = 0 \tag{1.3.28b}$$

$$C\ddot{\varphi} + 3(B-A)\omega_c^2\varphi = 0 \tag{1.3.28c}$$

Equation (1.3.28c) is the linearized equation of Eq. (1.3.15), and the stability condition is obviously $B > A$. In order to analyze stability of θ and ψ, insert the special solutions $\theta = \theta_0\exp(st)$ and $\psi = \psi_0\exp(st)$ into Eqs. (1.3.28a) and (1.3.28b). Hence, the characteristic equation is derived as

$$\left(\frac{s}{\omega_c}\right)^4 + a\left(\frac{s}{\omega_c}\right)^2 + b = 0 \tag{1.3.29}$$

where

$$a = 1 + 3k_1 + k_1k_2, \quad b = 4k_1k_2 \tag{1.3.30}$$

and

$$k_1 = \frac{C-A}{B}, \quad k_2 = \frac{C-B}{A} \tag{1.3.31}$$

Due to the inequalities

$$A+B>C, \ B+C>A, \ C+A>B \tag{1.3.32}$$

the inertia ratios k_1 and k_2 are restricted by

$$|k_1| < 1, \quad |k_2| < 1 \tag{1.3.33}$$

Therefore the diagram of parameter plane (k_1, k_2) is restricted in a square region with edges equal to 2 (Fig. 1.15). The stability of θ and ψ depends on the conditions of pure imaginary eigenvalues of Eq. (1.3.29)

$$a > 0,\ b > 0,\ a^2 - 4b > 0 \tag{1.3.34}$$

The conditions $B > A$ and $b > 0$ require that the stable regions should be in the first and third quadrants and under the straight line $k_1 = k_2$. The stable regions satisfying all conditions (1.3.34) consist of a triangle in the first quadrant and a small region in the third quadrant. According to Lyapunov's theory the stability of the first approximation is the necessary condition of stability for the complete equations.

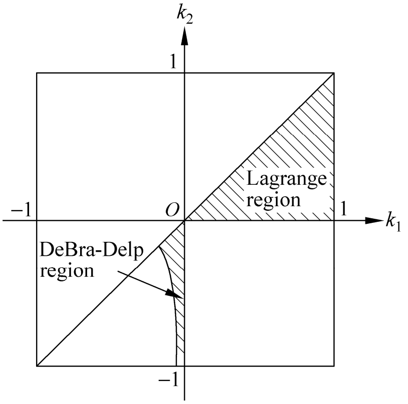

Figure 1.15 Stability diagram (k_1, k_2) of spatial libration

In order to obtain the sufficient conditions of stability, the kinetic energy T of the body is needed as

$$T = \frac{1}{2}\iiint\limits_S \dot{\boldsymbol{r}}' \cdot \dot{\boldsymbol{r}}' \mathrm{d}m \tag{1.3.35}$$

where $\boldsymbol{r}' = \boldsymbol{r} + \boldsymbol{\rho}$. Assume that the orbit is circular, and $\boldsymbol{\omega}' = \boldsymbol{\omega} - \boldsymbol{\omega}_c$ is the angular velocity of the body relative the orbital reference frame. Then

$$\boldsymbol{\omega}' = (\omega_1 - \omega_c\gamma_1)\boldsymbol{i} + (\omega_2 - \omega_c\gamma_2)\boldsymbol{j} + (\omega_3 - \omega_c\gamma_3)\boldsymbol{k} \tag{1.3.36}$$

Thus the derivative of $\boldsymbol{r}'$ with respect to t can be written as

$$\dot{\boldsymbol{r}}' = \dot{\boldsymbol{r}} + \dot{\boldsymbol{\rho}} = \boldsymbol{\omega}_c \times \boldsymbol{r} + \boldsymbol{\omega} \times \boldsymbol{\rho} = \boldsymbol{\omega}_c \times \boldsymbol{r}' + \boldsymbol{\omega}' \times \boldsymbol{\rho} \tag{1.3.37}$$

Substituting Eqs. (1.3.37) and (1.3.36) into Eq. (1.3.35) to calculate the kinetic energy and omitting the constant term $mv_c^2/2$ corresponding to the orbital motion, one obtains

$$T = T_0 + T_2 \tag{1.3.38}$$

where $T_i\ (i = 0, 2)$ are the zero-th and the second degree homogeneous terms of $\omega_i'\ (i = 1, 2, 3)$ in the kinetic energy expression

$$\begin{aligned} T_0 &= \frac{1}{2}\omega_c^2(A\gamma_1^2 + B\gamma_2^2 + C\gamma_3^2) \\ T_2 &= \frac{1}{2}(A\omega_1'^2 + B\omega_2'^2 + C\omega_3'^2) \end{aligned} \tag{1.3.39}$$

The gravitational energy V of the body is defined by Eq. (1.2.7). Omitting the constant terms in it leads to

$$V = \frac{3}{2}\omega_c^2(A\alpha_1^2 + B\alpha_2^2 + C\alpha_3^2) \tag{1.3.40}$$

The kinetic energy and the potential energy of the body are explicitly independent of time t. Therefore, Eqs. (1.3.8) and (1.3.10) permit Jacobi's integral as

$$\mathcal{H} = T_2 - T_0 + V = \text{const} \tag{1.3.41}$$

where $\mathcal{H}$ is the conservative Hamiltonian of the system:

$$\begin{aligned} \mathcal{H} = &\frac{1}{2}(A\omega_1'^2 + B\omega_2'^2 + C\omega_3'^2) - \frac{1}{2}\omega_c^2(A\gamma_1^2 + B\gamma_2^2 + C\gamma_3^2) \\ &+ \frac{3}{2}\omega_c^2(A\alpha_1^2 + B\alpha_2^2 + C\alpha_3^2) \end{aligned} \tag{1.3.42}$$

Eliminating α_1 and γ_3 in Eq. (1.3.42) by use of the geometric integrals of Eq. (1.3.5)

$$\sum_{i=1}^{3}\alpha_i^2 = 1,\quad \sum_{i=1}^{3}\beta_i^2 = 1,\quad \sum_{i=1}^{3}\gamma_i^2 = 1 \tag{1.3.43}$$

one obtains

$$\begin{aligned} \mathcal{H} = &\frac{1}{2}\left(A\omega_1'^2 + B\omega_2'^2 + C\omega_3'^2\right) + \frac{1}{2}\omega_c^2\left[(C - A)\gamma_1^2 + (C - B)\gamma_2^2\right] \\ &+ \frac{3}{2}\omega_c^2\left[(B - A)\alpha_2^2 + (C - A)\alpha_3^2\right] \end{aligned} \tag{1.3.44}$$

The function $\mathcal{H}$ is positive-definite if $C > B > A$. Applying the Lyapunov's direct method with the Hamiltonian $\mathcal{H}$ as Lyapunov's function, one obtains the sufficient stability condition of relative equilibrium:

$$C > B > A \tag{1.3.45}$$

The condition (1.3.45) is represented in the parameter plane (k_1, k_2) by a triangle region, which is called the Lagrange region. As a sufficient and necessary condition for the stability of relative equilibrium, it requires that the inertia moments of spacecraft have a minimum about the radial axis and a maximum about the normal axis of the orbital plane. The small region in the third quadrant of the plane (k_1, k_2) is called DeBra-Delp region [11], in which only the necessary stability conditions are satisfied and a slight damping can lead to instability in this region (Fig. 1.15).

1.3.4 Attitude Motion of a Gyrostat

A **gyrostat** (S) is a system composed of a rigid platform S_{P} and three axisymmetric rotors $S_{\mathrm{R}i}$ $(i=1,2,3)$ rotating about central principal axes $(O\text{-}xyz)$ of (S) with angular velocity $\varOmega_{\mathrm{R}i} (i=1,2,3)$ relative to S_{P} (Fig. 1.16). The mass geometry of system (S) is constant and is not influenced by the rotation of rotors. Assume that ω is the angular velocity of S_{P}, J is the tensor of central moment of inertia of (S). Then the angular momentum $\boldsymbol{G}$ of gyrostat (S) with respect to its mass center O is

$$\boldsymbol{G} = \boldsymbol{J} \cdot \boldsymbol{\omega} + \boldsymbol{g}_{\mathrm{R}} \tag{1.3.46}$$

where $\boldsymbol{g}_{\mathrm{R}}$ is the increment of angular momentum caused by the relative rotation of three rotors. Denote the principal inertia moments of the system (S) by A, B, C and the axial inertia moment of $S_{\mathrm{R}i}$ $(i=1,2,3)$ by $J_{\mathrm{R}i} (i=1,2,3)$. Then

$$G_1 = A\omega_1 + g_{\mathrm{R}1},\ G_2 = B\omega_2 + g_{\mathrm{R}2},\ G_3 = C\omega_3 + g_{\mathrm{R}3} \tag{1.3.47}$$

and

$$g_{\mathrm{R}i} = J_{\mathrm{R}i}\varOmega_{\mathrm{R}i} \quad (i=1,2,3) \tag{1.3.48}$$

Substitution of Eqs. (1.2.5) and (1.3.47) into the Euler's Eqs. (1.3.4) yields

$$A\dot{\omega}_1 + (C-B)\omega_2\omega_3 + \dot{g}_{\mathrm{R}1} + \omega_2 g_{\mathrm{R}3} - \omega_3 g_{\mathrm{R}2} = \frac{3\mu}{r^3}(C-B)\alpha_2\alpha_3 \tag{1.3.49a}$$

$$B\dot{\omega}_2 + (A-C)\omega_3\omega_1 + \dot{g}_{\mathrm{R}2} + \omega_3 g_{\mathrm{R}1} - \omega_1 g_{\mathrm{R}3} = \frac{3\mu}{r^3}(A-C)\alpha_3\alpha_1 \tag{1.3.49b}$$

$$C\dot{\omega}_3 + (B-A)\omega_1\omega_2 + \dot{g}_{\mathrm{R}3} + \omega_1 g_{\mathrm{R}2} - \omega_2 g_{\mathrm{R}1} = \frac{3\mu}{r^3}(B-A)\alpha_1\alpha_2 \tag{1.3.49c}$$

For a predetermined attitude motion of the platform S_0, the variables $g_{\mathrm{R}i}(t)$ $(i=1,2,3)$ can be solved from Eq. (1.3.49) and Poisson's Eqs. (1.3.10) when functions $\omega_i(t)$ $(i=1,2,3)$ are known. Therefore the relative rotation of rotors can be used to control the spacecraft to realize any predetermined attitude motion.

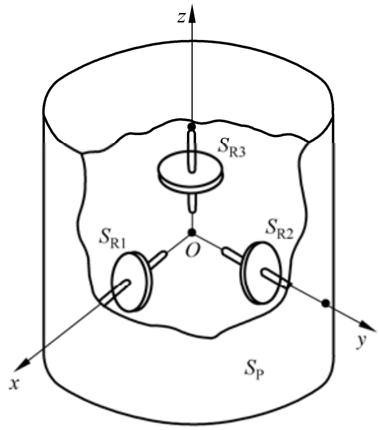

Figure 1.16 A gyrostat

In the case when the orbit is circular and each rotor rotates uniformly, let g_{Ri} $(i=1,2,3)$ be constant, and $\boldsymbol{\omega}'=\boldsymbol{\omega}-\boldsymbol{\omega}_c$ be the relative angular velocity of S_P, then Eqs. (1.3.49) and (1.3.10) permit Jacobi's integral as

$$\begin{aligned}\mathcal{H}=T_2-T_0+V=\frac{1}{2}(A\omega_1'^2+B\omega_2'^2+C\omega_3'^2)+\frac{3}{2}\omega_c^2(A\alpha_1^2+B\alpha_2^2+C\alpha_3^2)\\ -\frac{1}{2}\omega_c^2(A\gamma_1^2+B\gamma_2^2+C\gamma_3^2)-\omega_c(g_{R1}\gamma_1+g_{R2}\gamma_2+g_{R3}\gamma_3)=\text{const}\end{aligned}\tag{1.3.50}$$

1.4 Attitude Motion of Torque-free Spacecraft

1.4.1 Torque-free Rigid Body

In the analysis of the motion of spinning satellite, if the spin speed is so large that the kinetic energy of rotation is much larger than the work done by the gravitational force, then the body can be approximated as torque-free. When the right hands of Euler's Eqs. (1.3.8) vanish, one obtains

$$A\dot{\omega}_1+(C-B)\omega_2\omega_3=0\tag{1.4.1a}$$

$$B\dot{\omega}_2+(A-C)\omega_3\omega_1=0\tag{1.4.1b}$$

$$C\dot{\omega}_3+(B-A)\omega_1\omega_2=0\tag{1.4.1c}$$

Multiplying each Eq. of (1.4.1) successively by ω_1, ω_2 and ω_3, and by $A\omega_1$, $B\omega_2$ and $C\omega_3$, respectively, summing the resulting equations, and integrating them gives the integrals of energy and angular momentum as follows

$$A\omega_1^2 + B\omega_2^2 + C\omega_3^2 = 2E \tag{1.4.2}$$

$$A^2\omega_1^2 + B^2\omega_2^2 + C^2\omega_3^2 = G^2 \tag{1.4.3}$$

where the constants E and G are the conserved total energy and the conserved total angular momentum of the torque-free body. Both integrals (1.4.2) and (1.4.3) can be expressed by the components of angular momentum using Eq. (1.3.5).

$$\frac{G_1^2}{A} + \frac{G_2^2}{B} + \frac{G_3^2}{C} = 2E \tag{1.4.4}$$

$$G_1^2 + G_2^2 + G_3^2 = G^2 \tag{1.4.5}$$

The integrals (1.4.2) and (1.4.3) define two ellipsoids in three-dimensional space $(\omega_1, \omega_2, \omega_3)$. The ellipsoid defined by Eq. (1.4.2) is called the energy ellipsoid. The top of the vector ω is along the intersect curve of both ellipsoids. The trace of the top of ω on the energy ellipsoid is called polhode, which is composed of four sets of ellipses around two principal axes of the body (Fig. 1.17(a)). Similarly, the integrals (1.4.4) and (1.4.5) define analogous traces in space (G_1, G_2, G_3).

Equation (1.4.1) admits three sets of special solutions

$$\omega_1 = \omega_2 = 0, \quad \omega_3 = \omega_0 \tag{1.4.6a}$$

$$\omega_2 = \omega_3 = 0, \quad \omega_1 = \omega_0 \tag{1.4.6b}$$

$$\omega_3 = \omega_1 = 0, \quad \omega_2 = \omega_0 \tag{1.4.6c}$$

Each of them represents a rotation around principal axis. The rotation with constant angular velocity around an invariable axis in space is called a permanent rotation. The permanent rotation can be described by a special polhode, which is reduced to a single point on principal axis.

In order to analyze the stability of the permanent rotation about Oz-axis, let each hand of Eq. (1.4.1a) be divided by that of Eq. (1.4.1b) to yield

$$\frac{\mathrm{d}\omega_1}{\mathrm{d}\omega_2} = a\frac{\omega_2}{\omega_1} \tag{1.4.7}$$

where

$$a = \frac{B(C-B)}{A(A-C)} \tag{1.4.8}$$

The special solution (1.4.6a) is a singularity of Eq. (1.4.7). The type of the singularity can be determined by the sign of parameter a as

$$\begin{aligned} a < 0 &: \text{ Singularity is a center} \\ a > 0 &: \text{ Singularity is a saddle} \end{aligned} \tag{1.4.9}$$

Thus the following conditions of stability can be derived

$$\begin{aligned} C > A, C > B \text{ or } C < A, C < B &: \text{ stable} \\ A > C > B \text{ or } A < C < B &: \text{ unstable} \end{aligned} \tag{1.4.10}$$

It concludes that the permanent rotation about the axis with the maximal or the minimal moment of inertia is stable, and the permanent rotation about the axis with the middle moment of inertia is unstable.

If the body is axisymmetrical about the Oz-axis, then $A = B$. Equation (1.4.1c) requires that the angular velocity ω_3 about the axis of symmetry be constant. The polhode becomes a set of circles about the Oz-axis (Fig. 1.17(b)), and the permanent rotation about Oz is always stable regardless of whether $C > A$ or $C < A$. This phenomenon can be used to stabilize the satellite if its spinning axis is perpendicular to the orbital plane and coincides with the axis of symmetry.

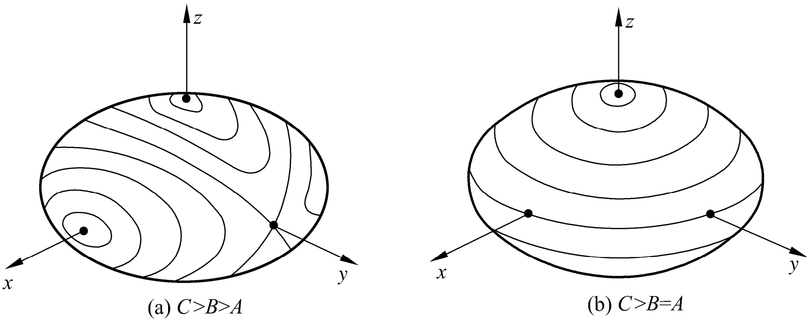

(a) $C>B>A$ (b) $C>B=A$

Figure 1.17 Polhode on energy ellipsoid

1.4.2 Torque-free Gyrostat

Consider a simple gyrostat (S) composed of an asymmetric platform S_{P} and a single rotor S_{R} as a model of a dual-spin satellite. Assume that S_{R} rotates about the Oz-axis with constant angular velocity Ω_{R} relative to S_{P}, and $g_{\mathrm{R}} = J_{\mathrm{R}}\Omega_{\mathrm{R}}$ (Fig. 1.18). Under the torque-free condition, the dynamical Eqs. (1.3.49) of a simple gyrostat can be simplified as

$$A\dot{\omega}_1 + (C - B)\omega_2\omega_3 + \omega_2 g_{\mathrm{R}} = 0 \tag{1.4.11a}$$

$$B\dot{\omega}_2 + (A-C)\omega_3\omega_1 - \omega_1 g_{\mathrm{R}} = 0 \tag{1.4.11b}$$

$$C\dot{\omega}_3 + (B-A)\omega_1\omega_2 = 0 \tag{1.4.11c}$$

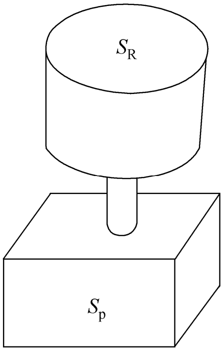

Figure 1.18 Gyrostat with a single rotor

The first integrals of kinetic energy and angular momentum of Eq. (1.4.11) are

$$A\omega_1^2 + B\omega_2^2 + C\omega_3^2 = 2E \tag{1.4.12}$$

$$A^2\omega_1^2 + B^2\omega_2^2 + (C\omega_3 + g_{\mathrm{R}})^2 = G^2 \tag{1.4.13}$$

Take the permanent rotation (1.4.6a) of the platform as the unperturbed motion, and introduce the perturbations as

$$\xi_1 = \omega_1, \xi_2 = \omega_2, \ \xi_3 = \omega_3 - \omega_0 \tag{1.4.14}$$

Substituting Eq. (1.4.14) into Eqs. (1.4.12) and (1.4.13), and retaining only the second terms of ξ_i $(i = 1,2,3)$, one obtains

$$V_1 = A\xi_1^2 + B\xi_2^2 + C(\xi_3^2 + 2\omega_0\xi_3) = \text{const} \tag{1.4.15}$$

$$V_2 = A^2\xi_1^2 + B^2\xi_2^2 + C^2(\xi_3^2 + 2\omega_0\xi_3) + 2Cg_{\mathrm{R}}\xi_3 = \text{const} \tag{1.4.16}$$

Define the Lyapunov function as

$$V = V_2 - \left(C + \frac{g_{\mathrm{R}}}{\omega_0}\right)V_1 + \frac{\lambda}{4\omega_0^2}V_1^2 \tag{1.4.17}$$

where λ is an arbitrary parameter. Substitution of Eqs. (1.4.15) and (1.4.16) into Eq. (1.4.17) leads to

$$V = A(A - C_1)\xi_1^2 + B(B - C_1)\xi_2^2 + C\left(\lambda C - \frac{g_{\mathrm{R}}}{\omega_0}\right)\xi_3^2 + \cdots \tag{1.4.18}$$

where

$$C_1 = C + \frac{g_{\mathrm{R}}}{\omega_0} \tag{1.4.19}$$

The parameter C_1 can be regarded as an enlarged moment of inertia of the body about the axis of symmetry. The function V is positive-definite if $C_1<A$ and $C_1<B$, or negative-definite if $C_1>A$ and $C_1>B$ for the suitably chosen parameter. Therefore, it is proved by the Lyapunov's direct method that the stability condition of a torque-free gyrostat is the same as (1.4.10) when the moment of inertia C is changed by the enlarged C_1.

1.4.3 Influence of Energy Dissipation on Spinning Spacecraft

If a spacecraft contains flexible appendages, the internal damping appears as a result of the elastic deformation of appendages. Consequently, the total energy E is dissipated while the angular momentum G remains constant. A rigid body with small elastic elements can be regarded as a near-rigid body. The kinetic energy and the angular momentum can be approximated by Eqs. (1.4.2) and (1.4.3). In the case that the body rotates about Oz-axis with a constant angular velocity, elimination of ω_3 from Eqs. (1.4.2) and (1.4.3) yields

$$A(C-A)\omega_1^2 + B(C-B)\omega_2^2 = 2CE - G^2 \tag{1.4.20}$$

Differentiating each term in Eq. (1.4.20) with respect to time and considering $\dot{E} < 0$, $\dot{G} = 0$, one obtains

$$A(C-A)\frac{\mathrm{d}}{\mathrm{d}t}(\omega_1^2) + B(C-B)\frac{\mathrm{d}}{\mathrm{d}t}(\omega_2^2) < 0 \tag{1.4.21}$$

The inequality (1.4.21) yields

$$\begin{aligned} &C > A, C > B: \ \omega_1^2 \text{ and } \omega_2^2 \ \text{ decrease} \\ &C < A, C < B: \ \omega_1^2 \text{ and } \omega_2^2 \ \text{ increase} \end{aligned} \tag{1.4.22}$$

Then the stability condition (1.4.10) should be corrected as

$$\begin{aligned} &C > A, C > B: \ \text{asymptotic stable} \\ &C < A, C < B: \ \text{unstable} \end{aligned} \tag{1.4.23}$$

It means that the permanent rotation of a torque-free body is asymptotically stable only when the rotation axis is the axis of symmetry with maximal moment of inertia.

A similar conclusion as (1.4.23) can be drawn for a torque-free gyrostat when the moment of inertia C about Oz is changed by the enlarged moment of inertia C_1:

$$\begin{aligned} &C_1 > A, C_1 > B: \ \text{asymptotic stable} \\ &C_1 < A, C_1 < B: \ \text{unstable} \end{aligned} \tag{1.4.24}$$

The stability condition in (1.4.24) requires

$$J\Omega_\mathrm{R} > \max\left((A-C)\omega_0, (B-C)\omega_0\right) \tag{1.4.25}$$

In the case of an earth-pointing satellite, let $\omega_0 = \omega_c$, $\omega_\mathrm{R} = \omega_c + \Omega_\mathrm{R}$ be the absolute angular velocity of the rotor, and $C_\mathrm{P} = C - J$ be the moment of inertia of the platform. Then the stability criterion (1.4.25) becomes

$$J\omega_\mathrm{R} > \max\left((A-C_\mathrm{P})\omega_c, (B-C_\mathrm{P})\omega_c\right) \tag{1.4.26}$$

It means that a stable permanent rotation can be realized by increasing the rotor speed Ω_R, even if the gyrostat is in a slender form. A gyrostat-satellite stabilized by the gyroscopic effect of the rotor is called a dual-spin satellite.

References

[1] Beletsky VV. *The Motion of an Artificial Satellite about Its Center of Mass*. New York: Plenum, 1963

[2] Thomson WT. *Introduction to Space Dynamics*. New York: John Willy & Sons, 1963

[3] Kaplan MH. *Modern Spacecraft Dynamics and Control*. New York: John Willy & Sons, 1976

[4] Hughes PC. *Spacecraft Attitude Dynamics*. New York: John Willy & Sons, 1985

[5] Wie B. *Space Vehicle Dynamics and Control*. AIAA Education Series, 1988

[6] Rimrott EPJ. *Introductory Orbit Dynamics*. Braunschweig: Friedrich Vieweg & Sohn, 1989

[7] Rimrott EPJ. *Introductory Attitude Dynamics*. New York: Springer-Verlag, 1989

[8] Wiesel WE. *Spaceflight Dynamics*. New York: McGraw-Hill, 1989

[9] Liu YZ. *Attitude Dynamics of Spacecraft*. Beijing: Defense Industry Press, 1995 (in Chinese)

[10] Sidi MJ. *Spacecraft Dynamics and Control: A Practical Engineering Approach*. Cambridge: Cambridge University Press, 2000

[11] Likins PW. Stability of a symmetrical satellite in attitude fixed in an orbital reference frame. *Journal of Astronautical Science*, 1965, 12(1), 18-24

[12] Zlatoustov VA, Okhotsimsky DE, Sarychev VA, Torzhevsky AP. Investigation of satellite oscillations in the plane of an elliptic orbit. *Proceedings of 11th International Congress of Applied Mechanics* (Munich, 1964), Springer-Verlag, 1966

Chapter 2 A Survey of Chaos Theory

Abstract This chapter briefly summarizes chaos theory. The chapter begins with describing chaos as bounded aperiodic random-like deterministic motion, which is sensitive to initial states and thus unpredictable after a certain time of a system. The geometrical structure of chaos is analyzed via the Poincaré map. Three typical routes to chaos are introduced as period-doubling sequence, intermittency, and quasiperiodic torus breakdown. The chapter covers two main numerical approaches to identify chaos, Lyapunov exponents and power spectra. The Melnikov theory is presented to predict the transversal intersection of stable and unstable manifolds of a saddle point. Such an intersection results in complicated dynamical behaviors which are sensitive to initial conditions. Finally, chaos is treated in the context of Hamiltonian systems. KAM theorem is stated without the proof. Two mechanisms of Hamiltonian chaos are illustrated as KAM tori breakup and Arnol'd diffusion. The Melnikov theory is generalized to higher-dimensional Hamiltonian systems.

Keywords chaos, Poincaré map, period-doubling sequence, intermittency, quasiperiodic torus breakdown, Lyapunov exponents, power spectra, Melnikov theory, KAM theorem, KAM tori breakup, Arnol'd diffusion

This chapter briefly summarizes chaos theory, most of which will be applied in the subsequent chapters. The chapter begins with describing chaos as bounded aperiodic random-like deterministic motion, which is sensitive to initial states and thus unpredictable after a certain time of a system. The geometrical structure of chaos is analyzed via the state space as well as the Poincaré map. Three typical routes to chaos are introduced as period-doubling sequence, intermittency, and quasiperiodic torus breakdown. The chapter covers two main numerical approaches to identify chaos, Lyapunov exponents and power spectra. The Melnikov theory is presented to predict the transversal intersection of stable and unstable manifolds of a saddle point. Such an intersection is explained to result in complicated dynamical behaviors which are sensitive to initial conditions. Finally, chaos is treated in the context of Hamiltonian systems. KAM theorem is stated without the proof. Two mechanisms of Hamiltonian chaos are illustrated as KAM tori breakup and Arnol'd diffusion. The Melnikov theory is generalized to higher-dimensional Hamiltonian systems. This chapter is only a brief survey of chaos, and references [1-6] present a more comprehensive treatment of chaos with the emphasis on engineering applications.

2.1 The Overview of Chaos

2.1.1 Descriptions of Chaos

Motions of many natural or engineering systems, including attitude motion of spacecraft, can be governed by a set of equations derived from the natural laws such as Newton's laws or Euler's equation. The set of equations, defined mathematically as a **dynamical system**, yields the time evolution of the state of a system from the knowledge of its previous history. Therefore, the state at any time can be determined by the governing equations and the initial states. The equations desceibing a dynamical system may be algebraic or differential equations.

In modern science, **chaos** is a term to describe a type of motion, or time evolution resulting from a dynamical system, that appears, on detailed examination, to be completely disordered and extremely complex. The disorder and complicacy are due to the following reasons.

Chaos is a recurrent aperiodic motion. Hence, chaos can be practically defined as a bounded steady-state response that is not an equilibrium state or a periodic motion, or a quasiperiodic motion. For systems with finite degrees of freedom, a bounded response of linear systems must be an equilibrium state, a periodic motion, or a quasiperiodic motion. Hence chaos is a striking feature of a nonlinear system. As a recurrent motion, chaos is bounded so that it will trend to the infinite.

Chaotic motions are also characterized by **sensitivity to initial states**; that is, tiny differences in the initial conditions can be quickly amplified to produce huge differences in the response. Due to such sensitivity, the long-term prediction for chaos is impossible, because all initial conditions have to be prescribed in a certain precision, while, after enough time, the motion depends on the digits in the conditions beyond the precision. That is, chaos is unpredictable after enough time because a small difference in the initial conditions beyond their precision will result in rapidly (usually exponentially) growing perturbation of the motion. This phenomenon is vividly called **butterfly effect**. A disturbance caused by the wings of a butterfly in Shanghai can lead to a rainstorm a few days later in Toronto.

Chaos, as a recurrent aperiodic motion, has no pattern or order to follow, just like a stochastic process. Actually, the spectrum of a chaotic motion has a continuous broadband, which is the same as a true random signal. In contrast, the spectra of periodic or quasiperiodic motions consist of a number of sharp spikes. In addition to the broadband component, the spectrum of a chaotic motion often contains spikes, which indicate the predominant frequencies of the motion. Chaos is the superposition of an infinite number of unstable periodic motions. Therefore, a chaotic motion may settle for a short time near a periodic motion and then may switch to another periodic motion with a different period. However, chaos usually describes a special type of motion in a deterministic system that is without any random inputs. Hence, the random-likeness of chaotic motion is called **intrinsic stochasticity** or **spontaneous stochasticity**. A true stochastic process is unpredictable at any time, while chaos can be predicted only after a very short time from the beginning.

In short, as a steady-state response of a deterministic system, chaos is sensitive to initial states and thus unpredictable after a certain time, and is recurrent but either periodic or quasiperiodic hence like a random single.

2.1.2 Geometrical Structures of Chaos

The recurrent aperiodicity of chaos can be intuitively illustrated in the phase plane. For a single degree of freedom, two independent parameters are needed to describe the state of motion completely (not only the position, but also the position change). These parameters are usually chosen as the generalized displacement and velocity of the system. When the parameters are used as coordinate axes, the resulting graphical illustration of the motion is called the phase plane representation. Thus each point in the phase plane represents a possible state of the system. The state of the system changes with the time evolution. A typical of representative point in the phase plane, such as the point representing the state of the system at time $t=0$, moves and traces a curve known as a **trajectory** or an **orbit**. The trajectory demonstrates how the motion beginning at a given initial state varies with time. On the phase plane, an equilibrium state is represented by a point on the displacement (usually horizontal) axis. The trajectory of a periodic motion is a closed curve, because the trajectory repeats itself after a period. A chaotic motion is represented by a trajectory that never closes and repeats itself because of the aperiodicity of the motion, and the trajectory is located in a bounded region due to the recurrence of the motion. Therefore, the trajectory of chaos in the phase plane usually occupies a part of the phase space. However, the trajectory of a quasiperiodic motion does not close on itself either, although it looks much more regular than a chaotic trajectory. In addition, it is difficult in practice to differentiate a trajectory of chaos from that of a periodic motion with a sufficient large period. Therefore, new techniques are necessary to describe the recurrent aperiodicity of chaos and distinguish chaos from periodic or quasiperiodic motions.

Consider a set of ordinary differential equations in the vector form

$$\dot{\boldsymbol{x}} = \boldsymbol{f}(\boldsymbol{x},t) \quad \boldsymbol{x} \in R^n, \quad t \in R \tag{2.1.1}$$

where ***f*** is a vector function defined in R^{n+1} with its value range in R^n, $\boldsymbol{x}$ is a n dimensional vector to specify the state of the system, and t is time. The vector $\boldsymbol{x}$ is called a state vector, and R^n in which $\boldsymbol{x}$ evolves is called a state space. A stage space is called a phase space when half of the state variables are displacements and the other half are velocities. Obviously, the phase space is the generalization of the phase plane. If the vector function does not depend explicitly on time t, the dynamical system governed by Eq. (2.2.1) is call autonomous; otherwise, it is called nonautonomous.

The geometrical structure representing an asymptotically long-time behavior in a state space is called an attractor. Mathematically, an **attractor** is an indecomposable, closed, invariant set that attracts all trajectories starting at points in some neighborhood. Here, an **indecomposable set** is a set that cannot be separated into smaller pieces, and an **invariant set** is a set that trajectories starting in the set remain in it for all time.

An attractor may be a point, called a **point attractor**, which represents an asymptotically stable equilibrium state. An attractor may be a closed curve, called a **periodic attractor**, which represents a periodic motion. An attractor may be a torus, called a **quasiperiodic attractor**, which represents a quasiperiodic motion. If an attractor is not a point attractor, a periodic attractor, or a quasiperiodic attractor, it is call a **strange attractor**. A strange attractor usually represents a chaotic motion, and thus it is also referred as a **chaotic attractor**. A chaotic attractor has typically embedded within it an infinite number of periodic orbits that are unstable. Mathematically, unstable periodic orbits are dense in a chaotic attractor. The orbits pass through any neighborhood, no matter how small it is, of any point on the attractor.

The Ponicaré map will be defined in a state space. It can discretize a trajectory of a dynamical system governed by a set of ordinary-differential equations into a set of points. The **Poincaré map** or the **Poincaré section map**, named after Henri Poincaré, is the intersection of a trajectory, which moves periodically, quasi-periodically, or chaotically, in an n-dimensional state space, with a transversal hypersurface whose dimension is $n-1$. Here a transversal hypersurface means that, at the intersection point, the normal of the hypersurface is not orthogonal to the tangent of the trajectory. More specifically, one considers a trajectory with initial conditions on the hyperplane and observes the point at which this trajectory returns to the hyperplane. The **Poincaré section** refers to the hyperplane, and the Poincaré map refers to the map of points in the hyperplane induced by the intersections. If the vector function ***f*** in Eq. (2.1.1) is periodic in time with period T, then the Poincaré map can be constructed by monitoring stroboscopically the state variables at intervals of the period T. The Poincaré map can be denoted by

$$\boldsymbol{X}_{i+1} = \boldsymbol{P}(\boldsymbol{X}_i) \qquad \boldsymbol{X} \in R^n, \quad i \in Z \tag{2.1.2}$$

The points on the Poincaré section obtained by iterating $\boldsymbol{P}$

$$\{\boldsymbol{X}_1, \boldsymbol{X}_2, \cdots, \boldsymbol{X}_i, \cdots\} \qquad (\boldsymbol{X}_i = \boldsymbol{x}(iT),\ i = 1, 2, \cdots) \tag{2.1.3}$$

which is also called sometimes the Poincaré map, can be used to determine if a motion is periodic, quasiperiodic, or chaotic.

For the Poincaré map obtained by sampling the state variables at intervals of T, a periodic motion with the period mT will collect m points on the Poincaré section. Therefore, the Poincaré map (2.1.3) of a periodic motion is a set of finite points. The Poincaré map (2.1.3) of a quasiperiodic motion does not contain finite points. To explore its characteristic, consider the following simple example. A motion given by

$$x_1(t) = A\sin t + B\sin \pi t,\ x_2(t) = C\cos t + D\cos \pi t \tag{2.1.4}$$

is quasiperiodic because it is characterized by the two incommensurate frequencies 1 and π, and called two-period quasiperiodic. A Poincaré map is constructed by sampling the trajectory at intervals 2π starting at $t = 0$. Then the discrete points are collected as

$$x_{1i} = B\sin i\pi^2,\ \ x_{2i} = C + D\cos i\pi^2 \ \ (B, D \neq 0) \tag{2.1.5}$$

Hence all mapping points on the closed curve are defined by

$$\frac{x_{1i}^2}{B^2} + \frac{(x_{2i} - C)^2}{D^2} = 1 \tag{2.1.6}$$

It can be further demonstrated that the points fill densely the closed curve. Therefore, the Poincaré map (2.1.3) of a quasiperiodic motion is a set of infinite points located densely on a loop or a torus. Since a chaotic motion is neither periodic nor quasiperiodic, the Poincaré map (2.1.3) of chaos is a set of infinite points that do not fill any loops or tori.

2.1.3 Routes to Chaos

In addition to its physics and geometry, chaos can also be investigated from the view of its emerging processes with the variation of system parameters. The processes are often referred as **routes to chaos** or **transitions to chaos**. In most systems, chaos occurs only for some range of parameter values. How a regularly behaving system becomes chaotic is a fundamental and significant problem. Theoretically, routes to chaos can reveal the nature and mechanisms of chaos. Practically, routes to chaos can serve as an effective approach to identify chaos, especially to distinguish chaos from truly random motion. Actually, for a system with bounded irregular motion, if a route to chaos appear with a change of a system parameter, then the motion is quite surely chaotic rather than stochastic. There are several fairly well-understood and (relatively) easily recognizable routes to chaos in a particular transition process in a prescribed system. These routes include period-doubling sequence, intermittency, and quasiperiodic torus breakdown.

The period-doubling cascade, also referred to as period-doubling scenario, is the best understood route to chaos. In the period-doubling cascade, as a system parameter is gradually varied, a periodic motion transitions to a chaotic motion via a sequence of period-doubling bifurcations. This route was discovered in the context of 1-dimensional maps by Feigenbaum in 1978 [7], and it is now known to occur in almost all kinds of systems.Consider a system with parameter μ. In multi-parameter systems, one can vary one of them and fix the others. Suppose the motion with period T for $\mu=\mu_0$. With changing μ, when $\mu=\mu_1$, the period of motion becomes $2T$. Such a sudden change of the motion is called a **period-doubling bifurcation**. Generally speaking, if the motion is with period 2^kT for $\mu=\mu_k$, the period-doubling bifurcation at $\mu=\mu_{k+1}$ turns the motion period into $2^{k+1}T$. As the motion period continues to double, it becomes larger and larger, and finally, infinite, which actually corresponds to aperiodic motion. Observing the Poincaré map, one finds that one point becomes two points, two points become four points, and so on. At last, an infinite point set is created, and chaos appears. Theoretically, in the absence of noise, an infinite number of period-doubling bifurcations occur in the transition to chaos. Practically, as noise is always present, some of the higher period-doubling bifurcations may be suppressed by the noise, resulting in a finite sequence of bifurcations. It should be remarked that

$$\delta=\lim_{n\to\infty}\frac{\mu_n-\mu_{n-1}}{\mu_{n+1}-\mu_n} \tag{2.1.7}$$

is a constant for the infinite sequence of period-doubling bifurcation values $\{\mu_n\}$. In fact, in a certain class of systems, different systems have the same constant regardless of the details of each system. Therefore, δ is called a universal constant. The universality characterizes the period-doubling cascade as a route to chaos.

Intermittency is another frequently observed route to chaos. **Intermittency** is a phenomenon characterized by random alternations between a regular motion and relatively short irregular bursts. The term *intermittency* has been used in the theory of turbulence to denote burst of turbulent motion on the background of laminar flow. During early stages of intermittency, for a certain system parameter value, the motion of the system is predominantly periodic with occasional bursts of chaos. As the parameter value is changed, the chaotic bursts become more frequent, and the time spent in a state of chaos increases and the time spent in periodic motion decreases until, finally, chaos is observed all the time. As a result, the periodic motion becomes chaotic motion. This route was found by Pomeou and Manneville in

1980 [8]. Geometrically, the intermittency route is associated with a periodic attractor in the state space bifurcating into a new, larger chaotic attractor, including previous periodic trajectories as its subset. The trajectory of a system can reside some time in the chaotic part of the attractor, but it is ultimately attracted back to the periodic part. As the system parameter is varied, the relative proportion of the chaotic part increases, ultimately covering the whole attractor.

Quasiperiodic torus breakdown is the third typical way that a system may evolve as its parameter is changed. **Quasiperiodic torus breakdown route** signifies the destruction of the torus and the emergence of a chaotic attractor. The system, if it is not externally driven by a periodic action, may be at equilibrium. As the system parameter is varied, the equilibrium may lose its stability, leading to the emergence of a stable periodic motion. Such a change resulting in a new motion frequency is called the **Hopf bifurcation**. In the state space, a point attractor becomes a periodic attractor. With a further change in the parameter, the periodic attractor undergoes a secondary Hopf bifurcation, resulting in a 2-period quasiperiodic attractor. The trajectories in the state space reside on the surface of a torus. If the two frequencies are incommensurable, the trajectory eventually covers the surface of the torus. For some systems, further changes in the parameter result in the introduction of a third frequency. In the state space, the trajectories live on a 3-dimensional torus. With further parameter changes, the motion of a system becomes chaotic. Some systems may apparently switch directly from two-periodic quasiperiodic motion to chaos. The discovery of the route to chaos started with Ruelle and Takens, who in 1971 proposed an alternative to the Landau-Hopf picture of infinitely increasing number of incommensurable frequencies for the onset mechanism of turbulence [9]. As Ruelle and Takens demonstrated, quasiperiodic motion on a torus with 4 incommensurable frequencies is generally unstable and can be perturbed into a strange attractor corresponding to turbulent motion. In 1978, Hewhouse, Ruelle and Takens proved that a torus with 3 incommensurable frequencies is generally unstable and can be perturbed into chaos [10]. In the same year, Swinney and Gollub experimentally showed that a quasiperiodic motion with 2 incommensurable frequencies directly leads to chaos [11]. In 1982, Feigenbaum, Kadanoff and Shenker revealed the universality in the quasiperiodic route to chaos [12]. In 1983, Grebogi, Ott, and Yorke confirmed that the quasiperiodic torus with 3 incommensurable frequencies is usually stable and thus a periodic motion becomes chaotic after only two bifurcations [13]. That is, the 2-period quasiperiodic motion may lead to chaos directly.

Chaos may suddenly occur in a system. One mechanism to account for a sudden appearance of chaos is crisis, the term introduced by Grebogi, Ott, and Yorke in 1983 [14]. A **crisis** is a sudden qualitative change in which a chaotic attractor disappears or suddenly expands in size as a system parameter is varied. Therefore, if a typical route to chaos is observed, one may conclude that chaos is taking place in a system. On the other hand, even if no typical route to chaos is observed, one cannot exclude the possibility of the appearance of chaos.

2.2 Numerical Identification of Chaos

2.2.1 Introduction

The numerical identification of chaos is an important aspect of nonlinear dynamics. The identification of chaos is some diagnostic tests to determine if chaotic behavior occurs in a specific system. Some numerical characteristics associated with the motion of a system can be used to identify chaos. These characteristics include Lyapunov exponents, fractal dimensions, power spectra, and entropies. If one or more of these characteristics satisfy certain conditions, the motion may be chaotic.

As explained in the previous section, chaos can be described in different aspects. Quantifying these descriptions leads to corresponding numerical characteristics. To specify the sensitivity of chaos to initial states, Lyapunov exponents are introduced. To highlight the recurrent aperiodicity of chaos, various dimensions can be defined. To detect the stochasticity of chaos, power spectra may be used. To reveal the unpredictability of chaos, entropies can be employed. However, only Lyapunov exponents and power spectra will be presented in this section. They will be applied in the following chapters.

2.2.2 Lyapunov Exponents

The extreme sensitivity to initial states makes neighboring trajectories diverge rapidly as the time elapses. Therefore, a numerical approach to identify chaos can be developed based on the quantitative characterization of the divergence among the neighboring trajectories. Lyapunov exponents are a set of numerical characteristics to quantify the divergence of trajectories. In an n–dimensional state space, the displacement between two points on two nearby trajectories has n components in n different directions. Trajectories may diverge in some directions, but they must converge in other directions. Otherwise, the motion will become unbounded. Hence the change rates of the distance along the n directions are different, and each change rate is a Lyapunov exponent. This intuitionistic idea can be presented in a more rigorous way as follows.

Consider a dynamical system governed by

$$\dot{\boldsymbol{x}} = \boldsymbol{f}(\boldsymbol{x}) \quad \boldsymbol{x} \in R^n \tag{2.2.1}$$

Choose two trajectories L_0 and L_1 starting at two close initial conditions $\boldsymbol{x}_0$ and $\boldsymbol{x}_0 + \Delta\boldsymbol{x}_0$, respectively. Define L_0 starting at $\boldsymbol{x}_0$ as the unperturbed trajectory, and L_1 starting at $\boldsymbol{x}_0+\Delta\boldsymbol{x}_0$ as a perturbed trajectory. Denote $\boldsymbol{x}(\boldsymbol{x}_0 + \Delta\boldsymbol{x}_0,t)$ and $\boldsymbol{x}(\boldsymbol{x}_0,t)$ as the points at time t on the perturbed and unperturbed trajectories respectively. Denote the difference as $\boldsymbol{w}(\boldsymbol{x}_0, t) = \boldsymbol{x}(\boldsymbol{x}_0 + \Delta\boldsymbol{x}_0, t) + \boldsymbol{x}(\boldsymbol{x}_0, t)$. Then for sufficient small $\boldsymbol{w}$, $\boldsymbol{w}$ satisfies the linearized equation of Eq. (2.2.1) at $\boldsymbol{x}_0$, namely,

$$\dot{\boldsymbol{w}} = \mathbf{D}\boldsymbol{f} \cdot \boldsymbol{w} \tag{2.2.2}$$

where $\mathbf{D}\boldsymbol{f}$ is the $n \times n$ Jacobi matrix calculated at $\boldsymbol{x}_0$. Now the averaged rate of exponential expansion or contraction in the direction of $\boldsymbol{w}$ on the trajectory starting at $\boldsymbol{x}_0$ is given by

$$\lambda(\boldsymbol{x}_0, \boldsymbol{w}) = \lim_{\substack{t\to\infty \\ w_0\to 0}} \frac{1}{t} \ln \frac{\|\boldsymbol{w}\|}{\|\boldsymbol{w}_0\|} \tag{2.2.3}$$

where the symbol $\|\ \|$ denotes a vector norm and $\boldsymbol{w}_0 = \boldsymbol{w}(\boldsymbol{x}_0, 0)$. In the n-dimensional state space, all $\boldsymbol{w}$ form n-dimensional state space moving along the trajectory L_0. Take a set of base vector $\{\boldsymbol{e}_i, i = 1, 2, \cdots, n\}$. For every $\boldsymbol{e}_i$, Eq. (2.2.3) yields $\lambda(\boldsymbol{x}_0, \boldsymbol{e}_i)$ $(i = 1, 2, \cdots, n)$. Those numbers are ordered such that

$$\lambda_1 \geqslant \lambda_2 \geqslant \cdots \geqslant \lambda_n \tag{2.2.4}$$

The number λ_i is called the **Lyapunov exponent**, and the set of n number λ_i is called the **Lyapunov spectrum**.

Roughly speaking, the Lyapunov exponents of a trajectory characterize the mean exponential rates of divergence (in different directions) of other trajectories surrounding it. A Lyapunov exponent may be positive or negative. A positive Lyapunov exponent implies the divergence in the corresponding direction. That is, all trajectories near the trajectory under consideration diverge locally from it along the direction. A negative exponent implies the constriction in the corresponding direction. All trajectories close to the trajectory under consideration locally converge toward it in the direction. Therefore, if all Lyapunov exponents are negative, the motion is in a stable equilibrium.

For a limit cycle of an autonomous system, there is always a zero Lyapunov exponent corresponding to an initial deviation along a tangent to the closed orbit. In addition, for a stable periodic motion, all other Lyapunov exponents are negative. Those negative exponents essentially correspond to perturbations along directions normal to the closed orbit. For an m-torus, m Lyapunov exponents are zero because there are m tangential directions to the torus along which there is neither growth nor decay.

If there are one or more positive Lyapunov exponents, these exponents correspond to the directions along which the initial disturbances become larger and larger. Thus a bounded trajectory with one or more positive Lyapunov exponents represents chaotic motion.

Based on the above-mentioned analysis, the types of attractors and motions can be summarized in Table 2.1 for low dimensional systems.

Table 2.1 Classification of Attractors in Low Dimensional State Spaces

Dimension	Sign of Lyapunov Exponents	Types of Attractors	Types of Motion
3	− − −	stable fixed point	equilibrium
	0 − −	limit cycle	periodic motion
	0 0 −	2-torus	quasiperiodic motion
	+ 0 −	strange attractor	chaotic motion
4	− − − −	stable fixed point	equilibrium
	0 − − −	limit cycle	periodic motion
	0 0 − −	2-torus	quasiperiodic motion
	0 0 0 −	3-torus	quasiperiodic motion
	+ 0 − −	strange attractor	chaotic motion
	+ 0 0 −	strange attractor on a 3-torus	chaotic motion
	+ + 0 −	strange attractor	chaotic motion
5	− − − − −	stable fixed point	equilibrium
	0 − − − −	limit cycle	periodic motion
	0 0 − − −	2-torus	quasiperiodic motion
	0 0 0 − −	3-torus	quasiperiodic motion
	0 0 0 0 −	4-torus	quasiperiodic motion
	+ 0 − − −	strange attractor	chaotic motion
	+ 0 0 − −	strange attractor on a 3-torus	chaotic motion
	+ 0 0 0 −	strange attractor on a 4-torus	chaotic motion
	+ + 0 − −	strange attractor on a 3-torus	chaotic motion
	+ + 0 0 −	strange attractor on a 4-torus	chaotic motion
	+ + + 0 −	strange attractor	chaotic motion

2.2.3 Power Spectra

The power spectra are a basic tool to analyze random vibrations. In a power spectrum, the square of the Fourier amplitude per unit time is displayed at each frequency. The power spectra also help in distinguishing among periodic, quasiperiodic, and chaotic motions.

For a sample function of a signal $x(t)$, the power spectrum can be defined in two ways. The power spectrum $\varPhi_x(\omega)$ is the time average of the square of its Fourier amplitude, namely,

$$\varPhi_x(\omega) = \lim_{T\to\infty}\frac{1}{T}\left|\int_0^T x(t)\,\mathrm{e}^{-\mathrm{i}\omega t}\,\mathrm{d}t\right|^2 \tag{2.2.5}$$

On the other hand, the power spectrum $\varPhi_x(\omega)$ is also the Fourier transform of the autocorrelation function, namely,

$$\varPhi_x(\omega) = \int_{-\infty}^{\infty} R_x(\tau)\,\mathrm{e}^{-\mathrm{i}\omega\tau}\,\mathrm{d}\tau \tag{2.2.6}$$

where the autocorrelation function $R_x(\tau)$ is defined as

$$R_x(\tau) = \lim_{T\to\infty} \frac{1}{T} \int_{-T/2}^{T/2} x(t)x(t+\tau)\,\mathrm{d}t \tag{2.2.7}$$

Based on the Wiener-Khinchin relations of stochastic processes, the above two definitions are equivalent to the condition that $R_x(\tau)$ decays rapidly with time.

In experimental measurements or numerical simulations, researchers often obtain a time series with the same delay interval,

$$x_1, x_2, \cdots, x_N \tag{2.2.8}$$

Adding a periodic condition $x_{N+i} = x_i\ (i = 1,2,\cdots)$, the autocorrelation can be calculated as the discrete convolution

$$c_i = \frac{1}{N}\sum_{j=1}^{N} x_j x_{j+i} \tag{2.2.9}$$

Its discrete Fourier transform

$$p_j = \sum_{j=1}^{N} c_i\, \mathrm{e}^{\frac{2\mathrm{i}\pi ki}{N}} \tag{2.2.10}$$

is the discrete power spectrum of the time series (2.2.8).

In practical calculations of discrete power spectra, a more effective approach is to evaluate directly the coefficients of the discrete Fourier transform

$$\begin{aligned} a_j &= \frac{1}{N}\sum_{k=1}^{N} x_k \cos\left(\frac{\pi kj}{N}\right) \\ b_j &= \frac{1}{N}\sum_{k=1}^{N} x_k \sin\left(\frac{\pi kj}{N}\right) \end{aligned} \tag{2.2.11}$$

and then compute

$$\overline{p}_j = a_j^2 + b_j^2 \tag{2.2.12}$$

Usually, for many sets of $\{x_i\}$ evaluate the corresponding $\{\overline{p}_j\}$. The average of many resulting $\{\overline{p}_j\}$ will approximate the discrete power spectrum defined by Eq. (2.2.10). In this way, it is unnecessary to calculate the discrete autocorrelation (2.2.9). That is the basic idea of the fast Fourier transform attributed to Cooley and Tukey [15]. Nowadays, there are many commercial software packages available for determining the fast Fourier transform of a given signal.

The spectrum of a periodic motion with period T consists of discrete spikes at the frequency $1/T$ and possibly a certain number of other spikes at m/T for an integer m. The spectrum of a k-period quasiperiodic motion is made up of spikes at integer multiples of all its frequencies. Theoretically, the spectrum of a quasiperiodic motion can be distinguished from that of a periodic motion, because the peaks of the quasiperiodic spectrum are not spaced at integer multiples of a particular frequency. Practically, due to the impossibility of determining whether a measured value is rational of irrational, a spectrum seeming to be quasi-periodic may actually be periodic with an extremely large period.

Chaos is a random-like motion. The power spectrum of chaos has a continuous, broad-band nature, which is a characteristic exhibited by all chaotic motion. In addition to the broad-band component, it is rather common for a chaotic spectrum to contain spikes indicating the predominant frequencies of the system. In practical simulations, chaotic spectra are much more complicated than regular ones. Typically, they consist of some dominant peaks surrounded by a lot of grass-like components. Although it is uncertain if the grassy portion of the spectrum is truly continuous, the difference in a spectrum between regular and chaotic motion is usually quite striking to provide a feasible means to identify chaos numerically. However, a power spectrum does not distinguish chaos from a truly random motion, which is a limitation of application of power spectra to identification of chaos.

2.3 Melnikov Theory

2.3.1 Introduction

In 1963, Melnikov developed an analytical technique to detect a geometrical structure with the hallmark of chaos [16]. The key issues are the consequence and the prediction of transversal intersection of stable and unstable manifolds. Therefore, the concepts of stable and unstable manifolds will be introduced at the beginning. Then it will be explained that such an intersection implies the resulting sensitive dependence on initial conditions. The Melnikov function will be derived to predict the transversal intersection in a planar integrable system with small periodic perturbations. This analytical prediction approach will be generalized to higher-dimensional systems in the next section. Finally, the relation between the Melnikov analysis and the occurrence of chaos is clarified.

2.3.2 Transversal Homoclinic/Heteroclinic Point

Consider a dynamical system governed by Eq. (2.2.1). The **stable manifold** of a fixed point $\boldsymbol{x}_0$, denoted by $W^{\mathrm{s}}(\boldsymbol{x}_0)$, is the set of all initial conditions such that the trajectories initiated at these points asymptotically approaches the fixed point $\boldsymbol{x}_0$ as $t \to +\infty$, whereas the **unstable manifold** of a fixed point $\boldsymbol{x}_0$, denoted by $W^{\mathrm{u}}(\boldsymbol{x}_0)$, is the set of all initial conditions such that the trajectories initiated at these points asymptotically approach the fixed point $\boldsymbol{x}_0$ as $t \to -\infty$. That is,

$$W^{\mathrm{s}}(\boldsymbol{x}_0) = \left\{ \boldsymbol{X} \in \mathrm{R}^n \,\middle|\, \lim_{t \to +\infty} \boldsymbol{x}(\boldsymbol{X}, t) = \boldsymbol{x}_0 \right\}$$
$$W^{\mathrm{u}}(\boldsymbol{x}_0) = \left\{ \boldsymbol{X} \in \mathrm{R}^n \,\middle|\, \lim_{t \to -\infty} \boldsymbol{x}(\boldsymbol{X}, t) = \boldsymbol{x}_0 \right\} \tag{2.3.1}$$

where $\boldsymbol{X}$ is a point in the state space, and $\boldsymbol{x}(\boldsymbol{X},t)$ is a trajectory stating at $\boldsymbol{X}$. The stable manifold and the unstable manifold share a common feature that a trajectory with a starting point in it remains in the manifold forever. Therefore, both the stable manifold and the unstable manifold are called the **invariant manifold**.

The concept of the invariant manifold of a fixed point can be generalized to that of a periodic orbit. The stable or unstable manifolds of a periodic orbit is the set of all initial conditions which approach the periodic orbit as $t \to +\infty$ or $t \to -\infty$. The invariant manifold of a periodic orbit corresponds to the invariant manifold of a fixed point on the Poincaré map. Consider a fixed point $\bar{\boldsymbol{x}}$ on the Poincaré map $\boldsymbol{P}$

$$\bar{\boldsymbol{x}} = \boldsymbol{P}(\bar{\boldsymbol{x}}) \quad \bar{\boldsymbol{x}} \in \mathrm{R}^{n-1} \tag{2.3.2}$$

Denote the Jacobian matrix of map $\boldsymbol{P}$ as $\mathbf{D}\boldsymbol{P}$. If $n-1$ eigenvalues of $\mathbf{D}\boldsymbol{P}$ are such that their magnitudes are either larger than 1 or smaller than 1, the fixed point is called a **hyperbolic fixed point**, and the corresponding periodic orbit is called a **hyperbolic periodic orbit**. A hyperbolic fixed point is called a **saddle point** (hyperbolic saddle point sometimes) if the magnitudes of some eigenvalues are larger than 1 and those of the rest are smaller than 1. For a saddle point $\boldsymbol{p}_{\mathrm{s}}$, its stable manifold $W^{\mathrm{s}}(\boldsymbol{p}_{\mathrm{s}})$ and its unstable manifold $W^{\mathrm{u}}(\boldsymbol{p}_{\mathrm{s}})$ are respectively defined as

$$W^{\mathrm{s}}(\boldsymbol{p}_{\mathrm{s}}) = \left\{ \boldsymbol{z} \,\middle|\, \boldsymbol{z} \in \mathrm{R}^{n-1}, \lim_{k \to \infty} \boldsymbol{P}^{k}(\boldsymbol{z}) = \boldsymbol{p}_{\mathrm{s}} \right\}$$
$$W^{\mathrm{u}}(\boldsymbol{p}_{\mathrm{s}}) = \left\{ \boldsymbol{z} \,\middle|\, \boldsymbol{z} \in \mathrm{R}^{n-1}, \lim_{k \to \infty} \boldsymbol{P}^{-k}(\boldsymbol{z}) = \boldsymbol{p}_{\mathrm{s}} \right\} \tag{2.3.3}$$

where $\boldsymbol{z}$ is a point on the Poincaré section hyperplane.

If the stable manifold $W^{\mathrm{s}}(\boldsymbol{p}_{\mathrm{s}})$ of a saddle point $\boldsymbol{p}_{\mathrm{s}}$ coincides with the unstable manifold $W^{\mathrm{u}}(\boldsymbol{p}_{\mathrm{s}})$, namely $W^{\mathrm{s}}(\boldsymbol{p}_{\mathrm{s}}) = W^{\mathrm{u}}(\boldsymbol{p}_{\mathrm{s}})$, the manifold is called a **homoclinic orbit**. The homoclinic orbit is a closed orbit on which all points tend to the same saddle points $\boldsymbol{p}_{\mathrm{s}}$ as $t \to \pm\infty$. For two different saddle points $\boldsymbol{p}_{\mathrm{s}1}$ and $\boldsymbol{p}_{\mathrm{s}2}$, if the stable manifold $W^{\mathrm{s}}(\boldsymbol{p}_{\mathrm{s}1})$ of $\boldsymbol{p}_{\mathrm{s}1}$ coincides with the unstable manifold $W^{\mathrm{u}}(\boldsymbol{p}_{\mathrm{s}2})$ of $\boldsymbol{p}_{\mathrm{s}2}$, the manifold is called a **heteroclinic orbit** on which all points tend to $\boldsymbol{p}_{\mathrm{s}1}$ and $\boldsymbol{p}_{\mathrm{s}2}$ as $t \to +\infty$ and $t \to -\infty$, respectively. If meanwhile the unstable manifold $W^{\mathrm{u}}(\boldsymbol{p}_{\mathrm{s}1})$ of $\boldsymbol{p}_{\mathrm{s}1}$ coincides with the stable manifold $W^{\mathrm{s}}(\boldsymbol{p}_{\mathrm{s}2})$ of $\boldsymbol{p}_{\mathrm{s}2}$ so that there is another heteroclinic orbit, the two heteroclinic orbits form a **heteroclinic cycle**. A heteroclinic cycle may consist of more than two heteroclinic orbits connecting a few saddle points. Fig. 2.1 shows examples of homoclinic orbits, heteroclinic orbits, and heteroclinic cycles on a plane.

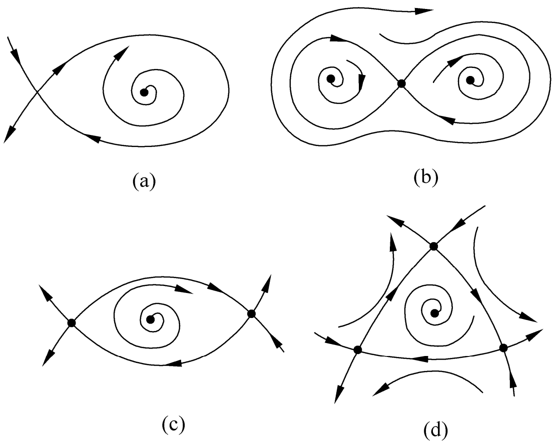

Figure 2.1 Homoclinic orbits, heteroclinic orbits, and heteroclinic cycles (a) a homoclinic orbit (b) two homoclinic orbits (c) heteroclinic cycle consisting of two heteroclinic orbits (d) heteroclinic cycle consisting of three heteroclinic orbits

If the stable manifold and the unstable manifold do not coincide with each other, they may intersect each other. If the stable manifold and the unstable manifold intersect transversally at a point, the point of intersection is called a **transversal homoclinic point**. Here the transversality of an intersection of manifolds means that the union of the tangent spaces of the intersecting manifolds spans the whole space. Intuitively, a transversal intersection means that two intersecting manifolds are not tangent to each other at the point of intersection. If the stable manifold of a saddle point intersects transversally the unstable manifold of another saddle point, the point of intersection is called a **transversal heteroclinic point**.

If there is a transversal homoclinic point $\boldsymbol{q} \in W^{\mathrm{s}}(\boldsymbol{p}_{\mathrm{s}}) \cap W^{\mathrm{u}}(\boldsymbol{p}_{\mathrm{s}})$. Then $\boldsymbol{q} \in W^{\mathrm{s}}(\boldsymbol{p}_{\mathrm{s}})$ and $\boldsymbol{q} \in W^{\mathrm{u}}(\boldsymbol{p}_{\mathrm{s}})$. Because both $W^{\mathrm{s}}(\boldsymbol{p}_{\mathrm{s}})$ and $W^{\mathrm{u}}(\boldsymbol{p}_{\mathrm{s}})$ are invariant manifolds, $\boldsymbol{P}^m(\boldsymbol{q}) \in W^{\mathrm{s}}(\boldsymbol{p}_{\mathrm{s}})$ and $\boldsymbol{P}^m(\boldsymbol{q}) \in W^{\mathrm{u}}(\boldsymbol{p}_{\mathrm{s}})$ for all integer m. Thus, $\boldsymbol{P}^m(\boldsymbol{q}) \in W^{\mathrm{s}}(\boldsymbol{p}_{\mathrm{s}}) \cap W^{\mathrm{u}}(\boldsymbol{p}_{\mathrm{s}})$. Similar argument is applicable in the case of a transversal heteroclinic point. That is, if the stable manifold and the unstable manifold intersect once, then they will intersect an infinite number of times, as shown in Fig. 2.2.

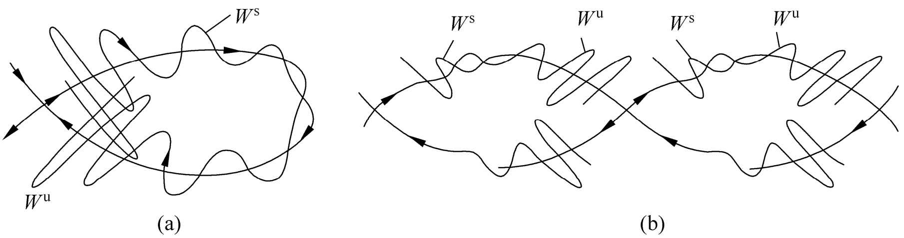

Figure 2.2 Intersections of the stable and unstable manifolds: (a) homoclinic point (b) heteroclinic point

Consider a rectangular area near a homoclinic point in a Poincaré section. Points in the area represent the intersections of trajectories starting at different initial conditions. In the process of mapping, the rectangle moves to the next homoclinic point. Meanwhile, the rectangle contracts in the direction of the stable manifold, stretches in the direction of the unstable manifold, and distorts as it moves. At a later time, the rectangle is transformed into a shape of horseshoe. The horseshoe overlaps the original rectangle to form two new smaller rectangular areas, which are still near the homoclinic point. Therefore, the whole transformation process can be repeated. It can be inferred from Fig. 2.3, two close points in the original rectangle may end up far away from each other and thus the initial difference is amplified. Therefore, such a geometrical structure is highly sensitive to initial conditions, which is a hallmark of chaos. In 1963, Smale proposed the map that contracts, stretches, and folds a rectangle and intersects the image with itself [17]. The map is called the **Smale horseshoe**.

2.3.3 Analytical Prediction

The above-mentioned analysis shows that the occurrence of a transversal homoclinic or heteroclinic point is a possible mechanism resulting in chaos. Melnikov developed an approximate analytical expression of the distance between the stable and unstable manifolds in a planar integrable system with small periodic disturbances. Therefore, a transversal homoclinic or heteroclinic point can be predicted.

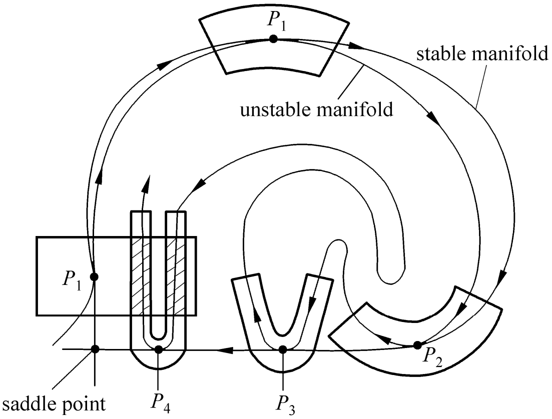

Figure 2.3 Illustration of the Smale horseshoe

Consider a planar nonautonomous system

$$\dot{\boldsymbol{x}} = \boldsymbol{f}(\boldsymbol{x}) + \varepsilon \boldsymbol{g}(\boldsymbol{x}, t) \qquad \boldsymbol{x} \in \mathrm{R}^2 \tag{2.3.4}$$

where ε is a small parameter and the disturbance $\boldsymbol{g}$ is a periodic function with respect to t. Suppose that when $\varepsilon = 0$, the unperturbed system

$$\dot{\boldsymbol{x}} = \boldsymbol{f}(\boldsymbol{x}) \qquad \boldsymbol{x} \in \mathrm{R}^2 \tag{2.3.5}$$

has a saddle point $\boldsymbol{p}_\mathrm{s}$ with a homoclinic orbit $\boldsymbol{x}^\mathrm{h}(t-t_0)$ such that

$$\lim_{t\to\pm\infty} \boldsymbol{x}^\mathrm{h}(t-t_0) = \boldsymbol{p}_\mathrm{s} \tag{2.3.6}$$

in which t_0 is the beginning time that can be an arbitrary real number.

If $\varepsilon \neq 0$ but still sufficiently small, Eq. (2.3.4) exists a unique periodic orbit $\boldsymbol{x}_{\mathrm{s}\varepsilon}(t) = \boldsymbol{p}_0 + \mathrm{O}(\varepsilon)$. Thus its Poincaré map has a unique saddle point $\boldsymbol{p}_{\mathrm{s}\varepsilon} = \boldsymbol{p}_0 + \mathrm{O}(\varepsilon)$. Although the stable and unstable manifolds of $\boldsymbol{p}_{\mathrm{s}\varepsilon}$ no longer coincide, both of them are still sufficiently close to the homoclinic orbit $\boldsymbol{x}^\mathrm{h}(t-t_0)$ for $\varepsilon = 0$. Therefore, the equations of the stable and unstable manifolds can be assumed as

$$\boldsymbol{x}^\mathrm{s}(t,t_0) = \boldsymbol{x}^\mathrm{h}(t-t_0) + \varepsilon \boldsymbol{x}_1^\mathrm{s}(t,t_0) + \mathrm{O}(\varepsilon^2) \tag{2.3.7}$$

$$\boldsymbol{x}^\mathrm{u}(t,t_0) = \boldsymbol{x}^\mathrm{h}(t-t_0) + \varepsilon \boldsymbol{x}_1^\mathrm{u}(t,t_0) + \mathrm{O}(\varepsilon^2) \tag{2.3.8}$$

Equations (2.3.7) and (2.3.8) can also be regarded as the expansions in terms of ε. At time t, the displacement of a point on the stable manifold relative to the point on the unstable manifold is

$$\begin{aligned} \boldsymbol{d}(t,t_0) &= \boldsymbol{x}^\mathrm{s}(t,t_0) - \boldsymbol{x}^\mathrm{u}(t,t_0) \\ &= \varepsilon(\boldsymbol{x}_1^\mathrm{s}(t,t_0) - \boldsymbol{x}_1^\mathrm{u}(t,t_0)) + \mathrm{O}(\varepsilon^2) \end{aligned} \tag{2.3.9}$$

Project $\boldsymbol{d}(t, t_0)$ to the normal $\boldsymbol{N}$ to the a homoclinic orbit of the undisturbed system (2.3.5). Notice that the normal, as shown in Fig. 2.4, is defined by

$$\boldsymbol{N}(t,t_0) = (-f_2(\boldsymbol{x}^\mathrm{h}(t-t_0)), f_1(\boldsymbol{x}^\mathrm{h}(t-t_0))) \tag{2.3.10}$$

where $(f_1, f_2) = \boldsymbol{f}$. One gets

$$d_N(t,\tau) = \boldsymbol{N} \cdot \boldsymbol{d} = \boldsymbol{f} \wedge \boldsymbol{d} = \varepsilon(d_N^\mathrm{s} - d_N^\mathrm{u}) + \mathrm{O}(\varepsilon^2) \tag{2.3.11}$$

where

$$\begin{aligned} d_N^\mathrm{s} &= \boldsymbol{f} \wedge \boldsymbol{x}_1^\mathrm{s} \\ d_N^\mathrm{u} &= \boldsymbol{f} \wedge \boldsymbol{x}_1^\mathrm{u} \end{aligned} \tag{2.3.12}$$

and the wedge product is defined by

$$\boldsymbol{a} \wedge \boldsymbol{b} = a_1 b_2 - a_2 b_1 \tag{2.3.13}$$

for the vectors $\boldsymbol{a} = (a_1, a_2)$ and $\boldsymbol{b} = (b_1, b_2)$. Actually, the wedge product is a vector cross product in which only the magnitude is taken into consideration.

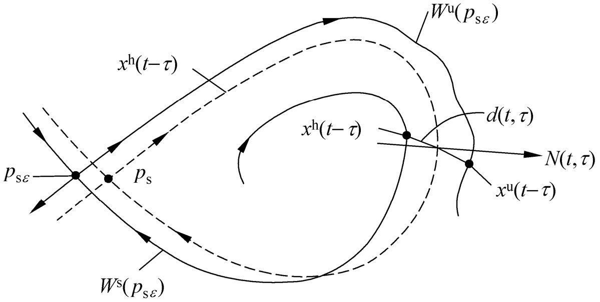

Figure 2.4 Illustration of the derivation of Melnikov's function

Differentiating d_N^s with respect to t yields

$$\dot{d}_N^{\mathrm{s}} = \dot{\boldsymbol{f}} \wedge \boldsymbol{x}_1^{\mathrm{s}} + \boldsymbol{f} \wedge \dot{\boldsymbol{x}}_1^{\mathrm{s}} = \mathbf{D}\boldsymbol{f} \cdot \dot{\boldsymbol{y}}^{\mathrm{h}} \wedge \boldsymbol{x}_1^{\mathrm{s}} + \boldsymbol{f} \wedge \dot{\boldsymbol{x}}_1^{\mathrm{s}} \tag{2.3.14}$$

where the Jacobian $\mathbf{D}\boldsymbol{f}$ is calculated at $\boldsymbol{x}^{\mathrm{h}}$. Substituting Eq. (2.3.7) into Eq. (2.3.4) and neglecting ε^2 and higher order terms in the resulting equation lead to

$$\dot{\boldsymbol{x}}_1^{\mathrm{s}} = \mathbf{D}\boldsymbol{f} \cdot \boldsymbol{x}_1^{\mathrm{s}} + \boldsymbol{g}(\boldsymbol{x}^{\mathrm{h}}(t-t_0),t) \tag{2.3.15}$$

Substituting Eqs. (2.3.7) and (2.3.15) into Eq. (2.14) and omitting ε^2 and higher order terms in the resulting equation give

$$\dot{d}_N^{\mathrm{s}} = \mathbf{D}\boldsymbol{f} \cdot \boldsymbol{f} \wedge \boldsymbol{x}_1^{\mathrm{s}} + \boldsymbol{f} \wedge \mathbf{D}\boldsymbol{f} \cdot \boldsymbol{x}_1^{\mathrm{s}} + \boldsymbol{f} \wedge \boldsymbol{g} \tag{2.3.16}$$

Direct computation of the first two terms on the right hand of Eq. (2.3.16) yields

$$\dot{d}_N^{\mathrm{s}} = \mathrm{tr}\left(\mathbf{D}\boldsymbol{f}\right) \boldsymbol{f} \wedge \boldsymbol{x}_1^{\mathrm{s}} + \boldsymbol{f} \wedge \boldsymbol{g} \tag{2.3.17}$$

Equations (2.3.12) and (2.3.17) mean that

$$\dot{d}_N^{\mathrm{s}} = \mathrm{tr}\left(\mathbf{D}\boldsymbol{f}\right) d_N^{\mathrm{s}} + \boldsymbol{f} \wedge \boldsymbol{g} \tag{2.3.18}$$

Equation (2.3.18) is a first order linear ordinary differential equation of d_N^s, and it can be integrated from τ to $+\infty$ as

$$d_N^{\mathrm{s}}(+\infty,t_0) - d_N^{\mathrm{s}}(t_0,t_0) = \int_{\tau}^{+\infty} \boldsymbol{f} \wedge \boldsymbol{g}\, \mathrm{e}^{-\rightarrow \int_0^{t-t_0} \mathrm{tr}(\mathbf{D}\boldsymbol{f}(\boldsymbol{x}^{\mathrm{h}}(z)))\mathrm{d}z} \mathrm{d}t \tag{2.3.19}$$

Using Eqs. (2.3.12) and (2.3.6) and noticing that $\boldsymbol{p}_{\mathrm{s}}$ is the saddle point, one has

$$d_N^{\mathrm{s}}(+\infty,t_0) = \boldsymbol{f}(\boldsymbol{x}^{\mathrm{h}}(+\infty - t_0)) \wedge \boldsymbol{x}_1^{\mathrm{s}} = \boldsymbol{f}(\boldsymbol{p}_{\mathrm{s}}) \wedge \boldsymbol{x}_1^{\mathrm{s}} = 0 \tag{2.3.20}$$

Hence

$$d_N^{\mathrm{s}}(t_0,t_0)=-\int_{\tau}^{+\infty}\boldsymbol{f}\wedge\boldsymbol{g}\,\mathrm{e}^{-\int_0^{t-t_0}\mathrm{tr}(\mathbf{D}\boldsymbol{f}(\boldsymbol{x}^{\mathrm{h}}(z)))\mathrm{d}z}\mathrm{d}t \tag{2.3.21}$$

A similar procedure yields

$$d_N^{\mathrm{u}}(t_0,t_0)=\int_{-\infty}^{\tau}\boldsymbol{f}\wedge\boldsymbol{g}\,\mathrm{e}^{-\int_0^{t-t_0}\mathrm{tr}(\mathbf{D}\boldsymbol{f}(\boldsymbol{y}^{\mathrm{h}}(z)))\mathrm{d}z}\mathrm{d}t \tag{2.3.22}$$

Based on Eqs. (2.3.11), (2.3.21), and (2.3.22), if one defines the Melnikov function $\mathcal{M}(\tau)$ as

$$\mathcal{M}(t_0)=\int_{-\infty}^{+\infty}\boldsymbol{f}(\boldsymbol{x}^{\mathrm{h}}(t-t_0))\wedge\boldsymbol{g}(\boldsymbol{x}^{\mathrm{h}}(t-t_0),t)\,\mathrm{e}^{-\int_0^{t-t_0}\mathrm{tr}(\mathbf{D}\boldsymbol{f}(\boldsymbol{x}^{\mathrm{h}}(z)))\mathrm{d}z}\mathrm{d}t \tag{2.3.23}$$

then

$$d_N(t_0,t_0)=-\varepsilon\mathcal{M}(t_0)+\mathrm{O}(\varepsilon^2) \tag{2.3.24}$$

The existence of simple zeros of the Melnikov function $\mathcal{M}(t_0)$ indicates that the displacement $\boldsymbol{d}(t_0, t_0)$ vanishes. At a simple zero t_{z}, $\mathcal{M}(t_{\mathrm{z}})\,d_N(t_0,t_0)=0$, but d $\mathcal{M}(t_{\mathrm{z}})/\mathrm{d}t_0\neq 0$. In this case, the stable and unstable manifolds are to intersect transversely to form a transversal homoclinic point.

Equation (2.3.24) can be equivalently written as

$$\mathcal{M}(t_0)=\int_{-\infty}^{+\infty}\boldsymbol{f}(\boldsymbol{x}^{\mathrm{h}}(t))\wedge\boldsymbol{g}(\boldsymbol{x}^{\mathrm{h}}(t),t+t_0)\,\mathrm{e}^{-\int_0^{t}\mathrm{tr}(\mathbf{D}\boldsymbol{f}(\boldsymbol{x}^{\mathrm{h}}(z)))\mathrm{d}z}\mathrm{d}t \tag{2.3.25}$$

If the unperturbed system is Hamiltonian, then $\mathrm{tr}(\mathbf{D}\boldsymbol{f})=0$. Equation (2.3.25) becomes

$$\mathcal{M}(t_0)=\int_{-\infty}^{+\infty}\boldsymbol{f}(\boldsymbol{x}^{\mathrm{h}}(t))\wedge\boldsymbol{g}(\boldsymbol{x}^{\mathrm{h}}(t),t+t_0)\,\mathrm{d}t \tag{2.3.26}$$

2.3.4 Interruptions

The Melnikov theory is of considerable significance because it can be applied to check in specific systems whether the stable and unstable manifolds intersect transversely or not, by a direct calculation of the approximate distance between these manifolds. The Melnikov function is an explicitly computable function that can be evaluated analytically or numerically. The Melnikov theory has been extended to multi-degree-of-freedom systems [18] and infinite-degree-of-freedom systems [19, 20]. A generalized version for Hamiltonian systems with finite degrees-of-freedom will be presented in the next section, and it will be applied in the subsequent chapters.

It should be kept in mind that the Melnikov theory only predicts transverse intersections of stable and unstable manifolds, or the existence of a homoclinic point. Usually, such an intersection yields an invariant set with sensitivity to initial conditions. Not all invariant sets are an attractor, because they may be without attractability. In dissipative systems, all observable chaos, in laboratory experiments or numerical simulations, should be attractor, with significantly large basin of attraction. The collection of initial conditions under which the motion tends toward a given attractor is called a **basin of attraction**. In a more general sense, the range of values of certain system parameters for which the motion tends toward a prescribed attractor is called a basin of attraction in the parameter space. Therefore, in a practical system, the existence of such an invariant set does not imply that chaotic motion is observed.

In addition, not all attractors sensitive to initial conditions represent chaotic motion, because a periodic motion or even an equilibrium position may depend sensitively on initial conditions when there are two or more attractors in a nonlinear system. In this case, the basin boundary is nonsmooth, intertwined and complicated, actually fractal. The transition from one basin of attraction to another is called a **basin boundary**.

In spite of the limitations, the occurrence of transverse intersections of stable and unstable manifolds is a significant hint to the appearance of chaos. The basin boundary is identical to the stable manifold. A homoclinic point means that the stable and unstable manifolds touch an infinite number of times, which leads to an infinite folding of the stable manifold and hence an infinite folding of the basin boundary and the resulting sensitivity to initial conditions.

2.4 Chaos in Hamiltonian Systems

2.4.1 Hamiltonian Systems, Integrability and KAM Theorem

The Hamiltonian formulation is an effective and powerful approach to model and analyze dynamical problems. For a system with n degrees-of-freedom, its motion can be specified by n generalized coordinates $q_i (i = 1,2,\cdots,n)$ and n generalized momenta p_i. All (q_i, p_i) pairs form a $2n$-dimensional phase space $(\boldsymbol{q}, \boldsymbol{p})$. If all actions on the system are derived from a potential function, W. R. Hamilton (in 1834) proposed the following differential equation of motion

$$\begin{aligned} \dot{q}_i &= \frac{\partial \mathcal{H}}{\partial p_i} \\ \dot{p}_i &= -\frac{\partial \mathcal{H}}{\partial q_i} \end{aligned} \qquad (2.4.1)$$

which is called **Hamilton's canonical equations**. In Eq. (2.4.1),

$$\mathcal{H} = \mathcal{H}(\boldsymbol{q}, \boldsymbol{p}, t) \tag{2.4.2}$$

is called the **Hamiltonian**. For a mechanical system, $\mathcal{H}$ is the mechanical energy of the system. If a dynamical system is governed by the canonical equations, it is called a **Hamiltonian system**. Using Eq. (2.4.2), one has

$$\begin{aligned} \frac{\mathrm{d}\mathcal{H}}{\mathrm{d}t} &= \sum_{i=1}^{n}\left(\frac{\partial \mathcal{H}}{\partial q_i}\dot{q}_i + \frac{\partial \mathcal{H}}{\partial p_i}\dot{p}_i\right) + \frac{\partial \mathcal{H}}{\partial t} \\ &= \sum_{i=1}^{n}\left(\frac{\partial \mathcal{H}}{\partial q_i}\frac{\partial \mathcal{H}}{\partial p_i} - \frac{\partial \mathcal{H}}{\partial p_i}\frac{\partial \mathcal{H}}{\partial q_i}\right) + \frac{\partial \mathcal{H}}{\partial t} = \frac{\partial \mathcal{H}}{\partial t} \end{aligned} \tag{2.4.3}$$

Therefore, if the time variable t does not appear in $\mathcal{H} = \mathcal{H}(\boldsymbol{q}, \boldsymbol{p})$ explicitly, then $\mathcal{H}$ is a conserved quantity, a constant during the motion. Such a system is called a **conservative system**. If $\mathcal{H}$ depends on t explicitly, the original $2n$-dimensional phase space can be enlarged into $2(n+1)$-dimensional phase space $(\bar{\boldsymbol{q}}, \bar{\boldsymbol{p}})$ by introducing the $n+1$ generalized coordinate $\bar{q}_{n+1} = t$ and generalized momentum $\bar{p}_{n+1} = -\mathcal{H}$. Then the Hamiltonian of the enlarged system is

$$\bar{\mathcal{H}}(\bar{\boldsymbol{q}}, \bar{\boldsymbol{p}}) = \mathcal{H}(\boldsymbol{q}, \boldsymbol{p}, q_{n+1}) + p_{n+1} \tag{2.4.4}$$

and the corresponding canonical equations are

$$\left.\begin{aligned} \dot{\bar{q}}_i &= \frac{\partial \bar{\mathcal{H}}}{\partial \bar{p}_i} \\ \dot{\bar{p}}_i &= -\frac{\partial \bar{\mathcal{H}}}{\partial \bar{q}_i} \end{aligned}\right. \quad (i = 1, 2, \cdots, n+1) \tag{2.4.5}$$

The construction of the enlarged system means the equivalence of Eqs. (2.4.1) and (2.4.5), while the enlarged system is conservative as its Hamiltonian is explicitly independent of t. Thus all Hamiltonian systems can be equivalently transformed into a conservative one. In the following, only conservative systems will be considered.

A Hamiltonian system can be substantively simplified via an appropriate transform from one set of variables $(\boldsymbol{q}, \boldsymbol{p})$ to some new set $(\boldsymbol{Q}, \boldsymbol{P})$,

$$\begin{aligned} \boldsymbol{Q} &= \boldsymbol{Q}(\boldsymbol{q}, \boldsymbol{p}) \\ \boldsymbol{P} &= \boldsymbol{P}(\boldsymbol{q}, \boldsymbol{p}) \end{aligned} \tag{2.4.6}$$

Equation (2.4.1) is accordingly changed into the form

$$\begin{aligned}\dot{\boldsymbol{Q}} &= \dot{\boldsymbol{Q}}(\boldsymbol{Q},\boldsymbol{P})\\ \dot{\boldsymbol{P}} &= \dot{\boldsymbol{P}}(\boldsymbol{Q},\boldsymbol{P})\end{aligned} \tag{2.4.7}$$

If the structure of Eq. (2.4.1) is still preserved, that is, Eq. (2.4.7) takes the form

$$\left.\begin{aligned}\dot{Q}_i &= \frac{\partial h}{\partial P_i}\\ \dot{P}_i &= -\frac{\partial h}{\partial Q_i}\end{aligned}\right. \quad (i=1,2,\cdots,n) \tag{2.4.8}$$

where $h = h(\boldsymbol{Q}, \boldsymbol{P})$, then the transformation is called a **canonical transformation**. A canonical transformation changes a set of canonical equations into another set of canonical equations. It can be proved that the inverse of a canonical transformation and the composition of canonical transformations are still canonical transformations.

Suppose there are a series of canonical transformations to change variables $(\boldsymbol{q},\boldsymbol{p})$ into variables $(\boldsymbol{I},\boldsymbol{\theta})$, such that the Hamiltonian in the new variables depends only on $\boldsymbol{I}$, and that

$$\mathcal{H} = H(\boldsymbol{I}) \tag{2.4.9}$$

is independent of $\boldsymbol{\theta}$. Then the Hamiltonian equations are

$$\left.\begin{aligned}\dot{I}_i &= -\frac{\partial H}{\partial \theta_i} = 0\\ \dot{\theta}_i &= \frac{\partial H}{\partial I_i} = \varOmega_i(I_1,I_2,\cdots,I_n)\end{aligned}\right. \quad (i=1,2,\cdots,n) \tag{2.4.10}$$

Integration of Eq. (2.4.10) yields

$$\begin{aligned}&I_i(t) = I_i(0)\\ &\theta_i(t) = \varOmega_i(I_1(0),I_2(0),\cdots,I_n(0))t + \theta_i(0)\end{aligned} \tag{2.4.11}$$

where $2n$ constants $\boldsymbol{I}(0)$ and $\boldsymbol{\theta}(0)$ can be determined by initial condition $(\boldsymbol{q}(0),\boldsymbol{p}(0))$. Variables $(\boldsymbol{I},\boldsymbol{\theta})$ are called **action-angle variables**. According to Eq. (2.4.11), the motion of Eq. (2.4.10) can be uniquely specified by n angle variables θ_i. Mathematically, an n-dimensional manifold where the point is specified by n angles is called an ***n*-torus**, denoted as T_n. An 1-torus T_1 is a circle, and 2-torus T_2 is a usual tori, while there is no plot of n-torus T_n for $n \geqslant 3$ in 3-dimensional physical space. Actually, I_i is the n radii of the n-torus. As explained in 2.1.2, if $\boldsymbol{\varOmega}_i$ are incommensurable, that is, there do not exist not all zero integer k_i such that $\sum_{i=1}^{n} k_i \varOmega_i = 0$, then it can be proved that the trajectory winds up on the torus endlessly without closing, and is dense there. The corresponding motion is quasiperiodic. If Ω_i is commensurable, then the trajectory closes on the torus, and the motion is periodic.

Hamiltonian systems expressed in action-angle variables are integrable. Generally, a Hamiltonian with n degree-of-freedom is an **integrable system**, if there exist n independent isolating integrals of motion

$$I_i(\boldsymbol{q},\boldsymbol{p}) = C_i \quad (i = 1, 2, \cdots, n) \tag{2.4.12}$$

where C_i are constants. Functions I_i are independent if the differentials $\mathrm{d}I_i$ are linearly independent. Since n isolating integrals of motion exist, the $2n$ dimensional phase space is confined in an n-dimensional manifold that is homeomorphic to n-tori. The manifold is an invariant torus, because all trajectories starting on it remain there all the time. Hence integrable systems can never be chaotic, and their motion is periodic or quasiperiodic.

In 1892, Poincaré proved that many dynamical systems, including the three-body problem, are not integrable. A system that has fewer constants of motion than degrees-of-freedom is called a **nonintegrable system**. Integrability is an exceptional property for Hamiltonian systems with degrees-of-freedom larger than 2. In fact, integrable systems are so rare that in general it is impossible to approximate a nonintegrable Hamiltonian system by a series of integrable ones. However, there is no direct criterion to determine the integrability. An integrable system is made slightly nonintegrable by adding a small disturbance. Such a system is called **near integrable system**. In terms of action-angle variables, the Hamiltonian of a near integrable system can be written as

$$\mathcal{H}(\boldsymbol{I},\theta) = \mathcal{H}_0(\boldsymbol{I}) + V(\boldsymbol{I},\theta) \tag{2.4.13}$$

where $\mathcal{H}_0$ is integrable and V is sufficiently small. If no disturbance is present, then $V = 0$ and the system is integrable. If $V \neq 0$, the integrability is usually violated.

In 1954, Kolmogorov described the qualitative picture of near integrable systems [21]. Arnol'd and Moser completely proved the conclusion that is known as famous Kolmogorov-Arnol'd-Moser theorem. In the following, KAM theorem is presented without proof, which is outside the scope of this monograph.

KAM theorem: Suppose that Hamiltonian (2.4.13) satisfies the following conditions:

(i) $\mathcal{H}(\boldsymbol{I},\boldsymbol{\theta})$ is a real analytic function on a region Σ_0: $|\mathrm{Im}\boldsymbol{\theta}| \leqslant t$, $|\boldsymbol{I}-\boldsymbol{I}_0| \leqslant s$;

(ii) $\Omega_j = \dfrac{\partial \mathcal{H}_0}{\partial I_j}$ $(j = 1, 2, \cdots, n)$ calculated at I_0 such that $\left|\dfrac{\partial \Omega_j}{\partial I_k}\right| \neq 0$ (nondegeneracy conditions);

(iii) For arbitrary integer vector $\boldsymbol{k} = (k_1, k_2, \cdots, k_n)$ there exist $C(\boldsymbol{\Omega})>0$ and $\mu>n-1$ such that the nonresonance condition holds as follows

$$\left|\sum_{j=1}^{n} k_j \Omega_j\right| \geqslant C\left(\sum_{j=1}^{n}|k_j|\right)^{-\mu} \tag{2.4.14}$$

Then for any $\varepsilon>0$, there is a $\delta=\delta(\varepsilon, C, \mu, s, t)$ such that, if $|V|<\delta$ in Σ_0, the solution to equation

$$\begin{aligned} \dot{\theta}_i &= \frac{\partial \mathcal{H}}{\partial I_i} \\ \dot{I}_i &= -\frac{\partial \mathcal{H}}{\partial \theta_i} \end{aligned} \quad (i=1,2,\cdots,n) \tag{2.4.15}$$

lies on an n-dimensional invariant torus

$$\begin{aligned} \boldsymbol{I} &= \boldsymbol{I}_0 + \Gamma(\Theta) \\ \theta &= \Theta + \Phi(\Theta) \end{aligned} \tag{2.4.16}$$

where Γ and Φ are real analytic functions with period 2π defined on $|\mathrm{Im}\Theta| \leqslant t/2$. The trajectory on the torus is governed by

$$\begin{aligned} I_i(t) &= I_i(0) \\ \Theta_i(t) &= \left.\frac{\partial \mathcal{H}}{\partial I_i}\right|_{I_j(t)=I_j(0)} t + \Theta_i(0) \end{aligned} \tag{2.4.17}$$

The torus is sufficiently close to the torus of the undisturbed system, that is,

$$|\Gamma| + |\Theta| < \varepsilon \tag{2.4.18}$$

The conditions in the KAM theorem require the disturbance leading to the nonintegrability to be sufficiently small, the Hamiltonian to be analytic function, the system to be nondegenerate, and the undisturbed frequencies to be nonresonant, in which the analytical condition and the nondegenerate condition can be technically weakened. Under these conditions, most nonresonant tori survive but may be slightly deformed. Hence the tori exist in the phase space of the disturbed system, and the trajectories wind densely on them. The number of independent frequencies is equal to the number of degrees-of-freedom of the system. Those tori are called **KAM tori**, **KAM surfaces** or **KAM curves**.

2.4.2 Stochastic Layers and Global Chaos

Now consider the resonance of a near integrable Hamiltonian system. In this case, Ω_i is commensurable. The trajectories of Eq. (2.4.1) are periodic orbits on the n-dimensional invariant torus T_n. Since a conservative Hamiltonian always has its energy as its constant of motion, its motion in $2n$-dimensional phase space is confined to a $(2n-1)$-dimensional energy surface after given an initial energy. The intersection of the energy surface and the n-dimensional invariant tori yields a $(2n-2)$-dimensional surface Σ that can serve as a cross section to define a Poincaré map $\boldsymbol{P}_0$. The surface Σ cuts the torus T_n on a level curve Γ. Due to the periodicity of the motion, every point of curve Γ is a k-periodic point of $\boldsymbol{P}_0$ for some integer k. A k-periodic point of a map f is defined as the fixed point of f^k but not the fixed point of f^m for any $m<k$. For the disturbed system (2.4.13), the same surface Σ still defines a Poincaré map $\boldsymbol{P}$, and the change of the level curve Γ reflects deformation of the invariant torus T_n.

Before the discussion of Poincaré map $\boldsymbol{P}$, some basic concepts of Hamiltonian maps need to be presented. A **Hamiltonian map** is a map that conserves volume in the phase space. Hence the determinant of its Jacobian is equal to 1. The Poincaré map of a Hamiltonian system is a Hamiltonian map. Consider a 2-dimensional Hamiltonian map $\boldsymbol{M}$, which can serve as a Poincaré map of a Hamiltonian system with 2 degree-of-freedom. The Hamiltonian system has a 4-dimensional phase space, a 3-demensional energy surface, a 2-dimensional Poincaré section Σ, a 2-dimensional invariant torus T_2, and a 1-dimensional level curve Γ. Suppose z_0 to be a k-periodic point $\boldsymbol{M}$. Then the Jacobian of $\boldsymbol{M}^k$ calculated at z_0 with two eigenvalues λ_1 and λ_2 satisfying $\lambda_1\lambda_2 = 1$ because $\det \mathrm{D}\boldsymbol{M}^k = 1$. Therefore, λ_1 and λ_2 are two real numbers with $0<\lambda_1<1<\lambda_2$ or a pair of complex conjugates with the unit modulus. The periodic point is defined as a hyperbolic point in the first case and an elliptic point in the second case. This conclusion is true for general cases. A periodic point of a Hamiltonian map must be either a hyperbolic point or an elliptic point.

In 1935, based on Poincaré's previous work in 1899, Birkhoff proved the following conclusion: For a sufficiently small disturbance, the level curve Γ breaks up into $2mk$ k-periodic points of Poincaré's map $\boldsymbol{P}$ for some integer m; these periodic points lie near Γ; mk points are hyperbolic and mk points are elliptic. This conclusion is referred as the **Poincare-Birkhoff theorem**. However, the theorem does not specify the value of the integer m.

In the situation described by the Poincaré-Birkhoff theorem, Γ is called a **resonant level curve**, and a certain region around Γ containing the hyperbolic and elliptic points is called a **resonance zone**. Around each elliptic point there is a series of periodic orbits. Any two adjacent hyperbolic points are connected by heteroclinic orbits. If the heteroclinic orbits intersect transversely in a homoclinic point, then, according to the analysis presented in 2.3.2, the transverse heteroclinic point results in an infinitely complicated set of intersections, which are a cause of chaotic behavior. Such a complicated geometrical structure in a Hamiltonian system is called a **stochastic layer**. The regions around the elliptic points bounded by the heteroclinic orbits are called **islands**. Those islands compose an **island chain** if there are several elliptic points. For the situation $mk=3$, Fig. 2.5 shows the breakup of a resonant level curve, and Fig. 2.6 illustrates a stochastic layer.

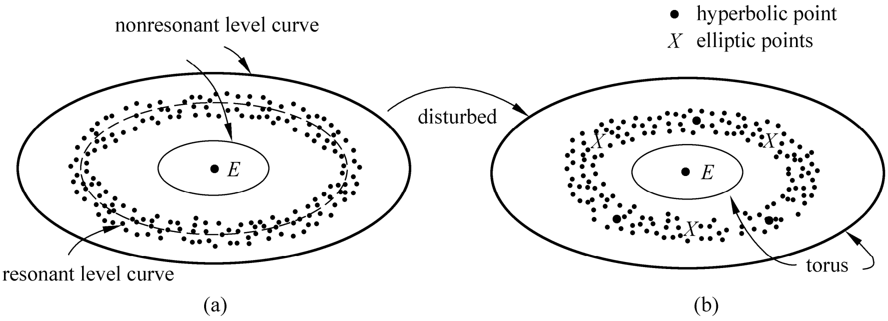

Figure 2.5 A resonant level curve breakup into hyperbolic points (•) and elliptic points (*X*)

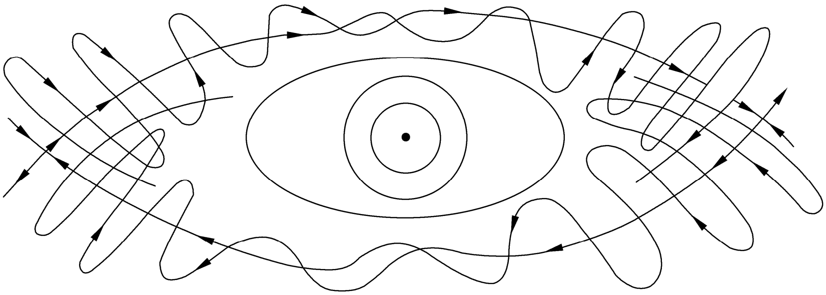

Figure 2.6 A stochastic layer in a Hamiltonian system

The newly formed elliptic points due to the breakup of a resonant level curve are surrounded by smaller level curves. In the resonance, according to the Poincaré-Birkhoff theorem, those curves become a chain of elliptic and hyperbolic points around the earlier elliptic points. This self-similar pattern can repeated infinitely, as depicted in Fig. 2.7, while most of these points on such a small scale that it is difficult to locate them in numerical simulations. Meanwhile, there are nonresonant

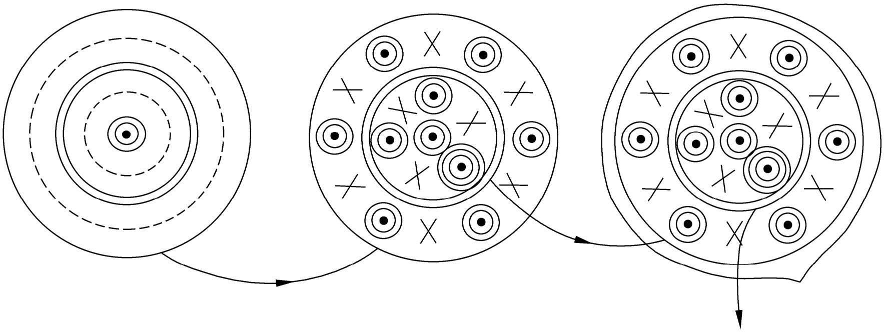

Figure 2.7 Self-similarity near an elliptic point

level curves corresponding to KAM tori, which are preserved, near each elliptic point. Regular behaviors represented by nonresonant level curves coexist with chaos represented by stochastic layers in resonance zones. Thus, in Hamiltonian systems, initial conditions are so crucial that some sets of initial conditions lead to regular motion while others lead to chaos for the same set of system parameters. Therefore there is a complex nested structure of KAM tori surrounded by chains of elliptic and hyperbolic points.

Stochastic layers exist in all nonintegrable Hamiltonian systems. However, for an integrable Hamiltonian system with very small disturbance, the stochastic layers may be so slight that they cannot be found in numerical calculations. Hence only regular motion occurs in the system. With the increase of the disturbance, the system exhibits chaotic behavior manifested in the emergence of observable stochastic layers. According to the KAM theorem, there still exist nonresonant KAM tori that divide the stochastic layers. Irregular motion due to the stochastic layers separated by the KAM tori is called **local chaos**. With further increase of the disturbance, the KAM tori separating the adjacent stochastic layers successively break up and the stochastic layers merge into larger stochastic layers. Thus the thickness of stochastic layers expands with the disturbance. For a sufficiently large disturbance, the resonance zones may overlap so that there is a transverse intersection of stable and unstable manifolds for two hyperbolic points from two different resonance zones. In this case, stochastic layers are no longer confined by KAM tori, and the corresponding behavior is called **global chaos**. In global chaos, there may still exist KAM tori not destroyed by the disturbance. Those tori resemble islands in a chaotic ocean, while there are smaller stochastic layers and KAM tori on the islands. Hence global chaos is a very complicated self-similar structure in the phase space.

2.4.3 Arnol'd Diffusion

The motions of integrable Hamiltonian (2.4.9) are confined in an n-dimensional torus (2.4.11) in a $2n$-dimensional phase space. For a nonintegrable Hamiltonian system, stochastic layers appear near the intersection of $(2n-1)$-dimensional energy surface and $(2n-1)$-dimensional **resonance surface** defined by

$$\sum_{i=1}^{n} k_i \Omega_i(\boldsymbol{J}_0) = 0 \tag{2.4.19}$$

where k_i are integers not all equal to zero. The energy surface and the resonance surface intersect on a surface with the dimension $(2n-1)-1=2n-2$. The stochastic layers around the surface in a space with dimension $(2n-2)+1=2n-1$. Diverse curves form when the resonance surface cuts the energy surface, and these curves interconnect each other to constitute a complex network spreading all over the energy surface. Such a network is called an **Arnol'd web**.

In an m-dimensional space, an $(m-1)$-dimensional closed surface, such as T_{m-1}, can divide the space into two distinct parts, while the closed surface of less than $m-1$ dimension cannot do so. In a Hamiltonian system with n degrees-of-freedom, KAM tori is n-dimensional. Only if $(2n-1)-1=n$ i.e. $n=2$, a KAM torus divides the $(2n-1)$-dimensional energy surface into two disconnected parts, and thus it can isolate stochastic layers. For $n \geqslant 3$, trajectories in gaps between the tori can escape to other regions of the energy surface. Therefore, all stochastic layers on the energy surface are connected into a single complex network, which is the above-mentioned Arnol'd web. The web permeates the entire energy surface, intersecting or lying infinitesimally close to every point. For an initial condition within the web, the subsequent trajectory will eventually intersect every finite region of the energy surface. Such an irregular motion in a higher degree-of-freedom Hamiltonian system is called the **Arnol'd diffusion**. In 1964, Arnol'd proved that stochastic layers merge into a single web in a specific nonlinear Hamiltonian system [22].

The structures of Arnol'd web depends on the energy surface and the resonance surface, which are both dependent on the integrable Hamiltonian and independent of the disturbance. Thus there are global Arnol'd diffusions for arbitrary small disturbances. In the case when the disturbances are large enough to yield observable stochastic layers, the Arnol'd diffusion links together the chaotic regions on all scales. However, the Arnol'd diffusion is usually very slow. In 1977, N. N. Nehoroshev proved a rigorous but overestimated upper bound on the diffusion rate. For an integrable Hamiltonian system with a disturbance of the order ε, the change of system momentum satisfies

$$\|\boldsymbol{p}(t)-\boldsymbol{p}(0)\| < \varepsilon^{a} \qquad t \in \left[0, \frac{1}{\varepsilon}\mathrm{e}^{\varepsilon^{-b}}\right] \tag{2.4.20}$$

where a and b are positive constants determined by the undisturbed integrable Hamiltonian system [23].

2.4.4 Higher-Dimensional Version of Melnikov Theory

The idea of the Melnikov theory can be generalized to higher-dimensional system to develop quantitative methods for handling the Poincare-Birkhoff breakup of resonance zones. In the following, a version [24] proposed by Holmes and Marsden in 1983 is presented without proof. This version will be applied to treat a gyrostat with a rotor in the following chapter.

Consider an $n+1$ degrees-of-freedom integrable Hamiltonian system with small disturbance

$$\begin{aligned}\mathcal{H}(\boldsymbol{\mu},\theta_1,\cdots,\theta_n,I_1,\cdots,I_n;\varepsilon)&=F(\boldsymbol{\mu})+\sum_{i=1}^{n}G_i(I_i)+\varepsilon\mathcal{H}_1(q,p,\theta_1,\cdots,\theta_n,I_1,\cdots,I_n)\\&=\mathcal{H}_0(\boldsymbol{\mu},I_1,\cdots,I_n)+\varepsilon\mathcal{H}_1(q,p,\theta_1,\cdots,\theta_n,I_1,\cdots,I_n)\end{aligned}\tag{2.4.21}$$

where μ are a set of m Lie-Poisson variables, $(\theta_1,\cdots,\theta_n, I_1,\cdots, I_n)$ are action-angle coordinates ($n\geqslant 2$), ε is a small parameter, and $\mathcal{H}_1$ is 2π-periodic in $\theta_1,\cdots,\theta_n$.

For integrable Hamiltonian system with $\varepsilon=0$, $\boldsymbol{\mu}$ is decoupled from action coordinates $(I_1,\cdots, I_n)$. Suppose that F contains a homoclinic (or heteroclinic) orbit $\boldsymbol{\mu}^{\mathrm{h}}$ with energy h_0. The coadjoint orbit containing $\boldsymbol{\mu}^{\mathrm{h}}$ is assumed to be two-dimensional. The saddle points for $\boldsymbol{\mu}^{\mathrm{h}}$ are denoted $\boldsymbol{\mu}_{\pm}$, which may be coincident. Suppose for $j=1,\cdots, n$, $\Omega_j(I_j)=G_j'(I_j)>0$. For a given energy

$$\mathcal{H}(\boldsymbol{\mu},\theta_1,\cdots,\theta_n,I_1,\cdots,I_n;\varepsilon)=h\tag{2.4.22}$$

System (2.4.21) has a reduced integrable part with the Hamiltonian

$$L_0(\boldsymbol{\mu},I_1,\cdots,I_{n-1},h)=G_n^{-1}\left(h-F(\boldsymbol{\mu})-\sum_{j=1}^{n-1}G_j(I_j)\right)\tag{2.4.23}$$

The Hamiltonian system L_0 has two $(n-1)$-parameter family of invariant $(n-1)$-dimensional tori $T_{\pm}(h_1,\cdots, h_{n-1})$ defined by

$$\boldsymbol{\mu}=\boldsymbol{\mu}_{\pm},\ G_j(I_j)=h_j,\ \theta_j=\Omega(G_j^{-1}(h_j))\theta_n+\theta_j(0)\quad(\mathrm{mod}\ 2\pi)\quad(j=1,\cdots,n-1)\tag{2.4.24}$$

where h_j is a constant. Correspondingly, the system for H_0 has two n-parameter family of invariant tori $T_{\pm}(h_1,\cdots,h_n)$. Henceforth the phase constants of integration $\theta_j(0)$ is written as θ_{0j} for $j=1,\cdots,n$. The tori $T_{\pm}(h_1,\cdots, h_{n-1})$ are connected by the n-dimensional homoclinic manifold defined by

$$\boldsymbol{\mu}=\boldsymbol{\mu}^{\mathrm{h}}(\theta_n+\theta_{0n}),\ G_j(I_j)=h_j,\ \theta_j=\Omega(G_j^{-1}(h_j))\theta_n+\theta_{0j}\quad(\mathrm{mod}\ 2\pi)\quad(j=1,\cdots,n-1)\tag{2.4.25}$$

where the phase constant θ_{0n} associated with the reduced degrees-of-freedom appears explicitly. This manifold consists of the coincident stable and unstable manifolds of the tori $T_{\pm}(h_1,\cdots,h_{n-1})$; i.e. $W^{\mathrm{s}}(T_{\pm}(h_1,\cdots,h_{n-1}))=W^{\mathrm{u}}(T_{\pm}(h_1,\cdots,h_{n-1}))$ given by Eq. (2.4.25).

For $\varepsilon\neq 0$, a system defined by Hamiltonian (2.4.21) possesses a Poincaré map $\boldsymbol{P}_{\varepsilon}$ from a piece of $(\boldsymbol{\mu},\theta_1,\cdots\theta_{n-1}, I_1,\cdots, I_{n-1})$ space to itself where θ_n goes through an increment of 2π, starting at some fixed value θ_{n0}. Assume that the constants

$G_i'(I_i) = h_i (i = 1, \cdots, n)$ are chosen so that the disturbed frequencies $\Omega_i(I_i)$ satisfy the nondegeneracy conditions $\Omega_i'(I_i) \neq 0$ and the nonresonance condition (2.4.14) of the KAM theorem. These conditions ensures that the tori $T_{\pm}(h_1, \cdots, h_{n-1})$ perturb to invariant tori $T_{\varepsilon\pm}(h_1, \cdots, h_{n-1})$ for $\boldsymbol{P}_\varepsilon$ with sufficiently small ε. Let $h = h_0 + h_1 + \cdots + h_n$ where $h_i > 0$ $(i = 1, \cdots, n)$ and the undisturbed homoclinic manifold be filled with an n-parameter family of orbits given by

$$(\boldsymbol{\mu}, \theta_1, \cdots, \theta_n, I_1, \cdots, I_n) = (\boldsymbol{\mu}^{\mathrm{h}}(t), \Omega_1(I_1)t + \theta_{01}, \cdots, \Omega_n(I_n)t + \theta_{0n}, I_1, \cdots, I_n) \tag{2.4.26}$$

Pick one such orbit and let $\{\{F, \mathcal{H}_1\}\}$ denote the Lie-Poisson bracket of $F(\boldsymbol{\mu})$ and $\mathcal{H}_1(\boldsymbol{\mu}, \theta_1, \cdots \theta_n, I_1, \cdots, I_n)$ evaluated on this orbit. Similarly, let $\{I_j, H_1\} = -\partial H_1/\partial \theta_j$ $(j = 1, \cdots, n-1)$ be evaluated on this orbit. Define the **Melnikov vector**

$$\begin{aligned}\boldsymbol{\mathcal{M}}(\theta_0) = (&\mathcal{M}_1(\theta_{10}, \cdots, \theta_{n0}, h, h_1, \cdots, h_{n-1}), \cdots, \mathcal{M}_{n-1}(\theta_{10}, \cdots, \theta_{n0}, h, h_1, \cdots, h_{n-1}),\\ &\mathcal{M}_n(\theta_{10}, \cdots, \theta_{n0}, h, h_1, \cdots, h_{n-1}))\end{aligned} \tag{2.4.27}$$

by

$$\begin{aligned}\mathcal{M}_j(\theta_{10}, \cdots, \theta_{n0}, h, h_1, \cdots, h_{n-1}) &= \int_{-\infty}^{+\infty} \{I_j, \mathcal{H}_1\} \mathrm{d}t \quad (j = 1, \cdots, n-1)\\ \mathcal{M}_n(\theta_{10}, \cdots, \theta_{n0}, h, h_1, \cdots, h_{n-1}) &= \frac{1}{\Omega_n} \int_{-\infty}^{+\infty} \{F, \mathcal{H}_1\} \mathrm{d}t\end{aligned} \tag{2.4.28}$$

Assume that the multiply 2π-periodic Melnikov vector $\boldsymbol{\mathcal{M}}$ has at least one simple zero; i.e. there is a point $\boldsymbol{\theta}_0 = (\theta_{10}, \cdots \theta_{n0})$ for which

$$\boldsymbol{\mathcal{M}}(\boldsymbol{\theta}_0) = 0, \det(\mathbf{D}\boldsymbol{\mathcal{M}}(\boldsymbol{\theta}_0)) \neq 0 \tag{2.4.29}$$

where $\mathbf{D}\boldsymbol{\mathcal{M}}$ is the $n \times n$ matrix of partial derivatives of $\mathcal{M}_1, \cdots, \mathcal{M}_n$ with respect to $\theta_{10}, \cdots \theta_{n0}$, the initial phases of the orbit. Under these assumptions, Holmes and Marsden demonstrated that, for sufficiently small ε, the disturbed stable and unstable manifolds $W^{\mathrm{s}}(T_{\varepsilon\pm})$ and $W^{\mathrm{u}}(T_{\varepsilon\pm})$ of the disturbed tori $T_{\varepsilon\pm}$ intersect transversely.

References

[1] Moon FC. *Chaotic and Fractal Dynamics*: *An Introduction for Applied Scientists and Engineers*. New York: John Wiley & Sons, 1992

[2] Nayfeh AH, Balachandran B. *Applied Nonlinear Dynamics: Analytical, Computational, and Experiment Methods*. New York: John Wiley & Sons, 1995

[3] Thompson JMT, Stewart HB. *Nonlinear Dynamics and Chaos*: *Geometrical Methods for Engineers and Scientists* (2nd edn.). New York: John Wiley & Sons, 2002

[4] Ott E. *Chaos in Dynamical Systems* (2nd edn.). Cambridge: Cambridge University Press, 2002

[5] Wiggins S. *Introduction to Applied Nonlinear Dynamical Systems and Chaos* (2nd edn.). Berlin: Springer-Verlag, 2003

[6] Chen LQ, Liu YZ. *Nonlinear Dynamics* (2nd edn.). Beijing: Higher Education Press, 2008 (in Chinese)

[7] Feigenbaum MJ. Quantitative universality for a class of nonlinear transformations. *Journal of Statistical Physics*, 1978, 19, 25-52

[8] Pomeau Y, Manneville P. Intermittent transition to turbulence in dissipative dynamical systems. *Communications in Mathematical Physics*, 1980, 74, 189-197

[9] Ruelle D, Takens F. On the nature of turbulence. *Communications in Mathematical Physics*, 1971, 20, 167-192

[10] Newhouse SE, Ruelle D, Takens F. Occurrence of strange axiom A attractors near quasiperiodic flows on T^m, $m \geqslant 3$. *Communications in Mathematical Physics*, 1978, 64, 35-40

[11] Swinney HL, Gollub JP. The transition to turbulence. *Physics Today*, 1978, 31, 41-49

[12] Feigenbaum MJ, Kadanoff LP, Shenker SJ. Quasiperiodicity in dissipative systems: a renormalization group analysis. *Physics D*, 1982, 5, 370-386

[13] Grebogi C, Ott E, Yorke JA. Are three-frequency quasiperiodic orbits to be expected in typical dynamical systems? *Physical Review Letters*, 1983, 51, 339-342

[14] Grebogi C, Ott E, Yorke JA. Crises, sudden changes in chaotic attractors and transient chaos. *Physics D*, 1983, 7, 181-200

[15] Cooley TW, Tukey JW. An algorithm for the machine calculations of complex Fourier series. *Mathematics of Computation*, 1965, 19, 297-301

[16] Melnikov VK. On the stability of the center for time periodic perturbations. *Transactions of Moscow Mathematical Society*, 1963, 12, 1-57

[17] Smale S. *The Mathematics of Time: Essays on Dynamical Systems, Economic Processes, and Related Topics*. Berlin: Springer-Verlag, 1980

[18] Wiggins S. *Global Bifurcations and Chaos: Analytical Methods*. Berlin: Springer-Verlag, 1988

[19] Mclaughlin D W, Shatah J. Melnikov analysis for Pde's. *Lectures in Applied Mathematics*, 1996, 31, 51-100

[20] Guo BL, Gao P, Chen HL. *Near Integrable Infinite-Dimensional Systems*. Beijing: Defense Industry Press, 2004 (in Chinese)

[21] Kolmogorov AN. Preservation of conditionally periodic movements with small change in the Hamiltonian function. *Dokl. Akad. Nauk SSSR*, 1954, 98, 525-530 (in Russian)

[22] Arnol'd VI. Instability of dynamical systems with several degrees of freedom. *Soviet Mathematics*, 1964, 5, 581-585

[23] Nekhoroshev NN. An exponential estimate of the time of stability of nearly-integrable Hamiltonian systems. *Russian Mathematical Surveys*, 1977, 32(6), 1-65

[24] Holmes PJ, Marsden JE. Horseshoes and Arnold diffusion for Hamiltonian systems on Lie groups. *Indiana University Mathematics Journal*, 1983, 32, 273-310

Chapter 3 Chaos in Planar Attitude Motion of Spacecraft

Abstract The chaos of spacecraft in planar attitude motion is discussed in this chapter. A rigid-body spacecraft in elliptic orbit considering the gravitational and damping torque is discussed, and the Melnikov's theory is applied to predict the transverse heteroclinic point. The numerical simulations and Poincaré maps are performed to confirm the existence of chaos. The same methods are used to analyze the motion of a tethered satellite in circular orbit considering the gravitational torque and the elastic deformation of the tether, as well as a magnetic rigid spacecraft in elliptic orbits under the action of gravitational and magnetic field of the Earth. The numerical results not only confirm the existence of chaotic motion, but also serve as examples of geometrical structure of chaos, routes to chaos, and numerical identification of chaos.

Keywords planar attitude motion, rigid-body spacecraft, tethered satellites, Melnikov theory, routes to chaos, Poincaré map, Lyapunov exponents, power spectra

This chapter deals with chaos in planar attitude motion of spacecraft. The models of spacecraft treated here are rigid-body spacecraft in elliptic orbits and tethered satellites in circular orbits in the gravitational field of the Earth, as well as magnetic rigid spacecraft in circular and elliptic orbits in the gravitational and magnetic field of the Earth. For each model, previous related research results are summarized to present the necessary background, the governing equations are derived from spacecraft dynamics surveyed in chapter 1, the Melnikov theory introduced in Section 2.3 is applied to predict transverse heteroclinic points, and numerical simulations are performed employing methods described in Sections 2.1 and 2.2. The computations not only confirm the existence of chaotic motion, but also demonstrate the transition from periodic motion to chaos. Actually, these numerical results can also serve as examples of geometrical structure of chaos, routes to chaos, and numerical identification of chaos.

3.1 Rigid Spacecraft in an Elliptic Orbit

3.1.1 Introduction

Since 1989 [1-3], much work has been done on the simplest spacecraft model with chaotic behaviors, the planar libration of a rigid body spacecraft in an elliptic orbit in the gravitational field of the Earth. If no disturbances are taken into consideration, the motion is governed by Eq. (1.3.26). If the disturbances are modeled, there will be additional small terms in the governing equation. Those disturbances include atmosphere resistance [2, 4], internal damping [4], tidal moments [5-7], Earth oblateness [3], the Earth magnetic field, third body gravitation [5, 6, 8-12], the solar-radiation pressure [12], and the control inputs [13-15]. The interaction of the magnetic field will be treated in Section 3.4.

For the cases without any disturbances, Gouliaev, Zubritska and Koshkin constructed the universal sequences of the period-doubling bifurcations for the periodic attitude motion generated from the stable state [1]. They also studied the case generated from the unstable state [16]. Gouliaev and Zavrazhina further built the scaling function to describe the spacecraft phase trajectory evolution at transition to chaos [17]. Tong and Rimrott used the Melnikov method to show that chaos occurs for all values of the system parameters and then numerically studied the dynamics for a range of orbital eccentricities and inertia ratios [18]. Karasopoulos and Richardson showed bifurcation diagrams to reveal the dependence on eccentricity, especially the transition to chaos with increasing eccentricity [19]. Teofilatto and Graziani used the Melnikov method to explain the transition from regular to chaos and numerically documented the overlapping of resonances arising both for nearly circular and highly eccentric orbits [20]. Kirchgraber, Manz, Stoffer employed “shadowing”, a mathematical technique, to prove rigorously the existence of chaos in amplitude motion of a dumbbell spacecraft [21].

There are also some investigations on the planar libration of a rigid body spacecraft in an elliptic orbit under certain disturbances. Considering atmosphere resistance, Seisl and Steindl applied the Melnikov method to present the condition of appearing chaos confirmed via numerical simulations [2]. Koch and Bruhn studied a nonspherical spacecraft whose center of mass moves in an elliptic orbit around an oblate axially symmetric central body, and used the Melnikov method to reveal that the attitude motion is chaotic for all values of the orbital eccentricity and the oblateness of the central body [3]. Chen and Liu considered both atmosphere resistance and internal damping and derived the analytical condition of occurring chaos from the Melnikov method [4]. Beletsky, Pivovarov and Starostin treated tidal moments as a dissipative factor and performed numerical simulations to explain the capture of natural celestial bodies in resonance rotation modes [6]. Khan, Sharma and Saha considered the effects of tidal moments via the Melnikov method, and established the condition of occurring chaos [7]. Beletsky, Pivoarov and Starostin also investigated numerically chaotic attitude motion of a celestial body in gravitational field of two centers, assuming that the body moves in a circular orbit [6]. Ashenberg extended the investigation to the global dynamics in the elliptic orbit [9]. Bhardwaj and Bhatnagar applied the Melnikov method to a satellite in an elliptical orbit under the influence of third body torque and used the Chrikov criterion [22] to estimate the half-width of the chaotic separatrix [10]. Bhardwaj and Tuli presented graphically Melnikov's function in the Earth-Moon-Artificial Satellite (1958 B2 Vanguard 1) System [11]. Mehra and Bhatnagar considered both solar radiation pressure and 3rd body torque via the Melnikov analysis [12]. Gray and Stabb introduced damping and other effects to Eq. (1.3.26) through the addition of proportional-integral-derivative control, and employed a generalization of the Melnikov method to systems with slowly-varying parameters [45] to obtain the surface defining the boundary between chaotic and regular motion in physical and control parameters [13, 14]. The outcomes were compared with numerical results [15].

In this section, planar libration of a rigid-body spacecraft in an elliptic orbit with air drag and internal damping will be considered. The disturbing terms are added into the governing equation. The Melnikov analysis is performed to derive the condition of transverse heteroclinic points. Some mathematical details are included to demonstrate the application of the Melnikov theory. Numerical examples with periodic motion and chaotic motions are presented.

3.1.2 Dynamical Model

As shown in Fig. 3.1, an arbitrarily shaped rigid body spacecraft, whose principal inertia moments are A, B and C, moves in an elliptic orbit with one principal axis z normal to the orbital plane XY. Without loss of generality, suppose that $B>A$. Denote that φ is the libration angle in the orbital plane as measured from the local vertical, ν is the position angle of the spacecraft in its orbit as measured from perigee, r is the distance between the spacecraft mass center and the Earth mass center, μ is the gravitational attraction constant of the Earth. Assume that the internal

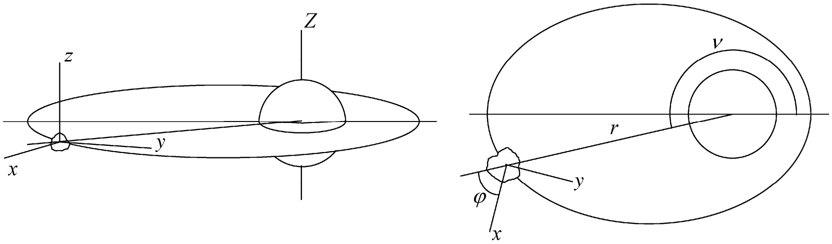

Figure 3.1 Planar motion of spacecraft in an elliptic orbit

damping and the atmosphere resistance are proportional to angular velocity and to the quadratic of angular velocity respectively, whose coefficients are γ and c.

Projection of the Euler equation in the z-direction leads to

$$\frac{\mathrm{d}}{\mathrm{d}t}\left(\frac{\mathrm{d}\nu}{\mathrm{d}t}+\frac{\mathrm{d}\varphi}{\mathrm{d}t}\right)=\frac{3\mu}{Cr^3}(B-A)\cos\varphi(-\sin\varphi)-c\frac{\mathrm{d}\varphi}{\mathrm{d}t}\left|\frac{\mathrm{d}\varphi}{\mathrm{d}t}\right|-\gamma\frac{\mathrm{d}\varphi}{\mathrm{d}t} \tag{3.1.1}$$

The orbital motion and the attitude motion are assumed to be decoupled. Thus the spacecraft moves in the Keplerian orbit defined by Eq. (1.3.24). Substitution of Eqs. (1.3.24) and (1.3.25) into Eq. (3.1.1) yields

$$\ddot{\varphi}-\frac{2e\sin\nu(1+\dot{\varphi})}{1+e\cos\nu}+\frac{\kappa\sin 2\varphi}{1+e\cos\nu}+c\dot{\varphi}|\dot{\varphi}|+\frac{\gamma\dot{\varphi}}{(1+e\cos\nu)^2}=0 \tag{3.1.2}$$

where e is the orbit eccentricity, $\kappa = 3(B-A)/(2C)$, and the over-dot denotes the derivative with respect to the position angle ν.

3.1.3 Melnikov Analysis

Since e, c, and γ are all small, introduce a dimensionless small parameter ε $(0<\varepsilon\ll 1)$ such that $e=\varepsilon e_1$, $c=\varepsilon c_1$, $\gamma=\varepsilon\gamma_1$. When the terms higher than second order of ε are omitted the Eq. (3.1.2) becomes an integrable Hamiltonian system under small perturbations

$$\ddot{\varphi}+\kappa\sin 2\varphi=\varepsilon\left[2e_1\sin\nu(1+\dot{\varphi})+e_1\kappa\cos\nu\sin 2\varphi-c_1\dot{\varphi}|\dot{\varphi}|-\gamma_1\dot{\varphi}\right] \tag{3.1.3}$$

If $\varepsilon = 0$, Eq. (3.1.3) reduces to the unperturbed planar Hamiltonian system, which is essentially the same as Eq. (1.3.15),

$$\ddot{\varphi}+\kappa\sin 2\varphi=0 \tag{3.1.4}$$

with first integral of motion given by Eq. (1.3.16)

$$\frac{1}{2}\dot{\varphi}^2+\kappa\sin^2\varphi=C_0 \tag{3.1.5}$$

where C_0 is a constant. When $C_0=\kappa$, Eq. (3.1.5) has two hyperbolic saddle points $(\pm\pi/2,\ 0)$, whose unstable manifolds and stable manifolds constitute a heteroclinic cycle defined by

$$\frac{1}{2}\left(\frac{\mathrm{d}\varphi}{\mathrm{d}\nu}\right)^2+\kappa\sin^2\varphi=\kappa \tag{3.1.6}$$

Suppose that $\varphi(0)=0$. Then $\dot{\varphi}(0)=\pm\sqrt{2\kappa}$. Integration of Eq. (3.1.6) leads to

$$\int_0^{\varphi} \frac{\mathrm{d}\varphi}{\pm\sqrt{\kappa-\kappa\sin^2\varphi}} = \nu \tag{3.1.7}$$

Evaluation of the finite integral in Eq. (3.1.7) and rearrangement of terms in the resulting equation yields

$$\varphi_{\pm}(\nu) = \pm\arcsin(\mathrm{th}(\sqrt{2\kappa}\nu)) \tag{3.1.8}$$

Therefore the heteroclinic orbits $\varGamma^{\pm}$ started at $(0, \pm\sqrt{2\kappa})$ are

$$(\varphi_{\pm}(\nu), \dot{\varphi}_{\pm}(\nu)) = (\pm\arcsin(\mathrm{th}(\sqrt{2\kappa}\nu)), \pm\sqrt{2\kappa}\,\mathrm{sech}(\sqrt{2\kappa}\nu)) \tag{3.1.9}$$

For $\varepsilon \neq 0$, Eq. (3.1.3) can be cast into the form of Eq. (2.3.4) with

$$\begin{gathered}
\boldsymbol{x} = \begin{pmatrix} \varphi \\ \dot{\varphi} \end{pmatrix}, \quad \boldsymbol{f}(\boldsymbol{x}) = \begin{pmatrix} \dot{\varphi} \\ \kappa\sin 2\varphi \end{pmatrix} \\
\boldsymbol{g}(\boldsymbol{x}, \nu) = \begin{pmatrix} 0 \\ 2e_1\sin\nu(1+\dot{\varphi}) + e_1\kappa\cos\nu\sin 2\varphi - c_1\dot{\varphi}|\dot{\varphi}| - \gamma_1\dot{\varphi} \end{pmatrix}
\end{gathered} \tag{3.1.10}$$

The unperturbed system (3.1.4) is Hamiltonian, and thus tr(**D***f*) = 0. Application of Eq. (2.3.26) yields

$$\begin{aligned}
\mathcal{M}_{\pm}(\nu_0) = \int_{-\infty}^{+\infty} \big[& 2e_1\sin(\nu+\nu_0)(1+\dot{\varphi}_{\pm}(\nu)) + e_1\kappa\cos(\nu+\nu_0)\sin 2\varphi_{\pm}(\nu) \\
& -c_1\dot{\varphi}_{\pm}(\nu)|\dot{\varphi}_{\pm}(\nu)| - \gamma_1\dot{\varphi}_{\pm}(\nu)\big]\dot{\varphi}_{\pm}(\nu)\,\mathrm{d}\nu
\end{aligned} \tag{3.1.11}$$

Notice that the integral of an odd function over a symmetrical interval is zero. Equation (3.1.11) can be simplified to

$$\mathcal{M}_{\pm}(\nu_0) = 2e_1 I_1\sin\nu_0 + 2e_1 I_2\sin\nu_0 + e_1\kappa I_3\sin\nu_0 - c_1 I_4 - \gamma_1 I_5 \tag{3.1.12}$$

where

$$I_1 = \int_{-\infty}^{+\infty} \cos\nu\dot{\varphi}_{\pm}(\nu)\,\mathrm{d}\nu \tag{3.1.13}$$

$$I_2 = \int_{-\infty}^{+\infty} \cos\nu\dot{\varphi}_{\pm}^{\,2}(\nu)\,\mathrm{d}\nu \tag{3.1.14}$$

$$I_3 = \int_{-\infty}^{+\infty} \sin\nu\sin 2\varphi_{\pm}(\nu)\dot{\varphi}_{\pm}(\nu)\,\mathrm{d}\nu \tag{3.1.15}$$

$$I_4 = \int_{-\infty}^{+\infty} \dot{\varphi}_{\pm}^{\,2}(\nu)|\dot{\varphi}_{\pm}(\nu)|\,\mathrm{d}\nu \tag{3.1.16}$$

$$I_5 = \int_{-\infty}^{+\infty} \dot{\varphi}_{\pm}^{\,2}(\nu)\,\mathrm{d}\nu \tag{3.1.17}$$

Substitution of Eq. (3.1.9) into Eqs. (3.1.13)-(3.1.15) and application of the theorem of residues to suitably constructed contours for I_1, I_2, and I_3 yield

$$I_1 = \pm\pi\,\mathrm{sech}\frac{\pi}{2\sqrt{2K}} \tag{3.1.18}$$

$$I_2 = \pi\,\mathrm{csch}\frac{\pi}{2\sqrt{2K}} \tag{3.1.19}$$

$$I_3 = -\frac{1}{4}\pi\,\mathrm{csch}\frac{\pi}{2\sqrt{2K}} \tag{3.1.20}$$

Application of Eq. (3.1.6) and the change of variable in I_4 and I_5 give

$$\begin{aligned} I_4 &= \int_{-\frac{\pi}{2}}^{\frac{\pi}{2}} \dot{\varphi}_\pm \left|\dot{\varphi}_\pm\right| \mathrm{d}\varphi_\pm = \pm\int_{\mp\frac{\pi}{2}}^{\pm\frac{\pi}{2}} \sqrt{2\kappa(1-\sin^2\varphi_\pm)}\left|\sqrt{2\kappa(1-\sin^2\varphi_\pm)}\right| \mathrm{d}\varphi_\pm \\ &= 2\kappa\int_{-\frac{\pi}{2}}^{\frac{\pi}{2}} \cos^2\varphi_\pm\,\mathrm{d}\varphi_\pm = \kappa\pi \end{aligned} \tag{3.1.21}$$

$$I_5 = \int_{\mp\frac{\pi}{2}}^{\pm\frac{\pi}{2}} \dot{\varphi}_\pm\,\mathrm{d}\varphi_\pm = \pm\int_{\mp\frac{\pi}{2}}^{\pm\frac{\pi}{2}} \sqrt{2\kappa(1-\sin^2\varphi_\pm)}\,\mathrm{d}\varphi_\pm = \sqrt{2\kappa}\int_{-\frac{\pi}{2}}^{\frac{\pi}{2}} \cos\varphi_\pm\,\mathrm{d}\varphi_\pm = 2\sqrt{2\kappa}\,\pi \tag{3.1.22}$$

Therefore, Eq. (3.1.11) becomes

$$\mathcal{M}_\pm(\nu_0) = \frac{\pi}{2}e_1\left(\mp 4\,\mathrm{sech}\frac{\pi}{2\sqrt{2\kappa}} + 3\,\mathrm{csch}\frac{\pi}{2\sqrt{2\kappa}}\right)\sin\nu_0 - \pi c_1\kappa - 2\sqrt{2\kappa}\pi\gamma_1 \tag{3.1.23}$$

If both $\mathcal{M}_+(\nu_0)$ and $\mathcal{M}_-(\nu_0)$ have simple zeros, then there exists a transverse heteroclinic point in the Poincaré map of Eq. (3.1.2). Notice $|\sin\nu_0| \leqslant 1$, if and only if

$$e > \frac{2c\kappa + 4\sqrt{2\kappa}\gamma}{\left|3\,\mathrm{csch}\frac{\pi}{2\sqrt{2\kappa}} - 4\,\mathrm{sech}\frac{\pi}{2\sqrt{2\kappa}}\right|} \tag{3.1.24}$$

Thus the transverse heteroclinic point exists.

3.1.4 Numerical Simulations

Fix $\kappa = 0.75$, $\gamma = 0.05$, and $c = 0.04$ in Eq. (3.1.2). Varying e may result in periodic or chaotic motion. For example, If e is very small, the attitude motion is periodic The case with $e = 0.080$ is shown in Fig. 3.2. The attitude motion chaotic motion appears if $e = 0.085$, and the time history and the phase trajectory are separately shown in Fig. 3.3.

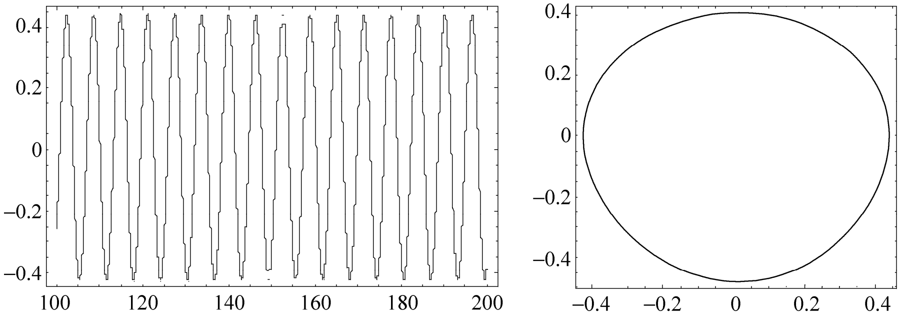

Figure 3.2 Periodic attitude motion of a rigid spacecraft in an elliptic orbit

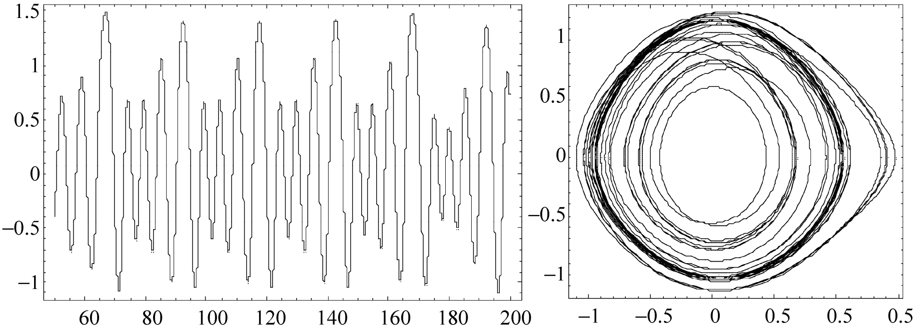

Figure 3.3 Chaotic attitude motion of a rigid spacecraft in an elliptic orbit

3.2 Tethered Satellite Systems

3.2.1 Introduction

A system of two or more subsatellites connected by a long cable is called a tethered satellite system. Tethered satellite systems have many applications in space exploration and development because tethers can be used to construct large-scale space structures. The study of the motion of tethered satellite systems is a challenging new field in spacecraft dynamics [23].

In 1993, Nixon and Misra first considered the possibility of chaotic motion in a two-body tethered satellite system with a rigid tether [24]. For a two-body tethered satellite system moving in a circular orbit, Peng and Liu applied the Melnikov method to predict chaos and performed numerical simulations to demonstrate periodic and chaotic motions in the case of decoupled longitudinal tether vibration, and also studied numerically the coupled case [25]. On the assumption that the center moves in an elliptic orbit and the tether is an ideally flexible mass-less inextensible thread, Béda numerically studied a two-body tethered satellite system subjected to the aerodynamical forces, and found chaotic regions in the parameter space [26]. For a linear spring connected two-body satellite system moving in an elliptical orbit, Fujji and Ichiki used Poincaré maps, bifurcation diagrams, and maximum Lyapunov exponents to demonstrate that chaos occurs for low tether elasticity and large orbit eccentricity [27]. For viscoelastically tethered satellite systems with two stable radial and two unstable tangent-to-orbit equilibria, Steiner employed the finite-element method to show numerically that asymptotic behavior of the transient chaotic motion strongly depended on the choice of initial conditions and that final equilibria on which it settled down are unpredictable for initial conditions near an unstable equilibrium [28, 29]. Beletsky and Pivovarov investigated numerically a tethered satellite system acted upon by gravitational and aerodynamic forces, and found that the aero-gradient effect may result in strong spinup of the system and the orbit eccentricity may lead to chaotic motion [30]. Based on the equations governing the three-dimensional motion of a two-body satellite system, Misra, Nixon and Modi observed numerically the existence of both regular and chaotic regions in the planar system for only elliptic orbits, but in the case of 3-dimensional motion for both circular and elliptic orbits they found that the size of the chaotic region grows with eccentricity, and in the 3-dimensional motion circular orbit case, it grows with increasing values of the Hamiltonian [31]. Takeichi, Natori and Okuizumi numerically simulated dynamic behavior of a tethered system with multiple subsatellites subjected to both atmospheric drag and changes of gravity gradient in elliptic orbits [32].

This section is devoted to chaotic attitude motion of a tethered satellite system. A dynamical model is developed on the assumption that the longitudinal vibration of tether is small and uncoupled from the attitude motion. The coupled model is also derived from the Hamiltonian equation. The Melnikov theory is applied to the uncoupled case. Numerical simulations are performed for both models.

3.2.2 Dynamical Models

Assume that each segment of a tethered satellite system is simplified as a mass point moving synchronously in a circular orbit, and the tether is stretched as a straight line as shown in Fig. 3.4.

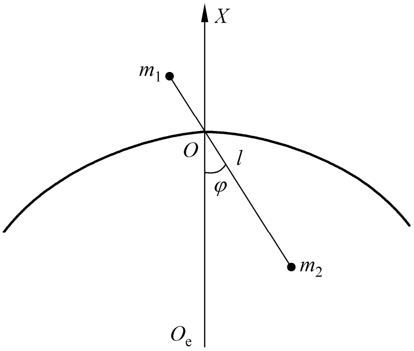

Figure 3.4 Tethered satellite

Let $m_i (i = 1,2)$ be the masses of segments and l be the length of the tether. Then the distance l_i of each segment $m_i (i = 1,2)$ to mass center O can be derived as

$$l_1 = \left(\frac{m_2}{m_1 + m_2}\right) l, \quad l_2 = \left(\frac{m_1}{m_1 + m_2}\right) l \tag{3.2.1}$$

Define the body-fixed frame O-xyz with Ox along the tether from m_2 to m_1, and Oz coincident with the normal axis of the orbital plane. Then the principal moments of inertia of the satellite with the mass-less tether about point O are

$$A = 0, \ B = C = m^* l^2 \tag{3.2.2}$$

where $m^* = m_2 m_1/(m_2 + m_1)$. The dynamical equation of planar libration with swing angle φ can be derived from the theorem of angular momentum (1.3.2).

The elastic deformation of the tether is specified by its length $l(t)$, which is a function of time. The gravitational torque on the tethered satellite is given by Eq. (1.3.13). Then one obtains

$$\ddot{\varphi} + \left(\frac{2\dot{l}}{l}\right)(\dot{\varphi} + \omega_c) + \left(\frac{3\omega_c^2}{2}\right)\sin 2\varphi = 0 \tag{3.2.3}$$

If the variation of the tether length is small, the coupling between the attitude motion and the longitudinal vibration of tether can be neglected. Thus it can be assumed that the longitudinal vibration of tether is described by

$$l = l_0 + \Delta l \cos \omega_0 t \tag{3.2.4}$$

where l_0 is the original length of the tether, Δl and ω_0 are the amplitude and the frequency of its vibration, respectively. Introduce the dimensionless time τ, and dimensionless parameters δ and ε as

$$\tau=\omega_0 t,\ \delta=\frac{\omega_c}{\omega_0},\ \varepsilon=\frac{\Delta l}{l_0} \tag{3.2.5}$$

Equation (3.2.3) can be cast into the dimensionless form as

$$\ddot{\varphi}-2\varepsilon(\dot{\varphi}+\delta)\sin\tau+\frac{3}{2}\delta^2\sin 2\varphi=0 \tag{3.2.6}$$

where the derivative is with respect to the dimensionless time.

When the longitudinal displacement of the tether is quite large, the swing and the longitudinal vibration are strongly coupled, and the system should be regarded as possessing two degrees of freedom. The kinetic energy of the system is

$$T=\frac{1}{2}\left[m^*\left(\dot{l}^2+l^2\dot{\varphi}^2\right)+\left(m_1+m_2\right)v_c^2\right] \tag{3.2.7}$$

The potential energy of gravitational field is derived from Eq. (1.3.40) in which

$$\alpha_1=\cos\varphi,\ \alpha_2=\sin\varphi,\ \alpha_3=0 \tag{3.2.8}$$

as

$$V_1=\frac{3}{2}\omega_c^2 m^* l^2\sin^2\varphi \tag{3.2.9}$$

Denote the coefficient of tether stiffness by K, then the potential energy of the elastic tether deformation is

$$V_2=\frac{1}{2}K(l-l_0)^2 \tag{3.2.10}$$

According to Eq. (1.3.41), omitting the constant terms and dividing it by $m^*\omega_0^2 l_0$, one obtains the normalized Hamiltonian of the system as

$$H=\frac{1}{2}\left[\left(\frac{\mathrm{d}\xi}{\mathrm{d}\tau}\right)^2+(1+\xi)\left(\frac{\mathrm{d}\varphi}{\mathrm{d}\tau}\right)^2+3\delta\xi^2\sin^2\varphi\right]+\frac{1}{2}k\xi^2 \tag{3.2.11}$$

where k is the dimensionless stiffness coefficient and ξ is a new variable defined as

$$k=\frac{K}{m^*\omega_0^2 l_0},\ \xi=\frac{l-l_0}{l_0} \tag{3.2.12}$$

The dynamical equations of the system can be written in canonical form, where the generalized momenta are defined as

$$p_\varphi=(1+\xi)\frac{\mathrm{d}\varphi}{\mathrm{d}\tau},\ p_\xi=\frac{\mathrm{d}\xi}{\mathrm{d}\tau} \tag{3.2.13}$$

Thus the Hamiltonian equations yield

$$\begin{aligned}
&\frac{\mathrm{d}\varphi}{\mathrm{d}\tau}=\frac{\partial\mathcal{H}}{\partial p_\varphi}=p_\varphi\\
&\frac{\mathrm{d}p_\varphi}{\mathrm{d}\tau}=-\frac{\partial\mathcal{H}}{\partial\varphi}=-\frac{3}{2}\delta\xi^2\sin 2\varphi\\
&\frac{\mathrm{d}\xi}{\mathrm{d}\tau}=\frac{\partial\mathcal{H}}{\partial p_\xi}=p_\xi\\
&\frac{\mathrm{d}p_\xi}{\mathrm{d}\tau}=-\frac{\partial\mathcal{H}}{\partial\xi}=-\frac{1}{2}\left(\frac{p_\varphi}{1+\xi}\right)^2-3\delta\xi\sin^2\varphi-k\xi
\end{aligned}\tag{3.2.14}$$

3.2.3 Melnikov Analysis of the Uncoupled Case

Equation (3.2.6) is established on the supposition that Δl is small. Thus ε, defined by Eq. (3.2.5), can be regarded as a small parameter. Consequently, Eq. (3.2.6) is an integrable Hamiltonian system experiencing small perturbations

$$\ddot{\varphi}+\frac{3}{2}\delta^2\sin 2\varphi=2\varepsilon(\dot{\varphi}+\delta)\sin\tau\tag{3.2.15}$$

If $\varepsilon = 0$, Eq. (3.2.15) becomes Eq. (3.1.4), in which $\kappa = 3\delta^2/2$. The unperturbed system has two hyperbolic saddle points (±π/2, 0) connected by the heteroclinic orbits $\Gamma^{\pm}$ obtained from Eq. (3.1.9).

$$(\varphi_\pm(\tau),\dot{\varphi}_\pm(\tau))=(\pm\arcsin(\mathrm{th}(\sqrt{3}\delta\tau)),\pm\sqrt{3}\delta\,\mathrm{sech}(\sqrt{3}\delta\tau))\tag{3.2.16}$$

For $\varepsilon \neq 0$, Eq. (3.2.15) can be written in the form of Eq. (2.3.4) with

$$\boldsymbol{x}=\begin{pmatrix}\varphi\\ \dot{\varphi}\end{pmatrix},\quad \boldsymbol{f}(\boldsymbol{x})=\begin{pmatrix}\dot{\varphi}\\ \kappa\sin 2\varphi\end{pmatrix},\quad \boldsymbol{g}(\boldsymbol{x},\tau)=\begin{pmatrix}0\\ 2(\dot{\varphi}+\delta)\sin\tau\end{pmatrix}\tag{3.2.17}$$

Equation (2.3.26) yields

$$\mathcal{M}_\pm(\tau_0)=\int_{-\infty}^{+\infty}[2(\dot{\varphi}_\pm(\tau)+\delta)\sin(\tau+\tau_0)]\dot{\varphi}_\pm(\tau)\,\mathrm{d}\tau\tag{3.2.18}$$

Substitution of Eq. (3.2.16) into Eq. (3.2.18) and evaluation of the resulting integrals in a similar way in 3.1.3 leads to the Melnikov function

$$\mathcal{M}(\tau_0)=\mathcal{M}_0\sin\tau_0\tag{3.2.19}$$

where $\mathcal{M}_0$ is a constant

$$\mathcal{M}_0 = -2\pi\left(\operatorname{csch}\frac{\pi}{2\sqrt{3}\delta} + \delta\operatorname{sech}\frac{\pi}{2\sqrt{3}\delta}\right) \tag{3.2.20}$$

Hence the function $\mathcal{M}(\tau_0)$ always possesses simple zeros.

3.2.4 Numerical Simulations

Equation (3.2.6) is integrated by use of the numerically integration algorithm so that the Poincaré map defined as $(\varphi(2k\pi), \dot{\varphi}(2k\pi))$ $(k = 1, 2, \cdots)$ can be computed. To obtain a global view of the system dynamics, the Poincaré maps from different initial conditions are put together to form a global Poincaré map. Figure 3.5 shows a global Poincaré map for Eq. (3.2.6) starting at 30 different initial conditions for different parameters. The two different types of motion, regular and chaotic,

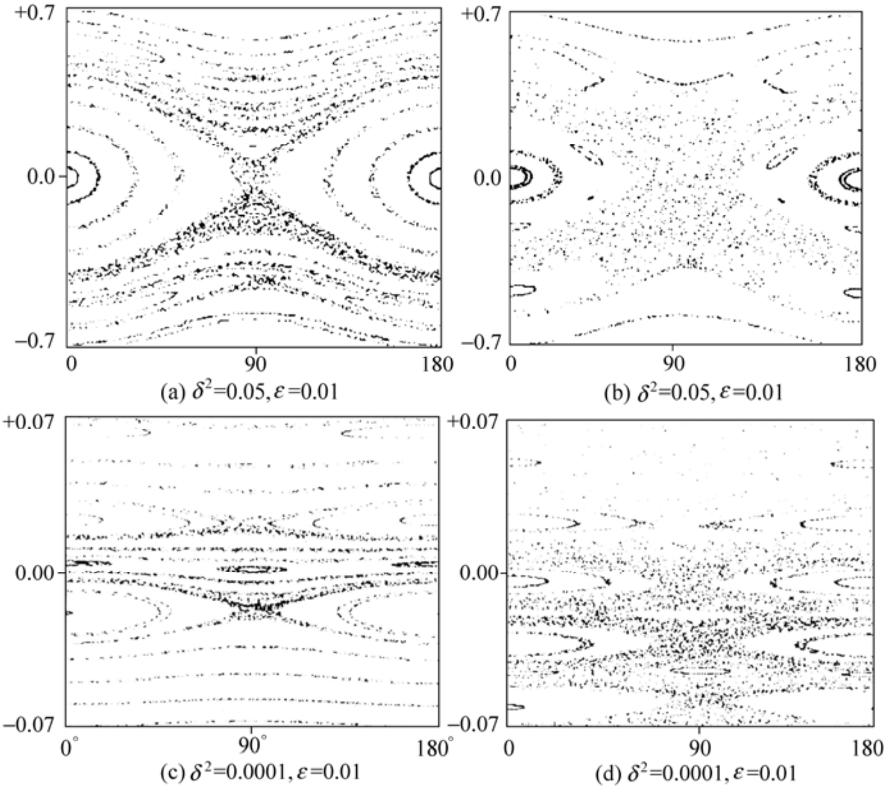

(a) δ^2=0.05, ε=0.01 (b) δ^2=0.05, ε=0.01

(c) δ^2=0.0001, ε=0.01 (d) δ^2=0.0001, ε=0.01

Figure 3.5 The global Poincaré map of a tethered satellite: uncoupled case are readily distinguished on the Poincaré maps. For the regular motion, successive points describe smooth curves or separate points, and for the chaotic motion, the points fill an area in apparently random manner. In Fig. 3.5(a) for a rather small ε, the Poincaré map is fairly well covered by invariant tori. It indicates that most of the motions are periodic or quasi-periodic. With increasing ε some tori break into chaotic trajectories in the sense that successive points on Poincaré map do not lie on a curve anymore, but densely fill an area. One can also see a hyperbolic point and homoclinic orbits connected to it, and the small region close to the separatrix is covered by chaotic trajectories as shown in Fig. 3.5 (b), (c), and (d).

For the case of coupled motion, Eq. (3.2.14) is numerically integrated for 4 different initial conditions. The resulting Poincaré maps in the (φ, p_φ) plane are shown in Fig. 3.3. In Fig. 3.3(a), for a low energy level, most of the Poincaré maps are fairly well covered by invariant tori indicating that most of the periodic and quasi-periodic motions are preserved. With increasing $\mathcal{H}$ some tori break into chaotic trajectories (see Fig. 3.3(b)~(d)), and for further increasing $\mathcal{H}$, regular motion gradually disappears finally ending in a chaotic ocean as shown in Fig. 3.3(e) and 3.3(f).

3.3 Magnetic Rigid Spacecraft in a Circular Orbit

3.3.1 Introduction

In addition to the gravitational torque, the magnetic torque plays a significant role in attitude motion of a magnetized spacecraft. In fact, gravitational and magnetic forces are dominant environmental effects for spacecraft moving at an altitude higher than 500 km [33]. This section begins to discuss chaotic attitude motion in the gravitational and magnetic fields, while the discussions here are limited to the case of spacecraft moving in a circular orbit.

Beletsky *et al.* investigated numerically chaotic attitude motion of a magnetic satellite in a circular orbit in the absence of a gravitational moment, and found that chaotization increases with the growth of the magnetic parameter [5, 6]. Bhardwaj and Bhatnagar applied the Melnikov method to rotational motion of a satellite in a circular orbit under the influence of magnetic torque [34]. They also used the Chrikov criterion [22] to estimate the chaotic separatrix and employed Poincaré map to highlight the important role of the magnetic torque and the mass distribution in changing the regular motion into chaos [35]. Beletsky, Lopes and Pivovarov studied the global phase portrait of a permanent magnetic satellite moving in a circular orbit without the gravitational moment and compared the chaotic region with its theoretical boundary obtained by the adiabatic approximation [36]. For the planar motion of a magnetic rigid spacecraft moving in a circular

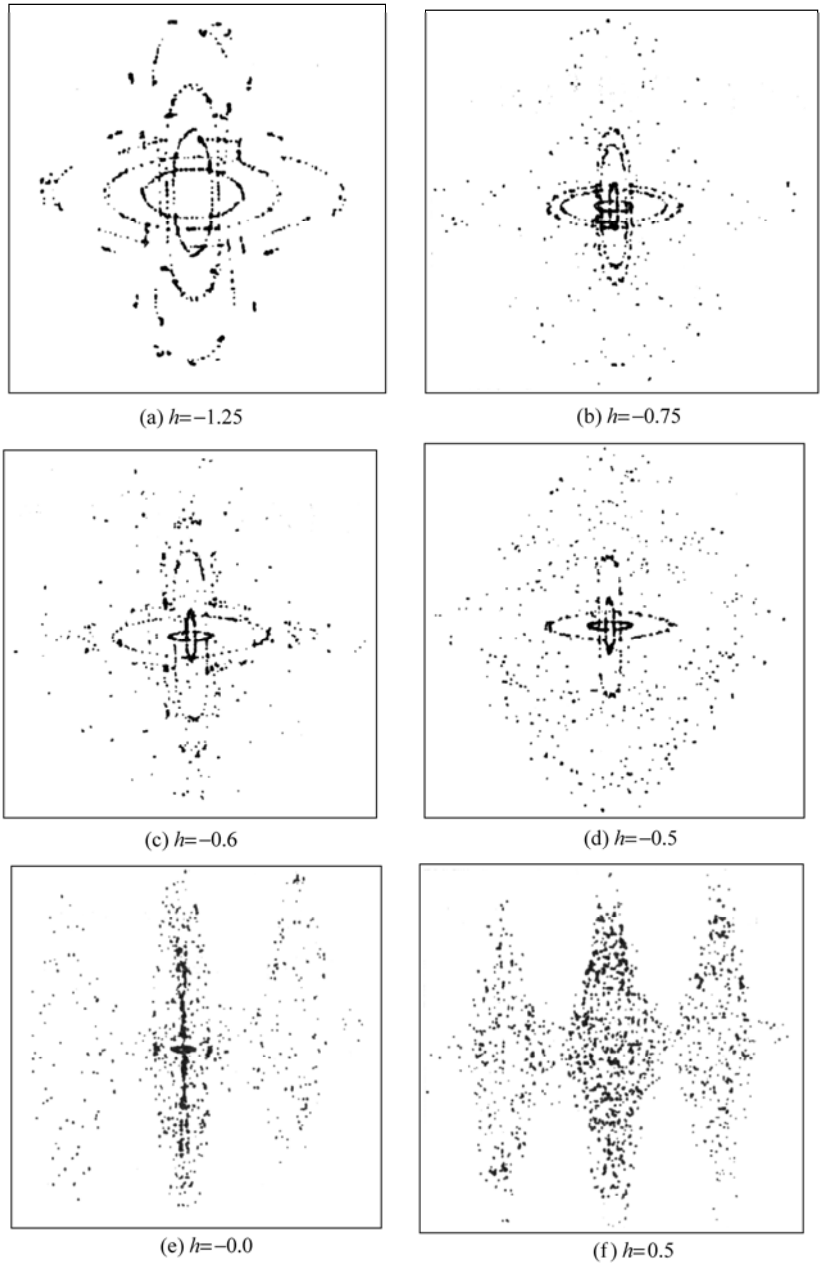

(a) $h=-1.25$

(b) $h=-0.75$

(c) $h=-0.6$

(d) $h=-0.5$

(e) $h=-0.0$

(f) $h=0.5$

Figure 3.6 The global Poincaré map in plane (φ, p_{φ}) of a tethered satellite: coupled case orbit near the equatorial plane of the Earth under the action of the gravitational and magnetic torques, Cheng and Liu found the existence of Smale's horseshoe via the Melnikov method and numerically demonstrated the intensification of chaos due to periodic disturbance of the magnetic field [37]. These investigations [5, 6, 34-37] used the Poincaré maps based on the numerical solutions to identify chaos. Chen and Liu employed the Poincaré map, the power spectrum and the Lyapunov exponents to demonstrate that the onset of chaos in a model developed in [37] is characterized by a breakup of torus as the torque of the magnetic forces is increased [38]. Considering the internal damping, which is an addition to the Melnikov analysis, Chen and Liu numerically investigated a magnetic rigid spacecraft in a circular orbit via the Poincaré map, the power spectrum and the Lyapunov exponents, and demonstrated the transition from periodic motion to chaos via intermittency as the increase of the torque of the magnetic field and the decrease of the damping [39]. Based on the Differential Galois Theory [40], Maciejewski and Przybylska proved the non-integrability of the dynamical system governing the attitude motion of a symmetric rigid satellite under the influence of gravitational and magnetic fields, with the only exception that the value of the induced magnetic moment along the symmetry axis is related to the principal moments of inertia in a special way [41].

This section treats a rigid-body spacecraft moving in a circular orbit. The dynamical model is derived from the theorem of angular momentum. The Melnikov theory is applied to predict the appearance of transverse heteroclinic points. In both undamped and damped cases, the routes to chaos are numerically examined via the Poincaré map, the power spectrum and the Lyapunov exponents. Numerical results demonstrate that the onset of chaos is characterized by the breakup of torus as the magnetic torque is increased in the undamped case and by the intermittency in the damped case as the magnetic torque is increased and the damping is decreased.

3.3.2 Dynamical Model

Consider a magnetic rigid spacecraft moving in a circular orbit with the orbital angular velocity ω_c in the gravitational and magnetic field of the Earth. Consider a magnetic rigid spacecraft moving in an elliptic orbit in the gravitational and magnetic field of the Earth. Assume that the inertial reference frame (O_e-$X_0Y_0Z_0$) has the origin O_e at the mass center of the Earth, with the polar axis of the Earth as Z_0-axis and the line from O_e to the ascending node as X_0-axis. The principal coordinate frame (O-xyz) has the mass center O as the origin. Principal moments of inertia of the arbitrarily shaped spacecraft are A, B and C. Suppose that $B>A$. The orbital coordinate frame (O-XYZ) is established with the radial vector from O_e to O as X-axis, the normal vector to orbital plane XY as Z-axis. The base vectors of (O-XYZ) are $\boldsymbol{i}$, $\boldsymbol{j}$, $\boldsymbol{k}$. Denote φ as the libration angle in the orbital plane with respect to X- or Y-axis, and i as the angle of inclination of the orbital plane, all shown in Fig. 3.7. Assume that the internal damping torque $\boldsymbol{M}_{\mathrm{d}}$ is proportional to angular velocity whose coefficients is c. Then

$$\boldsymbol{M}_{\mathrm{d}} = -c\dot{\varphi}\boldsymbol{k} \tag{3.3.1}$$

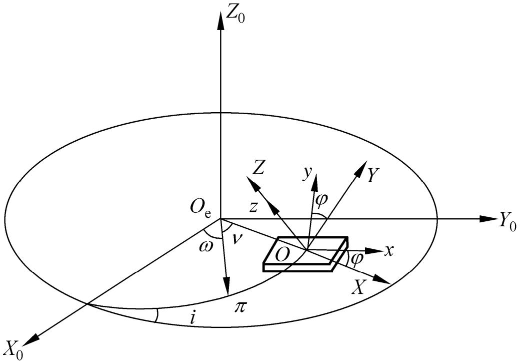

Figure 3.7 The reference frames

Application of the theorem of angular momentum to the spacecraft leads to

$$\dot{\boldsymbol{G}} = \boldsymbol{M}_{\mathrm{g}} + \boldsymbol{M}_{\mathrm{m}} + \boldsymbol{M}_{\mathrm{d}} \tag{3.3.2}$$

where $\boldsymbol{G}$ is the angular momentum, and $\boldsymbol{M}_{\mathrm{g}}$ and $\boldsymbol{M}_{\mathrm{m}}$ are the torques resulted form the gravitational and magnetic field respectively. When the orbit is circular, the gravitational torque $\boldsymbol{M}_{\mathrm{g}}$ is along the normal axis, and its magnitude is given by Eq. (1.3.12). Substitution of Eq. (1.3.14) into Eq. (1.3.12) yields

$$M_{\mathrm{g}z} = \frac{3}{2}\omega_{\mathrm{c}}^2(B - A)\sin 2\varphi \tag{3.3.3}$$

The magnetic field is assumed to be that of a dipole with the magnetic moment whose axis coincides the Earth's axis. For the orbital plane with the inclination angle i, the components of the magnetic flux density $\boldsymbol{H}_{\mathrm{m}}$ of the Earth in (O-XYZ) are given by Eq. (1.2.11). Assume that the magnetic moment $\boldsymbol{I}_{\mathrm{m}}$ of the spacecraft is along Ox-axis and the direction of the vector $\boldsymbol{I}_{\mathrm{m}}$ in the orbital plane is specified by the angle φ as shown in Fig. 1.11. Thus the direct cosines of $\boldsymbol{I}_{\mathrm{m}}$ with respect to (O-XYZ) are ($\cos\varphi$, $\sin\varphi$, 0). When the orbit is circular, the orbital angle u in Eq. (1.2.11) can be written as

$$u = \omega_{\mathrm{c}}t \tag{3.3.4}$$

Substitution of Eqs. (3.3.4), (1.2.11) and the direct cosines into Eq. (1.2.14) yields the projection of the magnetic torque $\boldsymbol{H}_{\mathrm{m}}$ on Oz-axis as

$$M_{\mathrm{m}z}=I_{\mathrm{m}}H_{\mathrm{m}0}\sin i(2\sin\varphi\sin\omega_{\mathrm{c}}t+\cos\varphi\cos\omega_{\mathrm{c}}t) \tag{3.3.5}$$

Projecting Eq. (3.3.2) on the *Oz*-axis and substituting Eqs. (3.3.1), (3.3.3) and (3.3.5) into the resulting equation, one obtains the dynamical equation in the dimensionless form

$$\ddot{\varphi}+\gamma\dot{\varphi}+\kappa\sin 2\varphi-\alpha(2\sin\varphi\sin\tau+\cos\varphi\cos\tau)=0 \tag{3.3.6}$$

where $\tau=\omega_{\mathrm{c}}t$ is defined as the dimensionless time and

$$\gamma=\frac{c}{C\omega_{\mathrm{c}}},\ \kappa=\frac{3(B-A)}{2C},\ \alpha=\frac{IH_{\mathrm{m}0}\sin i}{\mathrm{C}\omega_{\mathrm{c}}^{2}} \tag{3.3.7}$$

The derivatives in Eq. (3.3.6) are with respect to the dimensionless time τ.

3.3.3 Melnikov Analysis

Assume that both the damping coefficient γ and the magnetic parameter α are small and let $\gamma=\varepsilon\gamma_1$ and $\alpha=\varepsilon\alpha_1$ ($0<\varepsilon\ll 1$). Then Eq. (3.3.6) is an integrable Hamiltonian system under small perturbations

$$\ddot{\varphi}+\sigma\sin 2\varphi=\varepsilon\alpha_1(2\sin\varphi\sin\tau+\cos\varphi\cos\tau)-\varepsilon\gamma_1\dot{\varphi} \tag{3.3.8}$$

If $\varepsilon=0$, Eq. (3.3.8) becomes Eq. (3.1.4) with two hyperbolic saddle points ($\pm\pi/2$, 0) connected by the heteroclinic orbits $\Gamma^{\pm}$ defined by Eq. (3.1.9). For $\varepsilon\neq 0$, Eq. (3.3.8) can be cast into the form of Eq. (2.3.4) with

$$\begin{gathered}\boldsymbol{x}=\begin{pmatrix}\varphi\\ \dot{\varphi}\end{pmatrix},\quad \boldsymbol{f}(\boldsymbol{x})=\begin{pmatrix}\dot{\varphi}\\ \kappa\sin 2\varphi\end{pmatrix}\\ \boldsymbol{g}(\boldsymbol{x},\tau)=\begin{pmatrix}0\\ \alpha_1(2\sin\varphi\sin\tau+\cos\varphi\cos\tau)-\gamma_1\dot{\varphi}\end{pmatrix}\end{gathered} \tag{3.3.9}$$

Equation (2.3.26) yields

$$\begin{aligned}\mathcal{M}_{\pm}(\tau_0)=\int_{-\infty}^{+\infty}\big[&-\alpha_1\big(2\sin\varphi_{\pm}(\tau)\sin(\tau+\tau_0)\\ &+\cos\varphi_{\pm}(\tau)\cos(\tau+\tau_0)\big)-\gamma_1\dot{\varphi}_{\pm}(\tau)\big]\dot{\varphi}_{\pm}(\tau)\,\mathrm{d}\tau\end{aligned} \tag{3.3.10}$$

Substitution of Eq. (3.1.9) into Eq. (3.3.10) and calculation of the resulting integrals in a similar fashion in 3.1.1 leads to the explicit expression of the Melnikov function

$$\mathcal{M}_{\pm}(\tau_0)=\frac{\alpha_1\pi}{2\kappa}(1+\sqrt{2\kappa})\operatorname{csch}\left(\frac{\pi}{2\sqrt{2\kappa}}\right)\sin\tau_0-2\sqrt{2}\gamma_1\kappa \tag{3.3.11}$$

For the undamped case, let $\gamma_1 = 0$, thus function $\mathcal{M}_{\pm}(\tau_0)$ always has simple zeros. For the damped case, both $\mathcal{M}_{+}(\tau_0)$ and $\mathcal{M}_{-}(\tau_0)$ have simple zeros on the condition that

$$\frac{\alpha}{\gamma} = \frac{\alpha_1}{\gamma_1} > \frac{4\sqrt{2}\kappa^2}{\pi(1+\sqrt{2}\kappa)} \operatorname{sh}\left(\frac{\pi}{2\sqrt{2}K}\right) \tag{3.3.12}$$

3.3.4 Numerical Investigations: Undamped Case

The effect of the magnetic parameter α upon the spacecraft attitude motion is now investigated numerically by integrating Eq. (3.3.6) in which $\gamma = 0$. The global view of the Poincaré map is presented by the calculation based on a set of initial conditions. Then the routes to chaos are numerically investigated for a given initial condition.

Equation (3.3.6) is numerically integrated for 7 different initial conditions. The Poincaré maps defined as $(\varphi(2k\pi), \dot{\varphi}(2k\pi))$ $(k = 1, 2, \cdots)$ are shown in Fig. 3.8 for

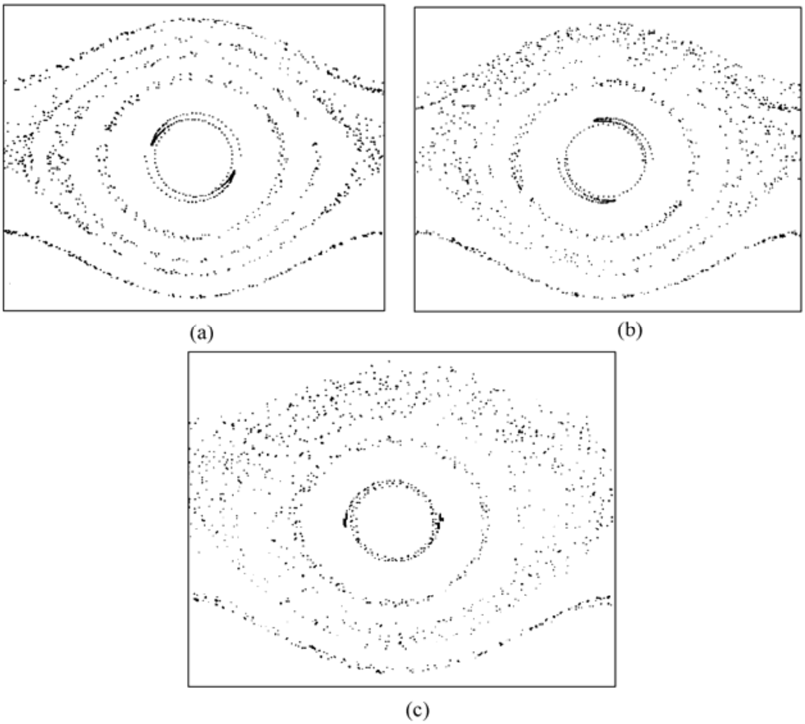
(a) (b) (c)

Figure 3.8 The global Poincaré maps of a magnetic spacecraft (a) $\alpha = 0.01$; (b) $\alpha = 0.02$; (c) $\alpha = 0.05$

$\alpha = 0.01$, 0.02 and 0.05. It can be seen that under the action of the periodic disturbance of magnetic torque, the motion of spacecraft rapidly becomes irregular and turns into chaotic motion. As the disturbance increases, the chaotic region is enlarged.

The characteristic dynamical behavior is investigated by varying the magnetic parameter α, while the gravitational parameter κ is kept constant at $\kappa = 0.75$. The numerical integration begins from the initial condition (0,0).

When α is small enough, the system experiences quasi-periodic motion. For $\alpha = 0.01$, the time history, the Poincaré map, power spectrum and the largest Lyapunov exponent are depicted in Fig. 3.9. The Lyapunov exponents are all very close to zero.

For relatively large α, the quasi-periodic torus begin to break up. For $\alpha = 0.12$ and $\alpha = 0.1275$, the time history, the Poincaré map, power spectrum and the largest Lyapunov exponent are shown in Fig. 3.10 and Fig. 3.11, respectively. Even if those Poincaré maps were almost the same as those in Fig. 3.9, the power spectra show differences. The Lyapunov exponents are 0.00, 0.00 and 0.01, −0.01.

For sufficiently large α, the quasi-periodic torus breaks up completely and chaotic motion occurs in the system. For $\alpha = 0.1276$, the time history, the Poincare map, power spectrum and the largest Lyapunov exponent are shown in Fig. 3.12. The Lypunov exponents are 0.12, −0.12.

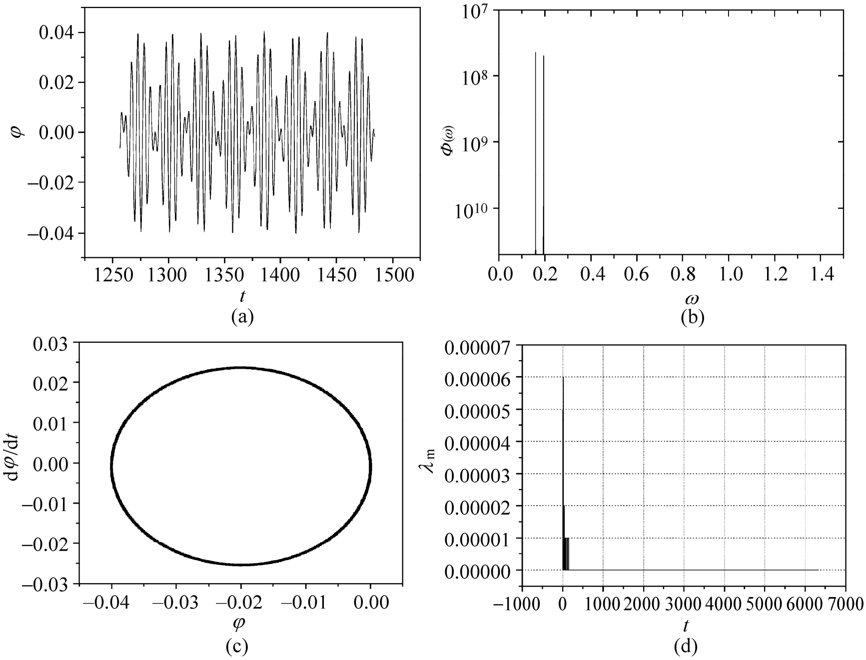

Figure 3.9 Quasi-periodic motion ($\alpha = 0.01$): (a) the time history; (b) power spectrum; (c) the Poincaré map; and (d) the largest Lyapunov exponent

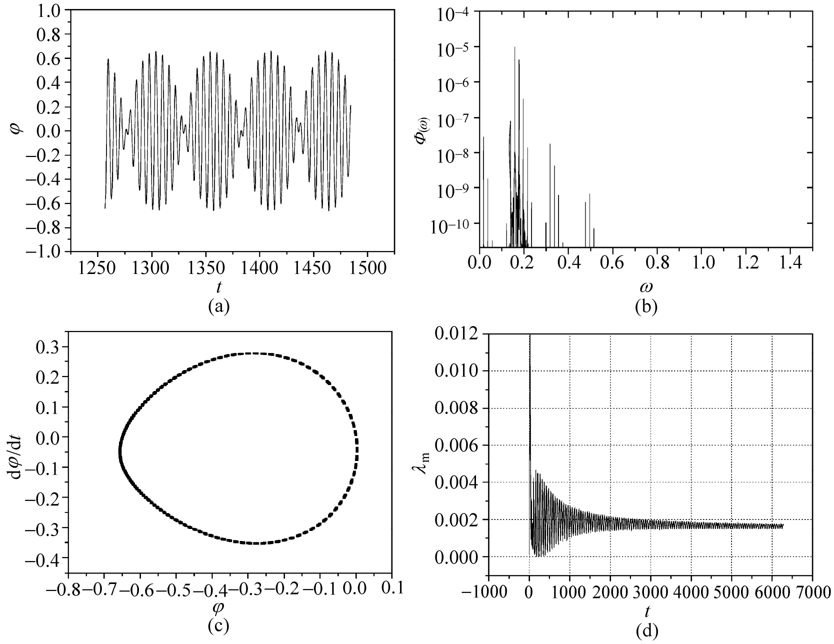

Figire 3.10 Breakup of the torus ($\alpha = 0.12$): (a) the time history; (b) power spectrum; (c) the Poincaré map; and (d) the largest Lyapunov exponent

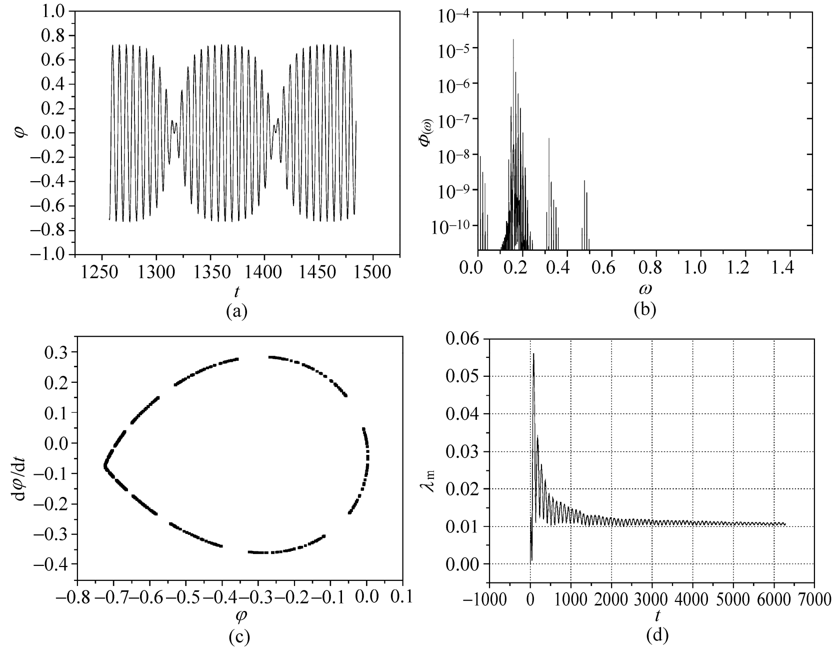

Figure 3.11 Breakup of the torus ($\alpha = 0.12175$): (a) the time history; (b) power spectrum; (c) the Poincaré map; and (d) the largest Lyapunov exponent

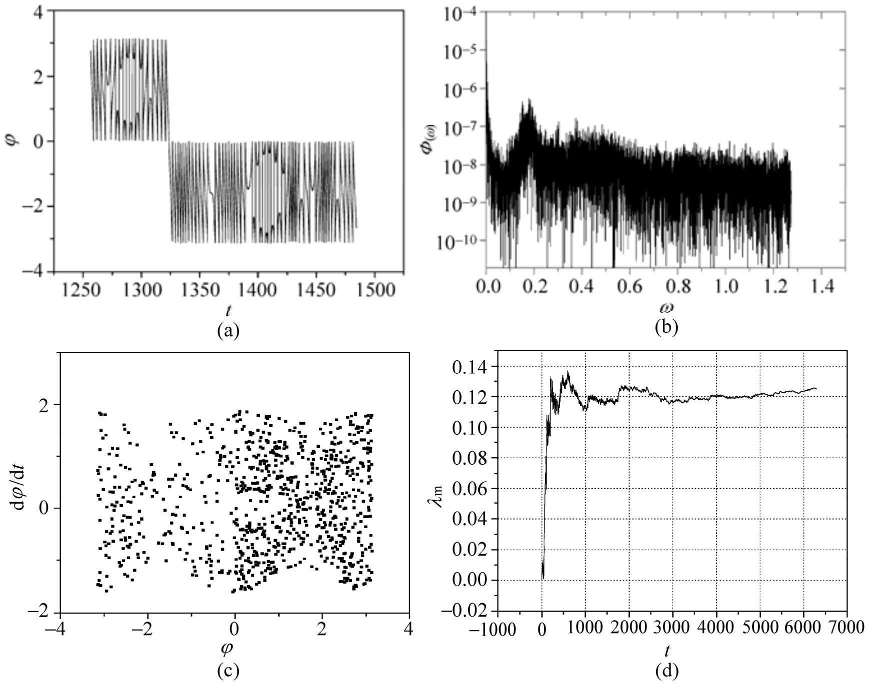

(a) (b)

(c) (d)

Figure 3.12 Chaotic motion ($\alpha = 0.12176$): (a) the time history; (b) power spectrum; (c) the Poincaré map; and (d) the largest Lyapunov exponent

3.3.5 Numerical Investigations: Damped Case

The effects of the magnetic parameter α and the damping coefficient γ upon the uncontrolled spacecraft attitude motion are respectively investigated numerically by integrating Eq. (3.3.6). Equation (3.3.6) can be cast into the following form

$$\begin{aligned}\dot{x}_1 &= x_2\\ \dot{x}_2 &= -\kappa \sin 2x_1 - \gamma x_2 + \alpha(2\sin x_1 \sin x_3 + \cos x_1 \cos x_3)\\ \dot{x}_3 &= 1\end{aligned} \tag{3.3.13}$$

The linearized system of Eqs. (3.3.13) is characterized by the Jacobian matrix

$$\begin{pmatrix} 0 & 1 & 0 \\ -2K\cos 2x_1 + \alpha(2\cos x_1 \sin x_3 - \sin x_1 \cos x_3) & \gamma & \alpha(2\sin x_1 \cos x_3 - \cos x_1 \sin x_3) \\ 0 & 0 & 0 \end{pmatrix} \tag{3.3.14}$$

which is needed in order to calculate the Lyapunov exponents. The characteristic dynamical behavior is investigated by varying the magnetic parameter α and the damping coefficient γ, respectively, while the gravitational parameter κ is kept constant at $\kappa = 1.1$. In this case, the condition of the Melnikov theory given by Eq. (3.3.12) is $\alpha/\gamma > 1.5738$. The numerical integration begins from the initial conditions described by $(x_1, x_2, x_3)^T = (0,0,0)$.

For a given γ, the intermittency transition accrues as the magnetic parameter α is increased. Let $\gamma = 0.2$, then the Melnikov theory requires $\alpha > 0.4452$. The dynamical behaviors of the system at $\alpha = 0.6984$, 0.6985, 0.69855,0.6986 are shown in Figs. 3.13, 3.14, 3.15, and 3.16. The corresponding Lyapunov exponents are shown in Table 3.1. As α is increased, the periodic behavior becomes the regular motion intermittently interrupted by a finite duration burst of irregular motion. For the further increase of α, the bursts become so frequent that the regular behavior can no longer be distinguished, and the chaotic motion is developed. Due to the transient behavior, the largest Lyapunov exponent is positive at the beginning of the periodic motion in Fig. 3.13. During the intermittency transition shown in Figs. 3.14 and 3.15, the motions depend sensitively on initial conditions so that the largest Lyapunov exponents are still positive in durations of the periodic motions between irregular bursts.

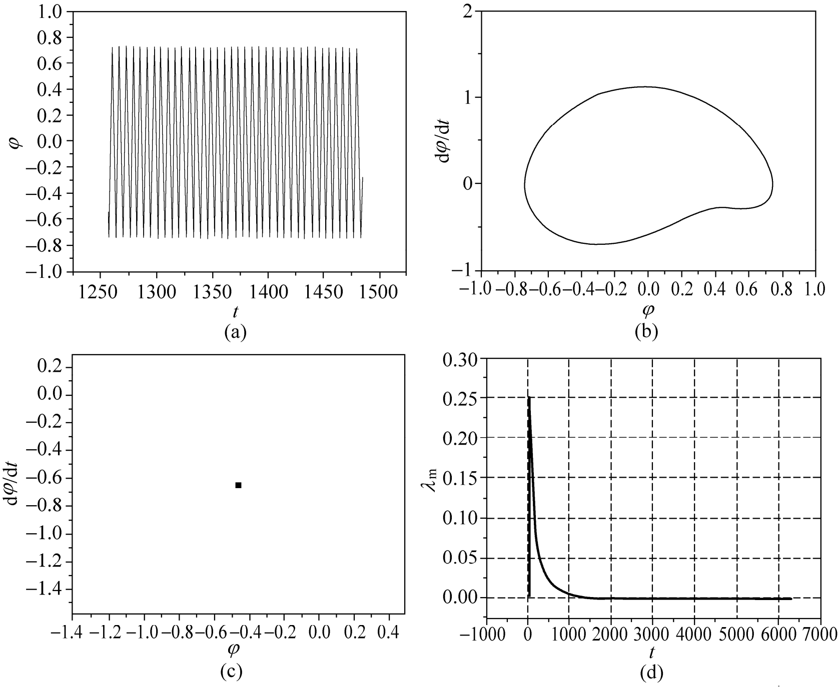

Figire 3.13 Periodic motion ($\alpha = 0.6984$, $\gamma = 0.2$): (a) the time history; (b) phase trajectory; (c) the Poincaré map; and (d) the largest Lyapunov exponent

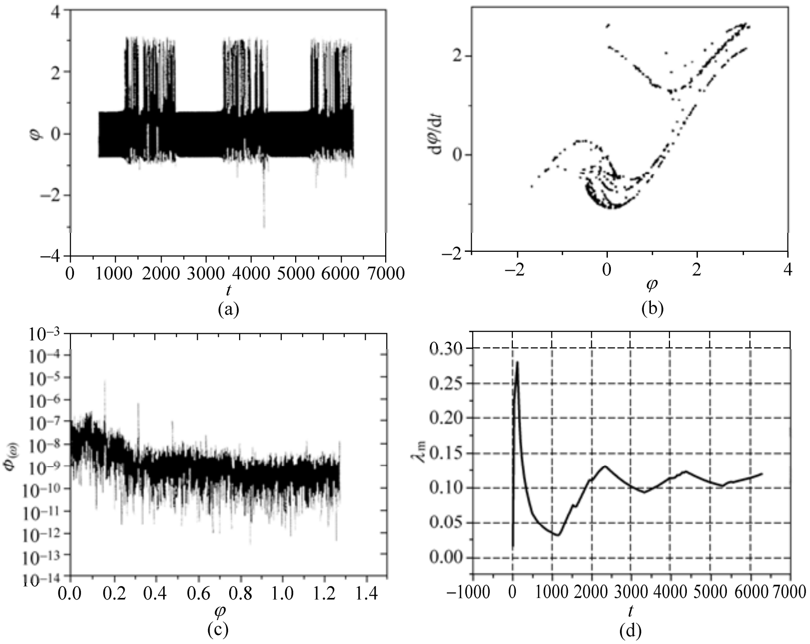

Figure 3.14 Intermittency ($\alpha = 0.6985$, $\gamma = 0.2$): (a) the time history; (b) the Poincaré map; (c) power spectrum; and (d) the largest Lyapunov exponent

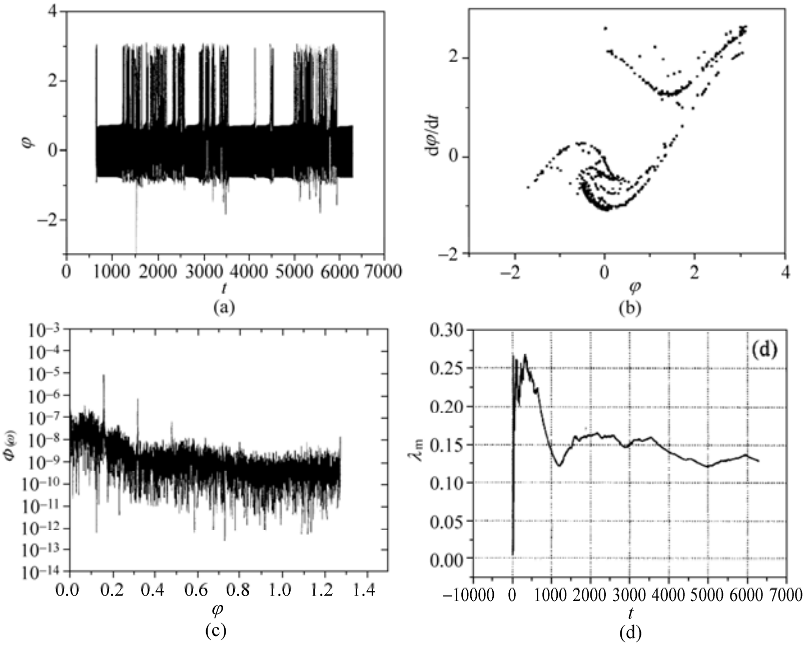

Figure 3.15 Intermittency ($\alpha = 0.69855$ $\gamma = 0.2$): (a) the time history; (b) the Poincaré map; (c) power spectrum; and (d) the largest Lyapunov exponent

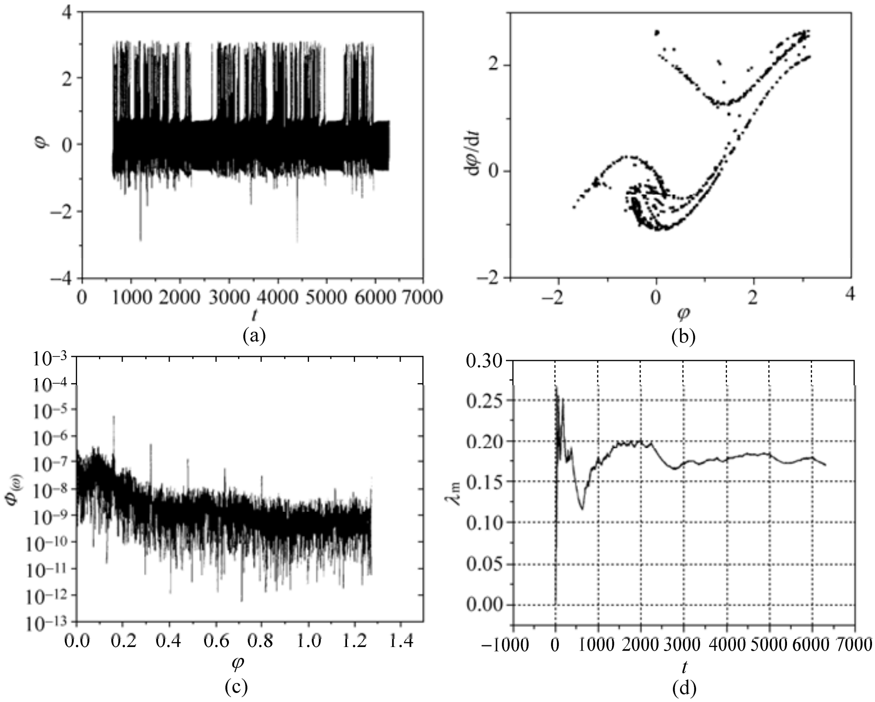

Figure 3.16 Chaotic motion ($\alpha = 0.6986$, $\gamma = 0.2$): (a) the time history; (b) the Poincaré map; (c) power spectrum; and (d) the largest Lyapunov exponent

Table 3.1 Lyapunov exponents ($\gamma = 0.2$)

α	λ_1	λ_2	λ_3
0.6984	0.00	−0.01	−0.19
0.6985	0.12	0.00	−0.32
0.69855	0.13	0.00	−0.33
0.6986	0.17	0.00	−0.37

For a given α, the intermittency transition accrues as the damping coefficient α is decreased. Let α be fixed as $\alpha = 0.7$, then the Melnikov theory requires $\gamma < 0.317$. The case that $\gamma = 0.295$, 0.290, 0.285,0.280 are shown in Figs. 3.17, 3.18, 3.19, and 3.20. The corresponding Lyapunov exponents are listed in Table 3.2.

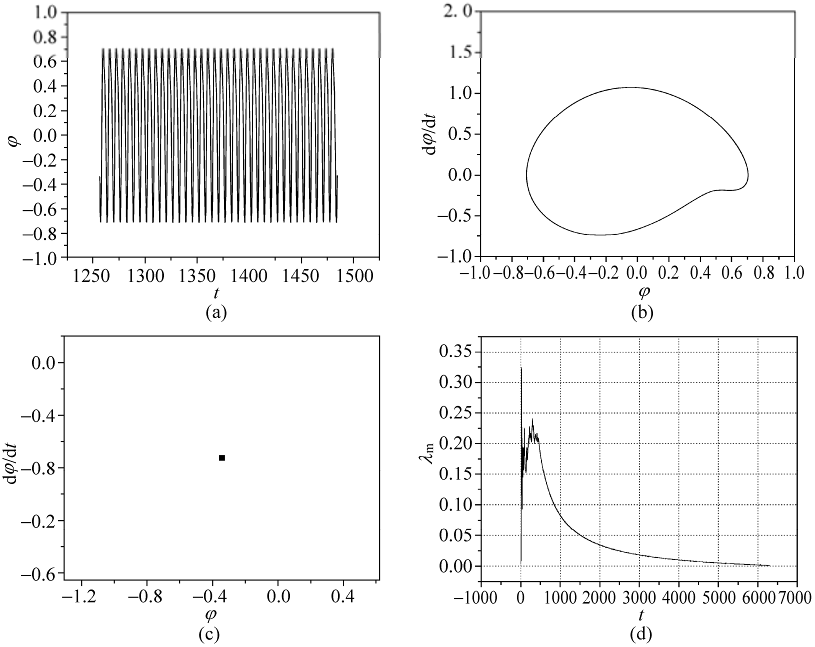

Figure 3.17 Periodic motion ($\alpha = 0.7$, $\gamma = 0.295$): (a) the time history; (b) phase trajectory; (c) the Poincaré map; and (d) the largest Lyapunov exponent

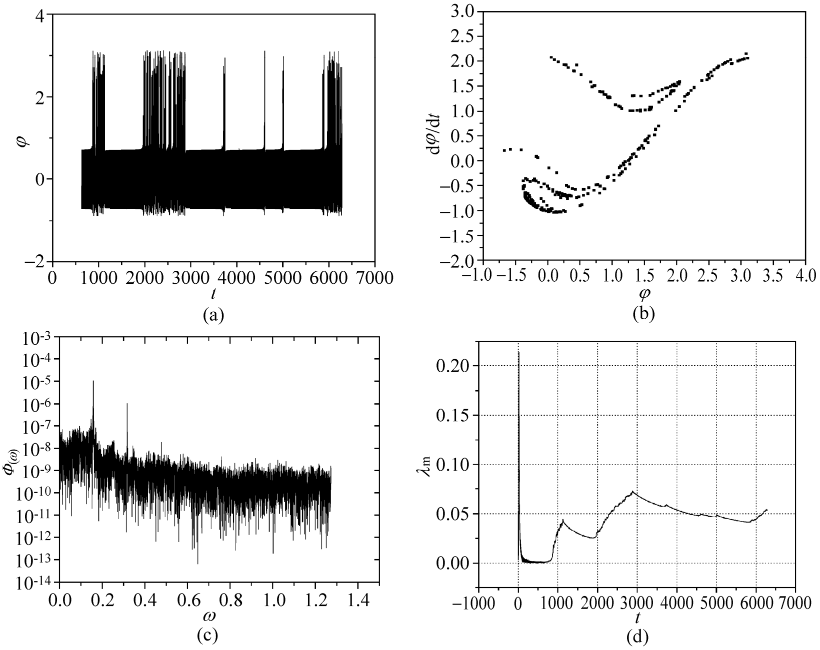

Figure 3.18 Intermittency ($\alpha = 0.7$, $\gamma = 0.290$): (a) the time history; (b) the Poincaré map; (c) power spectrum; and (d) the largest Lyapunov exponent

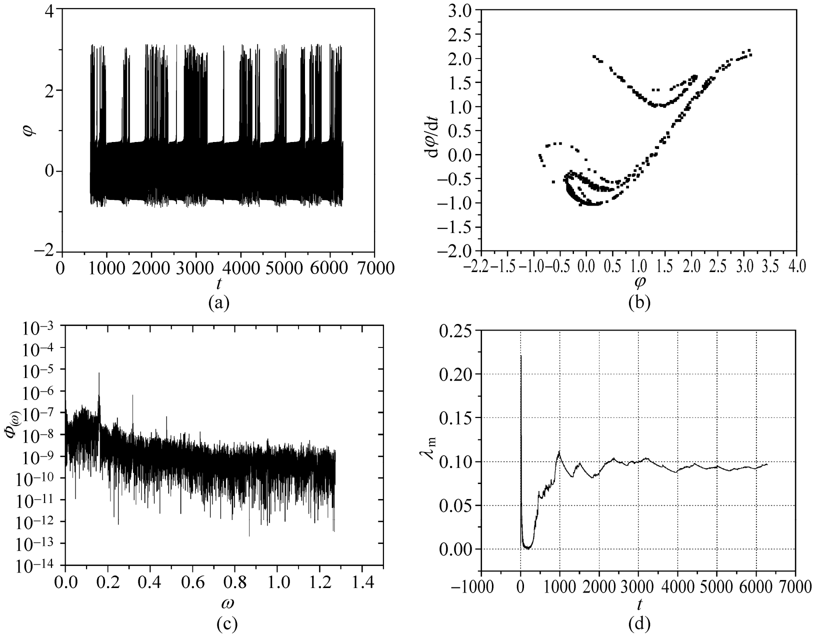

Figure 3.19 Intermittency ($\alpha = 0.7$, $\gamma = 0.285$): (a) the time history; (b) the Poincaré map; (c) power spectrum; and (d) the largest Lyapunov exponent

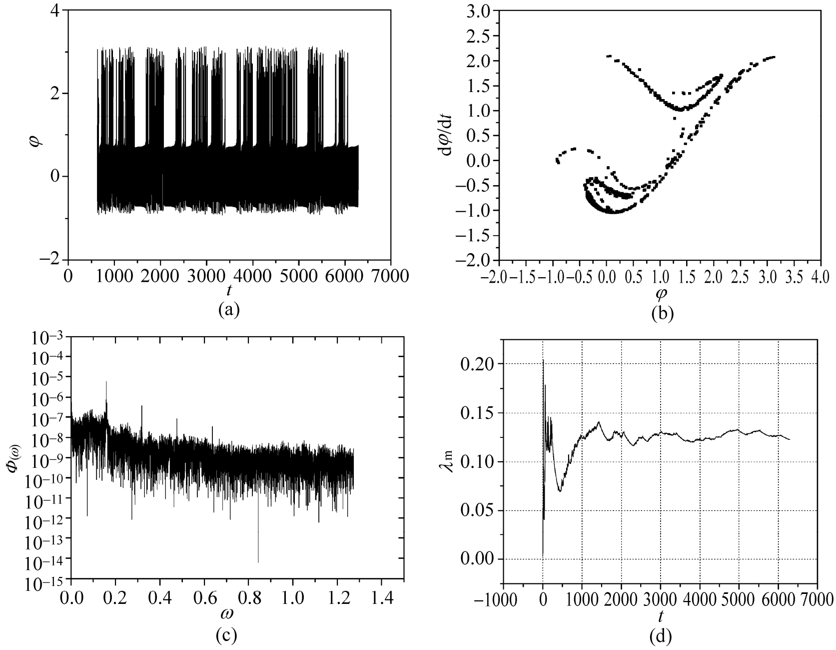

Figure 3.20 Chaotic motion ($\alpha = 0.7$, $\gamma = 0.280$): (a) the time history; (b) the Poincaré map; (c) power spectrum; and (d) the largest Lyapunov exponent

Table 3.2 Lyapunov exponents (α=0.7)

γ	λ_1	λ_2	λ_3
0.295	0.00	0.00	−0.30
0.290	0.05	0.00	−0.34
0.285	0.10	0.00	−0.38
0.280	0.12	0.00	−0.40

3.4 Magnetic Rigid Spacecraft in an Elliptic Orbit

3.4.1 Introduction

This section continues to discuss chaotic attitude motion in the gravitational and magnetic fields. The spacecraft considered here moves in an elliptic orbit instead of a circular orbit.

Although the dynamical equation for a magnetic rigid spacecraft in an elliptic orbit was established by 1985 [33], investigations of chaotic attitude motion were rather limited. Koch and Bruhn applied the Melnikov method to a polar satellite, a satellite whose orbital plane contains the symmetry axis of the central body, in an elliptic orbit under the action of the gravitational torque and the magnetic torque [3]. Liu and Chen investigated chaotic attitude motion of a magnetic rigid spacecraft with internal damping in an elliptic orbit. They used the Melnikov method to predict transverse heteroclinic cycles in the Poincaré map of the system, and employed the time history, the Poincaré map, the Lyapunov exponents and the power spectrum to identify chaos [42]. Bhardwaj and Kaur developed the Melnikov function for magnetic rigid spacecraft in an elliptic orbit and numerically showed the simple zeros of the function [43]. They also applied Chrikov's criterion [22] to estimate the half width of the chaotic separatrix and highlighted numerically the effects of the magnetic torque parameter, the orbital eccentricity, and the mass distribution parameter [44].

This section begins with modeling a magnetic rigid body spacecraft in an elliptic orbit. The Melnikov theory is applied to predict the appearance of transverse heteroclinic points. Chaotic attitude motion is numerically demonstrated via the Poincaré map, the power spectrum and the Lyapunov exponents.

3.4.2 Dynamical Model

Consider a magnetic rigid spacecraft moving in an elliptic orbit in the gravitational and magnetic field of the Earth. Assume that the inertial reference frame

(O_e-$X_0Y_0Z_0$) has the origin O_e at the mass center of the Earth, with the polar axis of the Earth as Z_0-axis and the line from O_e to the ascending node as X_0-axis. The principal coordinate frame (O-xyz) has the mass center O as the origin. Principal moments of inertia of the arbitrarily shaped spacecraft are A, B and C. Suppose that $B>A$. The orbital coordinate frame (O-XYZ) is established with the radial vector from O_e to O as X-axis, the normal vector to orbital plane XY as Z-axis. The base vectors of (O-XYZ) are $\boldsymbol{i}$, $\boldsymbol{j}$, $\boldsymbol{k}$. Denote φ as the libration angle in the orbital plane with respect to X- or Y-axes, ν as the true anomaly of the spacecraft as the position angle measured from perigee, and i as the angle of inclination of the orbital plane, and ω is the argument of perigee, all shown in Fig. 3.7.

The theorem of angular momentum about the center of mass is still expressed by Eq. (3.3.2), in which $\boldsymbol{G}$ is the angular momentum, $\boldsymbol{M}_g$ and $\boldsymbol{M}_m$ are the gravitational and magnetic torques, respectively, and $\boldsymbol{M}_d$ is the internal damping torque proportional to the angular velocity with coefficient c.

For planar libration, all vectors in Eq. (3.3.2) are along the normal axis of the orbital plane. The magnitudes of torques $\boldsymbol{M}_g$ and $\boldsymbol{M}_d$ are given by Eqs. (1.3.12) and (3.3.1), respectively. The components of the magnetic flux density $\boldsymbol{H}_m$ of the Earth in (O-XYZ) are given by Eq. (1.2.11). For the elliptic orbit, the orbital angle u in Eq. (1.2.11) can be expressed by Eq. (1.1.29). Assume that the magnetic moment $\boldsymbol{I}_m$ of the spacecraft is along Ox-axis and the direction of the vector $\boldsymbol{I}_m$ in the orbital plane is specified by the angle φ as shown in Fig. 1.11. Thus the direct cosines of $\boldsymbol{I}_m$ with respect to (O-XYZ) are ($\cos\varphi$, $\sin\varphi$, 0). Substitution of Eqs. (1.2.9) and (1.2.11) with $H_{m0}=\mu_m/r^3$ and the direct cosines into Eq. (1.2.14) yields the projection of the magnetic torque $\boldsymbol{H}_m$ on Oz-axis as

$$M_{mZ}=\frac{I_m\mu_m}{2r^3}\sin i(3\cos(\varphi-\nu-\omega)-\cos(\varphi+\nu+\omega)) \tag{3.4.1}$$

where r is distance between O and O_e, and μ_m is the Earth magnetic dipole strength. Projection of Eq. (3.3.2) on the Oz-axis and substitution of Eqs. (3.3.1), (1.3.12) and (3.4.1) into the resulting equation leads to

$$\begin{aligned} C\left(\frac{d^2\varphi}{dt^2}+\frac{d^2\nu}{dt^2}\right)&=-\frac{3\mu}{2r^3}(B-A)\sin 2\varphi \\ &+\frac{I_m\mu_m}{2r^3}\sin i(3\cos(\varphi-\nu-\omega)-\cos(\varphi+\nu+\omega))-c\frac{d\varphi}{dt} \end{aligned} \tag{3.4.2}$$

where μ is the gravitational attraction constant of the Earth.

The orbital motion and the attitude motion are assumed to be decoupled. The effect of the magnetic field on the orbital motion is neglected. The spacecraft undergoes the Kepler motion expressed by Eqs. (1.3.24). Substitution of Eqs. (1.3.24) and (1.3.25) into Eq. (3.1.1) yields dynamical model of a magnetic rigid spacecraft in an elliptic orbit

$$\begin{aligned}&\ddot{\varphi}-\frac{2e\sin\nu}{1+e\cos\nu}(1+\dot{\varphi})+\frac{\kappa\sin 2\varphi}{1+e\cos\nu}\\&+\frac{\gamma}{(1+e\cos\nu)^2}\dot{\varphi}-\alpha\frac{\cos(\varphi+\nu+\omega)-3\cos(\varphi-\nu-\omega)}{1+e\cos\nu}=0\end{aligned} \tag{3.4.3}$$

where

$$\kappa=\frac{3(B-A)}{2C},\quad \alpha=\frac{I_{\mathrm{m}}\mu_{\mathrm{m}}}{2C\mu}\sin i,\quad \gamma=\frac{cp\sqrt{p}}{C\sqrt{\mu}} \tag{3.4.4}$$

p is the semi-parameter of the orbit, e is the orbit eccentricity, and the over dot denotes the derivative with respect to the position angle ν.

3.4.3 Melnikov Analysis

Since e, α, and γ are all small, introduce a small dimensionless parameter $\varepsilon(0<\varepsilon\ll 1)$ such that $e=\varepsilon e_1$, $\alpha=\varepsilon\alpha_1$, $\gamma=\varepsilon\gamma_1$. Retaining the first order terms of ε and omitting the higher order terms in Eq. (3.4.3) lead to an integrable Hamiltonian system under small perturbations

$$\begin{aligned}\ddot{\varphi}+\kappa\sin 2\varphi=\varepsilon[&2e_1\sin\nu(1+\dot{\varphi})+e_1\kappa\cos\nu\sin 2\varphi\\&+\alpha_1(\cos(\varphi+\nu+\omega)-3\cos(\varphi-\nu-\omega))-\gamma_1\dot{\varphi}]\end{aligned} \tag{3.4.5}$$

If $\varepsilon=0$, Eq. (3.4.5) becomes Eq. (3.1.4) with two hyperbolic saddle points $(\pm\pi/2, 0)$ connected by the heteroclinic orbits $\Gamma^{\pm}$ defined by Eq. (3.1.9). For $\varepsilon\neq 0$, Eq. (3.4.5) can be cast into the form of Eq. (2.3.4) with

$$\boldsymbol{x}=\begin{pmatrix}\varphi\\ \dot{\varphi}\end{pmatrix},\quad \boldsymbol{f}(\boldsymbol{x})=\begin{pmatrix}\dot{\varphi}\\ \kappa\sin 2\varphi\end{pmatrix}$$

$$\boldsymbol{g}(\boldsymbol{x},\nu)=\begin{pmatrix}0\\ 2e_1\sin\nu(1+\dot{\varphi})+e_1\kappa\cos\nu\sin 2\varphi+\alpha_1(\cos(\varphi+\nu+\omega)-3\cos(\varphi-\nu-\omega))-\gamma_1\dot{\varphi}\end{pmatrix} \tag{3.4.6}$$

Equation (2.3.26) yields

$$\begin{aligned}\mathcal{M}_{\pm}(\nu_0)=\int_{-\infty}^{+\infty}&[2e_1\sin(\nu+\nu_0)(1+\dot{\varphi}_{\pm}(\nu))+e_1\kappa\cos(\nu+\nu_0)\sin 2\varphi_{\pm}(\nu)-\gamma_1\dot{\varphi}_{\pm}(\nu)\\&+\alpha_1(\cos(\varphi_{\pm}(\nu)+\nu+\nu_0+\omega)-3\cos(\varphi_{\pm}(\nu)-\nu-\nu_0-\omega))]\dot{\varphi}_{\pm}(\nu)\,\mathrm{d}\nu\end{aligned} \tag{3.4.7}$$

Substitution of Eq. (3.1.9) into Eq. (3.4.7) and calculation of the resulting integrals yield the Melnikov function

$$\begin{aligned}\mathcal{M}_{\pm}(\tau_0) = {} & \frac{\pi}{2} e_1 \left(\mp 4 \operatorname{sech} \frac{\pi}{2\sqrt{2\kappa}} + 3 \operatorname{csch} \frac{\pi}{2\sqrt{2\kappa}} \right) \sin \nu_0 \\ & + \alpha_1 \pi \left(\frac{1+\sqrt{2\kappa}}{2\kappa} \right) \operatorname{csch} \left(\frac{\pi}{2\sqrt{2\kappa}} \right) \sin(\nu_0 + \omega) - 2\sqrt{2}\gamma_1 \kappa \end{aligned} \tag{3.4.8}$$

Hence $\mathcal{M}_{\pm}(\nu_0)$ has simple zeros on the condition that

$$\gamma < \frac{\sqrt{2}\,\pi}{8\kappa} \sqrt{A^2 + B^2} \tag{3.4.9}$$

where

$$\begin{aligned} A &= e\left(-4 \operatorname{sech} \frac{\pi}{2\sqrt{2\kappa}} + 3 \operatorname{csch} \frac{\pi}{2\sqrt{2\kappa}} \right) + \alpha \left(\frac{1+\sqrt{2\kappa}}{\kappa} \right) \operatorname{csch} \left(\frac{\pi}{2\sqrt{2\kappa}} \right) \cos \omega \\ B &= \alpha \left(\frac{1+\sqrt{2\kappa}}{\kappa} \right) \operatorname{csch} \left(\frac{\pi}{2\sqrt{2\kappa}} \right) \sin \omega \end{aligned} \tag{3.4.10}$$

3.4.4 Numerical Simulations

Chaotic attitude motion of the spacecraft can be numerically demonstrated by integrating Eq. (3.4.3) which is rewritten as

$$\begin{aligned} \frac{\mathrm{d}x_1}{\mathrm{d}\nu} &= x_2 \\ \frac{\mathrm{d}x_2}{\mathrm{d}\nu} &= \frac{2e \sin x_3}{1 + e\cos x_3}(1 + x_2) - \frac{\kappa \sin 2x_1}{1 + e\cos x_3} - \frac{\gamma}{(1 + e\cos x_3)^2} x_2 \\ &\quad - \alpha \frac{3\cos(x_1 - x_3 - \omega) - \cos(x_1 + x_3 + \omega)}{1 + e\cos x_3} \\ \frac{\mathrm{d}x_3}{\mathrm{d}\nu} &= 1 \end{aligned} \tag{3.4.11}$$

where

$$x_1 = \varphi, \quad x_2 = \frac{\mathrm{d}\varphi}{\mathrm{d}\nu}, \quad x_3 = \nu \tag{3.4.12}$$

Various tools including the time history, Poincaré map, Lyapunov exponents and power spectrum are used to identify the dynamical behavior. The linearized system of Eq. (3.4.11) is characterized by the Jacobian matrix

$$\boldsymbol{A}=\begin{pmatrix} 0 & 1 & 0 \\ a_{21} & a_{22} & a_{23} \\ 0 & 0 & 0 \end{pmatrix} \tag{3.4.13}$$

where

$$\begin{aligned}
a_{21} &= -\frac{2\kappa\cos 2x_1}{1+e\cos x_3}+\alpha\frac{3\sin(x_1-x_3-\omega)-\sin(x_1+x_3+\omega)}{1+e\cos x_3} \\
a_{22} &= \frac{2e\sin x_3}{1+e\cos x_3}-\frac{\gamma}{(1+e\cos x_3)^2} \\
a_{23} &= \frac{2e(e+\cos x_3)}{(1+e\cos x_3)^2}(1+x_2)-\frac{e\kappa\sin 2x_1\sin x_3}{(1+e\cos x_3)^2}-\frac{2e\gamma\sin x_3}{(1+e\cos x_3)^3}x_2 \\
&\quad -\alpha\frac{3\sin(x_1-x_3-\omega)+\sin(x_1+x_3+\omega)}{1+e\cos x_3} \\
&\quad -\alpha\frac{e\sin x_3\left[3\cos(x_1-x_3-\omega)-\cos(x_1+x_3+\omega)\right]}{(1+e\cos x_3)^2}
\end{aligned} \tag{3.4.14}$$

The numerical integration begins from the initial conditions $(x_1, x_2, x_3)^{\mathrm{T}} = (0, 0, 0)^{\mathrm{T}}$ at $\nu = 0$.

Let successively

$$e=0.8,\ K=1.1,\ \gamma=0.1,\ \alpha=0.9,\ \omega=1.2 \tag{3.4.15}$$

$$e=0.4,\ K=1.0,\ \gamma=0.2,\ \alpha=0.7,\ \omega=0.1 \tag{3.4.16}$$

Chaos occurs in both cases. Their time histories, Poincaré maps, the largest Lyapunov exponents and power spectrums are shown in Figs. 3.21 and 3.22. Lyapunov exponents of chaos (3.4.15) are 0.55, 0.00 and -1.01. Lyapunov exponents of chaos (3.4.16) are 0.39, 0.00 and -0.65.

If e is small, chaos still appears due to the magnetic torque. For example, let

$$e=0.04,\ K=1.0,\ \gamma=0.2,\ \alpha=0.7,\ \omega=0.1 \tag{3.4.17}$$

The time histories, Poincaré map, the largest Lyapunov exponent and power spectrums are shown in Fig. 3.23. Lyapunov exponents in this case are 0.33, 0.00 and -0.52.

However, if both e and α are small, periodic motion appears. For example, let

$$e=0.08,\ K=1.1,\ \gamma=0.1,\ \alpha=0.09,\ \omega=1.2 \tag{3.4.18}$$

The phase trajectory and the largest Lyapunov exponent are shown in Fig. 3.24. The Lyapunov exponents in this case are 0.00, –0.05 and –0.05.

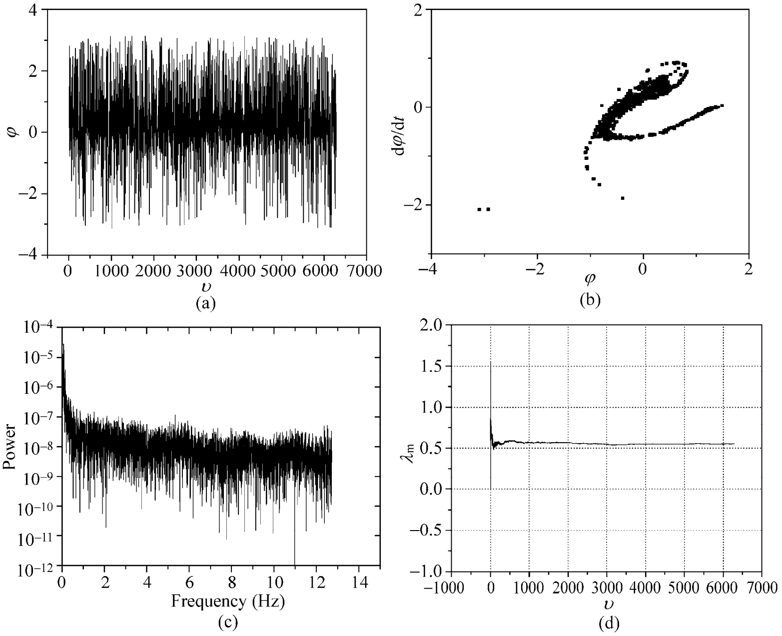

Figire 3.21 Chaos (3.4.16): (a) the time history; (b) the Poincaré map; (c) power spectrum; and (d) the largest Lyapunov exponent

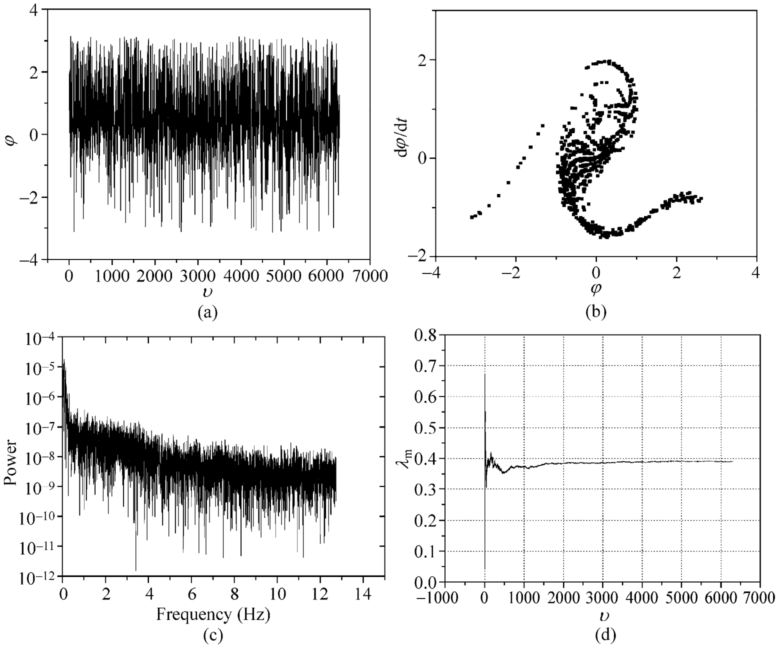

Figure 3.22 Chaos (3.4.17): (a) the time history; (b) the Poincaré map; (c) power spectrum; and (d) the largest Lyapunov exponent

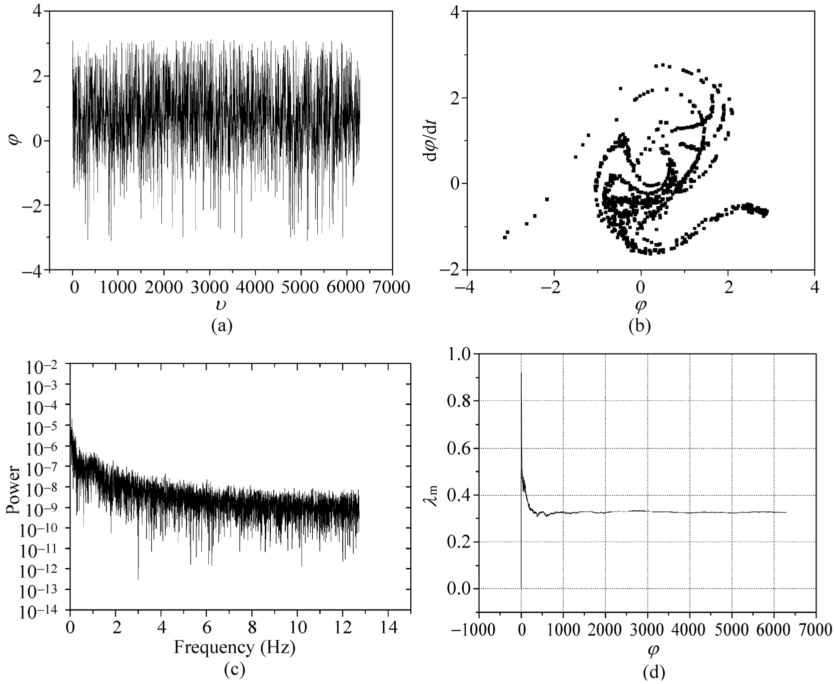

Figure 3.23 Chaos (3.4.17): (a) the time history; (b) the Poincaré map; (c) power spectrum; and (d) the largest Lyapunov exponent

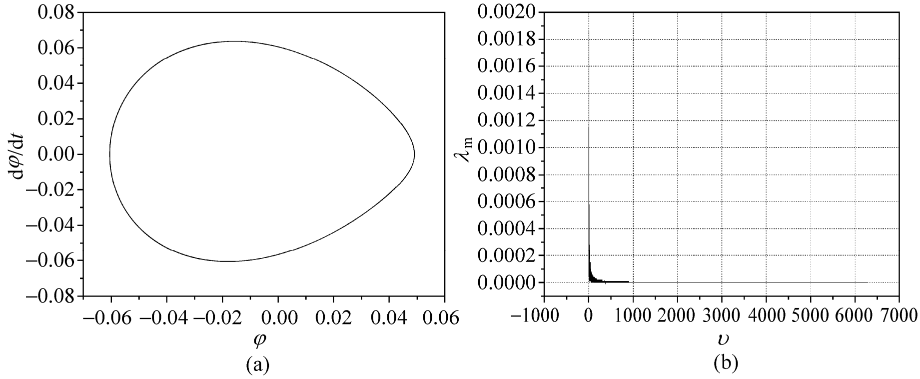

Figure 3.24 Periodic motion: (a) the time history; and (b) the largest Lyapunov exponent

References

[1] Gouliaev VI, Zubritska AL, Koshkin VL. Universal sequence of period-doubling bifurcation of satellite vibrations in an elliptical orbit. *Mechanics of Solids*, 1989, 24(3), 5-10

[2] Seisl M, Steindl AL. Chaoticsche schwingungen von satelliten. *Zeitschrift für Angewandte Mathematik und Mechanik*, 1989, 69, 352-354

[3] Koch BP, Bruhn B. Chaotic and periodic motions of satellites in elliptic orbits. *Zeitschrift für Naturforschung. Teil A*, 1989, 44, 1155-1162

[4] Chen LQ, Liu YZ. Chaotic attitude motion of a class of spacecrafts on an ellipic orbit. *Technische Mechanik*, 1998, 18, 41-44

[5] Beletsky VV. *Regular und Chaotisch Bewegung Sturrer Korper*. Berlin: Teubner-Verlag, 1995

[6] Beletsky VV, Pivovarov ML, Starostin EL. Regular and chaotic motions in applied dynamics of a rigid body, *Chaos*, 1996, 6(2), 155-166

[7] Khan A, Sharma R, Saha L M. Chaotic motion of an ellipsoidal satellite. *The Astronomical Journal*, 1998, 116, 2058-2066

[8] Richardson DL, Bartler T. Chaos in artificial satellite motion due to third-body effects. *Advances in the Astronautical Sciences,* 1995, 90(3), 1685-1700

[9] Ashenberg J(1996), Satellite pitch dynamics in the elliptic problem of three bodies, *Journal of Guidance, Control, and Dynamics*, 19(1), 68-74

[10] Bhardwaj R, Bhatnagar KB. Chaos in nonlinear planar oscillation of a satellite in an elliptical orbit under the influence of third body torque. *Indian Journal of Pure & Applied Mathematics*, 1997, 28 (3), 391-422

[11] Bhardwaj R, Tuli R. Chaos in attitude motion of a satellite under a third body torque in an elliptic orbit. *Indian Journal of Pure and Applied Mathematics*, 2003, 34 (2), 277-289

[12] Mehra VI, Bhatnagar KB. Planar oscillation of a satellite in an elliptic orbit under the influence of solar-radiation pressure and 3rd body torque. *Indian Journal of Pure and Applied Mathematics*, 1995, 26 (7), 725-742

[13] Stabb MC, Gray GL. Chaos in controlled, gravity gradient satellite pitch dynamics via the method of Melnikov-center stabilization, *Advances in the Astronautical Sciences,* 1993, 82(1), 147-166

[14] Gray GL, Stabb MC. Chaos in controlled, gravity gradient satellite pitch dynamics via the method of Melnikov-saddle stabilization. *Advances in the Astronautical Sciences*, 1993, 84(1), 441-449

[15] Toniolo MD, Lee M, Gray GL. Comparison of Melnikov's method and numerical simulation for predicting nonlinear dynamics in the pitch motion of actively controlled satellites in a gravity gradient field. *Advances in the Astronautical Sciences, Astrodynamics*, 1999, 103(2), 1159-1178

[16] Gouliaev VI, Zubritska AL and Koshkin VL. Universal sequence of period-doubling bifurcations for a satellite generated from the unstable steady state. *Mechanics of Solids*, 1991, 26(1), 8-12

[17] Gouliaev VI, Zavrazhina TV. Universal similarities of transition to chaos of satellite oscillation in elliptic orbit. *International Journal of Non-Linear Mechanics*, 1998, 33(2), 215-226

[18] Tong X, Rimrott FPJ. Numerical studies on chaotic planar motion of satellites in an elliptic orbit, *Chaos Solitons Fractals*, 1991, 1(2), 179-186

[19] Karasopoulos HA, Richardson DL. Numerical investigation of chaos in the attitude motion of a gravity-gradient satellite, *Advances in the Astronautical Sciences,* 1993, 85(3), 1851-1870

[20] Teofilatto P, Graziani F. On librational motion of spacecraft, *Chaos, Solitons and Fractals*, 1996, 7(10), 1721-1744

[21] Kirchgraber U, Manz U, Stoffer D. Rigorous proof of chaotic behaviour in a dumbbell satellite model. *Journal of Mathematical Analysis and Applications*, 2000, 251, 897-911

[22] Chirikov BV. A universal instability of many-dimensional oscillator systems. *Physics Reports*, 52,5(1979): 263-379

[23] Beletsky VV, Levin EM. *Dynamics of Space Tether Systems*, American Astronautical Society, San Diego, 1993

[24] Nixon MS, Misra AK. Nonlinear dynamics and chaos of two-body tethered satellite systems, *Advances in the Astronautical Sciences,* 1993, 85(1), 775-794

[25] Peng JH, Liu YZ. Chaotic motion of the tethered satellite system. *Technische Mechanik*, 1996, 16(4), 327-331

[26] Béda PB. On saddle-node bifurcation and chaos of satellites, *Nonlinear Analysis, Theory, Methods, & Applications*, 1997, 30(8), 4881-4886

[27] Fujii HA, Ichiki W. Nonlinear dynamics of the tethered subsatellite system in the station keeping phase, *Journal of Guidance, Control, and Dynamic*, 1997, 20(2), 403-406

[28] Steiner W. Transiently chaotic movements of tethered satellite systems, *Zeitschrift fuer Angewandte Mathematik und Mechanik*, 1997, 77(S1), 323-324

[29] Steiner W. Transient chaotic oscillations of a tethered satellite system. *Acta Mech.*, 1998, 127, 155-163

[30] Beletsky VV, Pivovarov ML. The effect of the atmosphere on the attitude motion of a dumb-bell-shaped artificial satellite, *Journal of Applied Mathematics and Mechanics*, 2000, 64(5), 691-670

[31] Misra AK, Nixon MS, Modi VJ. Nonlinear dynamics of two-body tethered satellite systems: Constant length case. *Journal of the Astronautical Sciences*, 2001, 49 (2), 219-236

[32] Takeichi N, Natori MC, Okuizumi N. Dynamics behavior of a tethered system with multiple subsatellites in elliptic orbits. *Journal of Spacecraft and Rockets*, 2001, 38, 914-921

[33] Beletsky VV, Hentov AA. *Rotational Motion of a Magnetized Satellite*. Moscow: Moscow University Press, 1985 (in Russian)

[34] Bhardwaj R, Bhatnagar KB, Nonlinear planar oscillation of a satellite in circular orbit under the influence of magnetic torque 1. *Indian Journal of Pure & Applied Mathematics*, 1995, 26(12), 1225-1240

[35] Bhardwaj R, Bhatnagar KB. Nonlinear planar oscillation of a satellite in circular orbit under the influence of magnetic torque 2. *Indian Journal of Pure & Applied Mathematics*, 1998, 29(2), 139-150

[36] Beletsky VV, Lopes RVF, Pivovarov M. Chaos in spacecraft attitude motion in Earth's magnetic field, *Chaos*, 1999, 9(2), 493-498

[37] Cheng G, Liu YZ. Chaotic motion of a magnetic rigid satellite in an orbit near the equatorial plane of the earth. *Technische Mechanik*, 1999, 19(3) , 199-201

[38] Chen LQ, Liu YZ, Cheng G. Chaotic attitude motion of a magnetic rigid spacecraft in a circular orbit near the equatorial plane, *Journal of The Franklin Institute*, 2002, 339(1) , 121-128

[39] Chen LQ, Liu YZ. Chaotic attitude motion of a magnetic rigid spacecraft and its control. *International Journal of Non-Linear Mechanics*, 2002, 37(3) , 493-504

[40] Morales-Ruiz JJ. *Differential Galois Theory and Non-integrability of Hamiltonian Systems*. Basel: Birkhäuser, 1999

[41] Maciejewski AJ, Przybylska M. Non-integrability of the problem of a rigid satellite in gravitational and magnetic fields. *Celestial Mechanics and Dynamical Astronomy*, 2003, 87, 317-351

[42] Liu YZ, Chen LQ. Chaotic attitude motion of a magnetic rigid spacecraft in an elliptic orbit and its control, *Acta Mechanica Sinica*, 2003, 19(1), 71-78

[43] Bhardwaj R, Kaur P. Satellite's motion under the effect of magnetic torque. *American Journal of Applied Sciences*, 2006, 3, 1899-1902

[44] Bhardwaj R, Kaur P. Chaotic attitude tumbling of satellite in magnetic field. *American Journal of Applied Sciences*, 2006, 3, 2037-2041

[45] Wiggins S. *Global Bifurcations and Chaos: Analytical Methods*. Berlin: Springer-Verlag, 1988

Chapter 4 Chaos in Spatial Attitude Motion of Spacecraft

Abstract This chapter treats chaos in spatial attitude motion of spacecraft. The motion of torque-free rigid bodies and gyrostats are discussed in terms of Serret-Andoyer variables, which are introduced to simplify the dynamical models. The influences of the gravitational and magnetic fields on the attitude motion are revisited using the new variables. A rigid body in elliptic orbit and gravitational field, a torque-free rigid body with eccentrically rotating mass, and a magnetic gyrostat in circular orbit acted by gravitational and magnetic torques are discussed with application of Serret-Andoyer variables. The dynamical equations for each model are transformed to an integrable Hamiltonian system with small disturbance. The generalized Melnikov theory is applied to predict transverse heteroclinic points. Poincaré maps are numerically calculated to demonstrate the process from regular to chaotic motions.

Keywords spatial attitude motion, Serret-Andoyer variables, rigid body spacecraft, generalized Melnikov theory, Hamiltonian system, Poincaré map

This chapter treats chaos in spatial attitude motion of spacecraft. To simplify the dynamical models, the Serret-Andoyer variables are introduced in 4.1. Torque free rigid bodies and gyrostats are discussed in terms of Serret-Andoyer variables, and the influences of the gravitational and magnetic fields are also revisited using the variables. The models of spacecraft covered here are rigid body spacecraft in an elliptic orbit in the gravitational field, rigid spacecraft with an eccentrically rotating mass in the absence of any external torques, and a magnetic gyrostat spacecraft in a circular orbit in the gravitational and magnetic fields. The Serret-Andoyer variables are used in the first and the last models. For each model, the previous related research results are summarized in the introduction to the corresponding section. The governing equation for each model is cast into an integrable Hamiltonian system with a small Hamiltonian disturbance. The generalized Melnikov theory presented in section 2.4 is applied to predict transverse heteroclinic points. Poincaré maps are numerically calculated to demonstrate regular and chaotic motions.

4.1 Attitude Motion Described by Serret-Andoyer Variables

4.1.1 Serret-Andoyer Variables

A canonical transformation proposed independently by Serret in 1866 [1] and Andoyer in 1923 [2] was used in the representation of the attitude motion of a rigid body. The Serret-Andoyer transformation can reduce the free rigid body or gyrostat to a 2-dimensional Hamiltonian system, and thus it is suitable to relevant discussions of the attitude dynamics of spacecraft under weak external torque. Due to Deprit's work [3], some researchers call Serret-Andoyer variables as Deprit's variables.

Consider a rigid body rotating about a fixed point O. Establish an inertial reference frame $(O\text{-}X_0Y_0Z_0)$ and a frame of angular momentum $(O\text{-}x_0y_0z_0)$ with O as the origin, where Oz_0 is along the angular momentum $\boldsymbol{G}$ of the body about O and Ox_0 is along the node line of the coordinate plane (X_0,Y_0) and the plane perpendicular to the vector $\boldsymbol{G}$ (Fig. 4.1). Define the spherical coordinates h and δ to determine the orientation of $\boldsymbol{G}$ in $(O\text{-}X_0Y_0Z_0)$, and Euler's angles g, l, σ to describe the attitude of the body-fixed principal coordinates frame $(O\text{-}xyz)$ in $(O\text{-}x_0y_0z_0)$ (Fig. 4.2). Then the attitude of the body in $(O\text{-}X_0Y_0Z_0)$ can be determined by 5 variables h, δ, g, l, and σ. The direct cosines between $(O\text{-}xyz)$ and $(O\text{-}X_0Y_0Z_0)$ are shown in Table 4.1.

Table 4.1 Direct cosines

	X_0	Y_0	Z_0
x	α_1	β_1	γ_1
y	α_2	β_2	γ_2
z	α_3	β_3	γ_3

The direct cosines in Table 4.1 are defined as

$$\begin{aligned}
\alpha_1 &= \mathrm{c}h(\mathrm{cgc}l - \mathrm{sgc}\sigma\mathrm{s}l) + \mathrm{s}h\left[\mathrm{s}\delta\mathrm{s}\sigma\mathrm{s}l - \mathrm{c}\delta(\mathrm{sgc}l + \mathrm{cgc}\sigma\mathrm{s}l)\right]\\
\alpha_2 &= -\mathrm{c}h(\mathrm{cgs}l + \mathrm{sgc}\sigma\mathrm{c}l) + \mathrm{s}h[\mathrm{s}\delta\mathrm{s}\sigma\mathrm{c}l + \mathrm{c}\delta(\mathrm{sgs}l - \mathrm{cgc}\sigma\mathrm{c}l)]\\
\alpha_3 &= \mathrm{c}h\mathrm{sgs}\sigma + \mathrm{s}h(\mathrm{s}\delta\mathrm{c}\sigma + \mathrm{c}\delta\mathrm{cgs}\sigma)
\end{aligned} \tag{4.1.1a}$$

$$\begin{aligned}
\beta_1 &= \mathrm{s}h(\mathrm{cgc}l - \mathrm{sgc}\sigma\mathrm{s}l) - \mathrm{c}h[\mathrm{s}\delta\mathrm{s}\sigma\mathrm{s}l - \mathrm{c}\delta(\mathrm{sgc}l + \mathrm{cgc}\sigma\mathrm{s}l)]\\
\beta_2 &= -\mathrm{s}h(\mathrm{cgs}l + \mathrm{sgc}\sigma\mathrm{c}l) - \mathrm{c}h[\mathrm{s}\delta\mathrm{s}\sigma\mathrm{c}l + \mathrm{c}\delta(\mathrm{sgs}l - \mathrm{cgc}\sigma\mathrm{c}l)]\\
\beta_3 &= \mathrm{s}h\mathrm{sgs}\sigma - \mathrm{c}h(\mathrm{s}\delta\mathrm{c}\sigma + \mathrm{c}\delta\mathrm{cgs}\sigma)
\end{aligned} \tag{4.1.1b}$$

$$\begin{aligned}
\gamma_1 &= \mathrm{s}\delta(\mathrm{sgc}l + \mathrm{cgc}\sigma\mathrm{s}l) + \mathrm{c}\delta\mathrm{s}\sigma\mathrm{s}l \\
\gamma_2 &= \mathrm{s}\delta(\mathrm{cgc}\sigma\mathrm{c}l - \mathrm{sgs}l) + \mathrm{c}\delta\mathrm{s}\sigma\mathrm{c}l \\
\gamma_3 &= \mathrm{c}\delta\mathrm{c}\sigma - \mathrm{s}\delta\mathrm{cgs}\sigma
\end{aligned} \tag{4.1.1c}$$

where s and c are abbreviations of sin and cos..

The components ω_i $(i = 1,2,3)$ of absolute angular velocity $\boldsymbol{\omega}$ of the body in $(O\text{-}xyz)$ can be calculated as

$$\begin{aligned}
\omega_1 &= \dot{h}\gamma_1 + \dot{\delta}(\mathrm{cgc}l - \mathrm{sgc}\sigma\mathrm{s}l) + \dot{g}\mathrm{s}\sigma\mathrm{s}l + \dot{\sigma}\mathrm{c}l \\
\omega_2 &= \dot{h}\gamma_2 - \dot{\delta}(\mathrm{cgs}l + \mathrm{sgc}\sigma\mathrm{c}l) + \dot{g}\mathrm{s}\sigma\mathrm{c}l - \dot{\sigma}\mathrm{s}l \\
\omega_3 &= \dot{h}\gamma_3 + \dot{\delta}\mathrm{sgs}\sigma + \dot{g}\mathrm{c}\sigma + \dot{l}
\end{aligned} \tag{4.1.2}$$

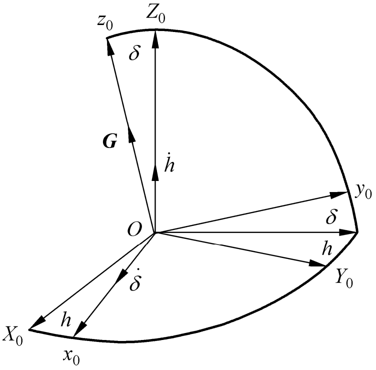

Figure 4.1 Reference frame of angular momentum and inertial frame

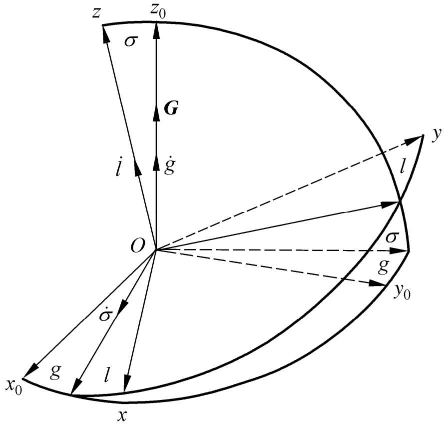

Figure 4.2 Body-fixed principal frame and frame of angular momentum

Let A, B, C be the principal moments of inertia of a body. The components G_i $(i = 1, 2, 3)$ of the angular momentum $\boldsymbol{G}$ in $(O\text{-}xyz)$ are written as

$$\begin{aligned} G_1 &= A\omega_1 = G\sin\sigma\sin l \\ G_2 &= B\omega_2 = G\sin\sigma\cos l \\ G_3 &= C\omega_3 = G\cos\sigma \end{aligned} \tag{4.1.3}$$

Then the angular velocities ω_i $(i = 1, 2, 3)$ can be expressed by G_i $(i = 1, 2, 3)$ as

$$\omega_1 = \frac{G}{A}\sin\sigma\sin l, \quad \omega_2 = \frac{G}{B}\sin\sigma\cos l, \quad \omega_3 = \frac{G}{C}\cos\sigma \tag{4.1.4}$$

Equating each equation in Eqs. (4.1.2) and (4.1.4) leads to 2 nonholonomic restraint conditions. Therefore, among h, δ, g, l, and σ there are only 3 independent variables, which can be selected as l, g, and h. Utilizing Eq. (4.1.2), one can conclude that the kinetic energy T is a homogeneous function of generalized velocities. Denote T_i $(i = 0, 1, 2)$ as the i-th degree homogeneous terms of generalized velocities. It follows that

$$T = T_2 = \frac{1}{2}(A\omega_1^2 + B\omega_2^2 + C\omega_3^2), \; T_0 = T_1 = 0 \tag{4.1.5}$$

Introduce the Lagrangian function

$$\mathcal{L} = T - V \tag{4.1.6}$$

where V is the potential energy. The generalized momenta p_l, p_g and p_h corresponding to l, g, and h can be calculated as

$$\begin{aligned} p_l &= \frac{\partial \mathcal{L}}{\partial \dot{l}} = \sum_{i=1}^{3} \frac{\partial \mathcal{L}}{\partial \omega_i}\frac{\partial \omega_i}{\partial \dot{l}} = G\cos\sigma = L \\ p_g &= \frac{\partial \mathcal{L}}{\partial \dot{g}} = \sum_{i=1}^{3} \frac{\partial \mathcal{L}}{\partial \omega_i}\frac{\partial \omega_i}{\partial \dot{g}} = G \\ p_h &= \frac{\partial \mathcal{L}}{\partial \dot{h}} = \sum_{i=1}^{3} \frac{\partial \mathcal{L}}{\partial \omega_i}\frac{\partial \omega_i}{\partial \dot{h}} = G\cos\delta = H \end{aligned} \tag{4.1.7}$$

where p_l, p_g and p_h are respectively equal to the modulus G, projection L on the Oz-axis, and projection H on the OZ_0-axis of the angular momentum G. Then the following relations can be obtained

$$\delta = \arccos(H/G), \quad \sigma = \arccos(L/G) \tag{4.1.8}$$

The six canonical variables l, g, h, L, G, H are defined as Serret-Andoyer variables, and the attitude motion of a rigid body can be described in a 6-dimensional phase space (l, g, h, L, G, H).

4.1.2 Torque-free Rigid Body

The Serret-Andoyer variables (l, g, h, L, G, H) are suitable for the analysis of the spatial attitude motion of spacecraft. Introduce the Hamiltonian function $H = T_2 - T_0 + V$. Substituting Eq. (4.1.4) into the Hamiltonian function and using Eq. (4.1.7), one obtains the function $\mathcal{H}$ expressed by the Serret-Andoyer variables

$$\mathcal{H} = \frac{1}{2}\left(\frac{\sin^2 l}{A} + \frac{\cos^2 l}{B}\right)(G^2 - L^2) + \frac{L^2}{2C} + V \tag{4.1.9}$$

In the torque-free case, since $V = 0$ and H does not depends on g and h explicitly, the corresponding generalized momenta G and H are constants. Then Eq. (4.1.9) is simplified into the Hamiltonian of a 2-dimensional system with a single independent coordinate l.

$$\mathcal{H} = \frac{1}{2}\left(\frac{\sin^2 l}{A} + \frac{\cos^2 l}{B}\right)(G^2 - L^2) + \frac{L^2}{2C} \tag{4.1.10}$$

The canonical equations with variables l, L can be derived as

$$\dot{l} = \frac{\partial \mathcal{H}}{\partial L} = L\left(\frac{1}{C} - \frac{\sin^2 l}{A} - \frac{\cos^2 l}{B}\right) \tag{4.1.11a}$$

$$\dot{L} = -\frac{\partial \mathcal{H}}{\partial l} = \frac{1}{2}(G^2 - L^2)\left(\frac{1}{B} - \frac{1}{A}\right)\sin 2l \tag{4.1.11b}$$

where $\dot{l}$ is the spin velocity of a body about Oz. Dividing each side of Eq. (4.1.11a) by that of Eq. (4.1.11b) to eliminate time variable t, one obtains a first-order autonomous system as

$$\frac{\mathrm{d}L}{\mathrm{d}l} = \frac{C(A-B)(G^2 - L^2)\sin 2l}{L[AB - C(A\cos^2 l + B\sin^2 l)]} \tag{4.1.12}$$

Equation (4.1.12) determines a set of trajectories in the phase plane (l, L) as shown in Fig. 4.3. There exist two types of singularities $S_i (i = 1, 2)$ as

$$\begin{aligned} &S_1: \quad l = 0 \text{ or } \pi, \qquad L = 0 \\ &S_2: \quad l = \pi/2 \text{ or } 3\pi/2, \quad L = 0 \end{aligned} \tag{4.1.13}$$

Since $L=0$ leads to $\sigma=\pi/2$, therefore the singularities S_1 and S_2 correspond to the permanent rotations of the body about axes Oy and Ox, respectively. Without loss of generality, it is assumed that $A>B>C$ or $A<B<C$. Then S_1 is a saddle and S_2 is a center. Thus the same conclusion as in 1.4.1 is obtained: the permanent rotation about the axis with maximal or minimal moment of inertia is stable, and the permanent rotation about the axis with middle moment of inertia is unstable. For an axisymmetrical body with $A=B$, the Hamiltonian (4.1.10) is simplified as

$$\mathcal{H}=\frac{1}{2A}(G^2-L^2)+\frac{L^2}{2C} \tag{4.1.14}$$

Since the function $\mathcal{H}$ does not contain l, the corresponding cyclic integral requires that L as well as σ are constant. The body performs a free regular precession about Oz_0 with a constant nutation angle σ.

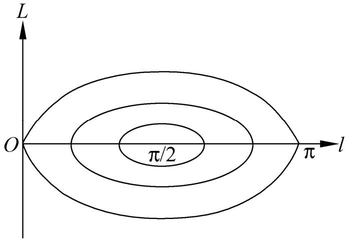

Figure 4.3 Trajectories in phase plane (l,L)

4.1.3 Torque-free Gyrostat

Consider the simple gyrostat discussed in 1.4.2. The components G_i $(i=1,2,3)$ of angular momentum $\boldsymbol{G}$ of the gyrostat in $(O\text{-}xyz)$ can be written by the Serret-Andoyer variables as

$$\begin{aligned} G_1 &= A\omega_1 = G\sin\sigma\sin l \\ G_2 &= B\omega_2 = G\sin\sigma\cos l \\ G_3 &= C\omega_3 + g_{\mathrm{R}} = G\cos\sigma \end{aligned} \tag{4.1.15}$$

where $g_{\mathrm{R}}=J_{\mathrm{R}}\Omega_{\mathrm{R}}$. Then the angular velocities ω_i $(i=1,2,3)$ can be expressed as

$$\omega_1=\frac{G}{A}\sin\sigma\sin l,\quad \omega_2=\frac{G}{B}\sin\sigma\cos l,\quad \omega_3=\frac{1}{C}(G\cos\sigma-g_{\mathrm{R}}) \tag{4.1.16}$$

The kinetic energy of the gyrostat is

$$T = \frac{1}{2}[A\omega_1^2 + B\omega_2^2 + C_P\omega_3^2 + J_R(\omega_3 + \Omega_R)^2] \tag{4.1.17}$$

where C_P is the inertia moment of the platform. For a torque-free gyrostat, there exists Jacobi's integral

$$\mathcal{H} = T_2 - T_0 \tag{4.1.18}$$

where T_0 and T_2 are, respectively, the zero-th and second degree homogeneous terms of generalized velocities in the expression of T. Substituting Eq. (4.1.16) into Eqs. (4.1.17) and (4.1.18), one expresses the Hamiltonian $\mathcal{H}$ by the Serret-Andoyer variables as

$$\mathcal{H} = \frac{1}{2}\left(\frac{\sin^2 l}{A} + \frac{\cos^2 l}{B}\right)(G^2 - L^2) + \frac{(L - g_R)^2}{2C} - \frac{g_R^2}{2J_R} \tag{4.1.19}$$

Then the canonical equations of a 2-dimensional system are obtained as

$$\dot{l} = \frac{\partial \mathcal{H}}{\partial L} = L\left(\frac{1}{C} - \frac{\sin^2 l}{A} - \frac{\cos^2 l}{B}\right) - \frac{g_R}{C} \tag{4.1.20a}$$

$$\dot{L} = -\frac{\partial \mathcal{H}}{\partial l} = \frac{1}{2}(G^2 - L^2)\left(\frac{1}{B} - \frac{1}{A}\right)\sin 2l \tag{4.1.20b}$$

Dividing each side of Eq. (4.1.20a) by that of Eq. (4.1.20b) to eliminate time t, one obtains an autonomous system as

$$\frac{\mathrm{d}L}{\mathrm{d}l} = \frac{C(A-B)(G^2 - L^2)\sin 2l}{AB(L - g_R) - LC(A\cos^2 l + B\sin^2 l)} \tag{4.1.21}$$

Equation (4.1.21) possesses the following singularities $S_i (i = 1, 2)$ corresponding to possible equilibrium states in the orbital frame $(O\text{-}XYZ)$

$$\begin{aligned} &S_1: \quad l = 0 \text{ or } \pi, \quad && L = \left(\frac{B}{B-C}\right)g_R \\ &S_2: \quad l = \pi/2 \text{ or } 3\pi/2, \quad && L = \left(\frac{A}{A-C}\right)g_R \end{aligned} \tag{4.1.22}$$

Since $L \leqslant G$, the following condition should be satisfied to ensure the existence of singularities

$$g_R \leqslant \left(1 - \frac{C}{B}\right)G \tag{4.1.23}$$

Similar to the case of a rigid body, S_1 is a saddle and S_2 is a center. The phase trajectories when $A = B$ are shown in Fig. 4.4.

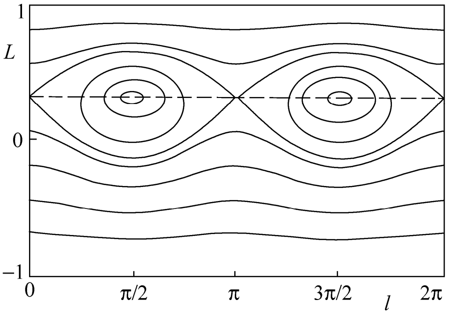

Figure 4.4 Trajectories in phase plane (l, L)

4.1.4 Gyrostat in the Gravitational Field

When the gravitational torque is considered for a gyrostat moving in a circular orbit, the inertial reference frame $(O\text{-}X_0Y_0Z_0)$ should be replaced by the orbital reference frame $(O\text{-}XYZ)$ in the definition of Serret-Andoyer variables. Then the rotation of the orbital frame must be taken into account, and the absolute angular velocity of a gyrostat should be $\boldsymbol{\omega} = \boldsymbol{\omega}' + \boldsymbol{\omega}_c$, where $\boldsymbol{\omega}'$ is the relative angular velocity of the gyrostat in $(O\text{-}XYZ)$. Projection of the angular momentum $\boldsymbol{G}$ onto $(O\text{-}xyz)$ leads to

$$\begin{aligned} G_1 &= A(\omega_1' + \omega_c \gamma_1) = G \sin\sigma \sin l \\ G_2 &= B(\omega_2' + \omega_c \gamma_2) = G \sin\sigma \cos l \\ G_3 &= C(\omega_3' + \omega_c \gamma_3) + g_{\mathrm{R}} = G \cos\sigma \end{aligned} \tag{4.1.24}$$

where γ_i $(i = 1,2,3)$ are direct cosines of axis OZ relative to $(O\text{-}xyz)$ as defined by Eq. (4.1.1c). Then the components of relative angular velocity ω_i' $(i = 1,2,3)$ can be expressed by the Serret-Andoyer variables as

$$\begin{aligned} \omega_1' &= \frac{G}{A} \sin\sigma \sin l - \omega_c \gamma_1 \\ \omega_2' &= \frac{G}{B} \sin\sigma \cos l - \omega_c \gamma_2 \\ \omega_3' &= \frac{1}{C}(G \cos\sigma - g_{\mathrm{R}}) - \omega_c \gamma_3 \end{aligned} \tag{4.1.25}$$

The Hamiltonian $\mathcal{H} = T_2 - T_0 + V$ of a simple gyrostat in the gravitational field can be derived from Eq. (1.3.42) as

$$\begin{aligned}\mathcal{H} &= \frac{1}{2}(A\omega_1'^2 + B\omega_2'^2 + C\omega_3'^2) - \frac{1}{2}\omega_c^2(A\gamma_1^2 + B\gamma_2^2 + C\gamma_3^2) \\ &+ \frac{3}{2}\omega_c^2(A\alpha_1^2 + B\alpha_2^2 + C\alpha_3^2)\end{aligned} \tag{4.1.26}$$

where α_i $(i = 1,2,3)$ are direct cosines of axis OX relative to $(O\text{-}xyz)$ defined by Eq. (4.1.1a). Substituting Eq. (4.1.25) into Eq. (4.1.26) and using the following relation

$$\gamma_1 \sin\sigma \sin l + \gamma_2 \sin\sigma \cos l + \gamma_3 \cos\sigma = \cos\delta \tag{4.1.27}$$

one obtains

$$\mathcal{H} = \mathcal{H}_0 + \omega_c \mathcal{H}_1 \tag{4.1.28}$$

where

$$\mathcal{H}_0 = \frac{1}{2}\left(\frac{\sin^2 l}{A} + \frac{\cos^2 l}{B}\right)(G^2 - L^2) + \frac{(L - g_R)^2}{2C} \tag{4.1.29}$$

$$\mathcal{H}_1 = \frac{3}{2}\omega_c(A\alpha_1^2 + B\alpha_2^2 + C\alpha_3^2) - H \tag{4.1.30}$$

in which $H = G\cos\delta$ is the projection of vector $\boldsymbol{G}$ onto axis OZ. The Hamiltonian $\mathcal{H}$ consists of two parts: the Hamiltonian of a torque-free body $\mathcal{H}_0$ and the increment $\omega_c\mathcal{H}_1$ reflecting the influence of the gravitational field.

4.1.5 Influence of the Geomagnetic Field

If the geomagnetic field contributes to the external torque, the potential energy of the magnetic field V_m should be added to the Hamiltonian $\mathcal{H}$. Consider a special case when a spacecraft is moving in an equatorial circular orbit with radius a, and the geomagnetic dipole O_eZ_m is approximately assumed to be coincident with geographic dipole O_eZ_e, i.e., the normal axis OZ of the orbital plane. Then $H_{mX} = H_{mY} = 0$, and the potential energy of magnetic field V_m expressed by Eq. (1.2.16) is simplified into

$$V_m = -I_m H_m \gamma_3 \tag{4.1.31}$$

where $H_m = \mu_m / a^3$ is the magnitude of magnetic flux density of the Earth, and γ_3 is the direct cosine of the magnetic moment $\boldsymbol{I}_m$ along the Oz-axis with respect to OZ. The Hamiltonian $\mathcal{H}$ has the same form as Eq. (4.1.28), but $\mathcal{H}_1$ is redefined as

$$\mathcal{H}_1 = \frac{3}{2}\omega_c(A\alpha_1^2 + B\alpha_2^2 + C\alpha_3^2) - H - \sigma I_{\mathrm{m}}\gamma_3 \tag{4.1.32}$$

where the parameter σ is given by

$$\sigma = \frac{\mu_{\mathrm{m}}}{\sqrt{\mu a^3}} \tag{4.1.33}$$

4.2 Rigid-body Spacecraft in an Elliptic Orbit

4.2.1 Introduction

Investigations on spatial chaotic attitude motion of rigid body spacecraft began in 1991. In order to demonstrate chaotic attitude motion of a spinning axisymmetric rigid body in a circular orbit Guran, Tong, and Rimrott calculated the Poincaré maps based on the numerical solutions to its Hamiltonian canonical equations [4]. Considering a spinning symmetric rigid body spacecraft in an elliptic orbit, Cole and Calico numerically solved its governing equation, derived by Kane and Barba [5], to examine the nonlinear behavior of both the controlled and uncontrolled cases via the Poincaré maps [6]. Beletsky and Starostin treated numerically attitude motion of symmetrical rigid spacecraft in sunlight flux, and Poincaré maps indicated the existence of regular (resonant and quasi-periodic), semi-regular (intermittent) and chaotic behaviors [7]. Balan analytically proved the existence of horseshoes and the nonintegrability of the equations governing a spinless axially asymmetric rigid body in an elliptic orbit [8]. Cheng and Liu applied the generalized version of Melnikov method and computed numerically the Poincaré maps to study the attitude motion of an asymmetric magnetic rigid body spacecraft on a circular orbit in the equator plane subjected to the geomagnetic torque [9]. Peng and Liu used the Serret-Andoyer variables to formulate attitude motion of a rigid body spacecraft in an elliptic orbit, applied the Melnikov method to detect transverse homoclinic points, and expressed chaotic behaviors in angular momentum space via the Poincaré maps [10].

This section treats a rigid-body spacecraft in an elliptic orbit. The Serret-Andoyer variables are employed to simplify the Hamiltonian description. By a contact transformation, the system is reduced to a torque-free rigid body with time-dependent moments of inertia. The system can be regarded as described by the completely integrable Euler equation under small periodic excitation. The generalized Melnikov theory is applied to the system. The Poincaré maps based on the numerical solutions are calculated to demonstrate chaotic motion.

4.2.2 Dynamical Model

Focus on attitude motion of a rigid body spacecraft in a Keplerian elliptic orbit. Both the gravitational torque and the coupling between orbital and attitude motions are taken into consideration. Then the Hamiltonian can be decomposed into the following form [11]

$$\mathcal{H} = \mathcal{H}_0 + \varepsilon \mathcal{H}_1 \tag{4.2.1}$$

where $\mathcal{H}_0$ is the Hamiltonian of a torque-free rigid body, $\mathcal{H}_1$ accounts for the disturbing and coupling terms, and a small parameter ε is the quotient of mean values of two different angular velocities, the orbital rate around the Earth and the angular velocities of attitude motion.

The Serret-Andoyer variables are used to formulate the Hamiltonian. Assume that (l, g, h, L, G, H) are defined for the rigid body in torque-free case. Then the Hamiltonian $\mathcal{H}_0$ is expressed by Eq. (4.1.10) as

$$H_0 = \frac{1}{2}\left(\frac{\sin^2 l}{A} + \frac{\cos^2 l}{B}\right)\left(G^2 - L^2\right) + \frac{L^2}{2C} \tag{4.2.2}$$

For the case of a rigid body in the gravitational field, according to [48], an infinitesimal contact transformation for the Serret-Andoyer variables was conducted as [12]

$$(l, g, h, L, G, H) \to (l', g', h', L', G', H') \tag{4.2.3}$$

The Hamiltonian $\mathcal{H}$ expressed by (l', g', h', L', G', H') has exactly the same form as the Hamiltonian $\mathcal{H}_0$ for a torque-free rigid body

$$\mathcal{H} = \frac{1}{2}\left(\frac{\sin^2 l'}{A^*} + \frac{\cos^2 l'}{B^*}\right)(G'^2 - L'^2) + \frac{L'^2}{2C^*} \tag{4.2.4}$$

The parameters A^*, B^* and C^* can be regarded as pseudo-moments of inertia with following definitions

$$\begin{aligned} \frac{1}{A^*} &= \frac{1}{A} + \frac{3\varepsilon}{4G'^2 r^3}(1 - 3\cos^2\delta')(A - B) \\ \frac{1}{B^*} &= \frac{1}{B} \\ \frac{1}{C^*} &= \frac{1}{C} + \frac{3\varepsilon}{4G'^2 r^3}(1 - 3\cos^2\delta')(C - B) \end{aligned} \tag{4.2.5}$$

where

$$\delta' = \arccos(H'/G') \tag{4.2.6}$$

Due to Eq. (4.2.4), $\mathcal{H}$ does not depend on the variables g' and h' explicitly. It follows that its corresponding momenta G' and H' as well as the parameter δ' defined by Eq. (4.2.6) are constant. When the orbit is circular, the pseudo-moments of inertia A^*, B^* and C^* are constants. In this case, the influence of the perturbation increases or decreases slightly the moments of inertia A and C, whereas B is not affected. Therefore the dynamical phase flows in plane (l', L') have the same qualitative behavior as the torque-free case (Fig. 4.1).

In the case of an elliptic orbit, the distance r of the spacecraft from the Earth center varies with time. Therefore, from Eq. (4.2.5), the pseudo-moments of inertia A^*, B^* and C^* are time dependent. Actually, substitution of Eq. (1.1.28) into Eq. (4.2.5) yields

$$\begin{aligned}
\frac{1}{A^*} &= \frac{1}{A} + \frac{3\varepsilon(1+e\cos\nu)^3}{4G'^2p^3}(1-3\cos^2\delta')(A-B) \\
\frac{1}{B^*} &= \frac{1}{B} \\
\frac{1}{C^*} &= \frac{1}{C} + \frac{3\varepsilon(1+e\cos\nu)^3}{4G'^2p^3}(1-3\cos^2\delta')(C-B)
\end{aligned} \tag{4.2.7}$$

The attitude motion problem of a rigid body under the gravitational torque is transformed to an equivalent torque-free rigid body with time-varied moments of inertia.

The Hamiltonian $\mathcal{H}$ of the rigid body under the gravitational torque can be formally expressed in Eq. (1.4.4), but the moments of inertia should be replaced by the pseudo-moments of inertia

$$\mathcal{H} = \frac{1}{2}\left(\frac{G_1^2}{A^*} + \frac{G_2^2}{B^*} + \frac{G_3^2}{C^*}\right) \tag{4.2.8}$$

Substituting Eq. (4.2.7) into Eq. (4.2.8), and writing the resulting equation in the form of Eq. (4.2.1), one obtains

$$\mathcal{H}_0 = \frac{1}{2}\left(\frac{G_1^2}{A} + \frac{G_2^2}{B} + \frac{G_3^2}{C}\right) \tag{4.2.9}$$

$$\mathcal{H}_1 = (c_1G_3^2 - c_3G_1^2)(1+3e\cos\nu) \tag{4.2.10}$$

where

$$c_1 = \lambda(C-B),\ c_2 = \lambda(C-A),\ c_3 = \lambda(B-A) \tag{4.2.11}$$

and

$$\lambda = \frac{3(1-3\cos^2\delta')}{8G'^2 p^3} \tag{4.2.12}$$

In above derivation, only the terms of the first order e are retained, because the eccentricity e of the orbit is assumed to be very small.

4.2.3 Melnikov Analysis

Euler's equations for the transformed torque-free system with pseudo-moments of inertia can be written as

$$\dot{G}_1 + \left(\frac{C^* - B^*}{B^* C^*}\right) G_2 G_3 = 0 \tag{4.2.13a}$$

$$\dot{G}_2 - \left(\frac{C^* - A^*}{C^* A^*}\right) G_3 G_1 = 0 \tag{4.2.13b}$$

$$\dot{G}_3 + \left(\frac{B^* - A^*}{A^* B^*}\right) G_1 G_2 = 0 \tag{4.2.13c}$$

Substituting Eqs. (4.2.7) into Eq. (4.2.13), omitting nonlinear terms of e, and using Eq. (1.3.25) in the resulting equation to replace time t by true anomaly ν, one transforms Euler's Eqs. (4.2.13) into the following form

$$\frac{\mathrm{d}G_1}{\mathrm{d}\nu} + c\alpha_1 \{1 + 2\varepsilon[e_1 \cos(\nu - \nu_0) - c_1]\} G_2 G_3 = 0 \tag{4.2.14a}$$

$$\frac{\mathrm{d}G_2}{\mathrm{d}\nu} - c\alpha_2 \{1 + 2\varepsilon[e_1 \cos(\nu - \nu_0) - c_2]\} G_3 G_1 = 0 \tag{4.2.14b}$$

$$\frac{\mathrm{d}G_3}{\mathrm{d}\nu} + c\alpha_3 \{1 + 2\varepsilon[e_1 \cos(\nu - \nu_0) - c_3]\} G_1 G_2 = 0 \tag{4.2.14c}$$

where $\alpha_i\ (i = 1,2,3)$ are defined by

$$\alpha_1 = \frac{C-B}{BC},\quad \alpha_2 = \frac{C-A}{CA},\quad \alpha_3 = \frac{B-A}{AB} \tag{4.2.15}$$

$c_i\ (i = 1,2,3)$ are defined by Eq. (4.2.11), and c and e_1 are defined as

$$c=\sqrt{\frac{p^3}{\mu}},\quad e_1=\frac{e}{\varepsilon} \tag{4.2.16}$$

In the unperturbed case with $\varepsilon = 0$, Euler's Eqs. (4.2.14) become

$$\frac{\mathrm{d}G_1}{\mathrm{d}\nu}+c\alpha_1 G_2 G_3=0 \tag{4.2.17a}$$

$$\frac{\mathrm{d}G_2}{\mathrm{d}\nu}-c\alpha_2 G_3 G_1=0 \tag{4.2.17b}$$

$$\frac{\mathrm{d}G_3}{\mathrm{d}\nu}+c\alpha_3 G_1 G_2=0 \tag{4.2.17c}$$

Equation (4.2.11) permits the first integral of angular momentum (1.4.5), which corresponds to the sphere of the angular momentum. On the sphere, there are two saddle points $(0, \pm G_0, 0)$ of the dynamical phase flows and four heteroclinic orbits connecting them. Denote the heteroclinic orbits by $\boldsymbol{G}^0(\nu)$, which can be solved from Eq. (4.2.17) as

$$\begin{aligned}
G_1^0(\nu)&=\pm G\sqrt{\frac{\alpha_1}{\alpha_2}}\operatorname{sech}(-c\sqrt{\alpha_1\alpha_3}G\nu)\\
G_2^0(\nu)&=\mp G\tanh(-c\sqrt{\alpha_1\alpha_3}G\nu)\\
G_3^0(\nu)&=\pm G\sqrt{\frac{\alpha_3}{\alpha_2}}\operatorname{sech}(-c\sqrt{\alpha_1\alpha_3}G\nu)
\end{aligned} \tag{4.2.17}$$

Higher-dimensional version of the Melnikov Theory presented in 1.4.4 will be applied. In this case, $\Omega_n = 1$ and Lie-Poisson bracket $\{F, H_1\}$ in Eq. (2.4.27) is given by [13]

$$\{F,H_1\}=\boldsymbol{G}^0(\nu)\cdot(\nabla_{\boldsymbol{G}^0}\mathcal{H}_0\times\nabla_{\boldsymbol{G}^0}\mathcal{H}_1) \tag{4.2.18}$$

Due to Eqs. (4.2.9) and (4.2.10)

$$\begin{aligned}
\nabla_{\boldsymbol{G}^0}\mathcal{H}_0&=\left(\frac{G_1^0}{A},\frac{G_2^0}{B},\frac{G_3^0}{C}\right)\\
\nabla_{\boldsymbol{G}^0}\mathcal{H}_1&=\left(-2c_3G_1^0\left[1+3e\cos(\nu-\nu_0)\right],0,2c_1G_3^0\left[1+3e\cos(\nu-\nu_0)\right]\right)
\end{aligned} \tag{4.2.19}$$

Hence

$$\begin{aligned}
&\boldsymbol{G}^0(\nu)\cdot(\nabla_{\boldsymbol{G}^0}H_0\times\nabla_{\boldsymbol{G}^0}H_1)\\
&=2(c_1\alpha_3+c_3\alpha_1)G_1^0(\nu)G_2^0(\nu)G_3^0(\nu)\left[1+3e\cos(\nu-\nu_0)\right]
\end{aligned} \tag{4.2.20}$$

Substitution of Eqs. (4.2.18) and (4.2.20) into Eq. (2.4.27) yields the generalized Melnikov function along the heteroclinic orbits as

$$\mathcal{M}(\nu_0)=\int_{-\infty}^{+\infty}2(c_1\alpha_3+c_3\alpha_1)G_1^0(\nu)G_2^0(\nu)G_3^0(\nu)[1+3e\cos(\nu-\nu_0)]\mathrm{d}\nu \quad (4.2.21)$$

Evaluation of the integral leads to

$$\mathcal{M}(\nu_0)=\mathcal{M}_0\sin\nu_0 \quad (4.2.22)$$

where

$$\mathcal{M}_0=-\frac{3\pi e(c_1\alpha_3+c_3\alpha_1)}{(c\sqrt{\alpha_1\alpha_3}G)^3}\operatorname{csch}\left(-\frac{\pi}{2c\sqrt{\alpha_1\alpha_3}G}\right) \quad (4.2.23)$$

There always exist simple zero points of the function $\mathcal{M}(\nu_0)$.

4.2.4 Numerical Simulations

Equation (4.2.14) is numerically integrated for thirty different initial points with fixed parameters, $A=1$, $B=1.5$, $C=2$, and $c_1=c_3=1$. The Poincaré maps in the planes (G_1, G_3) and (G_1, G_2) are obtained by plotting points with orbital period 2π. The two different types of motion, regular and chaotic, are readily distinguished as shown in Fig. 4.5. One can see from Fig. 4.5(a) and (b) that for fairly small eccentricity e, most of the Poincaré maps are fairly well covered by invariant tori. It means that most of the periodic and quasiperiodic motion are preserved. In Fig.4.5(c) and (d), as e and ε increase, some tori break into chaotic trajectories, in the sense that the successive points do not lie on a curve anymore but fill an area densely, and others break into island chains along which there is a succession of elliptic and hyperbolic orbits. As e and ε are further increased, more and more of the regular motion disappears, and finally the points are mixed chaotically as shown in Fig.4.5(e) and (f).

4.3 Rigid-body Spacecraft with an Eccentrically Rotating Mass

4.3.1 Introduction

In certain cases, single rigid body is too oversimplified to model spacecraft. Therefore, a rigid body with some moving parts is introduced as a possible model

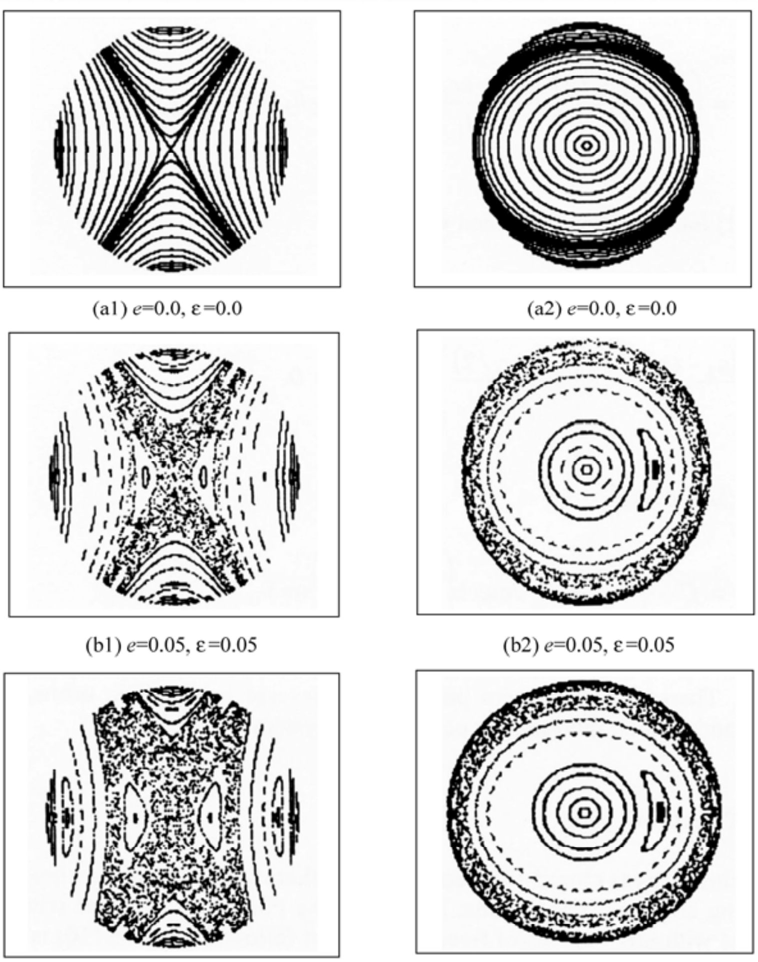

(a1) e=0.0, ε=0.0 (a2) e=0.0, ε=0.0

(b1) e=0.05, ε=0.05 (b2) e=0.05, ε=0.05

(c1) e=0.1, ε=0.1 (c2) e=0.1, ε=0.1

Figure 4.5 Poincaré maps of a rigid spacecraft in an elliptic orbit

of spacecraft. This section will deal with an example of such models, rigid body spacecraft with an eccentrically rotating mass. Chaotic attitude motion of a rigid body with moving parts will be surveyed in the following, while gyrostat spacecraft will be treated in the next section.

Gray, Kammer and Dobson employed the Melnikov method to predict chaos in a spacecraft model with small damping simulating the energy sink and two small masses oscillating symmetrically so that the system's mass center does not move relative to the carrier body [14, 15]. Gray, Dobson, and Kammer used the Melnikov method to investigate the onset of chaos in a viscously damped spacecraft that has small subbodies oscillating within it [16]. Meehan and Asokanthan numerically studied a spinning rigid spacecraft with an internal energy dissipater in the form of a spring-mass-dashpot, and calculated the time history, phase trajectory, frequency spectrum, Poincaré map and Lyapunov exponents to demonstrate periodical and chaotic motions [17]. They also computed a 3-dimensional Poincaré map and correlation dimension [18]. Gray, Mazzoleni, and Campbell applied the Melnikov method to a model consisting of a torque-free, undamped rigid carrier body with a small elastic appendage that is constrained to undergo torsional vibration only and an on-board nonlinear controller that quantitatively simulates an energy sink [19, 20]. Gray, Kammer, Dobson, and Miller further considered a more realistic case of larger damping that is implemented via a rotor immersed in a viscous fluid, applied the Melnikov method to give a necessary condition of chaos, and compared the condition with numerical simulations [21]. Miller, Gary, and Mazzoleni studied a rigid-body spacecraft that is perturbed by the motion of small oscillating submasses, a small flexible appendage constrained to undergo only torsional vibration, and a rotor immersed in a viscous fluid. They not only derived an analytical criterion for chaos from the Melnikov method, but also checked the range of validity of the criterion via extensive numerical simulations [22, 23]. Iñarrea, Lanchares, Rothos, and Salas applied a higher dimensional generalization of the Melnikov method [24] to chaotic attitude motion of a rotating asymmetric body with a periodically changing moment of inertia and under the influence of an aerodynamic drag proportional to the angular velocity, and confirmed the analytical results via numerical simulations [25]. Kuang, Meehan, Leung, Tan investigated chaotic attitude motion of a central rigid body with two hinge-connected, completely deployed solar panel arrays in a circular orbit under the influence of the gravity-gradient torques via the Melnikov method and numerical simulations [26].

In addition, chaos in some simplified models of liquid-filled rigid-body spacecraft has been investigated. Ge, Lee, Chen, and Lee numerically studied chaotic attitude motion of a damped rigid body carrier with partially-filled liquid excited by a harmonic variation internal momentum via phase portraits, Poincaré map, power spectrum, Lyapunov exponents, and detected the route to chaos as period-doubling bifurcation [27]. Ge also considered chaos in partially-filled liquid spacecraft with a feedback controller [28]. Kuang, Leung, Tan applied the Melnikov method to predict heteroclinic transversal intersections in a liquid-filled rigid body spacecraft [29].

In this section, chaotic attitude motion is examined for an asymmetrical rigid body with an eccentrically rotating mass. The model is developed as an integrable Hamiltonian system with a small Hamiltonian perturbation. The generalized Melnikov theory is applied to detect transverse heteroclinic points. The transitions to chaos are demonstrated via Poincaré maps.

4.3.2 Dynamical Model

Consider a torque-free asymmetrical rigid body attached by a small mass point P rotating in the plane (x, y) with relative angular velocity Ω_P about Oz-axis (Fig. 4.6). Assume that m_P is the mass of P, and $\boldsymbol{e}$ is the position vector from Oz-axis to the point P. Then

$$\boldsymbol{e} = e\left(\cos\theta \boldsymbol{i} + \sin\theta \boldsymbol{j}\right) \tag{4.3.1}$$

where θ is the angle of vector $\boldsymbol{e}$ to Ox-axis.

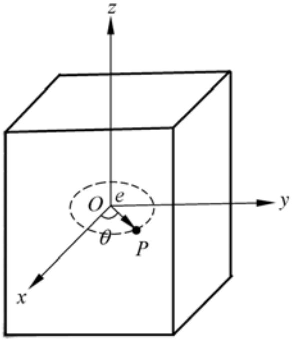

Figure 4.6 Rigid body with rotating mass point

The total angular momentum $\boldsymbol{G}$ of the system can be written as

$$\boldsymbol{G} = J \cdot \omega + g_\mathrm{P} \tag{4.3.2}$$

where $\boldsymbol{g}_\mathrm{P}$ is the increment of angular momentum caused by point P as

$$\boldsymbol{g}_\mathrm{P} = m_\mathrm{P}\boldsymbol{e} \times \left[(\boldsymbol{\omega} + \Omega_\mathrm{P}\boldsymbol{k}) \times \boldsymbol{e}\right] \tag{4.3.3}$$

In the torque-free case the angular momentum is conservative

$$G_1^2 + G_2^2 + G_3^2 = G^2 \tag{4.3.4}$$

where the components G_i $(i = 1, 2, 3)$ of $\boldsymbol{G}$ in central principal axes $(O\text{-}xyz)$ of the body are derived as

$$\begin{aligned} G_1 &= A\omega_1 + m_\mathrm{P}e^2 \sin\theta(\omega_1 \sin\theta - \omega_2 \cos\theta) \\ G_2 &= B\omega_2 - m_\mathrm{P}e^2 \cos\theta(\omega_1 \sin\theta - \omega_2 \cos\theta) \\ G_3 &= C\omega_3 + m_\mathrm{P}e^2 \Omega_\mathrm{P} \end{aligned} \tag{4.3.5}$$

Introduce a small parameter $\varepsilon = m_\mathrm{P}e^2 / A$. Then the components of angular velocity ω_i $(i = 1, 2, 3)$ can be expressed as functions of angular momentum

$$\begin{aligned}\omega_1 &= \frac{1}{A}\left[G_1 - \varepsilon A \sin\theta\left(\frac{G_1}{A}\sin\theta - \frac{G_2}{B}\cos\theta\right)\right]\\ \omega_2 &= \frac{1}{B}\left[G_2 + \varepsilon A \cos\theta\left(\frac{G_1}{A}\sin\theta - \frac{G_2}{B}\cos\theta\right)\right]\\ \omega_3 &= \frac{1}{C}(G_3 - \varepsilon A \Omega_{\mathrm{P}})\end{aligned} \tag{4.3.6}$$

The kinetic energy T of the system is

$$T = \frac{1}{2}(A\omega_1^2 + B\omega_2^2 + C\omega_3^2) + \frac{1}{2}me^2\left[(\omega_1 \sin\theta - \omega_2 \cos\theta)^2 + (\omega_3 + \Omega_{\mathrm{P}})^2\right] \tag{4.3.7}$$

The zero-th and second degree homogeneous terms of generalized velocities in Eq. (4.3.7) can be written as

$$\begin{aligned}T_2 &= \frac{1}{2}(A\omega_1^2 + B\omega_2^2 + C\omega_3^2) + \frac{1}{2}\varepsilon A\left[(\omega_1 \sin\theta - \omega_2 \cos\theta)^2 + \omega_3^2\right]\\ T_0 &= \frac{1}{2}\varepsilon A \Omega_{\mathrm{P}}^2\end{aligned} \tag{4.3.8}$$

Substituting Eq. (4.3.6) into Eq. (4.3.8) and neglecting the constant terms yield the Hamiltonian $\mathcal{H} = T_2 - T_0$ expressed by G_i $(i = 1,2,3)$ as

$$\mathcal{H} = \mathcal{H}_0 + \varepsilon \mathcal{H}_1 \tag{4.3.9}$$

where

$$\begin{aligned}\mathcal{H}_0 &= \frac{1}{2}\left(\frac{G_1^2}{A} + \frac{G_2^2}{B} + \frac{G_3^2}{C}\right)\\ \mathcal{H}_1 &= \frac{A}{2}\left[\frac{G_3}{C^2}(G_3 - 2C\Omega_{\mathrm{P}}) - \left(\frac{G_1}{A}\sin\theta - \frac{G_2}{B}\cos\theta\right)^2\right]\end{aligned} \tag{4.3.10}$$

4.3.3 Melnikov Analysis

Expressed by the Euler equations in the form of Eq. (1.3.7) in which M_i $(i = 1,2,3)$ are equal to zero and $C > B > A$ are assumed without loss of generality, the unperturbed system are

$$\dot{G}_1 + \alpha_1 G_2 G_3 = 0 \tag{4.3.11a}$$

$$\dot{G}_2 - \alpha_2 G_3 G_1 = 0 \tag{4.3.11b}$$

$$\dot{G}_3 + \alpha_3 G_1 G_2 = 0 \tag{4.3.11c}$$

where the constants α_i $(i=1,2,3)$ are defined by Eq. (4.2.15).

Equation (4.3.11) permits the first integral of the angular momentum (4.3.4), which corresponds to the sphere of the angular momentum. On the sphere there are two saddle points $(0,\pm G_0,0)$ connected by four heteroclinic orbits. Denote the heteroclinic orbits by $\boldsymbol{G}^0(t)$, which can be solved from Eq. (4.2.11). There exists the same sphere of angular momentum as described by Eq. (4.2.9). The heteroclinic orbits $\boldsymbol{G}^0(t)$ connecting two saddle points $(0,\pm G_0,0)$ have the similar form as Eq. (4.2.13)

$$\begin{aligned}
G_1^0(t) &= \pm G\sqrt{\frac{\alpha_1}{\alpha_2}}\operatorname{sech}(-\sqrt{\alpha_1\alpha_3}Gt)\\
G_2^0(t) &= \mp G\tanh(-\sqrt{\alpha_1\alpha_3}Gt)\\
G_3^0(t) &= \pm G\sqrt{\frac{\alpha_3}{\alpha_2}}\operatorname{sech}(-\sqrt{\alpha_1\alpha_3}Gt)
\end{aligned} \tag{4.3.12}$$

The Melnikov function along the heteroclinic orbits can be calculated based on Eqs. (2.4.27) and (4.2.18). In this case, noticing $\theta = \Omega_{\mathrm{P}}t$, one has

$$\begin{aligned}
&\boldsymbol{G}^0\cdot(\nabla_{\boldsymbol{G}^0}H_0\times\nabla_{\boldsymbol{G}^0}\mathcal{H}_1)\\
&= AG_1^0(t)G_2^0(t)G_3^0(t)\left[\frac{\alpha_1}{A^2}\sin^2\Omega_{\mathrm{P}}(t-t_0)-\frac{\alpha_2}{B^2}\cos^2\Omega_{\mathrm{P}}(t-t_0)\right]\\
&\quad+\frac{G_3^0(t)}{B}\left\{\alpha_2[G_1^0(t)]^2-\alpha_1[G_2^0(t)]^2\right\}\cos\Omega_{\mathrm{P}}(t-t_0)\sin\Omega_{\mathrm{P}}(t-t_0)\\
&\quad-\frac{\alpha_3A}{C^2}G_1^0(t)G_2^0(t)(G_3^0(t)-C\Omega_{\mathrm{P}})
\end{aligned} \tag{4.3.13}$$

Substituting Eqs. (4.3.13) and (4.2.18) into Eq. (2.4.27) and considering the fact that G_1, G_3 are even functions and G_2 is an odd function with respect to t, one calculates the Melnikov function after some trigonometric operations

$$\begin{aligned}
\mathcal{M}(t_0) = \frac{A}{2\Omega_{\mathrm{P}}}&\left[\left(\frac{\alpha_1}{A^2}+\frac{\alpha_2}{B^2}\right)\int_{-\infty}^{+\infty}G_1^0(t)G_2^0(t)G_3^0(t)\sin 2\Omega_{\mathrm{P}}t\mathrm{d}t\right.\\
&\left.+\frac{1}{AB}\int_{-\infty}^{+\infty}(\alpha_2(G_1^0(t))^2-\alpha_1(G_2^0(t))^2)G_3^0(t)\cos 2\Omega_{\mathrm{P}}t\mathrm{d}t\right]\sin 2\Omega_{\mathrm{P}}t_0
\end{aligned} \tag{4.3.14}$$

Substitution of Eq. (4.3.12) into the integrand in Eq. (4.3.14) and evaluation of the resulting integrals lead to the Melnikov function as

$$\mathcal{M}(t_0) = \mathcal{M}_0\sin(2\Omega_{\mathrm{P}}t_0) \tag{4.3.15}$$

where $\mathcal{M}_0$ is a constant defined by

$$\begin{aligned}\mathcal{M}_0 = {} & \frac{\pi}{4B}\left[G^2\left(1-\sqrt{\frac{\alpha_1}{\alpha_2}}\right)+\frac{4\Omega_{\mathrm{P}}^2}{\alpha_1\alpha_3}\left(1+\sqrt{\frac{\alpha_1}{\alpha_2}}\right)\right]\operatorname{sech}\left(-\frac{\pi\Omega_{\mathrm{P}}}{G\sqrt{\alpha_1\alpha_3}}\right) \\ & -\frac{\pi A\Omega_{\mathrm{P}}^2}{\alpha_1\alpha_2\alpha_3}\left(\frac{\alpha_1}{A^2}+\frac{\alpha_2}{B^2}\right)\operatorname{csch}\left(-\frac{\pi\Omega_{\mathrm{P}}}{G\sqrt{\alpha_1\alpha_3}}\right)\end{aligned} \tag{4.3.16}$$

Thus the Melnikov function $\mathcal{M}(t_0)$ always has simple zero points.

4.3.4 Numerical Simulations

The differential equation of motion derived from the Hamiltonian (4.3.9) can be numerically solved to construct the Poincaré maps in perturbed case. In the calculations, let parameters $A=1, B=1.5, C=2, G=15$ and sixty differential initial points be given. The phase portraits on the sphere (4.3.4) are projected onto the (x,z) plane. The Poincaré maps obtained from projection on (x,z) plane for different ε are shown in Fig. 4.7. Figure 4.7(a) is essentially the projection of

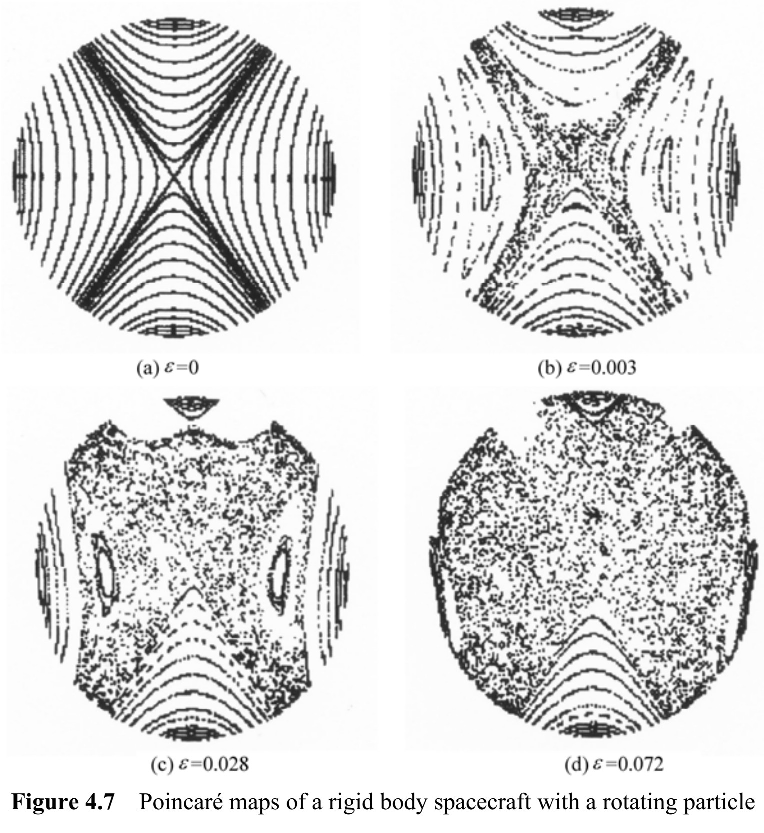

(a) $\varepsilon=0$ (b) $\varepsilon=0.003$ (c) $\varepsilon=0.028$ (d) $\varepsilon=0.072$

Figure 4.7 Poincaré maps of a rigid body spacecraft with a rotating particle

Fig. 1.17(a), as there are no perturbations. With the increase of ε, the heteroclinic orbits break up, and chaos occurs in the corresponding region (Fig. 4.7(b)). With the further increase of ε, the chaotic area is enlarged, and the local chaos becomes global (Fig. 4.7(c) and (d)).

4.4 Magnetic Gyrostat Spacecraft in a Circular Orbit

4.4.1 Introduction

As stated in 1.4.3, a gyrostat consists of two parts, a small axisymmetric rotor spinning about its axis of symmetry inside a large platform. The development of dual-spin satellites has attracted much attention on the motion of gyrostats. Chaotic attitude motion of gyrostat spacecraft has been investigated by some researchers since 1993, as documented by the following brief survey.

Tong and Rimrott developed the Hamiltonian canonical equation for an axisymmetric spinning gyrostat spacecraft in a circular orbit in a gravitational field, revealed regular and chaotic attitude motion via Poincaré maps, and found that increasingly chaotic trajectories disappeared as the spin speed of the rotor progressively increased [30]. Guran also investigated numerically chaotic attitude motion of a gyrostat spacecraft in a circular orbit in a gravitational field via Hamiltonian formalism and Poincaré map [31]. Meehan and Asokanthan developed Lagrange's equation for dual-spin spacecraft with an axial nutational damper excited by a sinusoidally varying torque, calculated numerically bifurcation diagrams, frequency spectrum, Poincaré map and Lyapunov exponents to demonstrate chaotic attitude motions, while they did not account for any field torques [32]. Tong, Tabarrok, and Rimrott formulated motion of an asymmetric gyrostat in uniform weight field via Hamiltonian canonical equation in the Serret-Andoyer variables, applied the generalized Melnikov method to detect Smale's horseshoes, and calculated numerically Poincaré maps to demonstrate regular and chaotic attitude motions [33]. Or used the Melnikov method to predict transverse homoclinic points in attitude dynamics of a dual-spinner subject to internal oscillatory torque and Coulomb friction between the two linked bodies, and numerically found that the attractor goes through a series of structures: limit cycle, quasi-periodic cycle, chaos, mode locking, intermittency, and chaos again [34]. Cheng, Liu, and Peng revisited the problem addressed in [33], while they considered the central gravitational field instead of the uniform weight field [35]. Peng and Liu investigated chaotic attitude motion of a gyrostat with an asymmetric rotor via the generalized Melnikov method and Poincaré maps [36]. Cheng and Liu expressed Hamiltonian function in the Serret-Andoyer variables for an asymmetric gyrostat spacecraft in a circular orbit subjected to both gravitational and magnetic torques. Applying the generalized Melnikov method and calculating numerically Poincaré maps, they found that the increase of the magnetic moment of the gyrostat can intensify the chaotic motion while the increase of the rotor speed can suppress the chaotic motion [37]. Iñarrea and Lanchares studied chaos in the spin-up process of a dual-spin spacecraft with time-dependent moments of inertia, used the Melnikov function to estimate analytically the width of the stochastic layer, and check the validity of the analytical estimation via numerical calculation of the width of the layer [38]. Kuang, Tan, and Leung applied the Melnikov method to study chaotic attitude motion of spacecraft under small perturbation torques, which can degenerate to a quasi-rigid satellite model investigated in [15] as well as a dissipative gyrostat under small perturbation torques [39]. Kuang, Tan, Arichandran, and Leung studied chaotic attitude motion of a gyrostat satellite spinning about arbitrarily body-fixed axes [40] as well as an asymmetrical gyrostat composed of an asymmetrical carrier and three wheels installed along its principle axes and rotating about the mass centre of the entire system under the action of both damping torques and periodic disturbance torques [41]. Kuang, Tan, and Leung researched on chaotic attitude tumbling of an asymmetric gyrostat with three symmetrical wheels along the principal axes rotating about a fixed point in a gravitational field without any damping [42] or with both nonlinear damping and periodic torques [43]. Kuang and Leung investigated bias momentum satellites and axisymmetric gyrostat satellites under gravity-gradient torques without damping [44]. In these works [39 – 44], the Serret-Andoyer variables are used to describe the Hamiltonian equations for attitude motions. The Melnikov functions are calculated to study analytically the criterion of chaos. Numerical examples are presented to reveal the existence of chaos. Considering asymmetrical gyrostat spacecraft whose rotor torque is generated by a potential field [45], Shirazi and Ghaffari-Saadat employed the Serret-Andoyer variables to describe the attitude motion, and calculated numerically second-order Poincaré maps to show that chaotic motion originates from the gravitational field effects [46]. They also applied the similar procedure to study an apparent-type gyrostat spacecraft, and calculated numerically the Lyapunov exponents to identify chaos quantitatively [47].

This section treats chaotic motion of an asymmetric magnetic gyrostat spacecraft in a circular orbit subjected to both gravitational and magnetic torques. The Hamiltonian formalism is expressed in the Serret-Andoyer variables as an integrable system with a small perturbation. The unperturbed system has saddle points connected by heteroclinic orbits. The Melnikov function for the heteroclinic orbits is calculated. Numerical evaluations show that the function has simple zeros. Poincaré maps are numerically computed to demonstrate regular and chaotic attitude motions. Numerical results reveal that chaotic areas in the Poincaré maps increase with the magnetic moment of the gyrostat and decrease with the rotor speed.

4.4.2 Unperturbed Motion of a Gyrostat

Consider a simple gyrostat (*S*) moving in a circular orbit as a model of a dual-spin satellite. The gyrostat is composed of a platform S_{P} and a rotor S_{P} rotating about axis *Oz* with relative angular velocity $\varOmega_0$. When the gravitational and geomagnetic torques are considered the Hamiltonian $\mathcal{H}$ of the system can be expressed in the Serret-Andoyer variables as shown in Eqs. (4.1.28), (4.1.29) and (4.1.31)

$$\mathcal{H} = \mathcal{H}_0 + \omega_c \mathcal{H}_1 \tag{4.4.1}$$

where

$$\begin{aligned} \mathcal{H}_0 &= \frac{1}{2}\left(\frac{\sin^2 l}{A} + \frac{\cos^2 l}{B}\right)(G^2 - L^2) + \frac{(L - g_{\mathrm{R}})^2}{2C} \\ \mathcal{H}_1 &= \frac{3}{2}\omega_c (A\alpha_1^2 + B\alpha_2^2 + C\alpha_3^2) - H - \kappa I_{\mathrm{m}}\gamma \end{aligned} \tag{4.4.2}$$

and $\mathcal{H}_0$ is the Hamiltonian of a torque-free gyrostat. Since ω_c is sufficiently small, the influence of gravitational and geomagnetic torques can be regarded as perturbations to the torque-free state.

For the unperturbed motion of a torque-free gyrostat, the canonical equations with variables *g* and *G* require

$$\dot{g} = \frac{\partial \mathcal{H}_E}{\partial G} = G\left(\frac{\sin^2 l}{A} + \frac{\cos^2 l}{B}\right) \tag{4.4.3}$$

Denote the right hand of (4.4.3) by $\varOmega$. Integration of Eq. (4.4.3) leads to

$$g(t) = \int_0^t \varOmega(\tau)\mathrm{d}\tau + g_0 \equiv \hat{g}(t) + g_0 \tag{4.4.4}$$

where g_0 is the initial value of g. The phase trajectories in phase plane (l, L) are determined by the following equations

$$\dot{l} = \frac{\partial \mathcal{H}}{\partial L} = L\left(\frac{1}{C} - \frac{\sin^2 l}{A} - \frac{\cos^2 l}{B}\right) - \frac{g_{\mathrm{R}}}{C}$$

$$\dot{L} = -\frac{\partial \mathcal{H}}{\partial l} = \frac{1}{2}(G^2 - L^2)\left(\frac{1}{B} - \frac{1}{A}\right)\sin 2l$$

There are two saddle points at $l = \pi/2$ and $3\pi/2, L = [A/(A - C)]g_{\mathrm{R}}$ as shown in Fig. 4.4. The heteroclinic orbits connected two saddle points can be solved from Eq. (4.4.5) and denoted by $(\hat{l}(t), \hat{L}(t))$ as

$$\begin{aligned} \tan\hat{l} &= \sqrt{\frac{A(B-C)(a-c)(c-d)}{B(A-C)(a-d)^2}}\cdot\frac{\operatorname{sech}^2 u}{\tanh u} \\ \frac{\hat{L}}{G} &= \frac{D_1 + D_2\tanh^2 u}{D_3 + D_4\tanh^2 u} \end{aligned} \tag{4.4.5}$$

where

$$u = \frac{G}{2C}\sqrt{\frac{(A-C)(B-C)(a-c)(c-d)}{AB}}\cdot(t-t_0) \tag{4.4.6}$$

The parameters $D_i\ (i=1,2,3,4), a, c, d$ are functions of constants $A, B, C, G, g_{\mathrm{R}}$ as

$$\begin{aligned} &D_1 = d(a-c), D_2 = a(c-d), D_3 = a-c, D_4 = c-d \text{ (if } d \leqslant L/G \leqslant c) \\ &D_1 = a(c-d), D_2 = d(a-c), D_3 = c-d, D_4 = a-c \text{ (if } c \leqslant L/G \leqslant a) \\ &a = \frac{Ag_{\mathrm{R}}}{(A-C)G} + D_0,\ b = \frac{Bg_{\mathrm{R}}}{(B-C)G},\ d = \frac{Ag_{\mathrm{R}}}{(A-C)G} - D_0 \\ &D_0 = \sqrt{\frac{C(A-B)}{B(A-C)} - \frac{AC(A-B)g_{\mathrm{R}}^2}{(A-C)^2(B-C)G^2}} \end{aligned} \tag{4.4.7}$$

4.4.3 Melnikov Analysis

According to Eq. (2.4.27) the Melnikov function can be calculated as

$$\mathcal{M}(g_0) = \int_{-\infty}^{\infty}\left\{\mathcal{H}_E, \frac{\mathcal{H}_C}{\Omega}\right\}_{\hat{l}(t),\hat{L}(t),\hat{g}(t)+g_0} \mathrm{d}t \tag{4.4.8}$$

where the Lie-Poisson bracket in the integral can be decomposed as

$$\left\{\mathcal{H}_E, \frac{\mathcal{H}_C}{\Omega}\right\} = \frac{1}{\Omega}\{\mathcal{H}_E, \mathcal{H}_C\} - \frac{\mathcal{H}_C}{\Omega^2}\{\mathcal{H}_E, \Omega\} \tag{4.4.9}$$

and

$$\begin{aligned} \{\mathcal{H}_E, \mathcal{H}_C\} &= \frac{\partial\mathcal{H}_E}{\partial l}\frac{\partial\mathcal{H}_C}{\partial L} - \frac{\partial\mathcal{H}_E}{\partial L}\frac{\partial\mathcal{H}_C}{\partial l} \\ \{\mathcal{H}_E, \Omega\} &= \frac{\partial\mathcal{H}_E}{\partial l}\frac{\partial\Omega}{\partial L} - \frac{\partial\mathcal{H}_E}{\partial L}\frac{\partial\Omega}{\partial l} \end{aligned} \tag{4.4.10}$$

Substitution of Eq. (4.4.2) into Eq. (4.4.9) leads to

$$\left\{\mathcal{H}_E, \frac{\mathcal{H}_C}{\Omega}\right\} = D(l,L) + E(l,L)\cos 2g + F(l,L)\sin 2g \tag{4.4.11}$$

where

$$\begin{aligned}
D(l,L) = {} & \frac{(A-B)\sin 2l}{(A\cos^2 l + B\sin^2 l)}\left\{\frac{3\omega_c}{4C}\sin^2\sigma\left[(C-A)(C-B)\cos\sigma - \frac{ABg_{\mathrm{R}}}{G}\right]\right.\\
& \left.+\frac{I_{\mathrm{m}}\kappa}{2}\left(1-\frac{L^2}{G^2}\right)\right\} + \frac{(A-B)\sin 2l}{(A\cos^2 l + B\sin^2 l)^2}\Big[(A\cos^2 l + B\sin^2 l)\cos\sigma\\
& +\frac{AB}{C}\left(\frac{g_{\mathrm{R}}}{G} - \cos\sigma\right)\Big]\left\{\frac{3\omega_c}{4}\big[A(\cos^2 l + \cos^2\sigma\sin^2 l)\right.\\
& \left.+B(\sin^2 l + \cos^2\sigma\cos^2 l) + C\sin^2\sigma\big] - G - I_{\mathrm{m}}\kappa\cos\sigma\right\}
\end{aligned} \tag{4.4.12a}$$

$$\begin{aligned}
E(l,L) = {} & \frac{(A-B)3\omega_c\sin 2l}{4(A\cos^2 l + B\sin^2 l)}\left\{-\left[2\cos^2\sigma(A\sin^2 l + B\cos^2 l) + C\sin^2\sigma\right.\right.\\
& \left.+\frac{AB}{C}(1+\cos^2\sigma)\right]\cos\sigma + [A\,(\cos^2 l - \cos^2\sigma\sin^2 l)\\
& + B(\sin^2 l - \cos^2\sigma\cos^2 l) - C\sin^2\sigma]\\
& \left.\cdot[1 - AB(A\cos^2 l + B\sin^2 l)^{-1}]\cos\sigma + \frac{g_{\mathrm{R}}}{GC}\right\}
\end{aligned} \tag{4.4.12b}$$

$$\begin{aligned}
F(l,L) = {} & \frac{(A-B)^2 3\omega_c}{4(A\cos^2 l + B\sin^2 l)}\left\{\sin^2\sigma\sin^2 2l - \cos\sigma\left[\frac{2\cos 2l}{A-B}(A\cos^2 l\right.\right.\\
& \left.\left.+B\sin^2 l) + \sin^2 l\right]\left[\cos\sigma + \frac{AB}{C}\left(\frac{g_{\mathrm{R}}}{G} - \cos\sigma\right)\right]\right\}
\end{aligned} \tag{4.4.12c}$$

Substitution of Eq. (4.4.12) into Eq. (4.4.8) yields

$$\begin{aligned}
\mathcal{M}(g_0) = {} & \int_{-\infty}^{\infty} D(\hat{l},\hat{L})\mathrm{d}t + \int_{-\infty}^{\infty}\left[E(\hat{l},\hat{L})\cos 2\hat{g} + F(\hat{l},\hat{L})\sin 2\hat{g}\right]\mathrm{d}t\cdot\cos 2g_0\\
& + \int_{-\infty}^{\infty}\left[-E(\hat{l},\hat{L})\sin 2\hat{g} + F(\hat{l},\hat{L})\cos 2\hat{g}\right]\mathrm{d}t\cdot\sin 2g_0
\end{aligned} \tag{4.4.13}$$

Since $D(\hat{l},\hat{L})$ and $E(\hat{l},\hat{L})$ are odd functions and $F(\hat{l},\hat{L})$ is an even function, Equation (4.4.13) can be simplified as

$$\mathcal{M}(g_0) = \int_{-\infty}^{\infty}\left[-E(\hat{l},\hat{L})\sin 2\hat{g} + F(\hat{l},\hat{L})\cos 2\hat{g}\right]\mathrm{d}t\cdot\sin 2g_0 \tag{4.4.14}$$

Denote the integral in Eq. (4.4.14) by f

$$f \equiv \int_{-\infty}^{\infty}\left[-E(\hat{l},\hat{L})\sin 2\hat{g} + F(\hat{l},\hat{L})\cos 2\hat{g}\right]\mathrm{d}t \qquad (4.4.15)$$

The integral f can be numerically evaluated for given parameters. For example, let $A=1.0, C=0.4, \omega_c=1, g_\mathrm{R}=1.6, G=10$. The dependence of f on the parameter B is shown in Fig. 4.8. One can see that f increases as B increases and $f \to 0$ only when $B \to A$. It follows that in general case the integral f is non-zero. Therefore the Melnikov function $\mathcal{M}(g_0)$ has simple zeros. Thus we conclude that the motion of the gyrostat under actions of the gravitational and magnetic torques is chaotic in the sense of Smale's horseshoe.

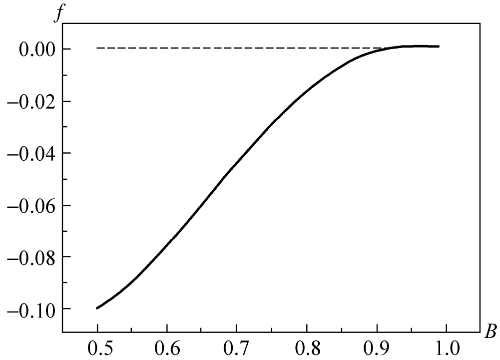

Figure 4.8 Dependence of f on parameter B

4.4.4 Numerical Simulations

Numerical integration of the canonical equations derived from the Hamiltonian (4.4.1) leads to the results on Poincaré maps. Since the Hamiltonian of the system is a constant, one may define the Poincaré map as a surface of section in the phase plane $(l, L/G)$ with the condition that $g=\pi/2$. At first the computations are performed for a gyrostat without magnetic moment in the gravitational field. The parameters are given as $A=1.0, B=0.8, C=0.4, \omega_c=1$, and the results of Poincaré maps for different g_R are shown in Fig. 4.6. When the rotor speed is fairly small as in Fig. 4.9(a), the Poincaré map is full of irregular points. As the rotor speed increases the chaotic trajectories gradually disappear and the motion becomes quite regular, as shown in Fig. 4.9(b), (c), (d).

For the case of a magnetized gyrostat in gravitational and geomagnetic fields for $\kappa=1, \mathcal{H}=90$, the results are shown in Fig. 4.10. As the magnetic moment I_m increases, the region of chaos is enlarged in Fig. 4.7(a), (b), (c), but as g_R increases, the chaotic trajectories in the chaotic region decrease and the motion gradually becomes regular as shown in Fig. 4.7(d), (e), (f).

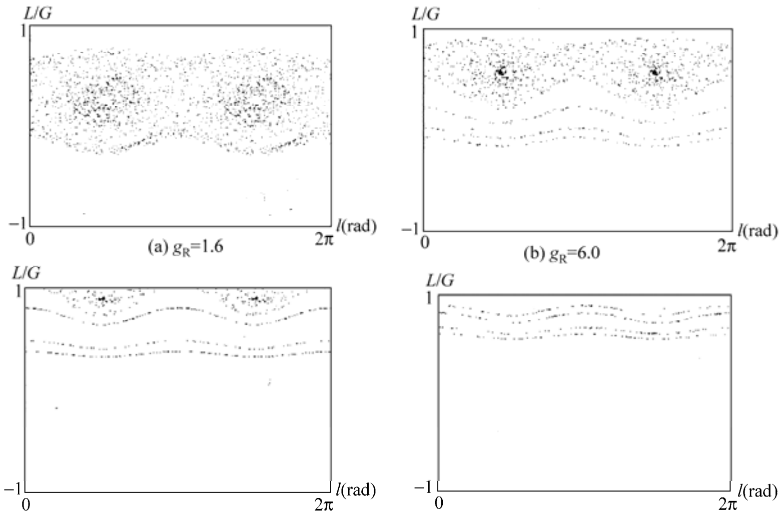

(a) g_R=1.6

(b) g_R=6.0

(c) g_R=16

(d) g_R=24

Figure 4.9 Poincaré maps of a gyrostat spacecraft

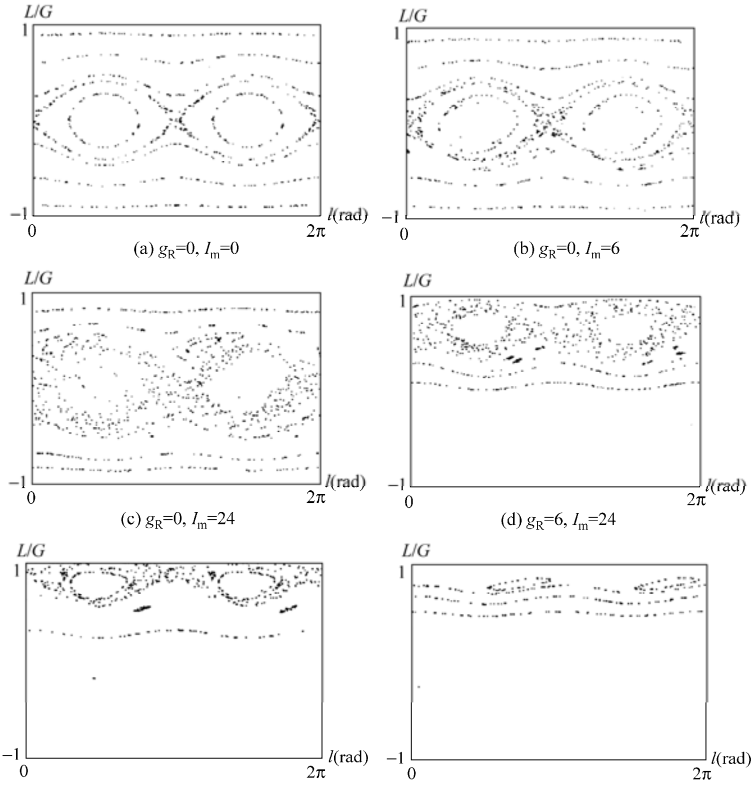

(a) g_R=0, I_m=0

(b) g_R=0, I_m=6

(c) g_R=0, I_m=24

(d) g_R=6, I_m=24

(e) g_R=8, I_m=24

(f) g_R=12, I_m=24

Figure 4.10 Poincaré maps of a magnetic gyrostat spacecraft

References

[1] Serret JA. Mémoire sur l'emploi de la méthode da la variation des arbitraries dans la théorie des mouvements de rotation. *Mémoire s de l'académie de science de Paris*, 1866, 35, 585-616

[2] Andoyer H. *Cours de mécanique céleste*. Paris: Gauthier-Villars, 1923, 1, 55-56

[3] Deprit, A. Free rotation of a rigid body studied in the phase plane. *Amer. J. Physics*, 1967, 35(5), 424-428

[4] Guran A, Tong X, Rimrott FPJ. Instabilities in a spinning axisymmetric rigid satellite, *Mech. Res. Comm.*, 1991, 18(5), 287-291

[5] Kane T R, Barba PM. Attitude stability of a spinning satellite in an elliptic orbit. *Journal of Applied Mechanics*, 1966, 33, 402-405

[6] Cole JW, Calico RA. Nonlinear oscillations of a controlled periodic system, *Journal of Guidance, Control, and Dynamics*, 1992, 15(3), 627-633

[7] Beletsky VV, Starostin EL. Regular and chaotic rotations of a satellite in sunlight flux; in: *Nonlinearity and Chaos in Engineering Dynamics*, Thomson JMT and Bishop SR eds., Wiley, New York. 193-204, 1994

[8] Balan R. Horseshoes and nonintegrability in the restricted cases of a spinless axisymmetric rigid body in a central gravitational field, *Celestial Mechanics and Dynamical Astronomy*, 1995, 63(1), 59-79

[9] Cheng G, Liu YZ. Chaotic motion of a rigid-body satellite in the magnetic field of the earth. *Journal of Shanghai Jiaotong University*, 1999, 33, 723-726 (in Chinese)

[10] Peng JH., Liu YZ. Chaotic attitude motion of a satellite on a Keplerian elliptic orbit. *Technische Mechanik*, 2000, 20(4), 311-318

[11] Kinoshita H. First-order perturbations of the two finite body problem. *Publications of the Astronomical Society of Japan*, 1972, 24, 423-457

[12] Cochran J. Effects of gravity-gradient torque on the motion of a triaxial satellite. *Celestial Mechanics*, 1972, 6, 131-152

[13] Holmes PJ, Marsden JE. Horseshoes and Arnold diffusion for Hamiltonian systems on Lie groups. *Indiana University Mathematics Journal*, 1983, 32, 273-310

[14] Gray GL, Kammer DC, Dobson I. Chaos in an attitude maneuver of a damped satellite due to time-periodic perturbations, *Advances in the Astronautical Sciences*, 1992, 79(1), 593-612

[15] Gray GL, Dobson I, Kammer DC. Chaos in a spacecraft attitude maneuver due to time-periodic perturbations. *ASME Journal of Applied Mechanics*, 1996, 63(2), 501-508

[16] Gray GL, Dobson I, Kammer DC. Detection of chaotic saddles in an attitude maneuver of a spacecraft containing a viscous damper, *Advances in the Astronautical Sciences*, 1993, 82(1), 167-184

[17] Meehan PA, Asokanthan SF. Chaotic motion in a rotating body with internal energy dissipation, *Fields Institute Communications*, 1996, 9, 175-202

[18] Meehan PA, Asokanthan SF. Chaotic motion in a spinning spacecraft with circumferential nutational damper, *Nonlinear Dyn.*, 1997, 12(1), 69-87

[19] Gray GL, Mazzoleni AP, Campbell IIIDR. Chaotic dynamics of a spacecraft with a nearly symmetric flexible appendage and energy dissipation via a nonlinear controller. *Advances in the Astronautical Sciences*, 1996, 93(2), 1093-1112

[20] Gray CL, Mazzoleni AP, Campbell DR. Analytical criterion for chaotic dynamics in flexible satellites with nonlinear controller damping, *Journal of Guidance, Control, and Dynamics*, 1998, 21(5), 558-565

[21] Gray GL, Kammer DC, Dobson I, Miller AJ. Heteroclinic bifurcations in rigid bodies containing internally moving parts and a viscous damper. *ASME Journal of Applied Mechanics*, 1999, 66(3), 720-728

[22] Miller AJ, Gary GL, Mazzoleni AP. Nonlinear dynamics of a viscously damped spacecraft with a flexible appendage and time-dependent forcing, *Advances in the Astronautical Sciences*, 1999, 103(2), 2453-2473

[23] Miller AJ, Gray GL, Mazzoleni AP. Nonlinear spacecraft dynamics with a flexible appendage, internal damping and moving internal submasses, *Journal of Guidance, Control and Dynamics*, 2001, 24(3), 605-615

[24] Wiggins S. *Global Bifurcations and Chaos: Analytical Methods*. Berlin: Springer-Verlag, 1988

[25] Iñarrea M, Lanchares V, Rothos VM, Salas JP. Chaotic rotations of an asymmetric body with time-dependent moments of inertia and viscous drag, *International Journal of Bifurcation and Chaos*, 2003, 13(2), 393-409

[26] Kuang J, Meehan PA, Leung AYT, Tan S. Nonlinear dynamics of a satellite with deployable solar panel arrays, *International Journal Non-Linear Mechanics*, 2004, 39(7), 1161-1179

[27] Ge ZM, Lee CI, Chen HH, Lee SC. Nonlinear dynamics and chaos control of a damped satellite with partially-filled liquid, *Journal of sound and Vibration*, 1998, 217, 807-825

[28] Ge ZM. *Nonlinear and Chaotic Dynamics of Satellites*. Taipei: Gau Lih Book Company, 1999

[29] Kuang J, Leung AYT, Tan S. Chaotic attitude oscillations of a satellite filled with a rotation ellipsoidal mass of liquid subject to gravity-gradient torques, *Chaos*, 2004, 14(1), 111-117

[30] Tong X, Rimrott FPJ. Chaotic attitude motion of gyrostat satellites in a central force field, *Nonlinear Dynamics*, 1993, 4, 269-278

[31] Guran A. Chaotic motion of a Kelvin type gyrostat in a circular orbit, *Acta Mechanica*, 1993, 98(1-4), 51-61

[32] Meehan PA, Asokanthan SF. Nonlinear instabilities in a dual-spin spacecraft with an axial nutational damper, *Advances in the Astronautical Sciences*, 1996, 93(1), 905-923

[33] Tong X, Tabarrok B, Rimrott FPJ. Chaotic motion of an asymmetric gyrostat in the gravitational field, *International Journal of Non-Linear Mechanics*, 1995, 30(3), 191-203

[34] Or AC. Chaotic motions of a dual-spin body, *ASME Journal of Applied Mechanics*, 1998, 65(1), 150-156

[35] Cheng G, Liu YZ, Peng JH. Chaotic motion of gyrostat in the central gravitational field. *Acta Mechanica Sinica*, 2000, 32(3), 379-384 (in Chinese)

[36] Peng, J, Liu, YZ. Chaotic motion of a gyrostat with asymmetric rotor. *Int. J. of Nonlinear*

Mechanics, 2000, 35(3), 431-437

[37] Cheng, G., Liu, YZ. Chaotic motion of an asymmetric gyrostat in the magnetic field of the Earth. *Acta Mechnica*, 2000, 141(3-4), 125-134

[38] Iñarrea M, Lanchares V. Chaos in the reorientation process of a dual-spin spacecraft with time-dependent moments of inertia. *International Journal of Bifurcation and Chaos*, 2000, 10(5), 997-1018

[39] Kuang J, Tan S, Leung AYT. Chaotic attitude motion of satellites under small perturbation torques, *Journal of Sound and Vibration*, 2000, 235(2), 175-200

[40] Kuang J, Tan S, Arichandran K, Leung AYT. Chaotic attitude motion of gyrostat satellite via Melnikov method. *International Journal of Bifurcation and Chaos*, 2001, 11(5), 1233-1260

[41] Kuang J, Tan S, Arichandran K, Leung AYT. Chaotic dynamics of an asymmetrical gyrostat, *International Journal of Non-Linear Mechanics*, 2001, 36, 1213-1233

[42] Kuang J, Tan S, Leung AYT. Chaotic attitude tumbling of an asymmetric gyrostat in a gravitational field, *Journal of Guidance, Control, and Dynamics*, 2002, 25(4), 804-815

[43] Kuang J, Tan S, Leung AYT. On Melnikov's method in the study of chaotic motions of gyrostat, *International Journal of Control*, 2002, 75(5), 328-351

[44] Kuang J, Leung AYT, Tan S. Hamiltonian and chaotic attitude dynamics of an orbiting gyrostat satellite under gravity-gradient torques, *Physica D*, 2003, 186, 1-19

[45] Shirazi KH, Ghaffari-Saadat MH. Near-integrability in a class of asymmetrical gyrostat satellites, *International Journal of Nonlinear Sciences and Numerical Simulation*, 2002, 3(2), 145-151

[46] Shirazi KH, Ghaffari-Saadat MH. Chaotic motion in a class of asymmetrical Kelvin type gyrostat satellite, *International Journal of Non-Linear Mechanics*, 2004, 39, 785-793

[47] Shirazi KH, Ghaffari-Saadat MH. Bifurcation and chaos in an apparent-type gyrostat satellite, *Nonlinear Dynamics*, 2005, 39(3), 259-274

[48] Kinoshita, H. First order perturbations of the two finite body problem. *Publications of the Astronautical Society of Japan*, 1972, 24, 423-457

Chapter 5 Control of Chaotic Attitude Motion

Abstract This chapter covers the control of chaos. It begins with an introduction to control of chaos. The control problem is formulated in the framework of system theory. The OGY method is presented as a significant and representative approach. Synchronization of chaos is briefly introduced. The parametric open-plus-closed-loop method and the stability criterion method are respectively proposed with the main ideas, the control laws, and the numerical examples. The chapter ends with controlling chaotic attitude motion. After the survey of recent investigations, planar libration of magnetic rigid spacecraft in an elliptic orbit in the gravitational and the magnetic field is treated as an example to demonstrate the applications of the parametric open-plus-closed-loop method and the stability criterion method.

Keywords control of chaos, system theory, synchronization of chaos, parametric open-plus-closed-loop method, stability criterion method, planar libration, magnetic rigid spacecraft, elliptic orbit

This chapter covers control of chaos. It begins with an introduction to control of chaos. The control problem is formulated in the framework of system theory. The OGY method is presented as a significant and representative approach. Synchronization of chaos is briefly introduced. The parametric open-plus-closed-loop method and the stability criterion method are respectively proposed with the main ideas, the control laws, and the numerical examples. The chapter ends with controlling chaotic attitude motion. After the survey of recent investigations, planar libration of magnetic rigid spacecraft in an elliptic orbit in the gravitational and the magnetic field is treated as an example to demonstrate the applications of the parametric open-plus-closed-loop method and the stability criterion method.

5.1 Control of Chaos: An Overview

5.1.1 Introduction

Chaos occurs in a large variety of engineering systems and natural processes. Identification and prediction of chaos is surely beneficial to scientific understanding and technical applications, but chaos has to be controlled so that the benefits will be maximized. Traditionally, chaos is believed to be uncontrollable because any small disturbance usually leads to other chaotic motions but not to any regular motion. However, the pioneering work of Ott, Grebogi, and Yorke in 1990 demonstrated that chaos can be converted to any one of a large number of periodic motions by making only small perturbations of an available system parameter [1]. The contributions by Ott, Grebogi, and Yorke referred to as the **OGY method**, and its generalization will be presented in 5.1.3. Since then, controlling chaos has been one of the most fascinating and rapidly growing directions within the research area of nonlinear dynamics.

Generally, **controlling chaos** is regarded as processes or mechanisms that purposefully change a chaotic motion to achieve a regular motion. Specifically, controlling chaos consists of suppression, direction, and control of chaos. **Suppression of chaos** eliminates chaotic motion while applies no requirements on the resulting motion. **Direction of chaos** targets a chaotic trajectory in the state space to a small neighborhood of previously prescribed points, circles or tori. **Control of chaos** is to manipulate a chaotic motion via an actively applied input in order to track a desired regular motion. Its special but significant case is stabilization of chaos that transforms one of an infinite number of unstable periodic orbits embedded within the chaotic attractor to stable ones. Suppression of chaos is, in the broadest sense, removing chaotic motions regardless of the outcomes. Direction of chaos is usually a necessary preparation for control of chaos. Control of chaos has the strict meaning that the controlled motion should be a periodic one with a previously given amplitude and period. Only control of chaos will be covered in this chapter.

Controlling chaos is widely investigated because of its theoretical importance and possible applications. Academically, controlling chaos is a new stage of the development of chaos theory. The development begins with the focus on the transition from order to chaos, including conditions, mechanisms, and routes of chaos occurrence. Order within chaos was then revealed as universality in chaos, statistical characteristics of chaos, and fractal structures of chaos. At the present stage, the processes that form chaos to order can be implemented via the active control. Practically, controlling chaos is an essential step toward the application of chaos theory. Controlling chaos can not only remove chaotic motion from a system when chaos is harmful but also take advantage of some aspects of chaos such as the extreme sensitivity to initial states. For example, based on the sensitivity of the three-body problem to small perturbations, NASA scientists utilized small amounts of residual fuel to send the spacecraft ISEE-3/IEC more than 50 million miles across the solar system, achieving the first scientific cometary encounter. Due to control of chaos, if a system is designed for several purposes or under diverse conditions at different times, purposefully building chaos into the system may allow the desired flexibilities for multiple uses.

5.1.2 Problem Formulations

As stated above, the problem of control of chaos contains a specified chaotic system to be controlled and a regular motion as the desired control goal, construction of a control law such that the controlled system display the desired motion. In order to facilitate the study of control design later, a formal definition of the problem is presented as follows. Consider a nonlinear system governed by a set of ordinary differential equations

$$\dot{\boldsymbol{x}} = \boldsymbol{f}(\boldsymbol{x}, t, \boldsymbol{u}) \tag{5.1.1}$$

with an observable output function

$$\boldsymbol{y} = \boldsymbol{h}(\boldsymbol{x}, t, \boldsymbol{u}) \tag{5.1.2}$$

where t is the time variable, $\boldsymbol{x} \in R^m$ is the state variable, $\boldsymbol{u} \in R^n$ is the control input, and $\boldsymbol{y} \in R^l$ are the output variable. If no control is applied, e.g. $\boldsymbol{u} = \boldsymbol{0}$, one or more components of $\boldsymbol{y}$ are chaotic. For a desired regular goal $\boldsymbol{y}_{\mathrm{d}}(t)$, a control law

$$\boldsymbol{u} = \boldsymbol{g}(\boldsymbol{x}, t) \tag{5.1.3}$$

is designed for the input $\boldsymbol{u}$, such that starting from any initial state in a region, within the precision of measurement, the desired regular motion

$$\boldsymbol{y}(t) = \boldsymbol{y}_{\mathrm{d}}(t) \tag{5.1.4}$$

can be realized for all $t > t_0$ (a given time instant). If the control law (5.1.3) is independent of the state $\boldsymbol{x}$, the control is called an **open-loop control**. If the control law (5.1.3) depends on both time t and state $\boldsymbol{x}$, the control is called a **closed-loop control** or **feedback control**. If the control goal $\boldsymbol{y}_{\mathrm{d}}(t)$ is one of the unstable solutions of Eq. (5.1.1), namely,

$$\dot{\boldsymbol{y}}_{\mathrm{d}} = \boldsymbol{f}(\boldsymbol{y}_{\mathrm{d}}, t, \boldsymbol{u}) \tag{5.1.5}$$

then it is the problem of chaos stabilization. In the following, the output variables are simply some state variables.

As formulated above, control of chaos is actually a tracking problem [2] in which the tracking goal is a periodic motion and the system to be controlled is chaotic. Therefore, the approaches developed for control of chaos are neither exclusive of nor conflictive with the established control strategies in system theory or control engineering. In fact, chaos can be successfully controlled via various methods, such as conventional linear feedback control, feedback linearization, optimal control, stochastic control, adaptive control, and intelligent control. On the other hand, control of chaos seeks to develop new theories and methods that are particularly appropriate for chaotic motions.

There are some qualitative specifications in the design of a control law for a nonlinear system. Stability must be guaranteed for the controlled system at least for reasonably large region of initial states. Accuracy and speed of response should be examined as the control performance. Robustness should be taken into consideration. Robustness is the insensitivity to effects that are not modeled. The controlled system should be able to withstand these neglected effects. The energy needed by the control, reflected in the control input should be as small as possible. However, the above-mentioned qualities conflict to some extend, and a good control design can be proposed only based on the effective trade-offs in terms of stability/robustness, stability/performance, performance/energy-saving, and so on.

5.1.3 OGY Method and Its Generalization

The OGY method is based on the geometrical structure of chaotic attractors. The control goal must be one of the infinitely many unstable periodic orbits embedded in the chaotic attractor. The unstable periodic orbit is stabilized via the linear feedback control. To highlight the essence of the method, only the stabilization of a fixed point is addressed.

Consider a 2-dimensional map with an adjustable parameter as the control input

$$\boldsymbol{z}_{i+1} = \boldsymbol{M}(\boldsymbol{z}_i, u_i) \quad (\boldsymbol{z}_i \in R^2) \tag{5.1.6}$$

If no control is applied, e.g. $u_i=0$, map (5.1.6) has a chaotic attractor in which a unstable fixed point is located that needs to be stabilized

$$\boldsymbol{z}_\mathrm{F} = \boldsymbol{M}(\boldsymbol{z}_\mathrm{F}, 0) \tag{5.1.7}$$

Local linearization of Eq. (5.1.6) in the neighborhood of ($\boldsymbol{z}_\mathrm{F}$, 0) yields

$$\boldsymbol{z}_{i+1} - \boldsymbol{z}_\mathrm{F} = \mathbf{D}_z\boldsymbol{M}(\boldsymbol{z}_i - \boldsymbol{z}_\mathrm{F}) + \frac{\partial \boldsymbol{M}}{\partial u} u_i \tag{5.1.8}$$

where the 2×2 Jacobian matrix $\mathbf{D}_z\boldsymbol{M}$ and 2-dimensional vector $\partial\boldsymbol{M}/\partial u$ are both calculated at ($\boldsymbol{z}_\mathrm{F}$,0). Assume that the eigenvalues λ_s and λ_u of $\mathbf{D}_z\boldsymbol{M}$ satisfy $|\lambda_\mathrm{s}|<1$ and $|\lambda_\mathrm{u}|>1$. Then the eigenvectors $\boldsymbol{e}_\mathrm{s}$ and $\boldsymbol{e}_\mathrm{u}$ corresponding to λ_s and λ_u determine the stable and unstable directions in the small neighborhood of ($\boldsymbol{z}_\mathrm{F}$, 0). Denote the contravariant eigenvectors of $\boldsymbol{e}_\mathrm{s}$ and $\boldsymbol{e}_\mathrm{u}$ as $\boldsymbol{f}_\mathrm{s}$ and $\boldsymbol{f}_\mathrm{u}$ such that

$$\boldsymbol{f}_\mathrm{s}^\mathrm{T} \cdot \boldsymbol{e}_\mathrm{s} = \boldsymbol{f}_\mathrm{u}^\mathrm{T} \cdot \boldsymbol{e}_\mathrm{u} = 1\,,\ \boldsymbol{f}_\mathrm{s}^\mathrm{T} \cdot \boldsymbol{e}_\mathrm{u} = \boldsymbol{f}_\mathrm{u}^\mathrm{T} \cdot \boldsymbol{e}_\mathrm{s} = 0 \tag{5.1.9}$$

then

$$\mathbf{D}_z\boldsymbol{M} = \lambda_\mathrm{s}\boldsymbol{e}_\mathrm{s}\boldsymbol{f}_\mathrm{s}^\mathrm{T} + \lambda_\mathrm{u}\boldsymbol{e}_\mathrm{u}\boldsymbol{f}_\mathrm{u}^\mathrm{T} \tag{5.1.10}$$

Therefore, if the control law is designed as

$$u_i = -\frac{\lambda_u}{\boldsymbol{f}_u \cdot \dfrac{\partial \boldsymbol{M}}{\partial \boldsymbol{u}}} \boldsymbol{f}_u \cdot (\boldsymbol{z}_i - \boldsymbol{z}_F) \tag{5.1.11}$$

then Eqs. (5.1.8), (5.1.9), (5.1.10), and (5.1.11) lead to

$$\boldsymbol{f}_u \cdot (\boldsymbol{z}_{i+1} - \boldsymbol{z}_F) = 0 \tag{5.1.12}$$

Equation (5.1.12) implies that the control law (5.1.11) moves $\boldsymbol{z}_{i+1}$ into the stable direction of $\boldsymbol{z}_F$. Hereafter, the control is unnecessary until $\boldsymbol{z}_{i+1}$ drifts away from the stable direction. In that case, the control law should be actuated again. This original idea was proposed by Ott, Grebogi and Yorke in 1990. Hence it is called the Ott-Grebogi-Yorke method or OGY method.

The above idea can be extended to higher-dimensional maps [3]. Consider an n-dimensional map with a controllable parameter

$$\boldsymbol{z}_{i+1} = \boldsymbol{M}(\boldsymbol{z}_i, u_i) \quad (\boldsymbol{x}_n \in R^n) \tag{5.1.13}$$

If $u_i = 0$, a fixed point

$$\boldsymbol{z}_F = \boldsymbol{M}(\boldsymbol{z}_F, 0) \tag{5.1.14}$$

embedded in the chaotic attractor is the control goal. Local linearization of Eq. (5.1.13) in the neighborhood of ($\boldsymbol{z}_F$, 0) gives

$$\boldsymbol{z}_{i+1} - \boldsymbol{z}_F = \boldsymbol{A}(\boldsymbol{z}_i - \boldsymbol{z}_F) + \boldsymbol{B}u_i \tag{5.1.15}$$

where both the $n \times n$ Jacobian matrix $\boldsymbol{A} = \mathbf{D}_x\boldsymbol{M}(\boldsymbol{x}, u)$ and $n \times 1$ Jacobian matrix $\boldsymbol{B} = \mathbf{D}_u\boldsymbol{M}(\boldsymbol{x}, u)$ are calculated at $(\boldsymbol{x}, u) = (\boldsymbol{x}_F, 0)$. To stabilize $\boldsymbol{x}_F$, let us introduce a linear feedback control law

$$u_i = \boldsymbol{k}^T (\boldsymbol{z}_i - \boldsymbol{z}_F) \tag{5.1.16}$$

where $\boldsymbol{k}^T$ is the transpose of $n \times 1$ matrix $\boldsymbol{k}$ to be determined later. Substitution of Eq. (5.1.6) into Eq. (5.1.15) leads to

$$\boldsymbol{z}_{i+1} - \boldsymbol{z}_F = (\boldsymbol{A} + \boldsymbol{B}\boldsymbol{k}^T)(\boldsymbol{z}_i - \boldsymbol{z}_F) \tag{5.1.17}$$

which implies that the fixed point $\boldsymbol{x}_F$ is stable on the condition that all eigenvalues of the $n \times n$ matrix $\boldsymbol{A} + \boldsymbol{B}\boldsymbol{k}^T$ have modulus smaller than 1. The solution to the problem of the determination of $\boldsymbol{k}$ for given $\boldsymbol{A}$ and $\boldsymbol{B}$ such that the eigenvalues of the matrix $\boldsymbol{A} + \boldsymbol{B}\boldsymbol{k}^T$ have specified values is well known in system theory. The eigenvalues of the matrix $\boldsymbol{A} + \boldsymbol{B}\boldsymbol{k}^T$ are called the regulator poles, and the problem is called the pole placement problem. There is a standard algorithm, Ackermann's method [4]. Obviously, the choices of poles are not unique. A natural and effective choice is setting n_s of these poles equal to the eigenvalues of $\boldsymbol{A}$ with modulus smaller than 1 and the remaining $n - n_s$ poles to zero. Under this circumstance, the control law (5.1.16) makes z_{i+1} into the local stable manifold of z_F.

The method is proposed for maps, but it can also be applied to systems governed by differential equations via the Poincaré map. In the method, the control goal must be an unstable periodic orbit embedded in the chaotic attractor, and thus the method only solves the stabilization of chaos. The control energy needed is reasonably small, as the intrinsic stable directions are used. Because the method is based on the local linearization, the control law can be actuated only if the chaotic trajectory is sufficiently close to the goal. In the absence of noise, the control input can be arbitrarily small, while it needs a long time to wait for the chaotic trajectory to enter a very small neighborhood of the goal. To increase the effectiveness of the method, direction of chaos can be performed to target the chaotic trajectory to the desired neighborhood of the goal.

5.1.4 Synchronization: Chaos Control in a Broader Sense

In a broader sense, chaos control is a process or a mechanism that suppresses existing chaotic motion when it is harmful, as well as creates chaotic motion or enhances chaotic motion when it is beneficial or useful. Making an original regular motion chaotic is referred as **anticontrol of chaos** or **chaotification**. Therefore, chaos control concerns two systems, which may be identical, one to be controlled and the other to be achieved. In this view, chaos control may be regarded as a special case of system synchronization.

Synchronization literally means correlated time-dependent behavior between different processes that interact with each other in one way or another. The relevant research on synchronization can be dated back to Huygens who investigated frequency locking between two clocks, which is perhaps first nonlinear phenomenon observed. Synchronization has become an active research topic in nonlinear dynamics since the early 1990s when researchers realized that chaotic systems can be synchronized and recognized its potential for communications [5]. A unifying definition of synchronization is proposed for systems with control inputs as follows [6].

Consider two finite dimensional systems governed by the ordinary differential equations

$$\dot{\boldsymbol{x}}_i = \boldsymbol{f}_i(\boldsymbol{x}_1, \boldsymbol{x}_2, t, \boldsymbol{u}) \quad (i = 1, 2) \tag{5.1.18}$$

with the observable output functions

$$\boldsymbol{y}_i = \boldsymbol{h}_i(\boldsymbol{x}_1, \boldsymbol{x}_2, t, \boldsymbol{u}) \quad (i = 1, 2) \tag{5.1.19}$$

where t is the time variable, $\boldsymbol{x}_i \in R^{m_i}$ is the state variables, $\boldsymbol{u} \in R^n$ is the control input, and $\boldsymbol{y}_i \in R^l$ are the output variables. If there exists the control law

$$\boldsymbol{u} = \boldsymbol{g}(\boldsymbol{x}_1, \boldsymbol{x}_2, t) \tag{5.1.20}$$

such that, within the measuring precision,

$$\boldsymbol{y}_1(t) = \boldsymbol{y}_2(t) \tag{5.1.21}$$

for all $t > t_0$ (a given time instant), there is **synchronization** at beginning time t_0 between the two systems (5.1.18) with respect to the output functions (5.1.19).

In the above-mentioned definition, no details of initial conditions are involved. Actually, initial conditions are crucial in nonlinear systems, especially chaotic systems. Synchronization with respect to initial conditions can be divided into two classes. Local synchronization holds only for trajectories starting in small neighborhoods of given initial states, while global synchronization holds for all trajectories. In fact, there is a special synchronization problem to identify chaotic behaviors of a dynamical system for different initial conditions, which may be regarded as the two dynamical systems defined here being identical.

According to the definition presented here, both widely studied control of chaos and newly proposed anticontrol of chaos are essentially synchronization of dynamical systems. In fact, controlling chaos is the synchronization between a specific chaotic system to be controlled and a prescribed periodical system. The anti-control of chaos is the synchronization between a specific non-chaotic system and a chaotic system, usually not prescribed.

5.2 The Parametric Open-plus-closed-loop Method

5.2.1 Introduction

In 1990, Jackson advanced the **entrainment control** [7], which is the development of the **resonant control** [8] presented by Hübler and Lüscher in 1989, one of the earliest methods of controlling chaos. Its essence is to design an external excitation based on the control goal, as the open-loop control, so that the control goal is a particular solution of the controlled system. To ensure the stability of a particular solution, it is required that the control goal be in suitable regions of the state space (called **convergent regions**) and there be suitable initial conditions (called the **basin of entrainment**) when the control is activated [9, 10]. The entrainment control established by Jackson is suitable for the systems with additive controllable parameters. Extension of its idea to the systems without additive controllable parameters forms the **parametric entrainment control** [11]. Both the entrainment control and the parametric entrainment control have two restrictions. The system must be dissipative, because the convergent region exists only in this case. The unstable periodic orbits of the uncontrolled system cannot be the goal of the control, that is, the methods cannot be applied to solve the problems of stabilization. In addition, the convergent regions and the basin of entrainment are difficult to determine in practical applications.

In 1995, Jackson and Grosu advanced an **open-plus-closed-loop control** based on the entrainment control [12]. For systems with additive controllable parameters, introducing a closed-loop part into the entrainment control law remedies its defects, and may be implemented in experiments [13]. In fact, the basin of entrainment in the open-plus-closed-loop control for all classic chaotic systems is infinitely large [12]. The authors modified the approach to control nonlinear oscillators governed by non-autonomous second-order ordinary differential equations [14]. For systems without additive controllable parameters, the authors developed a **parametric open-plus-closed-loop control** [15], which will be presented in this section. The necessary inputs of the control and the robustness of the control will be discussed in numerical examples. The final subsection will clarify the relations among the entrainment control, the parametric entrainment control, the open-plus-close-loop control, and the parametric open-plus-closed-loop control, as well as the differences between the controls of an oscillator and a general dynamical system.

5.2.2 The Control Law

Consider a controllable inertial uncoupling nonlinear oscillation system with n degrees-of-freedom

$$\ddot{\boldsymbol{q}} = \boldsymbol{f}(\boldsymbol{q}, \dot{\boldsymbol{q}}, \boldsymbol{u}, t) \tag{5.2.1}$$

where n dimensional vectors $\boldsymbol{q}$, $\dot{\boldsymbol{q}}$ and $\ddot{\boldsymbol{q}}$ are the generalized coordinate, velocity and acceleration, respectively, n dimensional vector $\boldsymbol{u}$ is a control parameter, and t is the time variable. Assume that the system displays chaotic motion when no control is applied ($\boldsymbol{u} = \boldsymbol{0}$). Give a periodic control goal $\boldsymbol{q}_{\mathrm{g}}(t)$. The local linearization of Eq. (5.2.1) in the neighborhood of $(\boldsymbol{q}_{\mathrm{g}}, \dot{\boldsymbol{q}}_{\mathrm{g}}, t, \boldsymbol{0})$ leads to

$$\ddot{\boldsymbol{q}} = \boldsymbol{f}(\boldsymbol{q}_{\mathrm{g}}, \dot{\boldsymbol{q}}_{\mathrm{g}}, t, \boldsymbol{0}) + \mathbf{D}_{\dot{q}}\boldsymbol{f}(\dot{\boldsymbol{q}} - \dot{\boldsymbol{q}}_{\mathrm{g}}) + \mathbf{D}_{q}\boldsymbol{f}(\boldsymbol{q} - \boldsymbol{q}_{\mathrm{g}}) + \mathbf{D}_{u}\boldsymbol{f} \cdot \boldsymbol{u} \tag{5.2.2}$$

where the Jacobians

$$\mathbf{D}_{u}\boldsymbol{f} = \left[\frac{\partial f_i}{\partial u_j}\right]_{n\times n}, \quad \mathbf{D}_{q}\boldsymbol{f} = \left[\frac{\partial f_i}{\partial q_j}\right]_{n\times n}, \quad \mathbf{D}_{\dot{q}}\boldsymbol{f} = \left[\frac{\partial f_i}{\partial \dot{q}_j}\right]_{n\times n} \tag{5.2.3}$$

are evaluated at $(\boldsymbol{q}_{\mathrm{g}}, \dot{\boldsymbol{q}}_{\mathrm{g}}, t, \boldsymbol{0})$. Assume $\mathbf{D}_{u}\boldsymbol{f}$ be an inevitable matrix. Let

$$\boldsymbol{u}=(\mathbf{D}_{\boldsymbol{u}}\boldsymbol{f})^{-1}\left[\ddot{\boldsymbol{q}}_{\mathrm{g}}-\boldsymbol{f}(\boldsymbol{q}_{\mathrm{g}},\dot{\boldsymbol{q}}_{\mathrm{g}},t,0)+(\mathbf{D}_{\dot{\boldsymbol{q}}}\boldsymbol{f}-\boldsymbol{A})(\dot{\boldsymbol{q}}_{\mathrm{g}}-\dot{\boldsymbol{q}})+(\mathbf{D}_{\boldsymbol{q}}\boldsymbol{f}-\boldsymbol{B})(\boldsymbol{q}_{\mathrm{g}}-\boldsymbol{q})\right] \tag{5.2.4}$$

where the $n\times n$ matrices of both $\boldsymbol{A}$ and $\boldsymbol{B}$ are diagonal

$$\boldsymbol{A}=\mathrm{diag}[\alpha_1,\alpha_2,\cdots,\alpha_n],\ \ \boldsymbol{B}=\mathrm{diag}[\beta_1,\beta_2,\cdots,\beta_n] \tag{5.2.5}$$

with the undetermined elements α_i and β_j $(i,j=1,2,\cdots,n)$. Substitution of Eq. (5.2.4) into Eq. (5.2.5) yields

$$(\ddot{\boldsymbol{q}}-\ddot{\boldsymbol{q}}_{\mathrm{g}})+\boldsymbol{A}(\dot{\boldsymbol{q}}-\dot{\boldsymbol{q}}_{\mathrm{g}})+\boldsymbol{B}(\boldsymbol{q}-\boldsymbol{q}_{\mathrm{g}})=0 \tag{5.2.6}$$

Hence coefficients α_i and β_j $(i,j=1,2,\cdots,n)$ can be determined by a normal design principle, such as pole placement, linear-quadratic optimal regulator, or robust service regulator, so that the differential equations

$$\ddot{y}_i+\alpha_i\dot{y}_i+\beta_i y_i=0\ \ (i=1,2,\cdots,n) \tag{5.2.7}$$

have asymptotically stable zero solutions.

Notice that the control input determined by Eq. (5.2.4) is composed of two parts. The open-loop part without feedback is

$$\boldsymbol{u}_{\mathrm{o}}=(\mathbf{D}_{\boldsymbol{u}}\boldsymbol{f})^{-1}\left[\ddot{\boldsymbol{q}}_{\mathrm{g}}-\boldsymbol{f}(\boldsymbol{q}_{\mathrm{g}},\dot{\boldsymbol{q}}_{\mathrm{g}},t,0)\right] \tag{5.2.8}$$

and the closed-loop part with feedback is

$$\boldsymbol{u}_{\mathrm{c}}=(\mathbf{D}_{\boldsymbol{u}}\boldsymbol{f})^{-1}\left[(\mathbf{D}_{\dot{\boldsymbol{q}}}\boldsymbol{f}-\boldsymbol{A})(\dot{\boldsymbol{q}}_{\mathrm{g}}-\dot{\boldsymbol{q}})+(\mathbf{D}_{\boldsymbol{q}}\boldsymbol{f}-\boldsymbol{B})(\boldsymbol{q}_{\mathrm{g}}-\boldsymbol{q})\right] \tag{5.2.9}$$

Besides, the system in (5.2.1) is not required to have additive controllable parameters. Therefore Eq. (5.2.4) gives a **parametric open-plus-closed-loop control law**.

Suppose to start control when $t=t_1$. To make Eq. (5.2.1) approximate Eq. (5.2.2) sufficiently well, the control should be actuated in a small neighborhood of $(\boldsymbol{q}_{\mathrm{g}},\dot{\boldsymbol{q}}_{\mathrm{g}},t,0)$. Hence the parametric open-plus-closed-loop control law takes the form

$$\begin{aligned}\boldsymbol{u}=(\mathbf{D}_{\boldsymbol{u}}\boldsymbol{f})^{-1}S(t-t_1)S(\varepsilon-|\boldsymbol{q}_{\mathrm{g}}-\boldsymbol{q}|-|\dot{\boldsymbol{q}}_{\mathrm{g}}-\dot{\boldsymbol{q}}|)\Big[\ddot{\boldsymbol{q}}_{\mathrm{g}}-\boldsymbol{f}(\boldsymbol{q}_{\mathrm{g}},\dot{\boldsymbol{q}}_{\mathrm{g}},t,0)\\+(\mathbf{D}_{\dot{\boldsymbol{q}}}\boldsymbol{f}-\boldsymbol{A})(\dot{\boldsymbol{q}}_{\mathrm{g}}-\dot{\boldsymbol{q}})+(\mathbf{D}_{\boldsymbol{q}}\boldsymbol{f}-\boldsymbol{B})(\boldsymbol{q}_{\mathrm{g}}-\boldsymbol{q})\Big]\end{aligned} \tag{5.2.10}$$

where ε is a small positive real number, and the switch function is defined by

$$S(z)=\begin{cases}0 & z\leqslant 0\\ 1 & z>0\end{cases} \tag{5.2.11}$$

In this chapter, only the nonlinear oscillator with one degree-of-freedom will be treated. For such an oscillator

$$\ddot{q} = f(q, \dot{q}, u, t) \tag{5.2.12}$$

where q, $\dot{q}$ and $\ddot{q}$ are the generalized coordinate, generalized velocity and generalized acceleration, respectively, u is a control parameter, and t is the time variable. For a given control goal q_g, the parametric open-plus-closed-loop control law starting at $t = t_1$ is designed as

$$\begin{aligned} u = {} & \frac{1}{f'_u} S(t - t_1) S(\varepsilon - |q_g - q| - |\dot{q}_g - \dot{q}|) \big[\ddot{q}_g - f(q_g, \dot{q}_g, 0, t) \\ & + (f'_{\dot{q}} + \alpha)(\dot{q}_g - \dot{q}) + (f'_q + \beta)(q_g - q) \big] \end{aligned} \tag{5.2.13}$$

where α and β can be determined via placing the poles of equation

$$(\ddot{q} - \ddot{q}_g) + \alpha(\dot{q} - \dot{q}_g) + \beta(q - q_g) = 0 \tag{5.2.14}$$

such that the solution asymptotically tends to zero.

5.2.3 Numerical Examples

The forced Duffing oscillator with a controllable parameter

$$\ddot{q} = -0.2\dot{q} + (1 + u)q - q^3 + 0.3\cos t \tag{5.2.15}$$

is treated as an example to demonstrate the application of the parametric open-plus-closed-loop control. Chaotic behavior appears without control. The control goals successively are an equilibrium point and a period 2 motion

$$q_g(t) = 1 \tag{5.2.16}$$

$$q_g(t) = 0.5 + 0.4\sin 0.5t \tag{5.2.17}$$

The control goals (5.2.16) and (5.2.17) satisfy $f'_u \neq 0$ evaluated at $(q_g, \dot{q}_g, 0, t)$. Let $\varepsilon = 1.0$, and the control is started after $t_1 = 40.0$.

The coefficients α and β are determined by the pole assignment. The roots of the characteristic polynomial associated with the closed-loop system

$$r^2 + \alpha r + \beta = 0 \tag{5.2.18}$$

should have negative real parts. Hence choose $\alpha = 2.8$ and $\beta = 4.0$.

The control can be implemented via the classical nonlinear system approaches, such as input-output linearization. The results for two goals are shown in Figs. 5.1 and 5.2, respectively. The solid lines denote the time histories of the system subjected to the parametric open-plus-closed-loop control law (5.2.13). The dashed lines denote the time histories of the system subjected to the input-output linearization control law. The dot lines denote the time histories of the uncontrolled system. In this example, the parametric open-plus-closed-loop control has a slightly longer time transition to achieve the goals than that of the input-output linearization control.

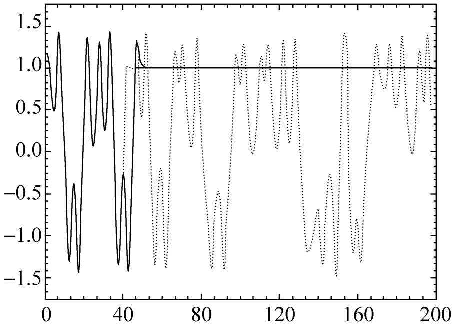

Figure 5.1 Controlling chaos to the equilibrium point

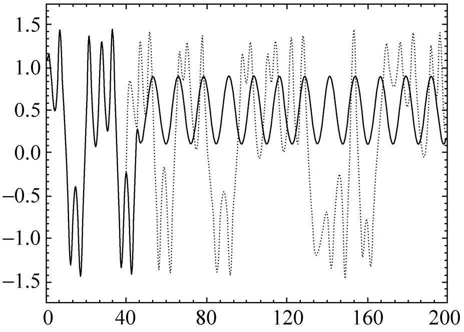

Figure 5.2 Controlling chaos to the period motion

The control inputs $u = u(t)$ for two goals are shown in Figs. 5.3 and 5.4. respectively. The solid lines denote the control signals given by Eq. (5.2.13), and the dashed lines denote the control signals given by the input-output linearization control. For both goals, a great pulse input is needed to activate the input-output linearization control. Since the parametric open-plus-closed-loop control starts just when the chaotic phase trajectory is closed to the goal periodic orbit, only a small pulse input is needed. Directly applying the input-output linearization control in the neighborhood of the goal gives the same results, but the nonlinear control law is not necessary in this case. In most practical circumstances, linear control laws are easy to implement.

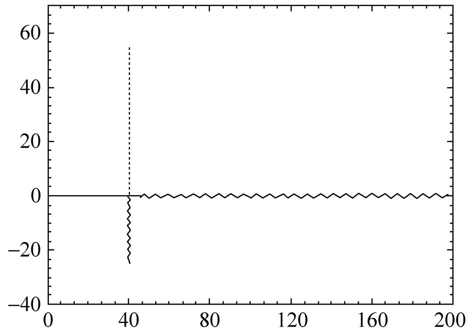

Figure 5.3 Control inputs for the equilibrium point

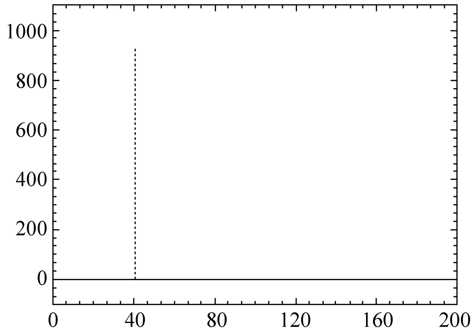

Figure 5.4 Control inputs for the period motion

The following example focuses on the robustness. Although the parametric open-plus-closed-loop control law (5.2.13) is model-based, the following example indicates that it is robust to model errors. Let us consider the forced oscillator with an additive controllable parameter

$$\ddot{q} = -0.2\dot{q} + q - 0.05q^2 - q^3 + 0.3\cos\omega t + u \tag{5.2.19}$$

Chaos occurs in it if $u = 0$. The control goals successively are an equilibrium point and a period 2 motion

$$q_{\mathrm{g}}(t) = 0 \tag{5.2.20}$$

$$q_{\mathrm{g}}(t) = \sin 0.5t \tag{5.2.21}$$

Suppose that the real model governed by Eq. (5.2.19) is unknown, and the control law is designed based on the approximate model

$$\ddot{q} = -0.2\dot{q} + 1.1q - q^3 + 0.3\cos\omega t + u \tag{5.2.22}$$

There exist both a structural error (no q^2 term) and a parametric error. Let $\varepsilon = 1.0$.

Choose $\alpha = 2.8$ and $\beta = 4.0$. Start control after $t_1 = 40.0$.

The results for both goals are shown in Figs. 5.5 and 5.6, respectively. The solid lines denote the time histories of the controlled system, and the dot lines denote the time histories of the uncontrolled system. The control error is defined as the difference between the system output and the desired goal. As shown in Figs. 5.7

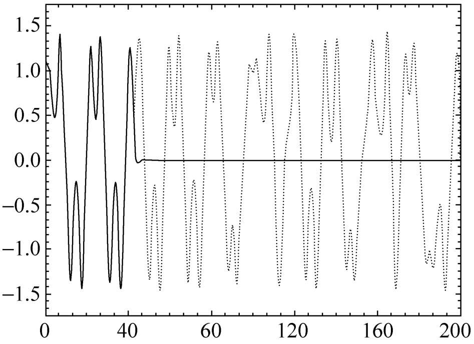

Figure 5.5 Control of chaos to the equilibrium point

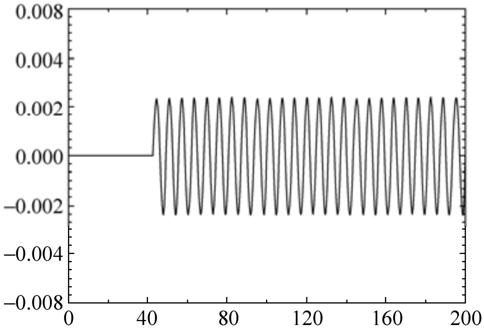

Figure 5.6 Control error to the equilibrium point

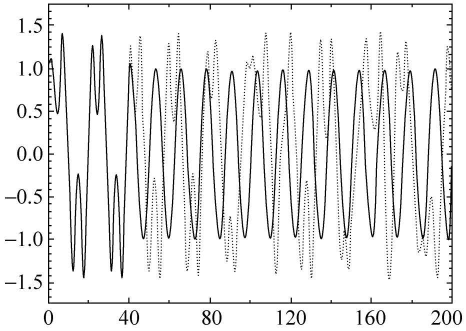

Figure 5.7 Control of chaos to the periodic motion

and 5.8, the control errors are small. Therefore the real system governed by Eq. (5.2.19) may be controlled sufficiently well by the control law (5.2.13) designed based on the model system represented by Eq. (5.2.20) if the model error is small enough.

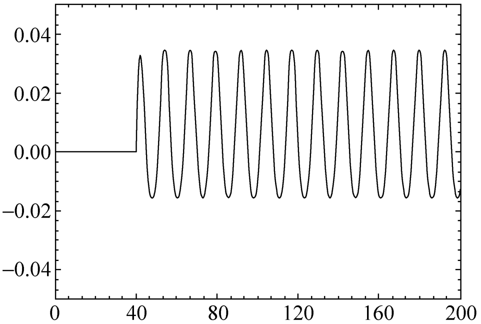

Figure 5.8 Control error to the periodic motion

5.2.4 Discussions

The parametric open-plus-closed-loop control law can also proposed for a general dynamical system (5.1.1) as

$$\boldsymbol{u} = (\mathbf{D}_u \boldsymbol{f})^{-1}[\boldsymbol{x}_{\mathrm{g}} - \boldsymbol{f}(\boldsymbol{x},t,0) + (\mathbf{D}_x \boldsymbol{f} - \boldsymbol{B}(t))(\boldsymbol{x}_{\mathrm{g}} - \boldsymbol{x})] \tag{5.2.23}$$

where $\boldsymbol{x}_{\mathrm{g}}$ is the control goal and the matrix function $\boldsymbol{B}(t)$ provides the solution to

$$\dot{\boldsymbol{y}} + \boldsymbol{B}(t)\boldsymbol{y} = 0 \tag{5.2.24}$$

asymptotically tending to zero. In practical designs, $\boldsymbol{B}(t)$ can be chosen as a constant matrix whose all eigenvalues have negative real parts.

For a system with an additive control input

$$\dot{\boldsymbol{x}} = \boldsymbol{f}(\boldsymbol{x},t) + \boldsymbol{u} \tag{5.2.25}$$

$\mathbf{D}_u \boldsymbol{f}$ is the unit matrix. Thus Eq. (5.2.23) leads to the open-closed-loop control law. If one lets

$$\boldsymbol{B}(t) = \mathbf{D}_x \boldsymbol{f} \tag{5.2.26}$$

then Eqs. (5.2.23) and (5.2.25) yield respectively the parametric entrainment control law and the entrainment control law.

The control law (5.2.23) can be employed to control nonlinear oscillators governed by non-autonomous second-order ordinary differential equations. Nevertheless the number of control inputs required by the open-plus-closed-loop control for general dynamical systems defined by Eq. (5.2.25) is equal to the dimension of state spaces. Consider a nonlinear oscillator with one degree-of-freedom, 2 control inputs are needed. The controlled system should take the form

$$\begin{aligned}\dot{x}_1 &= x_2 + v(x_1, x_2, t)\\ \dot{x}_2 &= f(x_1, x_2, t) + u(x_1, x_2, t)\end{aligned} \tag{5.2.27}$$

where x_1 and x_2 are state variables, and u and v are controllable inputs. In some practical circumstances, there may be no such controllable inputs available. Section 5.2.2 developed a control approach that requires only one control parameter. The controlled system should take the form

$$\begin{aligned}\dot{x}_1 &= x_2\\ \dot{x}_2 &= f(x_1, x_2, t) + u(x_1, x_2, t)\end{aligned} \tag{5.2.28}$$

or more general

$$\begin{aligned}\dot{x}_1 &= x_2\\ \dot{x}_2 &= f(x_1, x_2, u(x_1, x_2, t), t)\end{aligned} \tag{5.2.29}$$

5.3 The Stability Criterion Method

5.3.1 Introduction

This section presents a method for controlling chaos in the form of special nonlinear feedback proposed by Yu, Liu and Peng [16]. The method is inspired by Pyragas's continuous linear feedback control method [17] and Ushio's contraction mapping control method of discrete systems [18]. The validity of the method is based on the stability criterion of linear system, and it can be called **the stability criterion method**. The construction of a special form of a time-continuous perturbation feedback in the stability criterion method does not change the form of the desired unstable periodic orbit. The close return pairs technique [19] is utilized to estimate a desired periodic orbit chosen from numerous unstable periodic orbits embedded within a chaotic attractor. This method does not require linearization of the system around the stabilized orbit and calculation of the derivative at unstable periodic orbits. As examples of numerical simulations, the control of the Rössler system and the control of two coupled Duffing oscillators are investigated. The complexity of the experimental realization of the stability criterion method is mainly to input the desired unstable periodic orbits. Besides, the method relies on the explicit knowledge of the mathematical model of the system.

In this section, the stability criterion method is proposed only for the stabilization problem, while the idea can be employed to solve the tracking problem. The idea was also implemented in the synchronization of chaos [20].

5.3.2 The Control Law

Consider a system with an additive control input defined by Eq. (5.2.25). The system without control ($\boldsymbol{u}=\boldsymbol{0}$) has a chaotic attractor. Decompose the vector function $\boldsymbol{f}(\boldsymbol{x},t)$ into a suitably chosen linear part and the other nonlinear part

$$\boldsymbol{f}(\boldsymbol{x},t)=\boldsymbol{A}\boldsymbol{x}+\boldsymbol{h}(\boldsymbol{x},t) \tag{5.3.1}$$

where $\boldsymbol{A}$ is a constant matrix whose all eigenvalues have negative real parts and $\boldsymbol{h}(\boldsymbol{x},t)$ is a nonlinear function. Let the control goal $\boldsymbol{x}_{\mathrm{g}}(t)$ be an unstable periodic orbit embedded within the chaotic attractor. Then

$$\dot{\boldsymbol{x}}_{\mathrm{g}}=\boldsymbol{A}\boldsymbol{x}_{\mathrm{g}}+\boldsymbol{h}(\boldsymbol{x}_{\mathrm{g}},t) \tag{5.3.2}$$

Design the control input as

$$\boldsymbol{u}=\boldsymbol{h}(\boldsymbol{x}_{\mathrm{g}},t)-\boldsymbol{h}(\boldsymbol{x},t) \tag{5.3.3}$$

Substitution of Eq. (5.3.1) into Eq. (5.3.3) leads to the nonlinear feedback control law

$$\boldsymbol{u}=A(\boldsymbol{x}-\boldsymbol{x}_{\mathrm{g}})+\boldsymbol{f}(\boldsymbol{x}_{\mathrm{g}},t)-\boldsymbol{f}(\boldsymbol{x},t) \tag{5.3.4}$$

Equations (5.2.25), (5.3.1), (5.3.2) and (5.3.3) yield the governing equation of the controlled system

$$\dot{\boldsymbol{x}}-\dot{\boldsymbol{x}}_{\mathrm{g}}=A(\boldsymbol{x}-\boldsymbol{x}_{\mathrm{g}}) \tag{5.3.5}$$

Because all eigenvalues of matrix $\boldsymbol{A}$ have negative real parts, the stability criterion of linear systems guarantees the zero solution of the following equation

$$\dot{\boldsymbol{y}}=\boldsymbol{A}\boldsymbol{y} \tag{5.3.6}$$

is asymptotically stable. Therefore the controlled trajectory $\boldsymbol{x}(t)$ tends asymptotically to the goal $\boldsymbol{x}_{\mathrm{g}}(t)$. It implies that the unstable periodic orbit is stabilized. Note that the control input $\boldsymbol{u}(t)$ becomes zero after the state when the controlled system converges to the unstable periodic orbits.

Some very complicated periodically driven dynamical systems along with the stabilized unstable periodic orbit can have alternative stable solutions belonging to different basins of initial conditions. Besides, large initial values of the control input can be also undesired for some experiments. Such problems can be solved by restriction of the control input. Therefore the stabilization is achieved by small input values if Eq. (5.3.4) is modified as follows

$$\boldsymbol{u}=\begin{cases}A(\boldsymbol{x}-\boldsymbol{x}_{\mathrm{g}})+\boldsymbol{f}(\boldsymbol{x}_{\mathrm{g}},t)-\boldsymbol{f}(\boldsymbol{x},t) & \text{if } |\boldsymbol{x}-\boldsymbol{x}_{\mathrm{g}}|<\varepsilon \\ 0 & \text{otherwise}\end{cases}$$

where $\varepsilon>0$ is a restriction value of error within which $\boldsymbol{u}\neq\boldsymbol{0}$. The control input has a simple form as shown in Eq. (5.3.7). It is unnecessary to calculate any derivatives at the unstable periodic orbit of the uncontrolled system, while some Jacobian matrixes are required in the open-plus-closed-loop control.

In order to obtain the necessary information on an appropriate location of a desired periodic orbit $\boldsymbol{x}_{\mathrm{g}}(t)$, the strategy of the close return pairs described in [21, 22] is utilized. A time series of the chaotic trajectory generated by the system (5.2.25) is stroboscopically sampled in every period T when $\boldsymbol{u}=\boldsymbol{0}$. The data sampling can be used to detect the close return pairs, which consist of two successive points near each other, and indicate the existence of a periodic orbit nearby. Because of the ergodic character of orbits on a chaotic attractor, many such pairs can be obtained if the data string is long enough. Suppose that $\boldsymbol{x}_i^1$ and $\boldsymbol{x}_i^2$ are used to denote the first point and its successive point of the i-th collected return pair, $i=1,2,\cdots,M$, respectively, where M is the maximum number of collected return pairs. When the first close return pair has been detected within a predesignated region, let us take the first point $\boldsymbol{x}_1^1$ of this pair as a reference point. Then a number of close return pairs near the reference point is

$$|\boldsymbol{x}_i^1-\boldsymbol{x}_1^1|\leqslant\varepsilon_1,|\boldsymbol{x}_i^2-\boldsymbol{x}_1^2|\leqslant\varepsilon_2 \quad (i=1,2,\cdots,M) \tag{5.3.7}$$

The mean value

$$\boldsymbol{x}_{\mathrm{g}}=\frac{1}{2M}\sum_{i=1}^{M}(\boldsymbol{x}_i^1+\boldsymbol{x}_i^2) \tag{5.3.8}$$

can be regarded as an approximate fixed point. This fixed point can be used to define a restriction condition in Eq. (5.3.5).

5.3.3 Numerical Examples

The first numerical example is the Rössler system with control inputs as

$$\dot{x}_1=-x_2-x_3+u_1,\ \dot{x}_2=x_1+0.2x_2+u_2,\ \dot{x}_3=0.2x_3(x_1-5.7)+u_3 \tag{5.3.9}$$

The nonlinear vector function

$$\boldsymbol{f}(\boldsymbol{x},t)=\begin{pmatrix} -x_2-x_3 \\ x_1+0.2x_2 \\ 0.2x_3(x_1-5.7) \end{pmatrix} \tag{5.3.10}$$

can be cast into Eq. (5.3.1) with

$$\boldsymbol{A}=\begin{pmatrix} 0 & -1 & -1 \\ 1 & -\beta & 0 \\ 0 & 0 & -5.7 \end{pmatrix},\quad \boldsymbol{h}(\boldsymbol{x},t)=\begin{pmatrix} 0 \\ (\beta+0.2)x_2 \\ 0.2x_1x_3 \end{pmatrix} \tag{5.3.11}$$

where β is a constant that will be determined to satisfy the stability criterion of the linear system. The eigenvalues of matrix $\boldsymbol{A}$ are

$$r_1=-5.7,\ r_{2,3}=-0.5(\beta\mp\sqrt{\beta^2-4}) \tag{5.3.12}$$

Thus all eigenvalues of matrix $\boldsymbol{A}$ have negative real parts if and only if $\beta>0$. Equation (5.3.7) yields the following control input to stabilize the goal $\boldsymbol{x}_\text{g}(t)$

$$\boldsymbol{u}=\begin{cases} \begin{pmatrix} 0 \\ -(\beta+0.2)(x_2-x_{\text{g}2}) \\ -x_1x_3+x_{\text{g}1}x_{\text{g}3} \end{pmatrix} & \text{if}\,|\boldsymbol{x}-\boldsymbol{x}_\text{g}|<\varepsilon \\ \boldsymbol{0} & \text{otherwise} \end{cases} \tag{5.3.13}$$

where $\beta>0$.

The results of the stabilization of a period-3 motion of the Rössler system are illustrated in Figs. 5.9, 5.10, and 5.11 for $\beta=1$, $\varepsilon=2$, and $T=17.5$. The constant β cannot be very large. For example, if $\beta>11.1$, an unsuccessful control process results from the large control input u_2. The problem can be solved by restriction of control inputs. Fix a saturating value $U_0>0$ for the control input, and let $u_2=U_0$ if $u_2\geqslant U_0$ and $u_2=-U_0$ if $u_2\leqslant -U_0$. Figures 5.12 and 5.13 show the results of stabilization of period-3 unstable periodic orbit within the Rössler attractor at

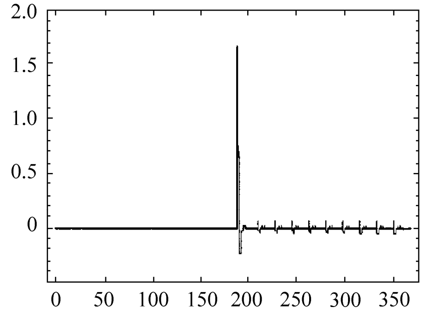

Figure 5.9 Control input u_2 to stabilize a period-3 motion

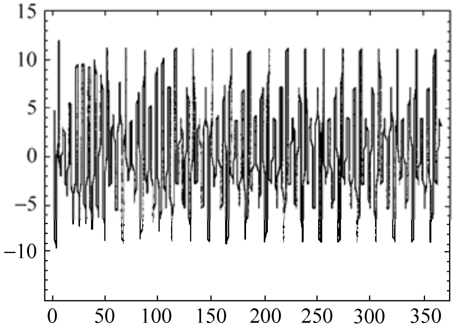

Figure 5.10 Time history of controlled state variable x_1

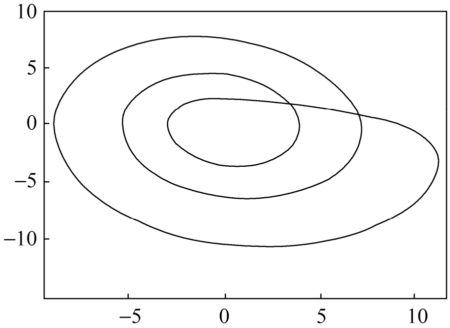

Figure 5.11 (x_1, x_3) phase portrait of the period-3 motion

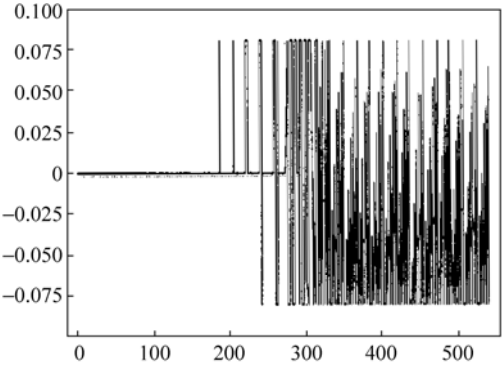

Figure 5.12 Control input with the restriction

$\beta = 13$, $\varepsilon = 2$, and $U_0 = 0.08$.

Next numerical example is a 4-dimensional nonautonomous system consisting of two coupled Duffing oscillators

$$\ddot{q}_1 + a\dot{q}_1 + q_1^3 = q_2 + b\cos t\,,\ \ddot{q}_2 + c\dot{q}_2 + q_2^3 = q_1 \tag{5.3.14}$$

The first oscillator is driven by an external periodic force, and two oscillators interact

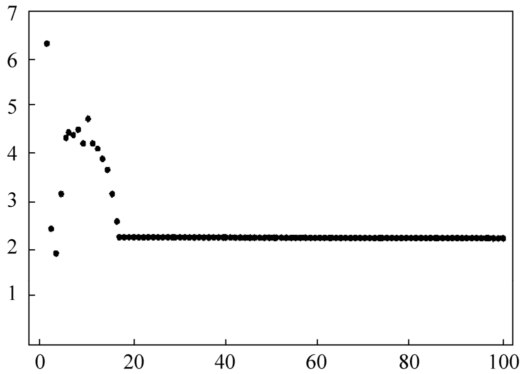

Figure 5.13 Process of stabilization of a prriod-3 motion: component x_1

with each other by q_1 and q_2. When the parameters are fixed at $a = 0.2$, $b = 10.0$, and $c = 0.45$, the chaotic behavior occurs in the system. Equation (5.3.14) can be rewritten in the form of Eq. (5.2.25) after introducing the additive control inputs and letting

$$q_1 = x_1 \,,\ \dot{q}_1 = x_2 \,,\ q_2 = x_3 \,,\ \dot{q}_2 = x_4 \tag{5.3.15}$$

Then the right hand nonlinear vector function is

$$\boldsymbol{f}(\boldsymbol{x},t) = \begin{pmatrix} x_2 \\ -ax_2 - x_1^3 + x_3 + b\cos t \\ x_4 \\ x_1 - cx_4 - x_3^3 \end{pmatrix} \tag{5.3.16}$$

The vector function $\boldsymbol{f}(\boldsymbol{x},t)$ can be decomposed into Eq. (5.3.1) where

$$\boldsymbol{A} = \begin{pmatrix} -1 & 1 & 0 & 0 \\ 0 & -a & 1 & 0 \\ 0 & 0 & -1 & 1 \\ 0 & 0 & 0 & -c \end{pmatrix}, \ \boldsymbol{h}(\boldsymbol{x},t) = \begin{pmatrix} x_1 \\ -x_1^3 + b\cos t \\ x_4 \\ x_1 - x_3^3 \end{pmatrix} \tag{5.3.17}$$

the matric $\boldsymbol{A}$ has negative real eigenvalues -1, $-a$, -1, and $-c$. Hence it satisfies the stability condition of linear systems. Equation (5.3.7) yields the following control input to stabilize the goal $\boldsymbol{x}_{\mathrm{g}}(t)$

$$\boldsymbol{u} = \begin{cases} \begin{pmatrix} -x_1 + x_{\mathrm{g}1} \\ x_1^3 - x_{\mathrm{g}1}^3 \\ -x_4 + x_{\mathrm{g}4} \\ -x_1 + x_3^3 + x_{\mathrm{g}1} - x_{\mathrm{g}3}^3 \end{pmatrix} & \text{if } |\boldsymbol{x} - \boldsymbol{x}_{\mathrm{g}}| < \varepsilon \\ \boldsymbol{0} & \text{otherwise} \end{cases} \tag{5.3.18}$$

Figures 5.14-5.16 show a chaotic trajectory in 2-dimentional subspaces (x_1, x_2), (x_3, x_4), and (x_1, x_3) respectively. The results of stabilization of the unstable period-1 orbit embedded in the chaotic attractor are shown in Figs. 5.17-5.19 in 2-dimentional subspaces (x_1, x_2), (x_3, x_4), and (x_1, x_3).

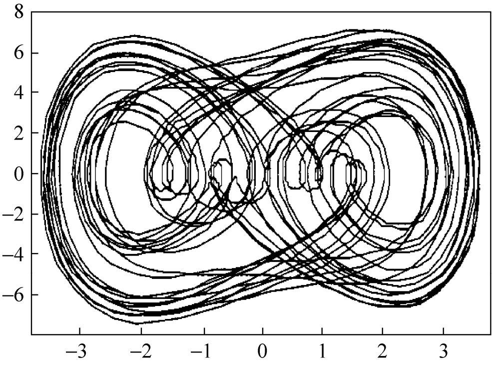

Figure 5.14 Uncontrolled chaos: subspaces (x_1, x_2)

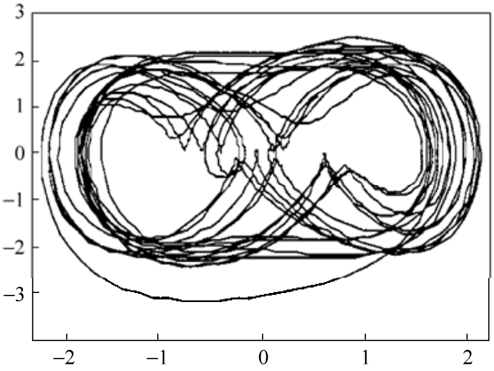

Figure 5.15 Uncontrolled chaos: subspaces (x_3, x_4)

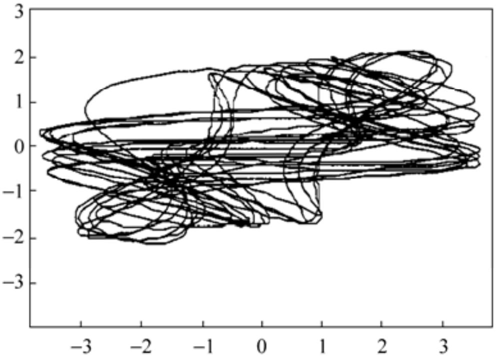

Figure 5.16 Uncontrolled chaos: subspaces (x_1, x_3)

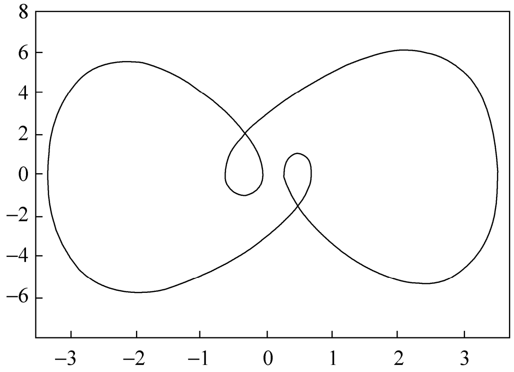

Figure 5.17 Stabilization of the period-1 motion: subspaces (x_1, x_2)

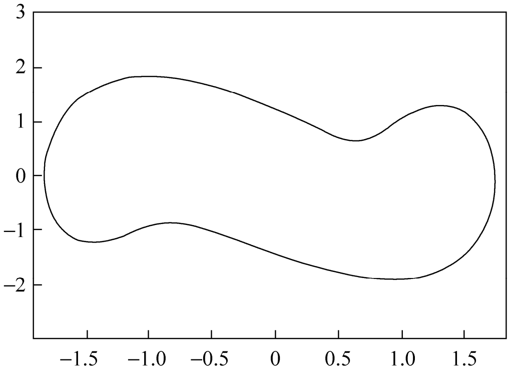

Figure 5.18 Stabilization of the period-1 motion: subspaces (x_3, x_4)

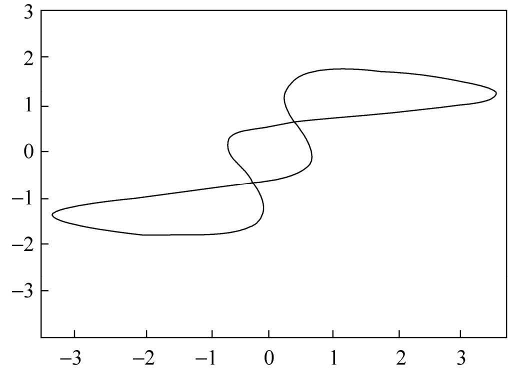

Figure 5.19 Stabilization of the period-1 motion: subspaces (x_1, x_3)

5.4 Controlling Chaotic Attitude Motions

5.4.1 Introduction

As many different control techniques are developed or employed for chaotic systems, control of chaotic attitude motion emerges as a new research direction of spacecraft attitude dynamics. Several investigators worked on the topic, and their contributions will be summarized as follows.

Dracopoulos and Jones used neural networks for modeling and genetic algorithms for control to develop a hybrid method of adaptive control [23, 24], and applied the method to control chaotic attitude motion of a rigid body spacecraft [25]. Ge, Lee, Chen, and Lee applied the continuous delayed feedback control [50] and an adaptive control [51] to regularize chaotic attitude motion of a damped satellite with partially-filled liquid [49]. Meehan and Asokanthan employed a recursive proportional feedback method [27], which is a variety of the OGY method [1], and the continuous delayed feedback method [17] to control chaotic attitude motion of a spinning spacecraft with a circumferential nutational damper [28]. Iñarrea, Lanchares, and Salas used a spinning rotor about one of the principal axes of inertia to stabilize chaotic attitude motion of a dual-spin spacecraft with time dependent moments of inertia [29]. Chen and Liu developed a parametric open-plus-closed-loop approach to control chaotic planar libration of a rigid body spacecraft in an elliptic orbit in the gravitational field with air drag and internal damping [30]. Chen and Liu revisited the problem in [31] via a modified inversion system control [30] and the input-output feedback linearization [32]. Fujii, Ichiki, Suda, and Watanabe applied the continuous delayed feedback method [17] to control chaotic planar libration of a rigid body spacecraft in an elliptic orbit in the gravitational field [33]. Tsui and Jones examined three techniques, the continuous delayed feedback method [17], a parametric control method using an artificial neural network [34], and a higher dimensional variation of the OGY method [35] in a six-dimensional system describing a rigid body spacecraft subjected to external perturbations, and found that the delayed feedback method yields the most satisfactory solution to control chaos [36]. Bernhard and Hans proposed a strategy for the deployment of a tethered satellite in a circular orbit by gravity gradient and used the chaos to fasten the process to the desired stable radial relative equilibrium [37]. Meehan and Asokanthan applied a recursive proportional feedback method [27] and the continuous delayed feedback method [17] to control chaotic attitude motion of a dual-spin spacecraft with a nutational damper [38]. They revisited the problem in [38] via a conventional energy method by minimizing the kinetic energy components associated with nutational motion that occurs during chaotic instability [39]. They also applied Lyapunov's direct method to design globally stable nonlinear control law for chaotic attitude motion of a spinning spacecraft with dissipation [40]. Chen and Liu modified the exact feedback linearization method [41] to control chaotic attitude motion of a magnetic rigid spacecraft in a circular orbit [47] and in an elliptic orbit [48] in the gravitational and magnetic fields. Kojima, Iwasaki, Fujii, Blanksby and Trivailo proposed a decoupling and model tracking control method, combined with the delayed feedback control method, for chaotic librational motion of the tethered satellite in an elliptic orbit, with the periodic motion of a tethered satellite in a circular orbit as the reference trajectory for tracking [42]. Liu and his coworkers applied stability criterion method to control chaotic attitude motion of magnetic rigid spacecraft in a circular orbit [43, 44]. Barkow, Steindl and Troger utilized chaotic dynamics of a tethered satellite system to steer the subsatellite with small control inputs into the final radial relative equilibrium position far away from the spaceship [45]. Kuang, Meehan, and Leung designed a linear feedback control law based on the Lyapunov-Krasovskii method for nonlinear systems with singular Jacobian matrixes and applied the control law to chaotic behavior of a disturbed gyrostat [46].

This section will treat controlling chaotic attitude motion of magnetic rigid spacecraft in an elliptic orbit in the gravitational and geomagnetic field. Based on the governing equation of controlled spacecraft, the parametric open-plus-closed-loop method and the stability criterion method will respectively apply to control chaos to a given fixed point or periodic motion and to stabilize chaos to a periodic motion.

5.4.2 Dynamical Model of Controlled Spacecraft

Consider a magnetic rigid spacecraft moving in an elliptic orbit in the gravitational and magnetic field of the Earth. The chaotic attitude motion was treated in Section 3.3.2. However, the spacecraft here has an actuator that can provide the control torque $\boldsymbol{M}_{\mathrm{c}}$. Then Eq. (3.3.2) becomes

$$\dot{\boldsymbol{G}} = \boldsymbol{M}_{\mathrm{g}} + \boldsymbol{M}_{\mathrm{m}} + \boldsymbol{M}_{\mathrm{d}} + \boldsymbol{M}_{\mathrm{c}} \tag{5.4.1}$$

With the same notations and in a similar way, the dimensionless governing equation of controlled spacecraft can be derived from the projection of Eq. (5.4.1) as

$$\begin{aligned} &\ddot{\varphi} - \frac{2e\sin\nu}{1+e\cos\nu}(1+\dot{\varphi}) + \frac{\kappa\sin 2\varphi}{1+e\cos\nu} + \frac{\gamma}{(1+e\cos\nu)^2}\dot{\varphi} \\ &-\alpha\frac{\cos(\varphi+\nu+\omega)-3\cos(\varphi-\nu-\omega)}{1+e\cos\nu} = \frac{u}{(1+e\cos\nu)^4} \end{aligned} \tag{5.4.2}$$

where

$$u = \frac{p^3}{C\mu}M_c$$

5.4.3 Applications of the Parametric Open-plus-closed-loop Method

Equation (5.4.2) can be cast into the form of Eq. (5.2.12) with

$$\begin{aligned} f(\varphi,\dot{\varphi},u,\upsilon) = {} & \frac{2e\sin\nu}{1+e\cos\nu}(1+\dot{\varphi}) - \frac{\kappa\sin 2\varphi}{1+e\cos\nu} - \frac{\gamma}{(1+e\cos\nu)^2}\dot{\varphi} \\ & + \alpha\frac{\cos(\varphi+\nu+\omega)-3\cos(\varphi-\nu-\omega)}{1+e\cos\nu} + \frac{u}{(1+e\cos\nu)^4} \end{aligned} \tag{5.4.3}$$

It follows that

$$\begin{aligned} f'_{\dot{\varphi}} &= \frac{2e\sin\nu}{1+e\cos\nu} - \frac{\gamma}{(1+e\cos\nu)^2} \\ f'_{\varphi} &= -\frac{2\kappa\cos 2\varphi}{1+e\cos\nu} - \alpha\frac{\sin(\varphi+\nu+\omega)-3\sin(\varphi-\nu-\omega)}{1+e\cos\nu} \\ f'_{u} &= \frac{1}{(1+e\cos\nu)^4} \end{aligned} \tag{5.4.4}$$

Substitution of Eqs. (5.4.3) and (5.4.4) into Eq. (5.2.13) yields the parametric open-plus-closed-loop control law for the spacecraft.

For the chaotic motions in Eq. (3.4.3) with the parameters given by Eqs. (3.4.16) and (3.4.17), respectively, the control goals successively are taken as a fixed point

$$\varphi_{g1}(\nu) = 0 \tag{5.4.5}$$

and a period-2 motion

$$\varphi_{g2}(\nu) = \sin 0.5\nu \tag{5.4.6}$$

Start control after $\nu_0 = 1300$. Let $\varepsilon = 1.0$, and choose $\alpha = 2.8$ and $\beta = 4.0$ in Eq. (5.2.14). The results for two goals are shown in Figs. 5.20 and 5.21, respectively. The solid lines stand for the libration angle subjected to the parametric open-plus-closed-loop control law (5.2.13). The dashed lines stand for the libration angle subjected to the input-output linearization control law [31]. The dot lines denote the libration angle of the uncontrolled system. In this example, the parametric open-plus-closed-loop control has a slightly longer transition process to achieve the goals.

The control signals $u = u(\nu)$ for φ_{g1} and φ_{g2} are respectively shown in Figs. 5.22 and 5.23. The solid lines stand for the control inputs given by Eq. (5.2.13), and the dashed lines stand for the control inputs of the input-output linearization control law. For both the goal φ_{g1} and φ_{g2}, a great pulse input is needed to activate the input-out linearization control. Since the parametric open-plus-closed-loop control begins just when the chaotic phase trajectory is close to the goal periodic orbit, only a small pulse signal is necessary.

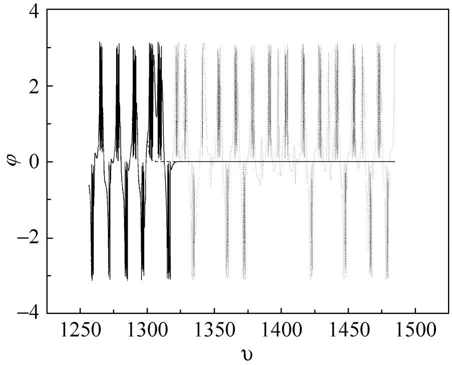

Figure 5.20 Control of chaos to the fixed point

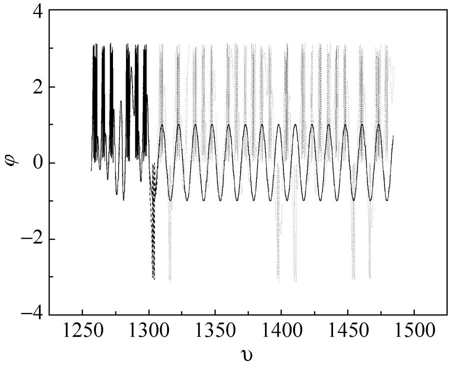

Figure 5.21 Control of chaos to the period-2 motion

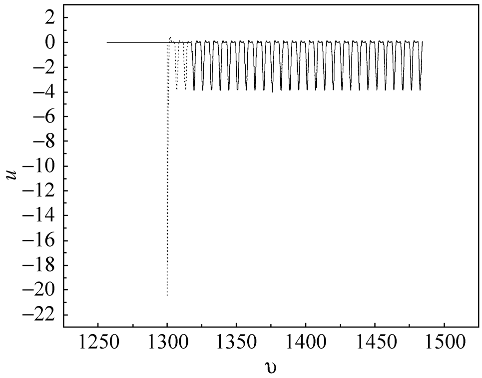

Figure 5.22 Control input for the fixed point

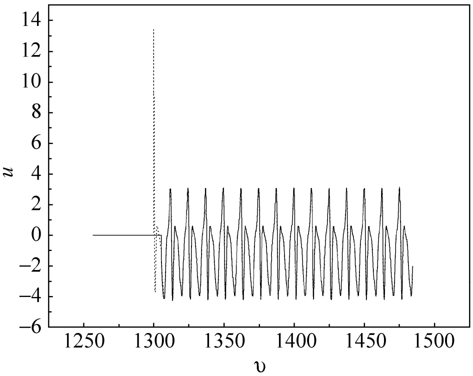

Figure 5.23 Control input for the period-2 motion

5.4.4 Applications of the Stability Criterion Method

Equation (5.4.2) can be rewritten in the form of Eq. (5.2.25) by introducing $x_1 = \varphi$ and $x_2 = \mathrm{d}\varphi/\mathrm{d}\nu$,

$$\begin{aligned} \dot{x}_1 &= f_1(x_1, x_2, \nu) + u_1 \\ \dot{x}_2 &= f_2(x_1, x_2, \nu) + u_2 \end{aligned} \tag{5.4.7}$$

where

$$\begin{aligned} &f_1(x_1, x_2, \nu) = x_2 \\ &f_2(x_1, x_2, \nu) = \frac{2e\sin\nu}{1+e\cos\nu}(1+\dot{\varphi}) - \frac{\kappa\sin 2\varphi}{1+e\cos\nu} - \frac{\gamma}{(1+e\cos\nu)^2}\dot{\varphi} \\ &\qquad + \alpha\frac{\cos(\varphi+\nu+\omega) - 3\cos(\varphi-\nu-\omega)}{1+e\cos\nu} \\ &u_2 = \frac{u}{(1+e\cos\nu)^4} \end{aligned} \tag{5.4.8}$$

and u_1 is an additional control input.

The nonlinear vector function

$$\boldsymbol{f}(\boldsymbol{x}, \nu) = \begin{pmatrix} x_2 \\ f_2(x_1, x_2, \nu) \end{pmatrix} \tag{5.4.9}$$

can be cast into Eq. (5.3.1) with

$$\boldsymbol{A} = \begin{pmatrix} -0.5 & 1 \\ 0 & -0.5 \end{pmatrix}, \quad \boldsymbol{h}(\boldsymbol{x}, t) = \begin{pmatrix} 0.5x_1 \\ f_2(x_1, x_2, \nu) + 0.5x_2 \end{pmatrix} \tag{5.4.10}$$

where matrix $\boldsymbol{A}$ has double negative real eigenvalues −0.5 satisfying the stability condition of linear system (5.3.6). The stability criterion method control law to stabilize goal $\boldsymbol{x}_{\mathrm{g}}(t)$ is derived from Eq. (5.3.7)

$$\boldsymbol{u}=\begin{cases}\begin{pmatrix}-0.5x_1+0.5x_{\mathrm{g}1}\\ -f_2(x_1,x_2,\nu)-0.5x_2+f_2(x_{\mathrm{g}1},x_{\mathrm{g}2},\nu)+0.5x_{\mathrm{g}2}\end{pmatrix} & \text{if } |\boldsymbol{x}-\boldsymbol{x}_{\mathrm{g}}|<\varepsilon\\ 0 & \text{otherwise}\end{cases} \tag{5.4.11}$$

For uncontrolled case with parameters given by Eq. (3.4.18), the chaotic motion occurs. The stability criterion method will be applied to stabilize the chaotic motion onto the period-1 trajectory as a fixed point in the Poincaré map. The fixed point is approximately estimated at $(0.50237, 0.74536)^{\mathrm{T}}$. The results of stabilization of the unstable period-1 orbit with $\varepsilon = 0.06$ are shown in Fig. 5.24, where i is the step of data sampling and δ is the error between the presently sampled point and its previous point, namely,

$$\delta=|\boldsymbol{x}(iT)-\boldsymbol{x}((i-1)T)| \tag{5.4.12}$$

After a transient process, the system comes into periodic region at 31st sampled $\nu = 31T$. The control input is maintained until $\nu = 81T$ and then it is turned off. The stabilization process of the period-1 trajectory is shown in Fig. 5.24(a). The

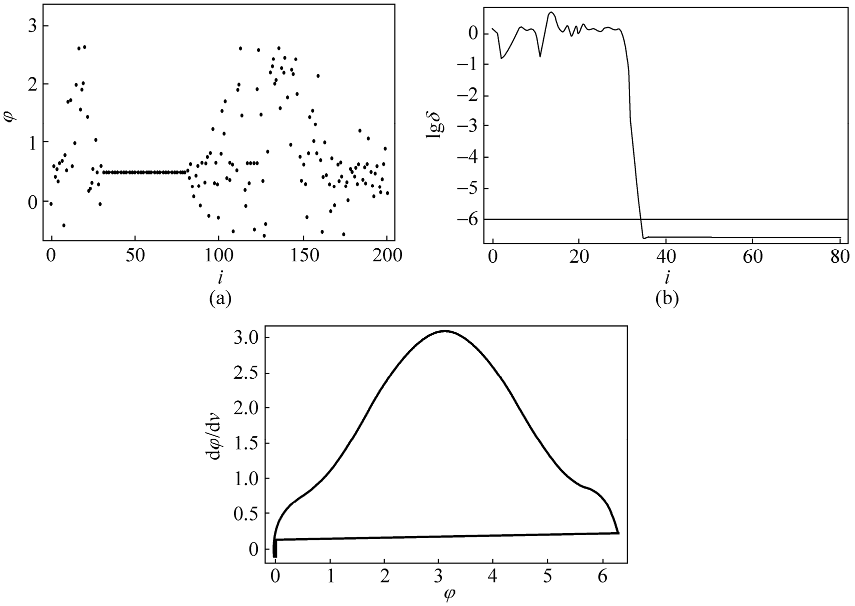

(a) (b) (c)

Figure 5.24 Results of stabilization of the unstable period-1 orbit with $\varepsilon = 0.06$: (a) stabilization process of period-1 orbit, (b) the plot of lgδ versus i and (c) the period-1 orbit error δ rapidly decreases with each step and eventually becomes less than 10^{-6} signifying that the period-1 orbit is automatically detected in the control process with increasing accuracy. The fast convergence property is shown in Fig. 5.24(b). The detected period-1 orbit is plotted in the phase plane as shown in Fig. 5.24(c), which is embedded within the chaotic attractor.

The magnitude of control input $u = |\boldsymbol{u}|$ for stabilization of period-1 orbit is shown in Fig. 5.25. In the transient process, u is rather large in the case of $\varepsilon = 1.5$ (Fig. 5.25(c)), and is sufficient small in the case of $\varepsilon = 0.06$ (Fig. 5.25(a)). The control is switched on only when the trajectory comes near the period-1 orbit at certain time, namely, when the condition of $\varepsilon<0.06$ is satisfied.

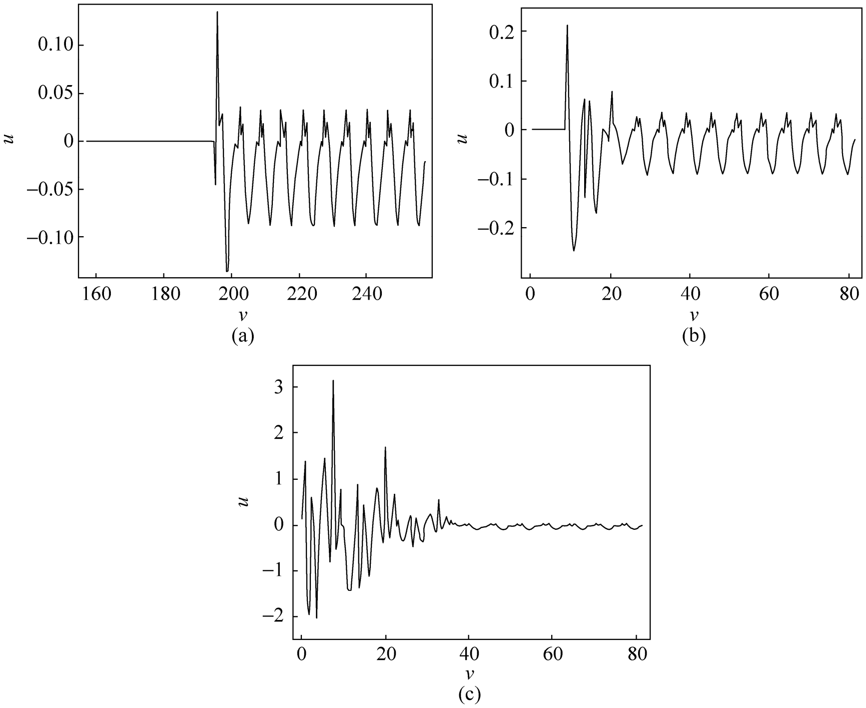

Figure 5.25 The control input $u(v)$, (a) $\varepsilon = 0.06$; (b) $\varepsilon = 0.3$ and (c) $\varepsilon = 1.5$

The influence of restriction value ε on the convergence speed of the control process is illustrated in Fig. 5.26. The shortest control steps $i_{\min}$ is defined as the step at which the error δ becomes 10^{-6}. It is shown in Fig. 5.26 that, if ε is larger than 0.26, the convergence of control is quite fast ($7<i_{\min}<10$). The shortest control steps $i_{\min}$ fluctuate between 6 and 65 for $0.04<\varepsilon<0.25$. Hence, an appropriate value of ε can be chosen to suit different control requirements.

The results of the flexible control of the chaos to unstable period-1 or period-2 orbits are shown in Fig. 5.27. The control is turned on at the 20th step after free running, and the chaos is stabilized on period-1 orbit. After the maintenance of the control for 50 steps, the orbit returns to chaos as the control is turned off. The control is turned on again to stabilize the period-2 orbit at the 100th step, and then lasts for 60 steps.

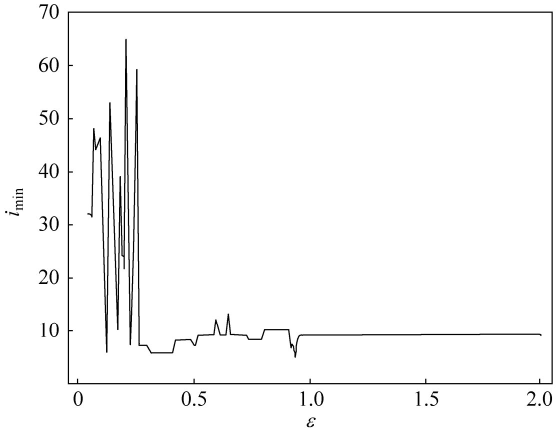

Figure 5.26 Influence of ε on shortest control steps $i_{\min}$

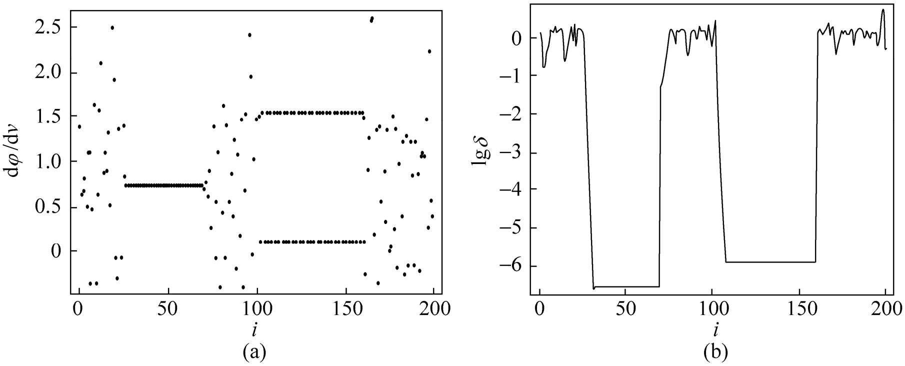

(a) (b)

Figure 5.27 Flexible control of the chaotic attitude motion: (a) process of stabilization of period-1 and period-2 orbits, and (b) the plot of $\lg\delta$ versus i

References

[1] Ott E, Grebogi C, Yorke JA. Controlling chaos. *Physical Review Letters*, 1990, 64, 1196-1199

[2] Slotine JJE, Li W. *Applied Nonlinear Control*. Englewood Cliffs: Prentice-Hall, 1991

[3] Auerbach D, Grebogi C, Ott E, Yorke JA. Controlling chaos in high dimensional systems. *Physical Review Letters*, 1992, 69, 3479-3482

[4] Ogata K. *Modern Control Engineering* (4th edn.). Englewood Cliffs: Prentice-Hall, 2002

[5] Boccaletti S, Kurths J, Osipov G, Valladares DL, Zhou CS. *The synchronization of chaotic systems*. *Physics Reports*, 2002, 366, 1-101

[6] Chen LQ. A general formalism for synchronization in finite dimensional dynamical systems. *Chaos*, *Solitons and Fractals*, 2004, 19(5), 1239-1242

[7] Jackson EA. The entrainment and migration controls of multiple-attractor systems. *Physics Letters A*, 1990, volume 151(9), 478-484

[8] Hübler AW, Lüscher E. Resonant stimulation and control of nonlinear oscillator. *Naturwissenschaft*, 1989, 76, 67-69

[9] Jackson EA. On the control of complex dynamic systems. *Physica D*, 1991, 50, 341-366

[10] Jackson EA. Controls of dynamic flows with attractors. *Physical Reviews A*, 1991, 44, 4839-4853

[11] Mettin R, Hübler A, Scheeline A, Lauterborn W. Parametric entrainment control of chaotic systems. *Physical Reviews E*, 1995, 51, 4065-4075

[12] Jackson EA, Grosu I. An open-plus-closed-loop (OPCL) control of complex dynamic systems. *Physica D*, 1995, 85, 1-9

[13] Jackson EA. The OPCL method of entrainment, model-resonance, and migration actions applied to multiple-attractor systems. *Chaos*, 1997, 7, 550-559

[14] Chen LQ, Liu YZ. A modified open-plus-closed-loop control of chaos in nonlinear oscillations. *Physics Letters A*, 1998, 245(1-2), 87-90

[15] Chen LQ, Liu YZ. A parametric open-plus-closed-loop approach to control chaos in nonlinear oscillations. *Physics Letters A*, 1999, 262, 350-357

[16] Yu HJ, Liu YZ, Peng JH. Continuous control of chaos based on the stability criterion. *Physical review E*, 2004, 69, 066203

[17] Pyragas K. Continuous control of chaos by self-controlling feedback. *Physics Letters A*, 1992, 170, 421-428

[18] Ushio T. Chaotic synchronization and controlling chaos based on contraction mappings. *Physics Letters A*, 1995, 198, 14-22

[19] Roy R, Murphy TW, Majer TD, Gills Z, Hunt E. Dynamical control of a chaotic laser: experimental stabilization of a globally coupled system. *Physical Review Letters*, 1992, 68, 1255-1258

[20] Yu HJ, Liu YZ. Chaotic synchronization based on stability criterion of linear systems. *Physics Letters* A, 2003, 314, 293-298

[21] Shinbrot T, Grebogi C, Ott E, Yorke JA. Using small perturbations to control chaos. *Nature*, 1993, 363, 411-417

[22] Xu D, Bishop SR. Self-locating control of chaotic systems using Newton algorithm. *Physics Letters A*, 1996, 210, 273-278

[23] Dracopoulos DC, Jones AJ. Neuro-genetic adaptive attitude control. *Neural Computing & Applications*, 1994, 2, 183-204

[24] Dracopoulos DC, Jones AJ. Neural networks and genetic algorithms for the attitude control problem, *Lecture Notes in Computer Science*, 1995, 930, 315-321

[25] Dracopoulos DC, Jones AJ. Adaptive neuro-genetic control of chaos applied to the attitude control problem, *Neural Computing & Applications*, 1997, 6(2), 102-115

[26] Sinha S, Ramaswamy R, Rao JS. Adaptive control in nonlinear dynamics. *Physica D*, 1991, 43, 118-128

[27] Rollins RW, Parmananda P, Sherard P. Controlling chaos in highly disspative systems: a simple recursive algorithm. *Physical Review E*, 1996, 47, R780-783

[28] Meehan PA, Asokanthan SF. Control of chaotic motion in a spinning spacecraft with a circumferential nutational damper. *Nonlinear Dynamics*, 1998, 17(3), 269-284

[29] Iñarrea M, Lanchares V, Salas JP, Spin rotor stabilization of a dual-spin spacecraft with time dependent moments of inertia, *International Journal of Bifurcation and Chaos*, 1998, 8(3), 609-617

[30] Chen LQ, Liu YZ. Chaotic attitude motion of non-spinning spacecraft and its parametric open-plus-closed-lop control. *Acta Mechanica Sinica*, 1998, 30, 363-369 (in Chinese)

[31] Chen LQ, Liu YZ. The inversion system control of chaotic oscillations. *Technische Mechanik*, 1999, 19(1), 1-4

[32] Chen LQ, Liu YZ. Controlling chaotic attitude motion of spacecraft by the input-output linearization. *Zeitschrift für Angewandte Mathematik und Mechanik*, 2000, 80, 701-704

[33] Fujii HA, Ichiki W, Suda S, Watanabe TR. Chaos analysis in librational control of gravity-gradient satellite in elliptic orbit, *Journal of Guidance, Control, and Dynamics*, 2000, 23(1), 145-146

[34] Oliveira AG, Jones AJ. Synchronization of chaotic trajectories using parameter control. *Proceedings of the* 1*st International Conference of Control of Oscillators and Chaos* (eds. Chernousko FL, Fradkov AL), 1997, 1, 46-49

[35] Ding M, Yang W, In V, Ditto WL, Spano ML, Gluckman B. Controlling chaos in high dimensions: theory and experiment. *Physical Reviews E*, 1996, 53, 4334-4344

[36] Tsui APM, Jones AJ. The control of higher dimensional chaos: comparative results for the chaotic satellite attitude control problem, *Physica D*, 2000, 135, 41-62

[37] Bernhard B, Hans T. A simple strategy for the deployment of a tethered satellite system. *Zeitschrift für Angewandte Mathematik und Mechanik*, 2001, 81, S177-S178

[38] Meehan PA, Asokanthan SF. Control of chaotic motion in a dual-spin spacecraft with nutational damping. *Journal of Guidance, Control, and Dynamics*, 2002, 25(2), 209-214

[39] Meehan PA, Asokanthan SF. Control of chaotic instability in a dual-spin spacecraft with dissipation using energy methods. *Multibody System Dynamics*, 2002, 7, 171-188

[40] Meehan PA, Asokanthan SF. Control of chaotic instabilities in a spinning spacecraft with dissipation using Lyapunov's method, *Chaos, Solitons and Fractals*, 2002, 13(9), 1857-1869

[41] Chen LQ, Liu YZ. A modified exact linearization control for chaotic oscillators. *Nonlinear Dynamics*, 1999, 20, 309-317

[42] Kojima H, Iwasaki M, Fujii HA, Blanksby C, Trivailo P. Nonlinear control of librational motion of tethered satellites in elliptic orbits, *Journal of Guidance, Control, and Dynamics*, 2004, 27(2), 229-239

[43] Yu HJ, Liu YZ. Control of chaotic attitude motion of a magnetic spacecraft in a complex force field. *Journal of Shanghai Jiao Tong University*, 2004, 38(8), 1408-1411 (in Chinese)

[44] Liu YZ, Yu HJ, Chen LQ. Chaotic attitude motion and its control of spacecraft in elliptic orbit and geomagnetic field. *Acta Astronautica*, 2004, 55(3-9), 501-508

[45] Barkow B, Steindl A, Troger H. A targeting strategy for the deployment of a tethered satellite system. *IMA Journal of Applied Mathematics*, 2005, 70, 626-644

[46] Kuang JL, Meehan PA, Leung AYT. Suppression chaos via Lyapunov-Krasovskii's method. *Chaos, Solitons and Fractals*, 2006, 27, 1408-1414

[47] Chen LQ and Liu YZ. Chaotic attitude motion of a magnetic rigid spacecraft and its control. *International Journal of Non-Linear Mechanics*, 2002, 37(3), 493-504

[48] Liu YZ, Chen LQ. Chaotic attitude motion of a magnetic rigid spacecraft in an elliptic orbit and its control, *Acta Mechanica Sinica*, Year???, 19(1), 71-78

[49] Ge ZM, Lee CI, Chen HH, Lee SC. Nonlinear dynamics and chaos control of a damped satellite with partially-filled liquid, *Journal of sound and Vibration*, 1998, 217, 807-825

[50] Nayfeh AH, Balachandran B. *Applied Nonlinear Dynamics: Analytical, Computational, and Experiment Methods*. New York: John Wiley & Sons, 1995

[51] Swinney HL, Gollub JP. The transition to turbulence. *Physics Today*, 1978, 31, 41-49